NORTHWESTERN UNIVERSITY

Manipulation of Intermolecular Interactions for Active Layer Morphology Optimization in Organic Photovoltaics

A DISSERTATION

SUBMITTED TO THE GRADUATE SCHOOL
IN PARTIAL FULFILLMENT OF THE REQUIREMENTS

for the degree of

DOCTOR OF PHILOSOPHY

Field of Chemistry

by

Leonel Barreda

EVANSTON, ILLINOIS

March 2017

Abstract

Organic photovoltaics (OPVs) are an attractive solar energy technology for low-current applications. Herein is described the supramolecular design and methodology to manipulate intermolecular interactions in order to create an active layer in OPVs devices composed of crystalline and amorphous donor-acceptor domains, which has been proposed as the ideal morphology for high performance. To this end, a series of symmetric and asymmetric diketopyrrolopyrrole (DPP) derivatives containing either an amide (capable of hydrogen-bonding) or ester endgroups were synthesized. The symmetric designs faced problems with solubility, strong segregation and low performance, so asymmetric donors having one amide/ester were used. Upon addressing initial stability problems, analysis of the ester films with X-ray diffraction displayed greater crystallinity and $\pi-\pi$ stacking. The amide formed short aggregates with smaller, less ordered domains, resulting from competition between hydrogen bonding and $\pi-\pi$ stacking, which interestingly endowed devices with higher current and 50% increase in device efficiency over the ester. To better match solar emission, the DPP core was substituted by benzodithiophene (BDT). Amides again outperformed esters, but introduction of a benzothiadiazole π-spacer between the amide/ester endgroups led to electron traps and lowered performance; replacing it with phenyldithiophene reduced stacking ability. A recurring issue was the competition between noncovalent interactions, which motivated the use of barbituric acid endgroups, but solubility was compromised. After addressing each problem, a design having a BDT core with planar π-spacers, connected by an alkyl linker to the hydrogen-

bonding endgroups is predicted to display optimized optoelectronic properties and cooperative noncovalent interaction. Next, a series of BDT-core molecules with DPP endgroups and alkyl tails resembling solvent additives (which improve donor-acceptor interaction but increase processing complexity) were synthesized. Preliminary molecules showed promising efficiency but lacked solubility. An asymmetric DPP group with less stacking ability was used, but exposed possible electron traps. The BDT core was then modified to be more electron-rich but led to lower performance. Consequently, an extended molecule with fully symmetric DPP endgroups was used, but the large number of alkyl tails caused segregation from the acceptor. Therefore, a BDT design with symmetric DPP termini and re-positioned alkyl tails is proposed to address electron traps, solubility and segregation problems.

Acknowledgements

The journey through graduate school has been by far the most challenging part of my life, but it has also been the time when I have learned the most, not only in the scientific realm, but the personal as well. The physical and emotional effects of having worked for such a long time with very little success can be detrimental to anyone's health, myself included, but the people that surrounded me during my time here have definitely had a positive influence on me, and have given me a different perspective on how to view scientific and personal setbacks, and helped me to move forward.

First and foremost is my family; my parents Luis and Carmen, who always encouraged me to do my very best. I also thank my five siblings, the heirs of the Barreda clan: Alejandro, Susana, Larissa, Leonardo and Liliana, for making the few moments of peace I had, so much more enjoyable. Six years is a long time, during which my family has grown considerably, so I thank my siblings for giving me the gift of nephews, Alex, Andres, Nicolas, Santino, Arlo and Harvey and to their spouses for allowing my nephews to be a reality, I thank Chayo, David, Ashley and KC.

Next I would like to thank the teachers, professors, and people in general who at some point in my life, showed me that I had the ability to go as far as I set up to. My first grade teacher, Teresa Soltero, who told me I could do great things, as long as I put in the effort. Jumping almost a decade in time, I met Bertha Olivas Trillo, who to-date is the most passionate person I have ever met. Sadly she passed away shortly after I graduated high school, but observing the way she taught chemistry opened my eyes to the possibility of loving my job, not just perform a function. Next, I would like to thank Prof. Juan C. Noveron, my undergraduate advisor, who talked me out chemical

engineering and convinced me to follow a chemistry degree, and more importantly, enlightened my perception of research.

While I was an undergraduate student, I visited the Stupp lab and met Dr. Yves Ruff, who became my mentor over the summer of 2009, and it is because of him that I became unafraid of purifying 50 g of material in a single sitting. Once in graduate school, Prof. Samuel I. Stupp became my thesis advisor and was most understanding in times when my project had to take a new direction without the possibility of publication; and for that I am grateful. My research changed from what I initially did in the summer of 2009, and in September of 2010, Dr. Amparo Ruiz-Carretero became my mentor, and it is because of her that I know OPVs and Stille couplings. I had the pleasure of attending her wedding in Spain, which has been probably the best experience of my life. After she left, many post-docs and upper level graduate students helped me with synthesis particularly. Prof. Liam Palmer has been a key member of the group and has always been available when I have needed his opinion or point of view. Prof. Martin Conda-Sheridan helped me enormously when I was working on charge-transfer complexes; Dr. Timmy Fyrner, a good source orthogonal protecting groups, spiced up with Swedish-style rage; Dr. Kohei Sato has also given me vital suggestions that have helped my synthesis significantly; Dr. Jose Betancourt-Borges, Dr. Elena Pazos-Chantrero, Dr. Job Boekhoven were very helpful in helping me finding jobs to apply for and for suggestions in general.

The recently appointed Dr. Taner Aytun deserves his own paragraph because through his work, I was able to get my molecules to work. He did all the device fabrication in this thesis, and he has been a brother in arms, partner in crime (not

literally speaking of course) and undoubtedly the collaborator who contributed the most to the development of my project. My disappointments and frustrations became his own after he tested the molecules I made, and we met countless times to try and design the miracle molecule, the one that would give us a much desired (and needed) publication. There are no words that can describe how thankful I am for his aid through these six years of agony.

Next, I'd like to thank my friends, who have definitely buffered an otherwise very sour experience. My friends from my first year, who have gone to a better life (i.e graduated), Dr. Mona "sister" Shresta, Dr. Olga "baby" Karagiaridi, Dr. Giang Nguyen, Dr. Monica So, Dr. Mark Bachrach, Dr. Alejo Lifschitz were always around to brighten my day up. I thank my roommates, Colin Calabrese and Dr. Sicelo Masango, who are incredible researchers and had the most awesome conversations outside of lab. Next, I thank the few remaining people who have gone through the agony of watching their friends graduate: Jose E. Mendez, Dana Cao, Cornelius Audu, Resham Banga, for always having some good topic to decompress busy days. As much as I dislike him sometimes, Adam "Pepito" Preslar has always been a sender/receiver of insults, and put me through the most annoying routine I ever had, which was driving him to groceries. Other office/party mates I have had the pleasure of meeting are Dr. Adam "hotsauce" Weingarten, for organizing karaoke night, an event where my credibility and dignity were thrown out the window; Roman Kazantsev, a source of interesting talks and judo techniques; Dr. Jessica Lehrman, for teaching me stannylations past midnight during my first summer in graduate school; Andrew Koltonow, who sadly left the group a few years ago, but who today still continues to be a reliable friend. My current office

Only one who devotes himself to a cause with his whole strength and soul can be a true master. For this reason mastery demands all of a person.

Albert Einstein

List of Abbreviations

°C Degree Celsius

°F Degrees Fahrenheit

3-D Three dimensional

A Acceptor

A/g Ampere per gram

ACN Acetonitrile

AFM Atomic force microscopy

Ag Silver

AgNO$_3$ Silver nitrate

Al Aluminum

AM 1.5G Air-mass 1.5 G (1 sun is defined as equal to 100 mW/cm^2)

B.C. Before Christ

BDT Benzodithiophene

BHJ Bulk heterojunction

BLA Bond length alternation

BTD Benzothiadiazole

C Capacitance

Ca Calcium

CB Chlorobenzene

CCL Crystalline correlation length

CDCl$_3$ Deuterated chloroform

CHCl$_3$ Chloroform

CNT Carbon nanotube

CO$_2$ Carbon dioxide

COF Covalent organic framework

CrO Chromium (II) oxide

CT Charge transfer

CuO Copper oxide

d Thickness of double layer

D Donor

DCB Dichlorobenzene

DCE Dichloroethane

DCM Dichloromethane

DIO Diiodooctane

DMF N,N-dimethylformamide

DMSO Dimethylsulfoxide

DPP Diketopyrrolopyrrole

DPPF Poly(diketopyrrolopyrrole-thiophene-fluorene-thiophene

DPTS (4-diethylamino)pyridinium sulfonate

EDC 1-Ethyl-3-(3-dimethylamimopropyl)carbodiimide

EDL Electric double-layer supercapacitor

EDOT Ethylenedioxythiophene

E$_g$ Band gap

EQE External quantum efficiency

ETL Electron transport layer

EtOAc Ethyl acetate

eV Electron volt

F/g Farad per gram

F_c/F_c^+ Ferrocene/ferrocinium

Fe_3O_4 Iron (IV) oxide

FF Fill factor

FIB Focused ion beam

fs Femtosecond

FTIR Fourier transform infrared spectroscopy

g Paracrystallinity parameter

GISAXS Grazing incidence small angle x-ray scattering

GIWAXS Grazing incidence wide angle x-ray scattering

GIXS Grazing incidence X-ray scattering

HBC Hexabenzocoronene

HCl Hydrochloric acid

HFAC Higjly functionalized activated carbon

HOBt Hydroxybenzotriazole hydrate

HOMO Highest occupied molecular orbital

HRMS High-resolution mass spectrometry

HTL Hole transport layer

IC60BA Indene-C60-bisadduct

ICT Intramolecular charge transfer

IIn Isoindigo

IQE Internal quantum efficiency

ITIC 3,9-bis(2-methylene-(3-(1,1-dicyanomethylene)-indanone))-5,5,11,11-tetrakis(4-hexylphenyl)-dithieno[2,3-d:2′,3′-d′]-s-indaceno[1,2-b:5,6-b′]dithiophene)

ITO Indium tin oxide

J-V Current-voltage

J$_M$ Maximum current

kWh Kilowatthour

La Crystal size

LiF Lithium fluoride

LUMO Lowest unoccupied molecular orbital

MeI Methyl iodide

MeOH Methanol

MgSO$_4$ Magnesium sulfate

Mn$_3$O$_4$ Manganese(IV) oxide

MnO$_2$ Mangenese (II) oxide

MO Molecular orbital

MOF Metal-organic framework

MoO$_3$ Molybdenum (VI) oxide

MoOx Molybdenum oxides

M$_W$ Molecular weight

mW/cm^2 Miliwatt per square centimeter

MWCNT Multi-wall carbon nanotubes

N2200 Poly{[*N*,*N*′-bis(2-octyldodecyl)-naphthalene-1,4,5,8-bis(dicarboximide)-2,6-diyl]-*alt*-5,5′-(2,2′-bithiophene)}

NaCl Sodium chloride

NaOH Sodium hydroxide

NBS N-bromosuccinimide

NEt$_3$ Triethylamine

Ni(OH)$_2$ Nickel (II) hydroxide

NiAc Nickel acetate

NiCoO$_4$ Nickel (II) cobalt (II) oxide

NiO Nickel oxide

NMe$_4$OAc Tetramethylammonium acetate

NMR Nuclear magnetic resonance spectroscopy

NPE Nonconjugated polyelectrolytes

ODT Octandithiol

OPV Organic Photovoltaics

P Power

P3HT Poly-3-hexylthiophene

PC$_{71}$BM Phenyl-C$_{70}$-butyric acid methyl ester

PCBM (PC$_{61}$BM) Phenyl-C$_{60}$-butyric acid methyl ester

PCE Power conversion efficiency

Pd(dba)$_2$ Dibenzylideneacetone palladium (0)

Pd(PPh$_3$)$_4$ Tetrakis(triphenylphosphine) palladium (0)

PDI Perylene diimide

PE-HF-CVD Plasma enhance hot filament chemical vapor deposition

PEDOT:PSS Polyethylenedioxythiophene-polystyrenesulfonate adduct

PEIE Polyethyleneimine ethoxylated

PITN Polyisothianaphtene

P$_M$ Max power

PP Polyphenylene

PPM Parts per million

PPV Polyphenylenevinylene

PSSA-g-PANI Postyrenesulfonic acid grafted polyaniline

PTB7 Benzodithiophene-thienothiophene high efficiency polymer

PV Photovoltaics

R-SoXS Resonant soft X-ray scattering

rr Regioregular

R$_S$ Series resistance

R$_{SH}$ Shunt resistance

RuO$_2$ Ruthenium (II) oxide

S Herman's orientation parameter

SANS Small angle neutron scattering

SCLC Space-charge limited current

Se Selenium

Si Silicon

SIMEF bis(imethylphenylsilylmethyl)[60]fullerene

S$_{N2}$ Nucleophilic substitution (concerted)

SOF Supramolecular organic framework

TBAB Tetrabutylammonium bromide

TEM Transmission Electron Microscopy

T$_g$ Glass transition temperature

THF Tetrahydrofuran

TiOx Titanium oxide mixture

TP Thienopyrrole

TT Thienothiophene

TW Terawatts

TWh Terawatthours

UPS Ultraviolet photoelectron spectroscopy

UV-Vis Ultraviolet-visible spectroscopy

V$_2$O$_5$ Vanadium (V) oxide

VBI Built-in voltage

V$_M$ Maximum voltage

V$_{OC}$ Open circuit voltage

VRS Voltage series resistance

Wh/g Watt-hour per gram

Wh/L Watt-hour per liter

WO$_3$ Tungsten (IV) oxide

ZnO Zinc oxide

ε Dielectric constant

π-π* First excited state

Table of contents

Chapter 3 Supramolecular Organic Frameworks for High Efficiency Photovoltaics

143

List of Figures

normal (parallel) to the plane of the film. The insets show schematically the different orientations of the microcrystalline grains with respect to the substrate. Retrieved from ref. 106.

List of Schemes

List of Tables

Chapter 1 Introduction to Photovoltaic Systems

1.1 The Need for Solar Energy

The number one challenge humanity faces today, is energy; that was the warning that Nobel Laureate Richard Smalley gave more than a decade ago.[1] The world's energy consumption is predicted to grow 56% from 2010 to 2040; that represents a total energy usage of 42.5 TW, to 67 TW in 2040.[2] In terms of electricity, the projected growth is even higher, with an impressive 93% increase in the same period, that is from 20.2 to 39 TWh.[2] Currently, and as it is projected for the next few decades, the market of electricity generation is largely dominated by fossil fuels (Figure 1.1). Coal is and will be the largest electricity production source; although it's predicted to decline in demand after 2025, it will still be the number one source of energy for the foreseeable future. Natural gas is the second largest energy source and its demand is projected to grow even more after hydraulic fracturing techniques are improved. Nuclear energy follows, but the recent Fukushima disaster will affect nuclear energy growth. The remaining minority sources are hydroelectric power, which by itself accounts for almost 80% of renewable electricity, and other renewables such as wind (second largest renewable), solar and geothermal constitute less than 5% of the total energy produced.[2]
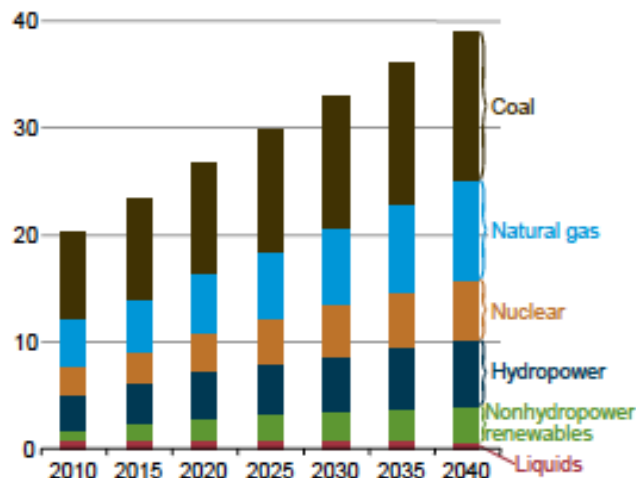
Figure 1.1. World energy generation by source. Retrieved from ref. 2.

The fact that the world's energy needs for the foreseeable future are covered does not imply the future is secured. By now, there is virtually no argument against anthropogenic climate change. The greenhouse gas emissions, particularly CO_2 have reached an excess of 400 ppm in the air, and the global temperature has risen 1.4 °F since the beginning of the industrial era in the late 1880s.[3] In an effort to mitigate the effect of climate change, nations around the world have set a limit of 2 °C temperature increase, and have vowed to take measures to reduce emissions to achieve that goal. For nations to recognize the magnitude of the problem was quite an achievement in itself, but recent studies suggest the limit of 2 °C temperature increase would require a third of oil reserves, half those of gas and over 80 % those of coal to be left unused by 2050 in order to achieve that goal.[4] Sadly, the news came in a time where technology once again paid off. At the moment, the oil and gas reserves have increased due to the

advent of fracking technology, and are estimated to last for about one and a half centuries, and coal will endure even longer, with a least one millennia worth of reserves.[5] Even the most optimistic environmentalist could agree the fight for climate change mitigation is far from over. In spite of the apparent wealth of fossil fuel resources, the quest for an abundant source of energy should not be abandoned.

The widely accepted idea that the climate is changing due to human activity has not come without rewards. Renewable energy will be the fastest growing energy field projected by 2050.[2] Although hydropower is largely responsible for that increase, technologies are still improving, for example in wind energy. Nevertheless, not even the oil, gas, coal nor the remaining renewable energies compare in magnitude to the energy the Earth receives from the sun. Every second, the sun irradiates 174000 TW to the upper atmosphere of the earth; due atmospheric absorption, scattering, land area (only 25% of the earth's surface) and latitude, that value decreases to ~13% of its original amount once it reaches land.[6] That 13% though, after doing some quick arithmetic, corresponds to over 23000 TW; the estimated global energy demand for 2040 is 67 TW, and the electric usage was mentioned to be ~ 40 TW, which means that the energy requirements for the next 24 years represent less than one percent of the energy received from the sun. As a matter of fact, they represent less than half of a percent. Every square meter, regardless of latitude or weather, has potentially 183 W of usable energy. Harvesting solar energy is for the most part aimed at transforming it to electricity, as is the case of solar concentrators and photovoltaics; a smaller, yet popular

field is known as solar fuels, where sunlight drives the splitting of water or carbon dioxide into oxygen/hydrogen or into useful fuels such as methanol, respectively.[7,8]

Solar concentrating systems were first built in the 1980s and their working principle is quite simple: sunlight from a large area of collectors is directed to a much smaller area, where the receiver, coated with an absorber material, heats to a high temperature, then transfers the heat to a fluid which can be stored for later use, or used to power a heat engine and produce electricity.[9] It is precisely the efficiency of electricity generation that is a major challenge of this technology; thermoelectric generators tend to have single-digit efficiencies, whereas steam (or other liquids) engines' efficiencies will vary significantly with the type of fluid used. Another issue is that only the infrared part of the solar spectrum is used to heat (in spite of the fact that all light is reflected), but the photon flux of the sun hits its maximum energy output in the visible spectrum (blue rectangle in Figure 1.2). Photovoltaic systems address precisely the latter point, utilizing the visible range of the solar spectrum.
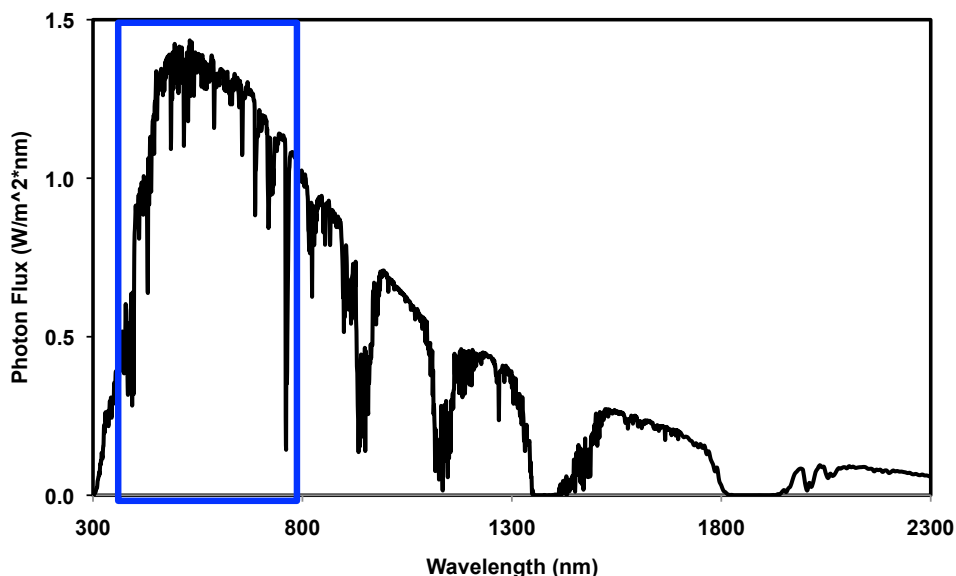
Figure 1.2. Solar photon flux; maximum occurs in the visible region (blue rectangle). Retrieved from Ref. 9

Solar photovoltaic (PV) systems are attractive because they capture the highest energy incident photons and convert them into electricity, without the need for additional steam engines or high working temperatures, making them more attractive for domestic uses. The history behind PV systems dates back to ancient Greek and Roman civilizations (3rd and 2nd century B.C.), who used mirrors to concentrate sunlight for fire purposes. The photovoltaic field began in 1839, when French scientist Edmond Becquerel discovered the photovoltaic effect; then in 1873, Willoughby Smith discovered the photoconductivity of selenium (Se), followed three years later by William Grylls Adams and Richard Evans Day, who observed Se's photovoltaic effect and by Charles Fritts, who built the first Se PV wafers in 1883. The photovoltaic effect was explained in 1905 by Einstein, and proved experimentally in 1916 by Robert Millikan. Silicon (Si) photovoltaics began in 1918 when Polish scientist Jan Czochralski

developed a way to grow single-crystal silicon, and in 1954, Daryl Chapin, Calvin Fuller, and Gerald Pearson developed the Si photovoltaic (PV) cell at Bell Labs (4% efficiency). During the 1960s PV systems were incorporated into satellites and into modules.[10] In the 1970s the Si PV costs were reduced significantly, and the field expanded with the discovery of new organic polymeric semiconductors.[11]

The success of any technology, as has always been the case, is partially dictated by its efficiency. The National Renewable Energy Lab keeps a record of not only inorganic, but organic and other types of solar cells (Figure 1.3).[12] From the chart, it can be seen that inorganic systems have the highest efficiency, and since they have been studied for nearly two centuries, they also have the highest possibility of competing with fossil fuels. The Department of Energy set a goal of reaching $0.06/kWh by 2020; at that price, solar electricity would be competitive enough with fossil fuels.[13] Along with reducing costs, other challenges to their grid-scale implementation is the inherently intermittency of sunlight, though battery systems could help address the latter point. Inorganic systems also have to compete with the microprocessor industry,[14] and their current payback time (the time it takes to produce the same amount of energy used to build them) is estimated to be between three and four years,[15] which may not be appealing to investors. Among the different materials in Figure 1.3, organic photovoltaics (OPV) are an attractive complementary technology to inorganic systems, both scientifically and financially. Although much lower in efficiency, the OPV field has grown enormously in the last 15 years, and has potential applications in power windows, built-in chargers for portable electronics or wearable power source applications,[16] where inorganic systems are not particularly adaptable. The remainder of

this thesis will focus on these materials, with special emphasis on issues related to the morphology of films.
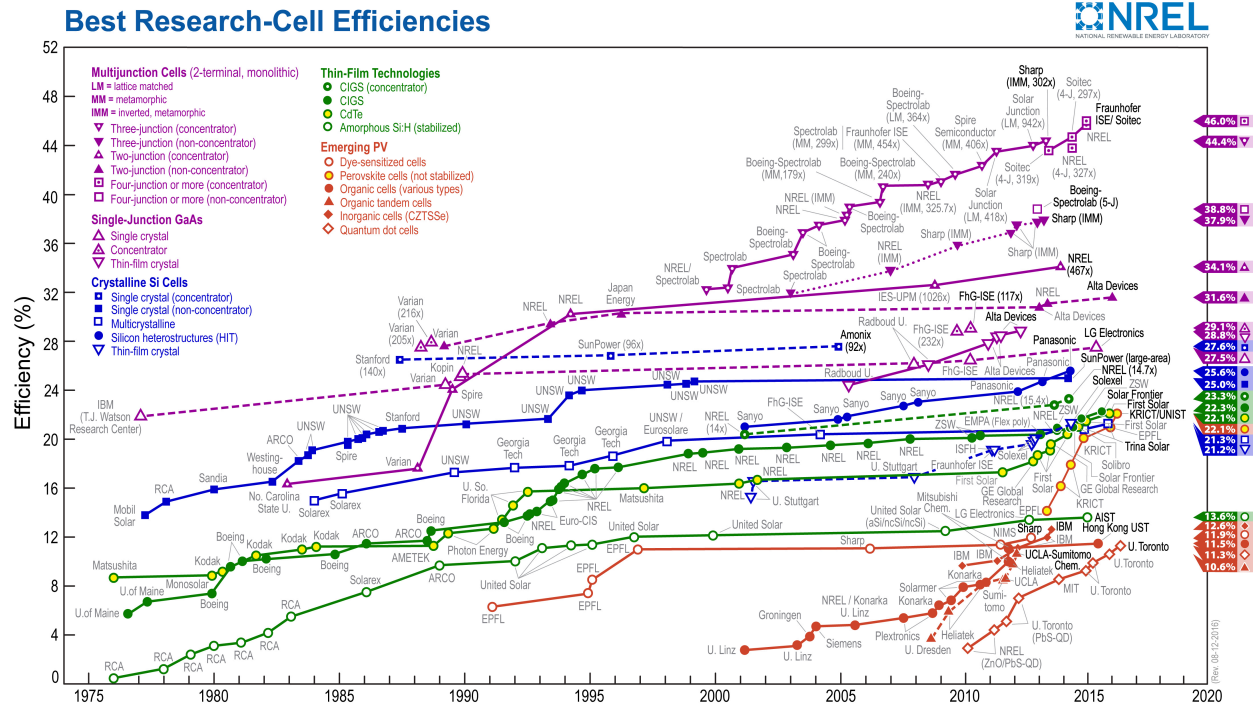
Figure 1.3 PV Efficiency chart. Retrieved from Ref. 12.

1.2 Introduction to Organic Photovoltaics

The discovery of organic polymeric semiconductors was the catalyst that allowed the OPV field to thrive. The electronic structure of conjugated polymers originates from the sp^2p_z-hybridized wavefunctions of the carbon atoms in the repeat unit;[17] the σ-bonds hold the structure together, but the π-bonds, in which the orbitals of successive atoms overlap, leads to electron delocalization along the backbone of the polymer, which gives rise to the properties that characterize conjugated polymers as semiconductors.[18] Polyacetylene, polyphenylene (PP) and polyaniline, to name a few, were the first generation semiconducting polymers, which required doping in some cases to show

enhanced conductivity. The second generation polymers became those that were made solution-processable by the addition of alkyl tails, such as poly-3-hexylthiophene (P3HT), poly(2,5-dialkoxy)paraphenylene vinylene (PPV), or polyfluorene (see Figure 1.4).[17] The first and second generations of semiconducting polymers amplified what was known about organic materials before 1972 and it was not until their discovery that the OPV field was able to move forward.
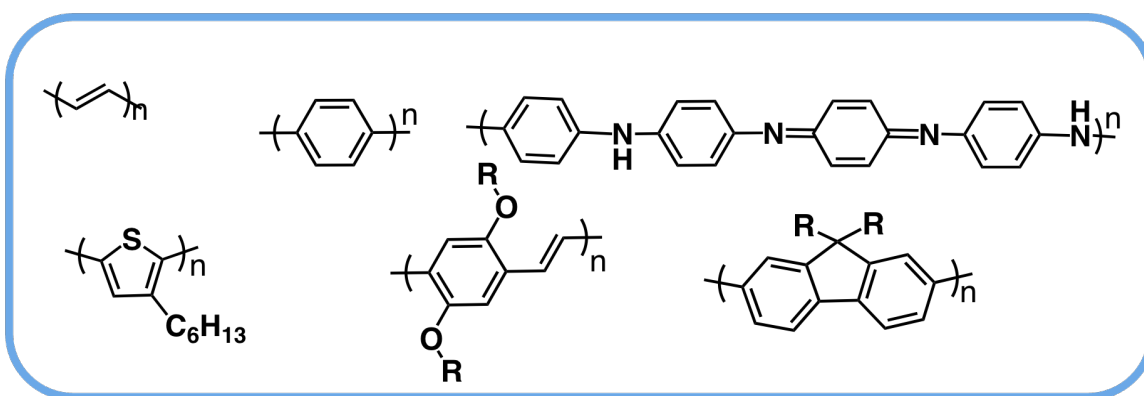
Figure 1.4. First and second generation semiconducting polymers. Retrieved from ref.17.

The very first OPVs were built using small molecule semiconductors (such as chlorophyll) which were sandwiched between two electrodes of differing work functions, and had power conversion efficiencies (PCE) of <<1%.[19] Then in 1986, a bilayer device, consisting of a copper pthalocyanine donor (D) and a perylene tetracarboxylic derivative acceptor (A), achieved a PCE of ~1%.[20] Almost a decade later, a PPV donor with [6]-phenyl butyric acid methyl ester (PCBM) acceptor, known previously for exhibiting ultrafast electron transfer from D to A,[21] were deposited as a single blend onto a film.[22] This was the first example of what became known as a bulk heterojunction (BHJ) blend, and it remains the standard in the field to date. For the next five years, PPV derivatives

remained the polymer of choice, but the relative large band gap (E_g), low mobilities and PCE spurred the search for new materials.[23] Finally, in 2003, a mixture of P3HT:PCBM in a BHJ OPV was heated (annealed) above the glass transition temperature (T_g) of the donor, then cooled, and in doing so, reported PCEs were higher than 3%.[24] The P3HT:PCBM system went on to become the most studied system in the field.

Before discussing the mechanism of operation of polymer OPVs, it is important to highlight the changes in device architectures since the early small molecule sandwiches, or bilayer devices discussed earlier (Figure 1.5a and b, respectively). The normal architecture consists of a glass or plastic substrate, coated with a transparent conducting anode, indium-doped tin oxide (ITO) in most cases, which is itself coated with a hole-transport buffer layer that prevents electrons from reaching the anode. Next, the BHJ blend that constitutes the active layer (the one responsible for generating current) is coated onto the buffer layer, and sandwiched between another buffer layer, for electron-transport (LiF or Ca); lastly, the optically reflective cathode (Al) is evaporated (Figure 1.5c).[25] The other type or configuration often used is the so-called inverted, in which the bottom transparent electrode becomes the cathode, and different buffer layers are employed (Figure 1.5d). Lastly, the tandem configuration is employed, similar to multijunction inorganic PV systems, where two or more active layers are used, sometimes complementary (i.e. large and small Eg)[26] and sometimes twin layers.[27]
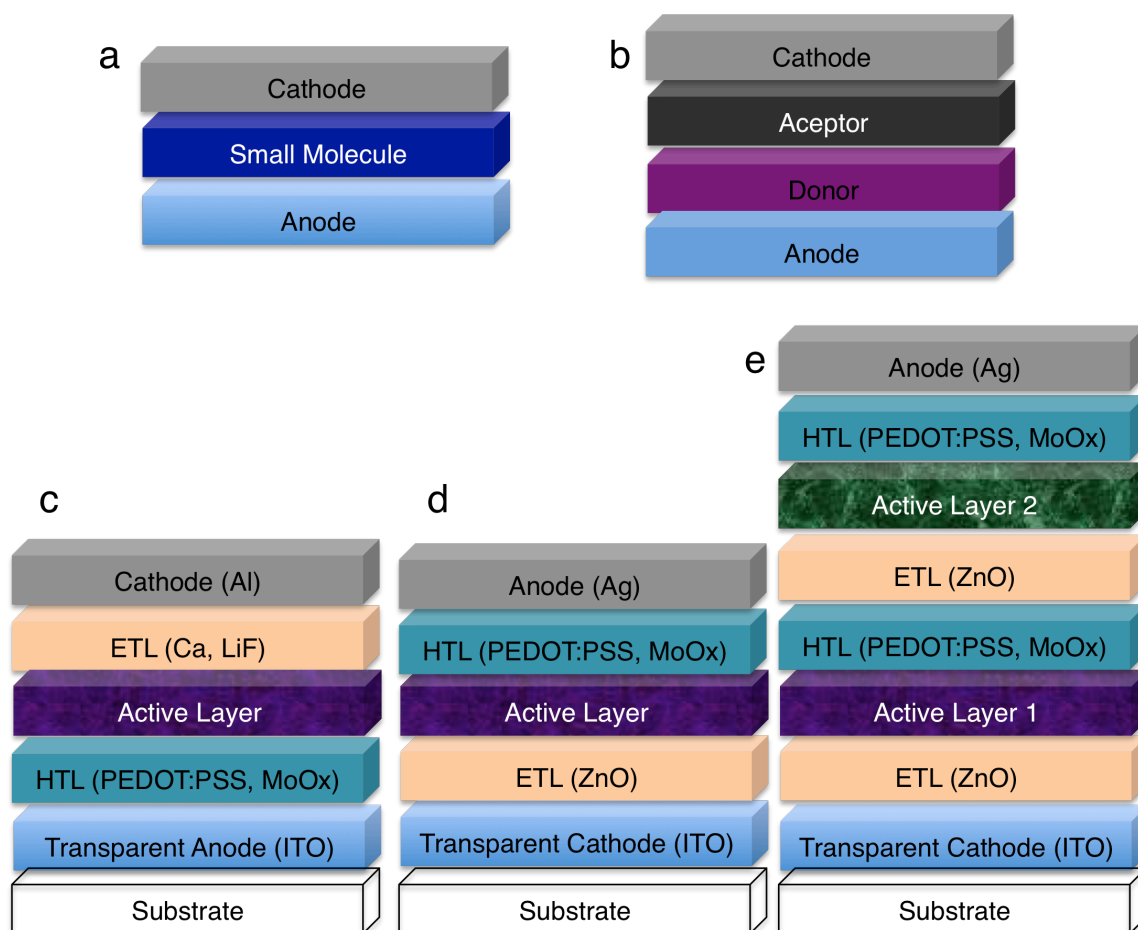
Figure 1.5. Device geometries. a) Initial OPV architecture of small molecules; b) bilayer geometry; c) classical architecture; d) Inverted architecture; e) tandem architeture.

The fact that an acceptor molecule had to be used in order to increase PCE is one the main differences between inorganic and organic semiconductors. There are four key steps necessary for the generation of current in an OPV (see Figure 1.6): **1)** exciton formation, which happens when light excites an electron from the highest occupied molecular orbital (HOMO) of the donor to the lowest unoccupied molecular orbital (LUMO); **2)** this electron-hole pair (exciton) is strongly bound by coulombic interactions, whose binding energy is sensitive to the dielectric constant of the material (in this case low, ~3-4), so if it does not form at the interface (an ultrafast process in the

order of 100 fs), it has to diffuse to it, via a chemical potential gradient (slower process, in the order of 100 ps), otherwise it will recombine; **3)** charge-transfer (CT) complex, or polaron pair formation occurs when the excited donor transfers an electron to the LUMO of the acceptor, which will be favorable to occur when the energy difference between the donor and acceptor LUMOs is greater than the binding energy of the exciton (typically on the order of a couple hundred meV); **4)** the CT state is still coulombically bound, but it can be dissociated by the electric field of the device, and only then can the hole and electron travel by a thermally activated hopping process through the D and A domains, respectively, to be collected at the electrodes.[14,28] In inorganic systems, light absorption generates loosely bound Wannier excitons, whose binding energy can be overcome at room temperature and produce free carriers (holes and electrons) without the need for acceptors;[25] thus, the major difference between inorganic and organic semiconductors is the low dielectric constant of the latter that requires the use of an acceptor.
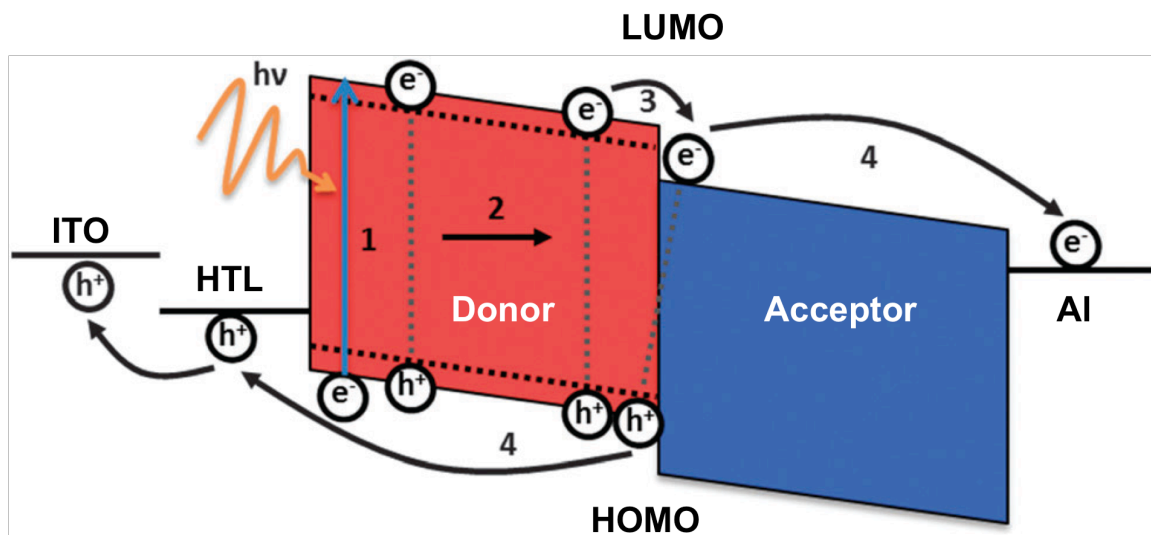
Figure 1.6. Energy diagram showing the steps to photocurrent generation. Retrieved from ref. 14.

In addition to needing an acceptor, charge recombination processes compete with charge collection. Recombination rates increase as the open circuit voltage (V_{OC}) is reached because the internal electric field decreases, thus less excitons dissociate, and in turn charge collection decreases. There are four main recombination mechanisms in OPVs, and are characterized by their recombination order; first order mechanisms are proportional to the free carrier concentration, and result in a cell's fill factor (FF) being almost unchanged with illumination, while second order recombination is proportional to the square of the free carrier concentration, and results in a FF that decreases as the illumination intensity increases. Geminate recombination (1st order) occurs when the CT state recombines before the electron and hole dissociate; mobile free carrier (Langevin) recombination (2nd order) is the recombination of mobile electrons and holes that can be identified and quantified from the light-intensity dependence; localized state recombination happens between a mobile and a trapped carrier; lastly, reverse diffusion to the contact occurs (rarely) when the "wrong" carrier diffuses against the internal field to reach the contact and recombine. [16]

Experimentally, there are a few metrics of importance in PV systems. A typical OPV equivalent circuit and current-voltage (J-V) response are shown in Figure 1.7. Under no illumination, very little current flows, also called dark current (**J_{Dark}**). Under illumination, the J–V curve shifts down in an amount equal to the photocurrent, J, and the device generates power (Figure 1.7b). The maximum power (P_M) is the location where the product of the current and voltage is maximized. Under no bias, the current flow is at a maximum, and it is called short-circuit current (J_{SC}), which depends on factors related to the efficiency of photogeneration. When no current flows, the voltage

measured is at its maximum, and is called open circuit voltage (V_{OC}). In inorganic PV, V_{OC} is determined by the difference in the quasi Fermi levels of the p-n junction, while in OPVs it has been found to be dependent on the difference between the HOMO of the donor and the LUMO of the acceptor. The primary figure of merit in OPVs is the PCE, or ne, which is the ratio of the maximum power output (P_{max}) to the power input (P_{in}), and is defined by equation (1);[14]

$$(1) \quad \eta_e = \frac{P_m}{P_{in}} \times 100\% = \frac{V_{OC} \times I_{SC} \times FF}{P_{in}} \times 100\%$$

the FF is defined by the equation FF = ($J_M V_M / J_{SC} V_{OC}$), where J_M and V_M are the current and voltage at P_M, respectively; it indicates how easily charges can be removed from a cell (ideally, it would be one), and is affected primarily by two factors: the series (R_s) and shunt (R_{SH}) resistances. The circuit in Figure 1.7a can be described by using Kirchoff's law, equation (2).[14]

$$(2) \quad J = J_{SC} - J_{dark} - J_{SH} = J_{SC} - J_0 \left(e^{\frac{q(V+JR_S)}{k_B T}} - 1 \right) - \frac{V + JR_S}{R_{SH}}$$

where J_{Dark} is dark current density, J_0 is the reverse saturation current (a constant), q is the electron charge, V is the applied bias voltage, k_B is Boltzmann's constant, and T is the absolute temperature. In practice, R_S accounts for bulk and interface resistances between layers and it is determined from the slope of the J–V curve around V_{OC} (ideally it should be zero); R_{SH} is a result of current leakage in the cell, generally as a result of trap states, pinholes, and edge effects (ideally, it should be infinite).[14] Lastly, the internal and external quantum efficiencies, IQE and EQE, respectively are a measure of how efficiently photons are converted to electrons at a particular wavelength; the IQE reflects

percentage of absorbed photons that are converted to electrons,[29] while EQE represents the ratio of incident photons converted to electrons;[14] overall, they describe the efficiency of photogeneration and in practice should be as close to 100% as possible.
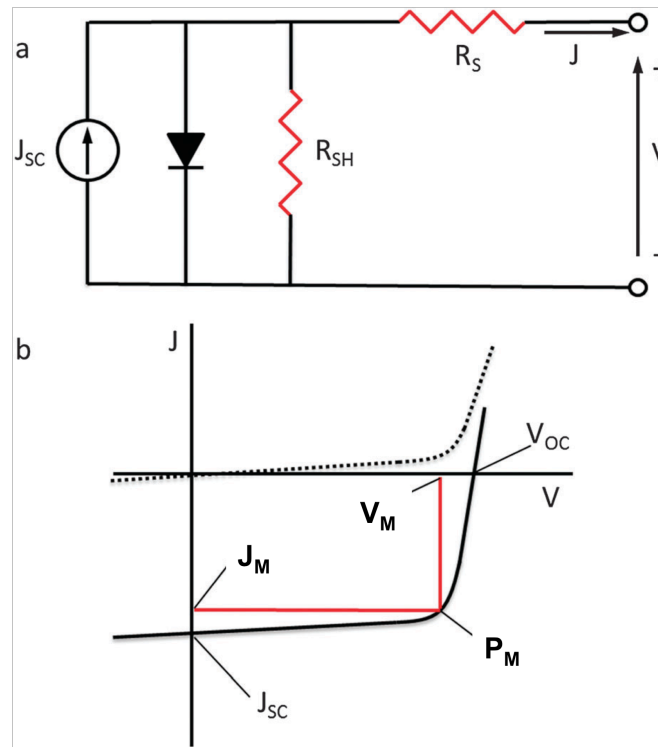
Figure 1.7 a) Equivalent circuit model for OPV and (b) J–V curves of an organic solar cell: dark (dashed line) and illuminated (solid). The characteristic intersections showing V_{OC}, J_{SC} and point for P_M. Retrieved from ref 14.

Device performance testing has been standardized by utilizing the AM 1.5 G Solar spectrum, which means setting illumination conditions to 100mW/cm^2.[16] The current record efficiencies in the field range in the 8-10% PCE range for the most optimized devices.[26,27,30–33] The maximum thermodynamic efficiency of a PV system was calculated by Shockley and Queisser to be ~30%,[34] but the parameters calculated were for a p-n junction made of inorganic materials. For an ideal OPV, the free energy

for charge transfer at the D-A interface causes an increase in the recombination rate, decreasing the maximum attainable efficiency to 22%.[35] It is quite obvious that there is still plenty of room for improvement; nevertheless, there are many factors that affect device performance, which range from material chosen, to processing conditions. The following section describes different strategies at optimizing the different layers in OPV devices.

1.3 Strategies to Increase Device Performance

As previously mentioned, there are many factors that contribute to the performance of a device. The choice of materials is an obvious one, but there are many processing conditions that affect significantly the morphology of the active layer. This section will highlight the materials used in high performance OPV systems, as well as some of the techniques that have expanded our understanding of OPV technology.

1.3.1 Interfacial Layers

In thin film devices such as OPVs, direct contact between the semiconductors and metallic electrodes is normally not the ideal since metallic surfaces have a high density of defects, causing surface recombination.[16] The maximum achievable V_{oc} is dependent on the difference between the quasi-Fermi levels of the photoinduced holes and electrons in the D-A couple. This result can only be obtained if Ohmic contacts are formed with both cathode and anode; this happens when the difference in Fermi levels between the metal and semiconductor is small, and charge transfer to/from the metal will not occur. When a Schottky contact is formed on either or both sides, there is a large difference in Fermi levels between a metal and semiconductor, creating a

depletion zone that has considerably fewer mobile charge carriers.[36] The multiple roles served by the interfacial layers include (1) promoting Ohmic contact at the active layer and electrode interface, (2) determining the polarity of the device (conventional device or inverted device), (3) improving selectivity toward holes or electrons, thus minimizing charge recombination in the interface, (4) enhancing light harvesting by introducing optical spacers, and (5) improving device stability. [37]

Hole Transport Layers (HTL)

In a conventional device structure, the most commonly used transparent electrode is ITO. However, its high work function (−4.7 eV) prevents formation of an Ohmic contact with most donors due to their deeper HOMO levels.[37] A conducting polymer, PEDOT:PSS, is the most commonly used HTL for anode modification in OPVs; it is obtained in the p-doped state by oxidative polymerization of ethylenedioxythiophene (EDOT) in an aqueous emulsion in the presence of polystyrene sulfonic acid (PSS). One of the advantages of PEDOT:PSS is that its conductivity can be modified either by changing the PEDOT/PSS ratio or by employing additives to modify the films; also, its work function (-5.1 eV) matches well with the HOMO of a wide range of polymer donors, allowing good Ohmic contact at the anode/BHJ layer interface. Nevertheless, the insulating PSS layer can limit the charge collection, making it electrically and structurally inhomogeneous.[38] In addition, the acidic and hygroscopic nature of PSS can induce chemical instability between the active layer and electrodes.[39] Other conducting polymers that have been used are PSS-doped graft polyaniline copolymer (PSSA-g-PANI)[40] due to its transparency over the absorption range of some semiconductors (P3HT for example), its high conductivity and good environmental

stability;[37] in addition, conjugated electrolytes have been reported with high efficiency polymer donors.[41]

Metal oxides are another popular alternative, as they show high work functions which can facilitate Ohmic contact with active layers, and their higher conduction band ensures efficient electron blocking, as well as providing good optical transparency in the visible and near-IR regions to allow photons to reach the active layer.[37] Among the different metal oxides used, nickel oxide (NiO),[42] vanadium oxide (V_2O_5),[43] copper oxide (CuO),[44] tungsten oxide (WO_3),[45] chromium oxide (CrO),[46] nickel acetate (NiAc),[47] have been tested with some promise, but it is molybdenum oxide (MoO_3)[48] that stands out among the different metal oxides since its conduction band is significantly deeper than the HOMOs of common organic semiconductors and p-doping through interfacial electron transfer from the organic semiconductor to MoO_3 is thermodynamically favorable.[16] A large portion of high performance OPV designs use this latest material as HTL.

Electron Transport Layers (ETL)

In conventional OPV devices, the cathode is for the most part thermally evaporated Al (in inverted devices is Ag), with Ca or LiF as ETLs for efficient hole blocking and electron collection.[37] In contrast to HTLs, which have high work functions and relatively good stability against ambient exposure, the ETL are in contact with low work function metals (such as Al), which are sensitive to oxygen and moisture, and that can lead to an unstable cathode contact. In the previous case p-type metal oxides were used as HTL, and in this case, n-type metal-oxides such as TiOx[49] are popular due to their superior stability in terms of both film morphology and electronic properties, but

ZnO is the most widely used due to its environmental friendliness, ambient stability, low cost, high transparency, high conductivity, and good hole-blocking properties.[37]

Other solution-processed ETLs have been developed to circumvent evaporating LiF or Ca, such as an inorganic cesium compound,[50] tungsten polyoxometalate,[51] titanium chelate.[52] In addition, water- and alcohol-soluble, inexpensive nonconjugated polyelectrolytes (NPEs), such as poly(ethylenimine)-ethoxylated (PEIE),[53] poly(vinylpyrrolidone),[54] among others, are employed to reduce the work function of the electrode by the formation of a dipole layer at the interfaces. Figure 1.8 shows some of the many materials, from electrodes, to donor and acceptor materials used in OPVs, which accentuates the progress and the efforts aimed at bringing this technology to its full potential.
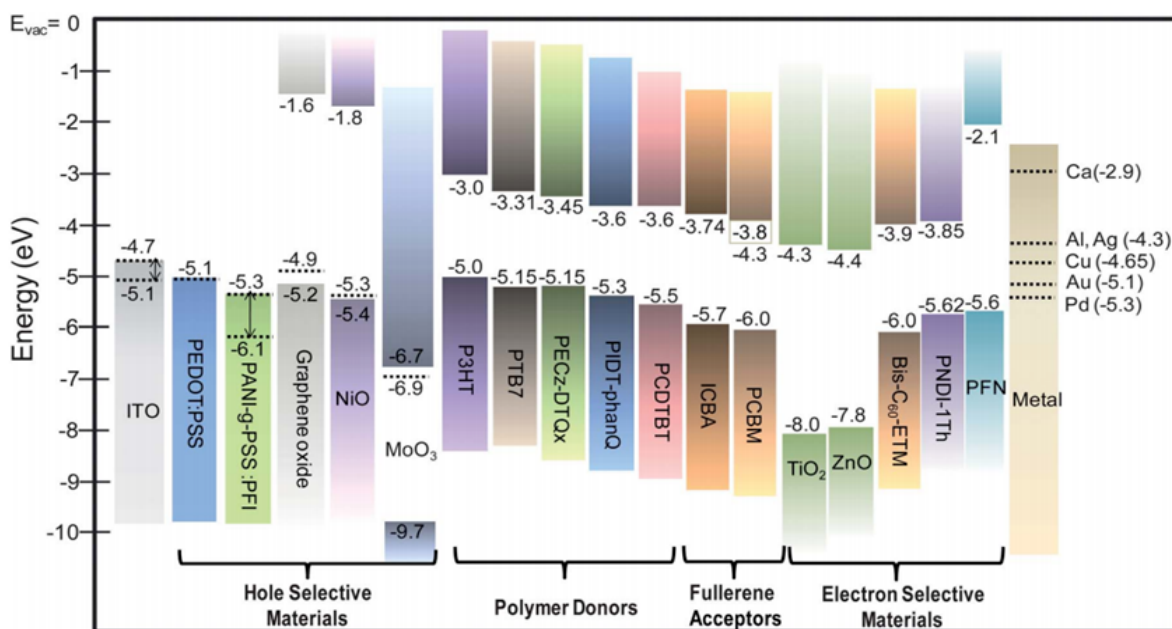
Figure 1.8. Schematic view of the energy levels of some common components of OPVs including electrodes, HTLs, polymer donors, fullerene acceptors and ETLs. Retrieved from ref. 36.

1.3.2 The Active Layer

Clearly the materials chosen to absorb light will probably have the biggest impact on the performance of the device. Section 1.2 discussed the historical highlights of D-A materials and the mechanism of OPV operation. This section will focus on the synthetic and electronic aspects of designing donors, their types, performance and current strategies to improve it. Then the discussion will focus on one of the most important aspects of BHJ devices, the morphology, techniques to study it and approaches to improve it.

1.3.2.1 OPV Donors

As Section 1.2 stated, in inorganic PVs, the exciton generation and charge collection happen very efficiently, but in organic systems, the low dielectric constant of the electron-donating material requires the use of an electron acceptor, which places some constrains and requires some considerations when designing donors. The optical properties of the donor will be dictated by the position of the HOMO and LUMO levels; while it is desirable to absorb the visible and near-IR regions, where the solar spectrum is at its maximum, a very low HOMO-LUMO gap (or band gap, E_g), may have a LUMO lower than that of the acceptor, and it has been shown that the appropriate LUMO of the donor should be ~0.3 V above that of the acceptor for efficient CT.[55] If that LUMO level were held constant, there is another issue, that of the V_{oc}. Maximizing the V_{oc} would imply a lower HOMO in the donor, which in turn implies larger E_g, so there is a inverse relationship between the maximum attainable V_{oc} and E_g, increasing either one will lower the other.[56]

Since the frontier orbitals (HOMO and LUMO) are vital for dictating optical properties of donors, it is important to emphasize the strategies used to modify their position. Organic donors are conjugated molecules, and in the simplest type of conjugated polymer (or oligomer), polyphenylene (PP), there are two possible resonance structures that arise from electron delocalization (see Figure 1.9a), the aromatic form (blue on the left), where each benzene unit maintains its aromaticity, and the quinoid form (red on the right), which is energetically less stable (due to diminished aromaticity) and hence has a smaller band gap. The ratio of the aromatic to quinoid character is represented by bond length alternation (BLA), the average of the difference in length between adjacent carbon-carbon bonds in a polyene chain.[56] The more aromatic form a given molecule adopts, the larger the BLA value obtained.[57] Qualitatively speaking, E_g decreases linearly as a function of the increasing quinoid character (and decreasing BLA value). The utility of the BLA concept can be exemplified by some of the cases in Figure 1.9. Benzene rings have a high degree of aromaticity, so by inserting a double bond to make PPV, the aromaticity is reduced, as is the band gap (Figure 1.9b). Similarly, thiophene, has lower aromaticity than benzene, thus polythiophene (PT) is more likely to adopt a quinoid form, and consequently, it has a lower E_g than PP (Figure 1.9c). A more creative way to increase the quinoid character of PT is by fusing it with a ring of higher aromaticity, as was done is polyisothianaphthene (PITN). The main chain of PITN tends to favor the quinoid form to maintain the benzene aromaticity.[58]
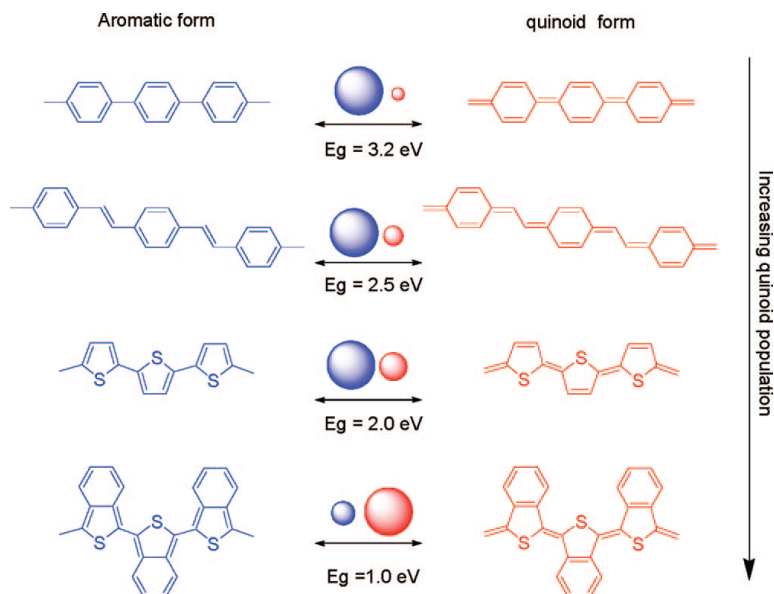
Figure 1.9 Aromatic and quinoid forms of commonly used conjugated rings. Retrieved from ref. 58.

Small Molecule Donors

In general, E_g can be lowered by just increasing the conjugation, but unlimited extension of a chain will eventually reach a point in which the effective conjugation is saturated, and further monomers will not affect the frontier orbitals significantly. A more effective strategy in tuning E_g consists of alternating a conjugated electron- rich donor (D) unit and a conjugated electron-deficient acceptor (A) unit in the same polymer backbone, creating a photoinduced intramolecular charge transfer (ICT) from the high-lying HOMO of the donor and the low-lying LUMO of the acceptor, and lowering E_g in the process.[59] Another way of viewing the so-called push-pull strategy is by considering the hybridization of the molecular orbital (MO) between the electron rich and poor units; when the two units interact, the frontier orbitals in both units will combine, creating a new pair of orbitals, intermediate between the parent units (see Figure 1.10).[60]
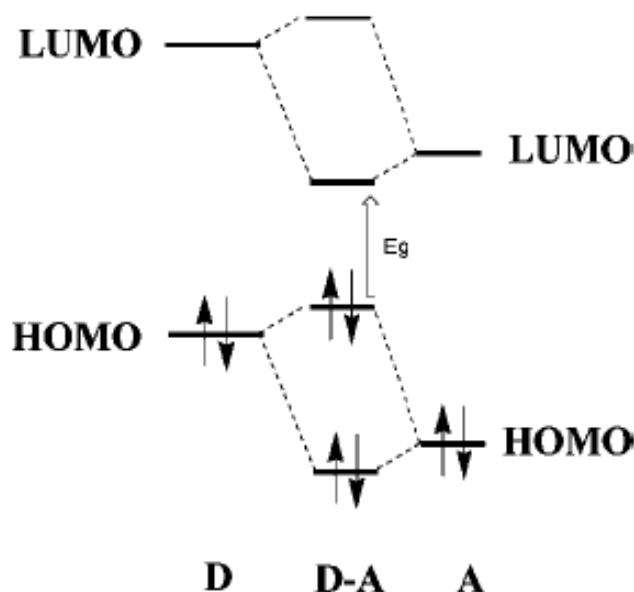
Figure 1.10 MO combination of a D-A pair to make a new molecule with intermediate energy level. Retrieved from ref. 60.

There are two types of donors used for OPV purposes: small molecules (or oligomers) and polymers. The early small molecules used for OPVs were not particularly solution processable, and were chosen for their good absorption, i.e. porphyrins or pthalocyanines.[19] After polymers such as PPV and especially P3HT were introduced, small molecules received little attention, but polymers pose several problems related to the control of their structure, molecular weight, polydispersity, and purification; in this context, small molecules present specific advantages in terms of structural definition, synthesis, and purification.[61]

A resurgence of research in small molecules happened in the early 2000s, when solution-processable designs were published. Some of the designs were aimed at creating a three-dimensional donor, unlike the 1-D polymers, in an effort to increase the interaction with the fullerene acceptors; consequently, multidimensional designs such as

a tetrasubsituted silicon (or carbon) atom with alkylated terthiophenes,[62,63] oligothiophene dendrimers,[64,65] columnar stacking molecules,[66,67] or soluble dyes[68] were reported. The major breakthroughs occurred when the push-pull principle was implemented. One case introduced the previously reported (in polymers) diketopyrrolopyrrole (DPP), flanked by two electron rich moieties (a D-A-D design),[69] that achived >4% PCE; the other case was a triphenylamine-based molecule (an A-D-A design), which was modified with dicyanovinyl electron-withdrawing groups, creating a strong intramolecular CT band that raised the PCE to almost 3%.[70] Afterwards, many small molecule designs were based on polymeric units (discussed in the next section), using the push-pull principle. To-date the highest designs are A-D-A type and consist of a benzodithiophene weak-donor core with electron-withdrawing moieties on the extremes; there was also a report of a diethienosilole core with benzothiadiazole flanking groups (Figure 1.11).[71,32,72,73,33]

Figure 1.11. High PCE small molecules. Retrieved from ref. 32-33, 71-73.

Polymer Donors

The field of OPV donors became mature with polymeric designs. Much of the strategies that allowed small molecules to thrive, and for all practical purposes, compete with polymeric designs, came from the latter. The very first polymers used for OPV were discussed in Section 1.2. This section will focus on the advancements after P3HT. The

third major family of polymers for OPVs was polyfluorene-benzothiadiazole derivatives, which had wide band gaps and low-lying HOMO levels and resulted in relatively small J_{SC} but high V_{OC} and PCEs up to 4.2% after optimization of devices.[74] Once polymers adopted the push-pull design, the field exploded, and although tens, if not hundreds of thousands of different designs have been reported, they are merely permutations of a number of electron-rich and poor units.

The most used units are included in Figure 1.12. In terms of electron-rich moieties, in addition to fluorene, other popular units are carbazole,[49] thiophene,[75] benzodithiophene (BDT) with alkoxy tails,[76] and many other types of modifications thereof.[77] One of the main reasons electron rich units are scarce is the fact that, qualitatively at least, the HOMO of a push-pull polymer tends to have a similar level as the parent electron-rich moiety; the electron-poor units tend to affect the LUMO of the copolymer more significantly,[60] so synthetic designs focus more on the latter than the former. Also, for stability purposes, polymers are prone to oxygen degradation if the HOMO is lower (more positive) than ~-5.5 eV,[78] so it is important not to modify the electron-rich moiety to a point where the resulting copolymer will decompose in air. The electron poor units more commonly used are thienothiophene (TT),[79] thienopyrrole (TP),[80] isoindigo (IIn),[81] DPP,[82,83] and benzothiadiazole (BTD),[49] among other less cited units. The most successful combinations of polymers using these units have been BDT based-TT (for example the well known PTB7), and some DPP and isoindigo-based designs (see Figure 12 bottom row).[79,81–88]
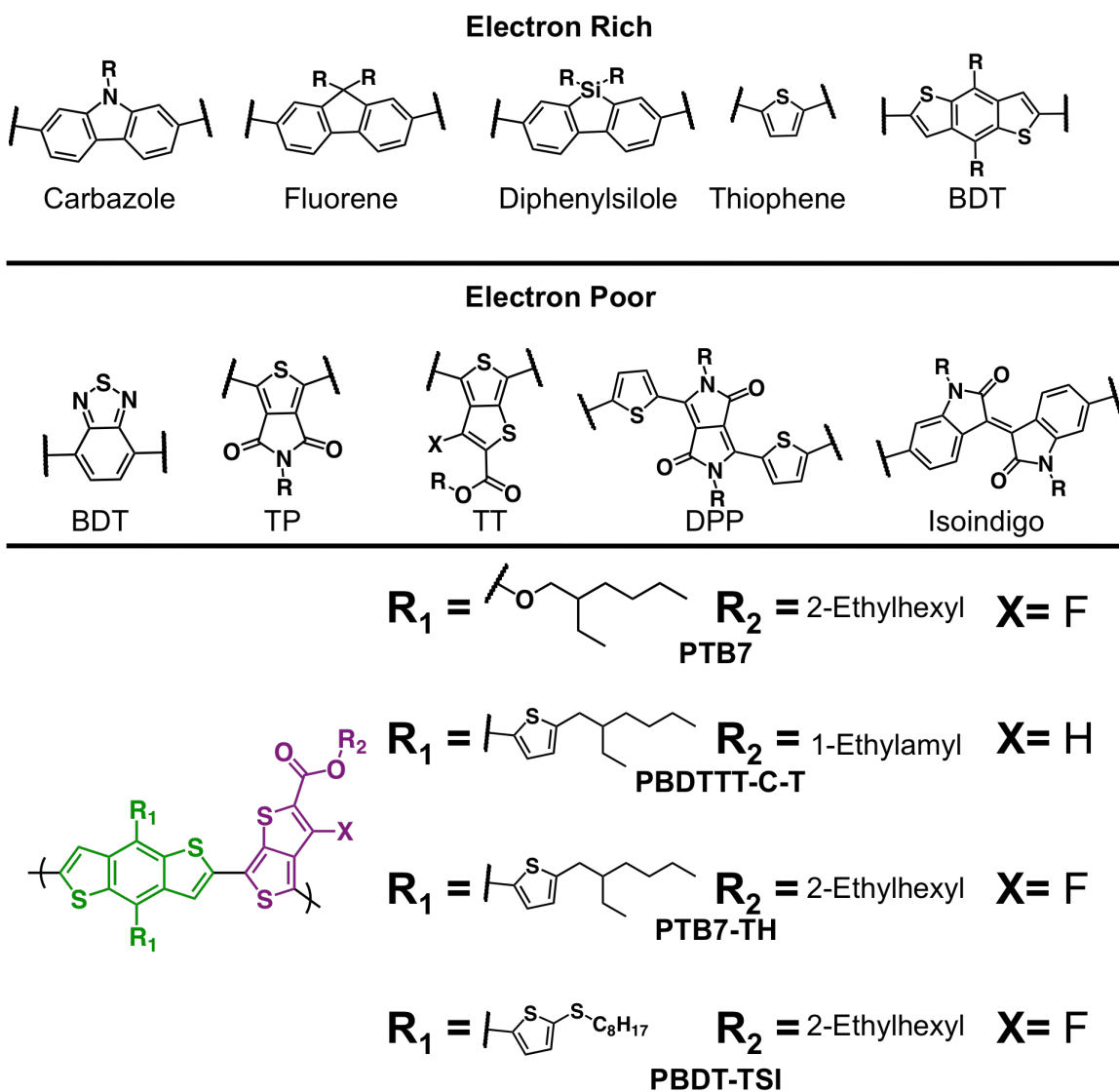
Figure 1.12. Electron rich and poor units in polymer donor design (top two rows). Highest PCE polymer reports. Retrieved from ref. 49, 79-88.

The examples cited in this thesis, are just a few out of the thousands of different designs reported. Given the large body of literature reports, attempts have been made at trying to predict the properties of polymers (not small molecules yet) before synthesis even begins, which in the long term could save not only time, but also money. One such case analyzed 26 different polymers and found a linear relation between V_{OC} and the

oxidation potential is found; based on that relation, the PCE was derived as a function of the bandgap and the energy levels of the conjugated polymer. Based on this study, a polymer with PCE of >10% would have an E_g of 2.7 eV, and after taking the assumptions in consideration, would have a LUMO at -4.0 eV and the HOMO at -5.7 eV.[89] This claim, however, was recently challenged by a report where the authors found the yield of free versus bound charges to be much more dependent on fullerene aggregate size than on energetic driving force, which suggest that energetic off sets between donor and acceptor levels are not an important criterion for efficient charge generation.[90]

Another study analyzed the PCE vs. cost of close to one hundred different permutations of the units in Figure 1.12, plus other ones and concluded that although fluorination consistently gives higher PCEs, it increases the cost dramatically; as a replacement, it suggested the use of alkoxyalkylated BDT-TP copolymer, since it gives an average PCE of ~7% and is significantly cheaper than any other copolymer.[91] The anaylisis was done taking into account PCBM, not the slightly bigger $PC_{71}BM$, which tends to give even higher PCEs.

1.3.2.2 Acceptors in OPVs

In OPVs, from the first bilayer device in 1986, to the first BHJ in 1995, end ever since, fullerenes have shown tremendous promise and excelled as electron acceptors. Some of the characteristics that make them popular are good electron mobility,[92] favorable nanoscale morphology, where D-A domains the size of the exciton diffusion length can be obtained,[93] the ability to support electron transport in three dimensions

(more than 2 or 1 as most molecules or polymers), and the existence of low lying (0.2–0.4 eV) excited states in their anions.[94]

Due to historical reasons, PCBM (also written $PC_{61}BM$)[21] and its more soluble $PC_{71}BM$[95] are by far the most popular fullerenes used (see Figure 1.13). Nevertheless, work on fullerene derivatives is aimed at raising the LUMO to enhance the V_{OC} of the devices. One approach is to make a bisadduct on it; one such example is indene-C60 bisadduct ($IC_{60}BA$), which was blended with P3HT and achieved a PCE of 6.5%, with a J_{SC} of 10.6 mA/cm2, high V_{OC} of 0.84 V, and a FF of 0.72, which is the highest value for a P3HT based solar cell device.[96] Another interesting fullerene acceptor is SIMEF, with a reported LUMO ~0.1 eV higher than $PC_{61}BM$; in devices made with a tetrabenzoporphyrin, it displayed a V_{OC} of 0.75 V, JSC of 10.5 mA/cm^2 and PCE of 5.2% ($PC_{61}BM$ achieved only 2.0% PCE).[97] Although the utility of fullerenes is undeniable, the need to reduce the cost and increase absorption in the visible spectrum has fueled work towards non-fullerene acceptors, especially in the last few years. Although many designs still lack the performance to compete with fullerenes, there have been some promising candidates, such as BTD-based acceptors,[98] perylene diimides (PDI),[99]and two especially high performing materials, N2200 (PCE close to 6% when mixed with PTB7),[100] and ITIC (recently achieved >10% PCE).[30]
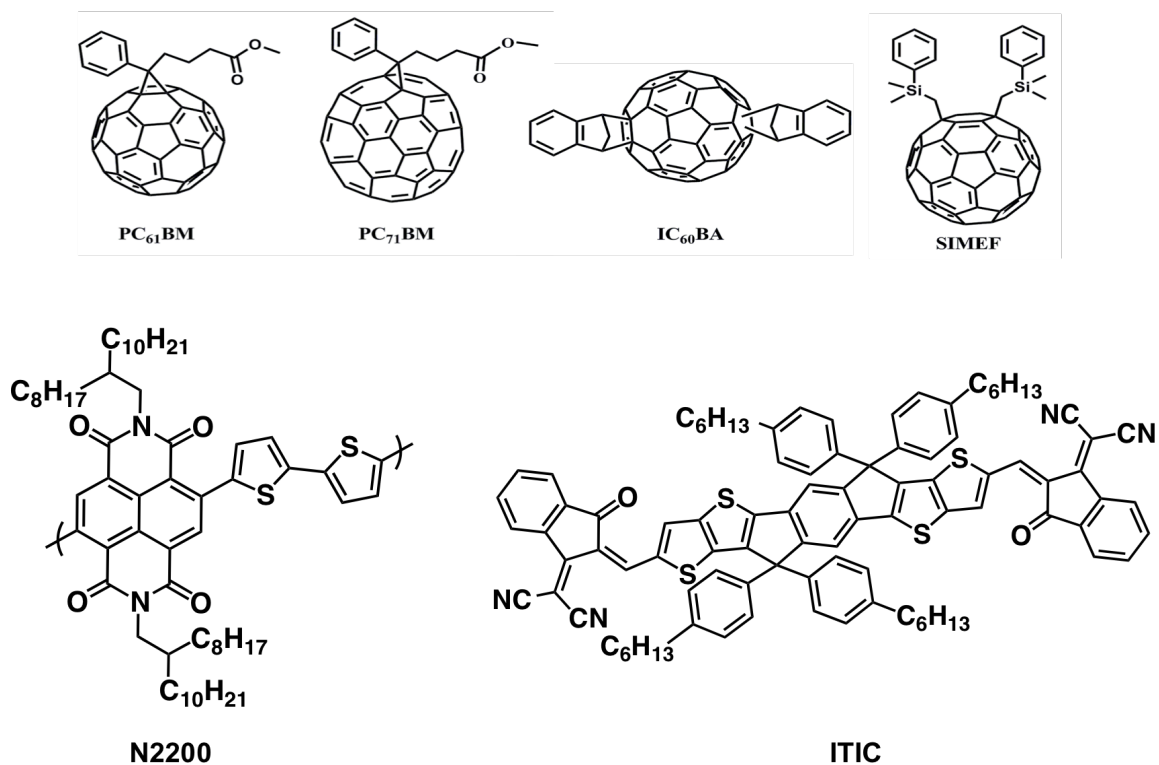
Figure 1.13. Fullerene acceptors (top row) and non-fullerene acceptors (bottom). Retrieved from ref. 21,95-97,100,30.

1.3.3 Active Layer Morphology

The discussion so far has focused on donors, and their optoelectronic properties, such as HOMO-LUMO levels and enhanced absorption, but the ultimate morphology of the film is just an essential contributor to PCE, as the materials in the active layer. As was discussed in Section 1.2, upon light absorption, there is an ultrafast charge transfer from D to A, which occurs within100 fs, and only a fraction of carriers are generated due to exciton diffusion. Nevertheless, the free electrons and holes must be transported through the D-A domains to their respective electrodes, keeping in mind that very small domains will increase opportunities for bimolecular recombination, so the morphology has to be a bicontinuous interpenetrating network morphology with domain size

between 10-20 nm (exciton diffusion length) to optimize exciton migration to the interface and large enough in order to efficiently generate current.[37,101]

1.3.3.1 Microscopy Techniques

Transmission Electron Microscopy

Before discussing the factors that affect, or strategies that optimize the morphology of the active layer, the techniques used to study it will be overviewed. Microscopy studies are useful to observe a film in real space, and in the bulk of the sample; transmission electron microscopy (TEM) is usually operated in the bright-field imaging mode. Here, the contrast is influenced greatly by the mass of the scattering atoms; thicker domains of the film, or regions containing heavier atoms, appear darker, while samples with thinner regions appear brighter.[101] A typical TEM micrograph is shown in Figure 1.14, which depicts the morphology of a polymer donor (DPPF), before an after treatment with the additive diiodooctane (DIO), discussed in the following sections. The image on the left exhibit large-scale phase-separated structures, where large PCBM-rich domains (dark regions) are seen; then after DIO treatment, the morphology was much finer, showing dark and bright areas due to thickness or density variations.[102] Regarding the morphology in the vertical direction, which is relevant for charge transport, cross-sectional TEM images have been collected on thin slices using the focused ion beam (FIB) technique and reveal bicontinuous phase separation, but the precise size is unknown because the technique sacrifices spatial resolution.[103]
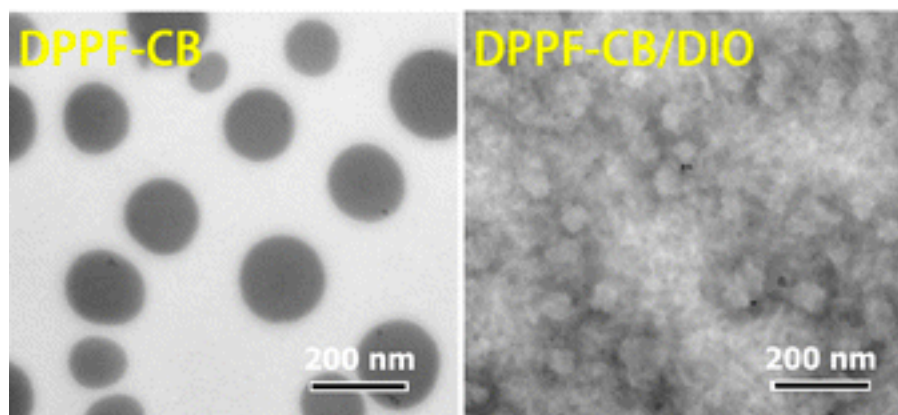
Figure 1.14. A typical TEM micrograph of an active layer showing the morphology of a polymer (DPPF) before and after DIO addition. Dark spots are fullerene domains. Retrieved from ref. 102.

Atomic Force Microscopy

Although a useful technique, TEM is not always accessible to researchers, not to mention that there is a risk of damaging the sample film due to over exposure of the high-energy beam. A much easier technique that offers the benefit of analyzing the morphology in bulk is atomic force microscopy (AFM); in a general sense, AFM images are collected by measuring the force on a sharp tip upon approaching the sample surface; the tapping mode of operation is widely used for organic electronic films to reveal the surface topography and nanoscale domain structures. A typical image is shown in Figure 1.15; it shows the surface morphology of P3HT with different molecular weights. Low-M_W films have a highly ordered nanorod structure and the high-M_W counterparts have a less ordered structure.[104]
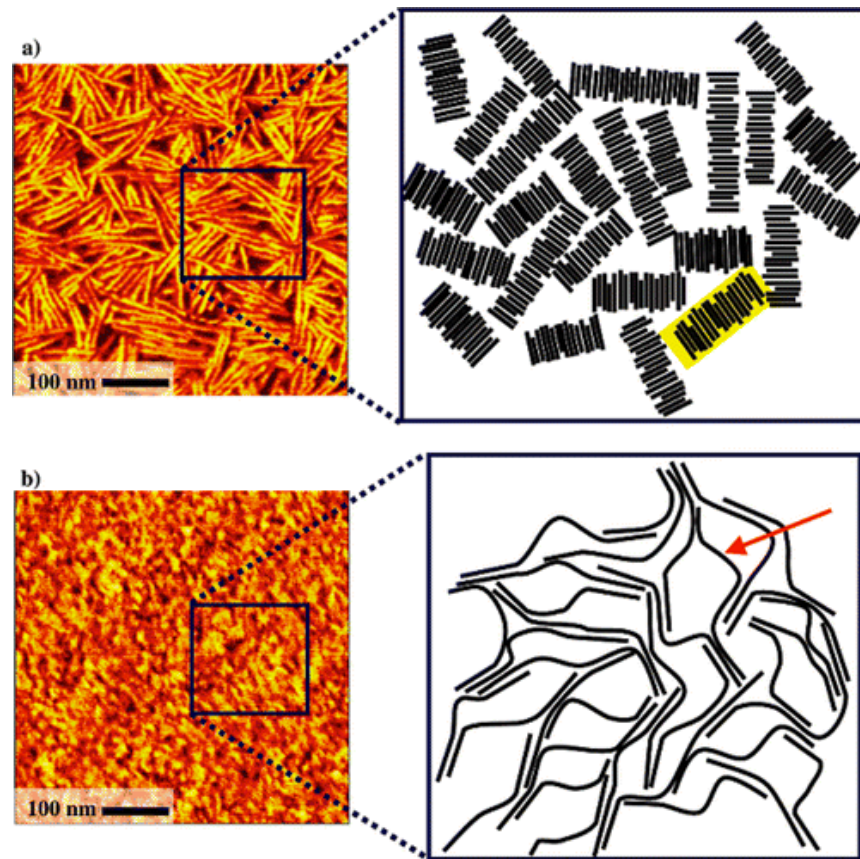
Figure 1.15. P3HT morphology imaged with AFM a)low Mw, b) High Mw. Retrieved from ref. 104.

1.3.3.2 X-Ray Techniques

Grazing incidence X-ray scattering (GIXS) techniques are used to elucidate film morphology and the nanostructure of thin films. Grazing incidence wide-angle X-ray scattering (GIWAXS) is relevant for structural characterization of BHJ films due to its large sampling volume and statistical information provided. It is used on organic films to determine both the crystalline lattice spacing from the diffraction peaks and the crystalline correlation length (CCL) from peak widths and to determine the orientation order parameters (Hermans orientation parameter) of the crystal planes. Statistics

extracted from GIWAXS provide a wider sampling volume than microscopy techniques.[101]

The experimental setup and a basic explanation of the data extracted from GIWAXS is shown in Figure 1.16. An X-ray beam is shined at the sample at a very small angle (<1), and a 2-D detector is placed a short distance from the sample (top image). The direction of the X-ray beam is chosen as the x coordinate (in-and-out of the detector), and the length and height of the detector are the y and z-coordinates, respectively. The complexity of the data depends on the degree of order of the film. The bottom of Figure 1.16 summarizes the possible scenarios: **a)** a highly crystalline film with a crystal parallel to the substrate surface gives well pronounced Bragg peaks in the z direction; **b)** smaller crystallites of parallel and perpendicular orientation give Bragg peaks along the y and z directions; **c)** having domains oriented with an angular distribution parallel to the substrate will give broadened Bragg peaks along the z-direction; **d)** powder-like films with large disorder of the crystallites will give cause Bragg peaks to smear out into Debye Scherrer-like rings.[105]
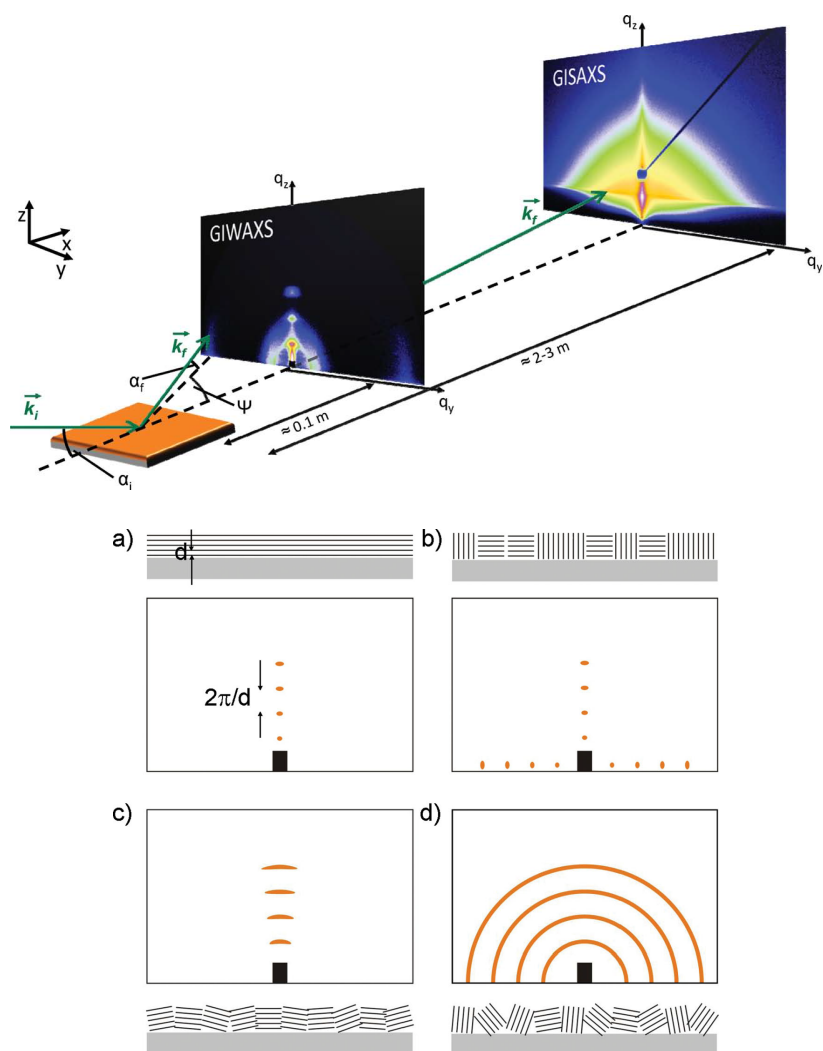
Figure 1.16. Top: Schematic of GIWAXS and GISAXS experimental setup. Bottom: a-d, crystal arrangement on a film and the corresponding scattering pattern. Retrieved from ref. 105.

A typical GIWAXS experiment would look similar to Figure 1.17. Two samples of P3HT were analyzed, one with high regioregularity (**rr**) and low molecular weight (M_w), and the other with low rr and high M_w. The (100) reflections come from the alkyl chain direction, and the (010) reflections are due to the interchain π–π stacking. For the first sample the (100) reflection is normal to the film while the (010) reflection is parallel to the film (this type of orientation is called edge-on); in the second sample, the (010)

reflection is in the out-of-plane direction and the (100) reflection is in the in-plane direction (face-on orientation).[106]
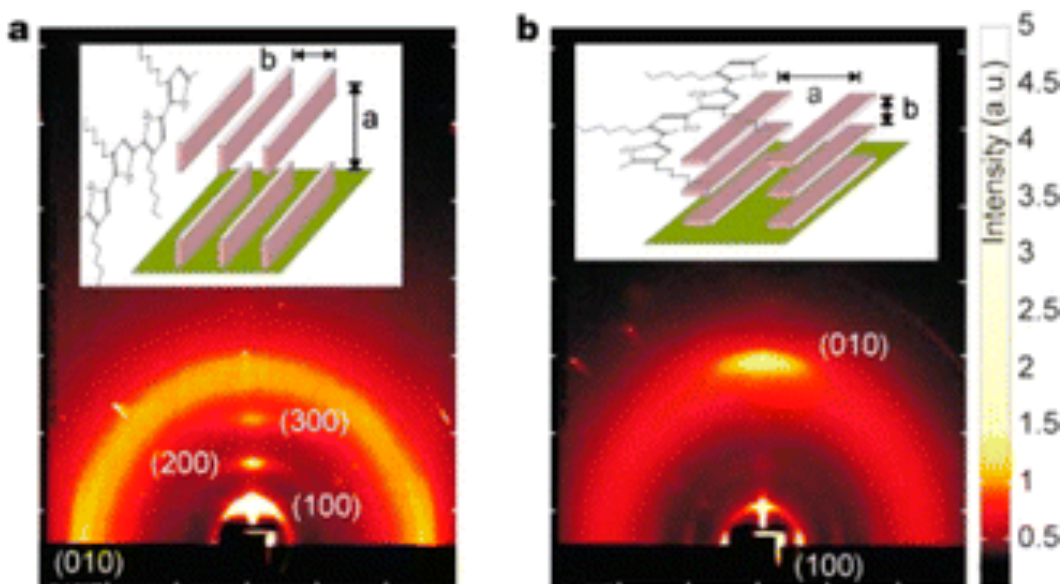
Figure 1.17. Two different orientations of ordered P3HT domains with respect to the field effect transistor (FET) substrate. The wide-angle X-ray scattering images are a color representation of the two-dimensional distribution of scattered X-ray intensity from P3HT films with regioregularity of 96% (a) and 81% (b) on SiO2/Si substrates. The vertical (horizontal) axes correspond to scattering normal (parallel) to the plane of the film. The insets show schematically the different orientations of the microcrystalline grains with respect to the substrate. Retrieved from ref. 106.

The top half of Figure 1.17 also shows the grazing incidence small-angle x-ray scattering (GISAXS) experimental setup, which is similar to GIWAXS, except that the detector is placed significantly farther than in GIWAXS. The small-angle regime is useful for detailing the size, shape, and interdomain correlation of the BHJ components. There are some challenges in the small-angle X-ray scattering experiments, such as interpretation of data from reciprocal space in BHJ systems, which are not amenable to simple modeling, thus making it difficult to assign a scattering pattern to a specific morphology (since two various morphologies may generate identical scattering

patterns). Consequently, GISAXS is often used in conjunction with electron microscopy as a supplemental tool to investigate large-scale domain sizes.[101]

1.3.4 Processing Methods

As synthesized donors have to be incorporated with an acceptor (PCBM for example, either 61 or 71) in the active layer. Though the BHJ has been universally adopted, not all designs have the same morphology, especially with regard to domain size and degree of D-A interpenetration. Processing conditons such as the solvent, co-solvents (additives), and annealing are a common strategy to modify domain sizes, and in the process increase the device performance.

Solvent selection

The solvents used for film deposition can greatly impact the final structural arrangement in the active layer. In an early example of a PPV derivative-$PC_{61}BM$ system, changing the solvent from toluene to chlorobenzene (CB) increased the PCE from 0.9% to 2.5%, and the enhanced performance was attributed to a better intermixed morphology upon using the latter solvent.[107] In a more systematic study, a carbazole-BTD copolymer was deposited from solution in chloroform ($CHCl_3$), CB and dichlorobenzene (DCB) and a high PCE of 6.1% was obtained in devices prepared from DCB, which results in significantly smaller nanoscale phase separation.[49] Usually the solvent selection is limited to the ones that dissolve fullerenes well enough, but there are cases in which either the donor or acceptor dissolve the best in different solvents; in such cases, it is possible to use mixtures of solvents. For example, a DPP-based polymer was deposited by using a combination of DCB and CHCl3 (the polymer having

better solubility in the later), and in doing so the performance increased from 1.1% in CHCl3 to 3.2%. The increased performance was attributed to the slower evaporation of DCB, which provided some opportunity for crystallization of the polymer.[95]

Solvent Additives

Solvent additives are becoming the primary method to control morphology during the spin casting of donor:PCBM solutions; they are usually employed in small percentages (1-10%) with the host solvent. The first reported case was the use of 1,8-octanedithiol (ODT) in a fluorine-BTD system, which increased the PCE from 2.8% to 5.5% through significantly improved morphology;[108] in a later study, it was found that ODT dissolves PCBM selectively, and allowed better polymer crystallinity by keeping PCBM molecules dissolved, given its slow evaporation.[109] One of the most popular additives to date is DIO,[103] in a BDT-TT polymer (PTB7)-PCBM system and found that DIO, just like ODT, selectively dissolves PCBM and allows for better D-A intermixed domains. The mechanism of action was thought to be a strong coupling between partial negative charges on iodine in DIO and electron-deficient PCBM.[110] Another commonly used additive is chloronapthalene, which was shown to promote smooth, well-mixed D:A domains in quinoxaline-thiophene copolymers, and helped achieve a high PCE of >7%.[111]

Additives were recently classified according to boiling point, volatility, and solubility for either D or A components. High volatile–low solubility additives (acetone for example) essentially dilute the solution and have little effect over the performance of the device. Additives with low volatility and poor solubility (like propylene carbonate) stay in the wet film longer than the host solvent, which leads to film inhomogeneity. Additives

with high solubility and volatility (like benzene) do not have a significant effect on device performance. Lastly, the most commonly used additives have selective solubility for PCBM and low volatility, which frequently leads to coarser, enhanced phase separation between the D-A domains.[112]

Thermal annealing

Thermal annealing became a popular treatment method for P3HT:PCBM systems, and since then has been adopted for all kinds of donors. One of the earliest reports involved a P3HT:PCBM system that upon thermal annealing above T_g, along with an applied external potential higher than the V_{OC} led to devices with an EQE above 70% and PCE of 3.5 %; the enhancement was presumed to result from an increase of the charge carrier mobility.[24] In more extensive studies, the structural and optical effects of annealing in P3HT:PCBM films were studied using an X-ray diffraction; it was found that thiophenes in P3HT became oriented parallel to the substrate, while alkyl chains oriented perpendicular to it after annealing.[113] In addition to P3HT systems, annealing was used in a dithienosilole-BTD copolymer with and without end-capping groups and it was found to increase PCE in the end-capped polymer (after being annealed at 150 °C), while the nonend-capped version, the highest PCE was attained at 70 °C, and decreased with rising temperatures.[114] In small molecules, or in materials that are already crystalline, annealing may help, as in a copper pthalocyane;PDI system, or it may be unnecessary,[115] as was reported for a DPP small molecule.[116]

Solvent annealing

Solvent annealing is another effective strategy to control the morphology of BHJ blends by slowing the evaporation rate of the solvent. In practice, this is done by placing the spin-cast films in a closed container, with a small amount of solvent, effectively slowing the drying process. Once again, in P3HT:PCBM blends, solvent annealed (slow drying DCB in a closed container) films had mobilites up to 30-fold higher than those thermally annealed.[117] Small molecules made of anthradithiophene:fullerene blends were also found to increase performance upon solvent vapor annealing; the increase was attributed to the formation of well-mixed spherulites along the film.[118] In a more recent case, the high performance polymer PTB7 with PC71BM acceptor was found to increase PCE by 11% upon exposure of the film to methanol, which was ascribed to passivation of surface traps and enhanced charge density.[119]

Additional Strategies

The techniques and strategies highlighted here are the most frequently used, but by no means are the only ones. Ellipsometry for example is used to measure the thickness of the film. Speaking of films, they can also be analyzed by resonant soft X-ray scattering (R-SoXS), which is useful in giving structural (chemical composition) insight; small angle neutron scattering (SANS), which takes advantage of the density difference between components of a BHJ device, to give information about interfacial areas. Similarly, there are microscopy and spectroscopic methods that can help in understanding a system's performance in more detail.[101]

There are also other device fabrication issues that need to be taken into account besides the one mentioned. For example, the donor:acceptor ratio, which was not

mentioned, greatly affects how a device will perform; the optimum ration may not always be 1:1, it is common to see 1:2 and even higher ratio of either component. As stated before, the previous sections are meant to give a brief introduction to the complexity behind an OPV design. Nevertheless, there is one aspect that has remained only lightly explored, which will be the focus of this thesis, and that is to chemically program molecules to assemble in a certain way. Annealing and choosing solvents, etcetera, have all shown great promise at improving the active layer morphology, but rare are the cases where a specific functional group, or combinations thereof, have been intentionally placed to modify and/or instruct molecules to pack in certain ways. The following section will introduce the concept of self-assembly and supramolecular chemistry as a means to achieve programmed morphologies in OPV active layers.

1.4 Introduction to Self-Assembly as a Means to Improve OPVs

The previous sections all dealt with how to modify a system beyond what simple deposition of D:A blends could do by themselves. To rely on thermal annealing to induce crystallization of P3HT is in some way to rely on the material, once it has the necessary energy, to spontaneously form a desired morphology, and that is one example of self-assembly. A self-assembling process is one in which humans are not actively involved, in which atoms, molecules, aggregates of molecules and components arrange themselves into ordered, functioning entities without human intervention.[120] Although heating a P3HT sample is intervening, the morphology formed once its cooled depends entirely on the identity of the molecule/polymer (in this case P3HT was used as an example). Yet, it is possible to look at nature and observe deoxyribonucleic acid

(DNA) forming highly organized, long polymers without ever undergoing a special chemical treatment. To be able to program a molecule or polymer to form a desired morphology on a film without the need for solvent additives or annealing, would open a new path for material selection, and material design.

The types of interactions that self-assembly involves are non-covalent in nature. Covalent bonds hold molecules together, but if they brake, then that means a chemical reaction happened; there are no intermediate regimes (i.e. there is no half water for example). Non-covalent interactions, or non-covalent bonds, are dynamic, always changing and hopping between molecules. There are a few non-covalent interactions that appear constantly in studies: the most well-known would be hydrogen bonding (the one holding DNA chains next to each other), π-π stacking (aromatic rings interacting with each other), dipole-dipole (polarized regions of a molecule interacting with each other), ion-dipole (charged ions interacting with a polarized molecule), ionic bonds (e.g. NaCl), π-cation (similar to ion-dipole but involves the polarized π-surface of aromatics, interacting with ions), van der Waals (extremely weak, only relevant in large quantities, everything interacting with itself). For the purposes of this thesis, there are two particular non-covalent interactions that will play a major role, hydrogen bonding, or H-bonding, and π-π stacking.

Since conjugated molecules inherently contain aromatic groups, π-π stacking is a given intermolecular interaction present, but H-bonding is the one that this thesis covers. *The goal of this thesis, which started in 2010, was (and still is) to incorporate hydrogen bonding groups in a small molecule OPV donor, for the purpose of creating an*

idealized active layer morphology. There are many concepts that still need to be explained, so the next few paragraphs will break down the objective.

There are two major, and well-studied fields that this thesis is trying to unite, the OPV field and what is termed the Supramolecular Chemistry field. Supramolecular is a word that literally means "beyond the molecule," and the field of supramolecular chemistry aims to control interactions beyond a single molecule, and expand its control to entire arrays of molecules that will achieve a structure or function cooperatively, which would otherwise not be achievable. The next concept to address is the idealized active layer.

Section 1.2 discussed the photogeneration of current in an OPV device, an Section 1.3 discussed the importance of the morphology of the active layer, and techniques to optimize it, but it never discussed what type of D:A arrangements are researchers aiming for. The truth is that the idealized active layer is a complicated concept. The field of transistors was influential in understanding the requirements for efficient charge transport. Small molecules, being more crystalline than polymers, often showed high mobilities in organic field-effect transistors (OFETs), such was the case of acenes (anthracene, tetracene, etc).[121] Since transistors have electrodes on the sides of the substrate, it comes to no ones surprise that when OPVs began to be used, the same concept was adopted, but for transport along the vertical direction.

Naturally, there was a tendency to use highly π-π stacked molecules such as hexabenzocoronene (HBC),[66,122,123,67] or molecules with high mobilities, such as rubrene,[124,125] anthradithiophene,[118,126] or chrysene.[127] When interest in small molecule faded and was replaced with polymers, the same concept was pursued. It was

previously shown by a TEM of a cross section of a device, that the active layer morphology of a typical device looks like a randomly oriented mixture of D:A domains (Figure 1.18a),[103] but there were studies suggesting that a lamellar[128],[129] or checkerboard[130] type of morphology would be the ideal active layer morphology (Figure 1.18b and c, respectively); there was no mentioning of what type of orientation the pi-stacks should have, but it was assumed (just like in transistors), that parallel to the substrate, or face-on, would be ideal.
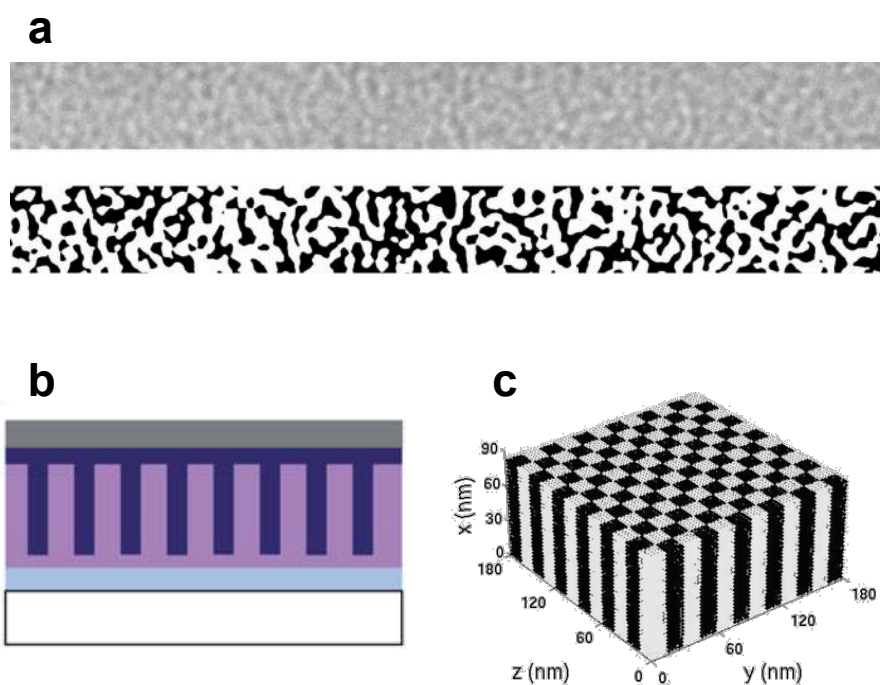
Figure 1.18. a) FIB image of an actual active layer cross section; b) Lamellar and c) Checkerboard-type morphologies thought to be ideal for high PCE. Retrieved from ref. 103,128-130.

As the field progressed, cases of polymers with high mobilities and fairly disordered films were reported.[131–133] In OPVs some of the best performing polymers like PTB7 (BDT-TT polymer) and small molecules don't have a strong propensity to pi-stack like hexabenzoronenes.[32,33,71,73,79] Moreover, in a HBC/PDI dyad system that was

designed to assemble either into hexagonal stacks or interdigitating networks (with HBC facing PDI), it was found that after photoexcitation of HBC, electron transfer competes with energy transfer in the interdigitated case, but charge could only be transported when HBC/PDI were not facing each other.[134] In addition, recent studies suggest that a more realistic version of an idealized active layer is one where (at least in polymer system) there is enough short-range intermolecular aggregation for efficient long-range charge transport, and that the important thing to keep in mind is the presence of interconnected aggregates, even if they are small and disordered;[135] another study suggests having D:A domains of 10-50nm wide and 200-400 nm long, which supports the previous statement.[136] Taking those suggestions into consideration, a more realistic version of the ideal active layer is shown in Figure 1.19, where smaller, vertical donor domains, intermixed with acceptor domains, have replaced the well-ordered lamellar columns from Figure 1.18b. That is the morphology that will be sought by introducing hydrogen bonding in the designs of this thesis. More details as to the how, are given in Chapter 2.
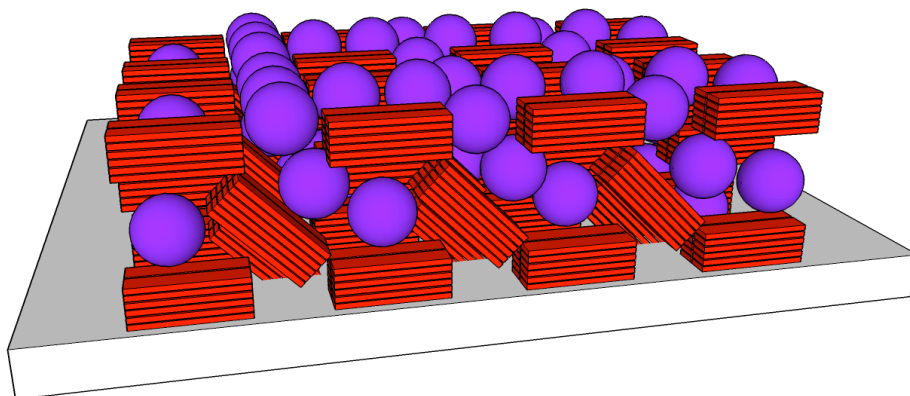
Figure 1.19. A more realistic ideal active layer.

Chapter 2. Improving Solar Cell Efficiency Through Hydrogen Bonding: A Method for Tuning the Active Layer Morphology

2.1. Introduction to DPP-Containing H-Bonding Donors

The importance of OPVs in the context of their low-cost processing,[137] added to their ease of synthesis and design versatility,[23,138–140] are valuable aspects not only for the purposes of this thesis, but also for their future commercialization. As was discussed in Chapter 1, there are two types of donors in the OPV field, polymers and small molecules. Historically polymer-fullerene systems have been the preferred system, but as of 2016, there is virtually no difference in using a small molecule or a polymer; studies even suggest fullerenes are no longer necessary since some all-polymer systems have achieved just as high performances as those that are fullerene-based. Replacement of fullerene acceptors is beyond the scope of this thesis, but the reader is directed to two recent reviews that highlight advances in this area.[141,142] Going back to the choice between polymer donors, both have advantages over each other. Monomers tend to have relatively simple synthesis, but once polymerization occurs, separation of the different populations of polymers can become problematic; it is especially important to have high yields of polymerizations because the PCE is directly proportional to molecular weight;[16] in addition, polymers require control or regioregularity and conformer orientation to achieve better planarity, which influences the performance of the device.[143–146] In contrast, small molecules, though greater in number of synthetic steps, tend to be easier to purify due to their inherent monodispersity; they also offer

enhanced local crystallinity, which translates into higher mobilities.[61] For this reason, small molecules were the choice of donor for this and the remaining chapters.

The idea of using H-bonded small molecules to create an idealized active layer was inspired by works from two former Stupp members. The first was a hairpin-shaped donor with sexithiophene arms that were coupled to a trans-1,2-diaminocyclohexane core. Upon H-bonding, the molecule exhibited both H- and J-aggregation modes by UV-Vis, which caused small fibers to bundle into much larger domains, eventually leading to gelation (Figure 2.1a).[147] It was thought that the V-shape would create a cavity where the fullerene acceptor could fit, but shortly thereafter, devices were not promising.[148] It was thought that better absorbance was necessary, so the design was modified to include a DPP dye, which ultimately did improve PCE,[149] but it became clear that the degree of H-bonding needed to be decreased (Figure 2.1b).

Material	I_{sc} (mA/cm^2)	V_{oc} (V)	FF (%)	η (%)
6T-Hairpin	1.79	0.62	35	0.48
6T-Onearm	1.55	0.71	28	0.39

Material	I_{sc} (mA/cm^2)	V_{oc} (V)	FF (%)	η (%)
DPP-Hairpin	2.76	0.69	27	0.52
One arm	1.39	0.58	28	0.23
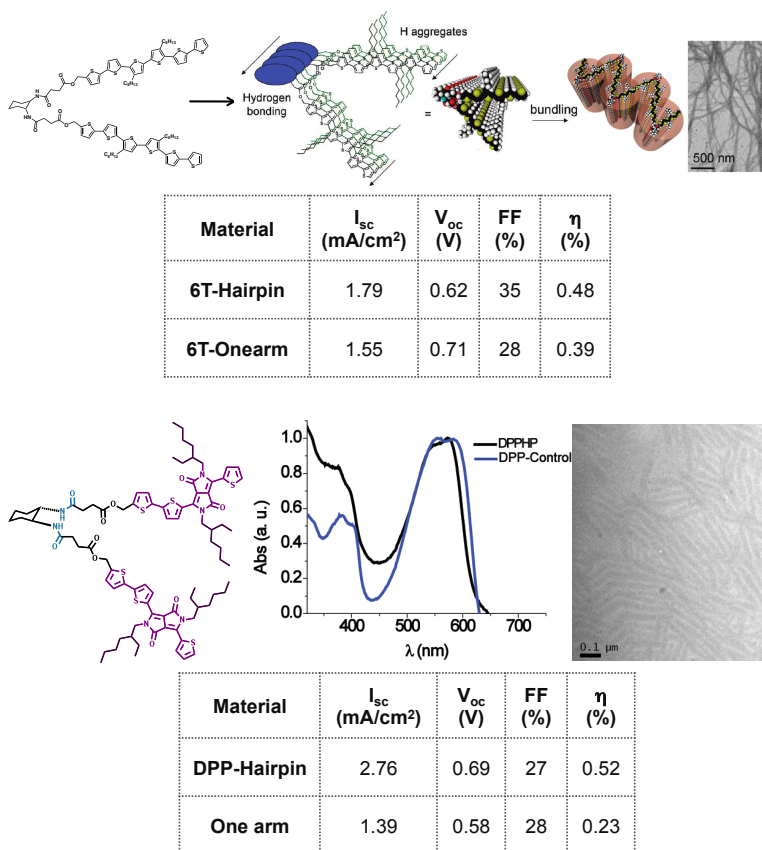
Figure 2.1. Hairpin designs that inspired this thesis. Retrieved from ref. 147-149.

To be able to decrease the H-bonding ability required looking at cases of supramolecular polymers using conjugated molecules, and also cases where such systems where used in OPVs. Supramolecular studies generally consisted on strongly pi-pi stacking molecules such as HBC[66,150] or PDIs;[151] then more related to OPVs were studies on oligothiophenes[152,153] or PPV derivatives with differing H-bonding groups, including melamine or guanosine derivatives.[154–158] In many of those cases there was a strong aggregation behavior, to the point of gelation, but at least that was one extreme of the H-bonding spectrum.

With regards to H-bonding incorporated into OPV designs, there were a few studies in molecules with diethienosilole,[159] dithienothiophene,[160] isoindigo,[161] or oligothiophenes,[162] where upon H-bonding, the morphology changes drastically and becomes detrimental to device performance. A larger number of studies though, report enhancement of performance upon H-bonding. For example, P3HT and PCBM modified to have complementary H-bonds achieved between 2-3% PCE,[163–165] or the morphology was enhanced;[166] another self-complimentary h-bonded P3HT increases in PCE by ~40% upon H-bonding.[167] Small-molecule systems composed mainly of oligothiophenes and H-bonding groups such as cyanopyridine,[168] pthalhydrazide,[169,170] or barbituric acid,[171–173] show enhancements either in PCEs that range between 1-3%, or enhancements in PCE that range from 10-250% upon H-bonding. There were even some cases of molecules where additional π-π stacking groups such as pyrene,[174] or 1,3-indacecedione,[175] helped improve the morphological order of the films, but in this case, it was believed that the conjugated core should provide enough π-stacking, after all, it is synthetically easier to add stacking ability than to reduce it.

The studies showed that H-bonding can be used to improve the performance of small molecules and polymers alike, but the greatest improvements were made in the former. Although the performance enhancement occasionally was above 100%, the overall efficiency was rather low, and one of the potential reasons could the use of large E_g small molecules. For this reason, for this thesis, a well known low E_g dye was chosen, DPP, which also has numerous publications in small molecule OPVs.[176–181] Since the H-bonding studies cited in small molecule OPV systems used simple amides, the same simplicity was adopted for this project. As part of the push-pull design,

thiophenes were used as π-bridges and cyanovinyl groups as electron withdrawing moieties. The working hypothesis at the moment was that the amide would be able to to h-bond and π-π stack, effectively creating organized domains (Figure 2.2a). As stated before, the ideal active layer should not be completely crystalline, but this fact was taken into account in the design, since upon addition of the fullerene acceptor, the domains were expected to be disrupted, but still able to split excitons and transport charges to the corresponding electrodes (Figure 2.2b). Since the ester cannot h-bond, it was expected to be able to π-π stack relatively well (Figure 2.2c), but upon the fullerene addition, the domains would become more disorganized and transport charge less efficiently (Figure 2.2d).
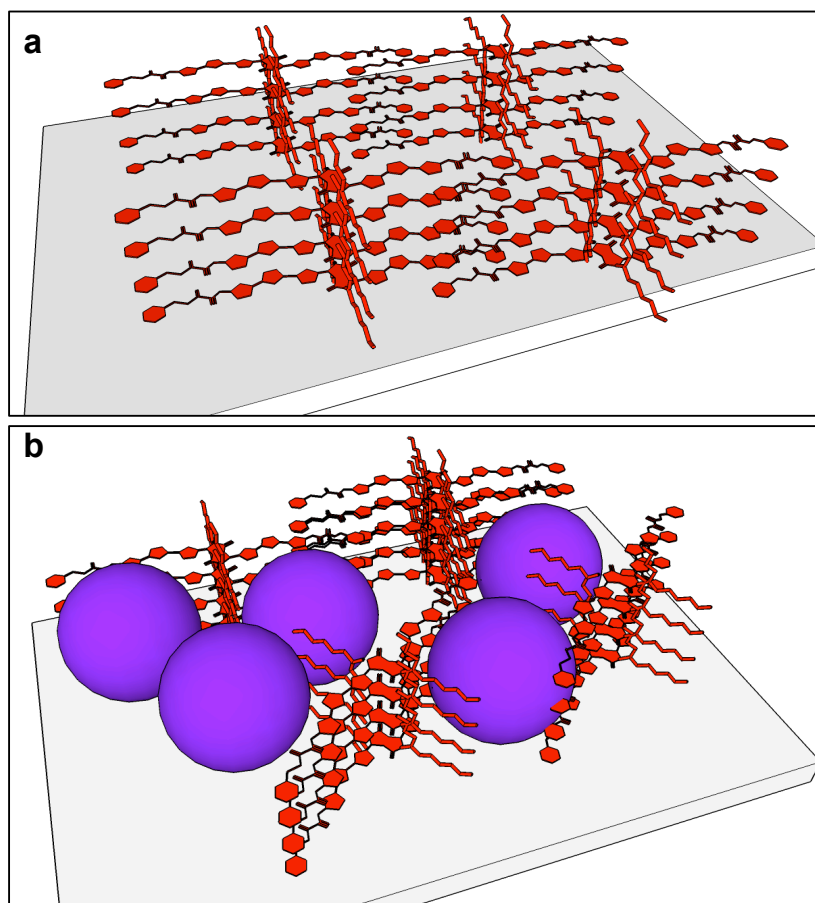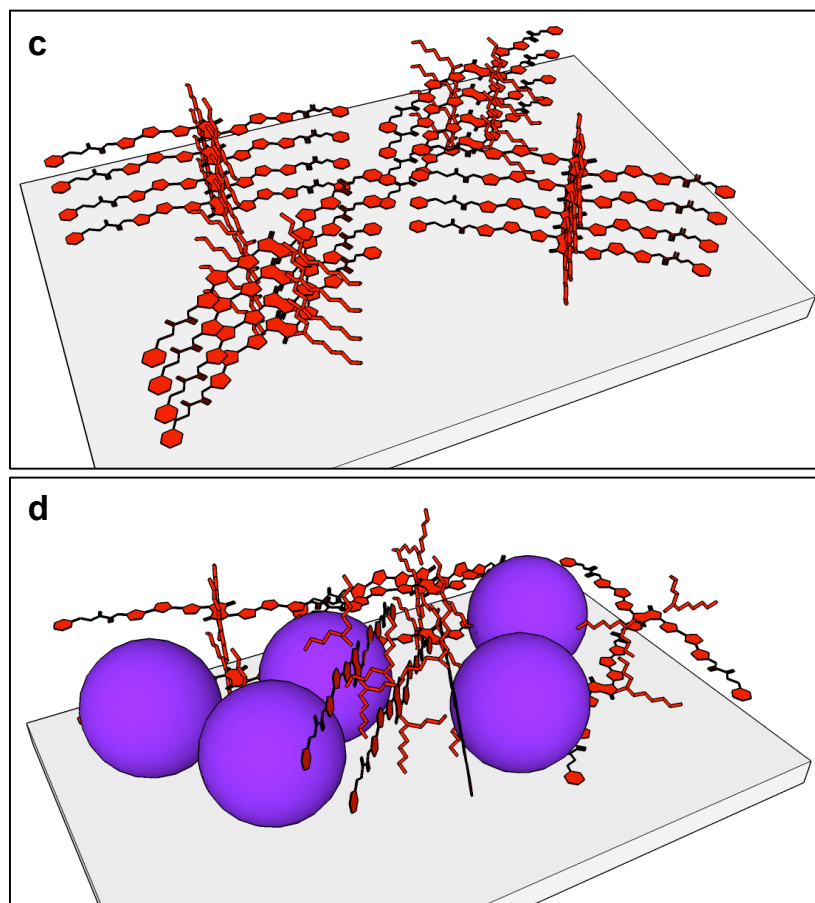
Figure 2.2. Expected amide packing before (a) and after (b) fullerene (purple sphere) addition. c) and d) are the expected ester packing before and after fullerene addition, respectively.

2.1.1. Preliminary Results

The first design was synthesized by a postdoctoral fellow in the lab; for effective solubilization, ethylhexyl chains were used in the DPP core. The molecule (Figure 2.3a) had strong CT absorption band from 500-700 nm and a smaller π-π* band between 350-500 nm, covering almost the entire visible spectrum. Solvents such as toluene enhanced vibronic features in solution that indicated H-aggregation (Figure 2.3c). After spin-coating and annealing at 120 °C for 5 min, this molecule formed short fibers, as can be observed by AFM (Figure 2.3b). Although fiber formation indirectly showed effective H-bonding, this aggregation on film was detrimental to device efficiencies, as

annealing resulted in 0.13 PCE with a low FF, indicating high resistivity in the film. Not annealing resulted in shorter nanowires and in a jump in the device efficiency to more than 2%, after some methanol was added (Figure 2.3d). After analysis of devices and AFM data, it was concluded that the design required more solubility, since it would decrease the aggregate size, and that seemed to have a significant effect in increasing the efficiency.

D:A (1:1)	V_{oc} (V)	J_{sc} (mA/cm²)	FF (%)	PCE (%)
Ann 120 °C 5 min	0.79	1.35	12	0.13
Unannealed	0.78	5.28	39	1.60
2% MeOH	0.83	5.55	45	2.1
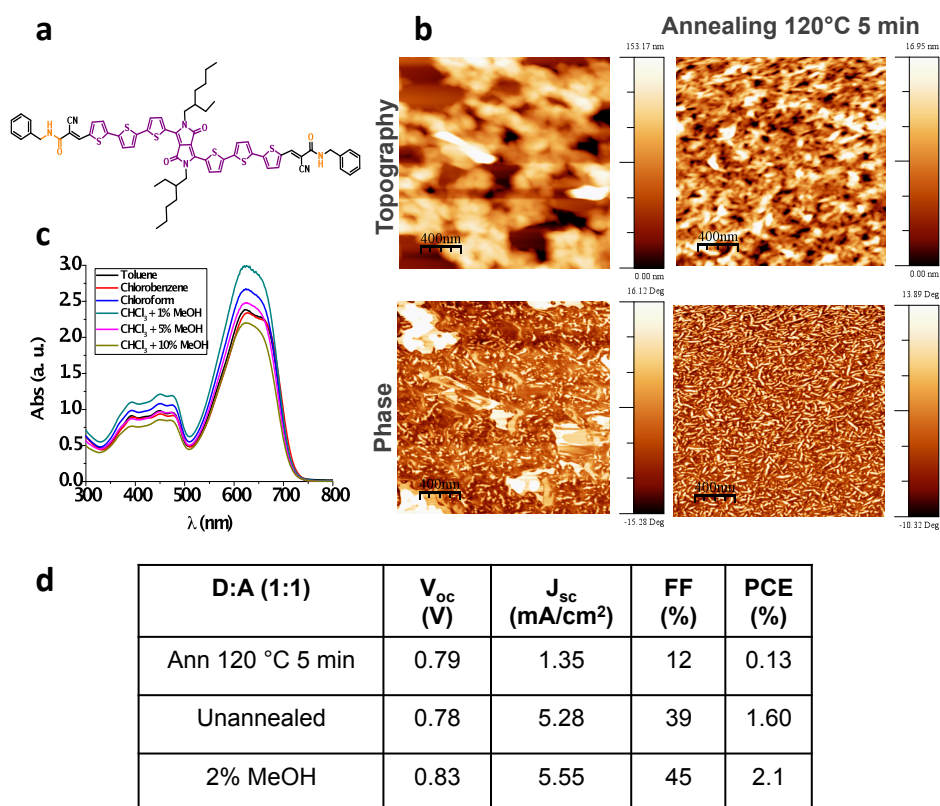
Figure 2.3. Summary of results for the ethylhexyl-solubilized initial H-bonding design. a) Molecular strucuture; b) AFM topology(top) and phase (bottom) images of amide before (left) and after (right) annealing; c) UV-Vis absorption spectrum; d) table of OPV device results.

2.2. Discovery and Properties of Asymmetric DPP H-bonding Donors

Synthesis

With the task of creating a more soluble version of the molecule shown in Figure 2.3a, the simplest thing to do was to increase the size of the alkyl tails. The first version used ethylhexyl tails, but upon addition of the thiophene π-spacers and condensation of the benzyl groups, the molecule aggregated somewhat strongly, and the concentration of the solution used for devices had to be decreased, which can affect the thickness (and light absorption ability) of the active layer. Consequently, the size of the alkyl tails was increased, and the new design incorporated butyloctyl groups. The synthesis, shown in Scheme 2.1, started with a dibrominated DPP core with butyloctyl tails; next, Stille coupling with a stannylated 2,2'-bithiophene gave the extended DPP core. Formylation of the extended core using a Vilsmeier reagent, followed by Knoevenagel condensation of the aldehyde with either benzylcyanoacetate or N-benzylcyanoacetamide gave the final product. One of the major discoveries while following this synthetic pathway was, as can be seen from Scheme 2.1, the synthesis yielded initially mostly an asymmetric molecule.
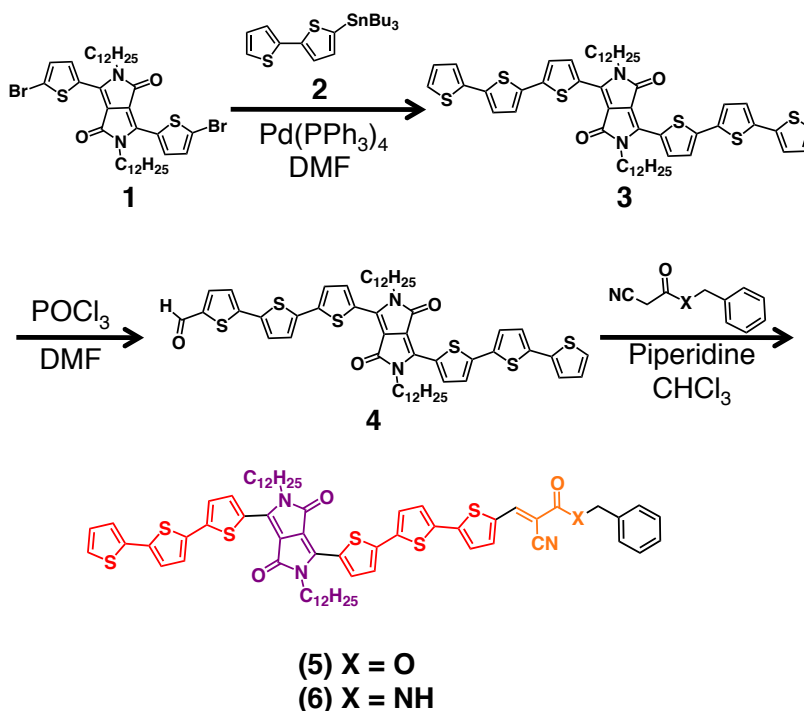
Scheme 2.1. Unintentional synthesis of asymmetric H-bonding donor.

Although it is possible to make the fully symmetric design using this synthetic pathway, the Vilsmeier formylation is relatively low yield, particularly if there are water traces in DMF. Finding the appropriate conditions to yield disubstituted (symmetric) products was challenging, but fortunately, a relatively simple and scalable strategy was found, which permitted the synthesis of many more design modifications. The next upcoming sections will discuss the modification of the synthetic pathway and the results of having made the originally intended molecules.

Absorption and Morphological Studies

Since the original ethyl-hexyl-containing DPP molecule was also asymmetric, it was interesting to compare the effect of one vs. two H-bonding groups, given that there is little precedence for intentionally making asymmetric designs. The now more soluble

butyl-octyl DPP H-bonding donor (Figure 2.4a) exhibited not surprisingly the same light absorbing behavior as its predecessor; an onset of absorbance at ~750 nm, maximum absorbance (λ_M) at 650 nm on film, and π-π band in the 350-500 nm (Figure 2.4b). Since molecules **5** and **6** were only a more soluble version of a previous design, the initial device conditions emulated those used for the ethylhexyl version (Figure 2.4d). The devices were all run using PEDOT:PSS as the electron-blocking layer, which has a HOMO of -5.0 eV, but ultraviolet photoelectron spectroscopy (UPS) revealed molecules **5**-**6** to have a HOMO more compatible with molybdenum oxides (MoOx); when the latter was used there was a slight drop of V_{OC}, but a significant gain in J_{SC} over the ethylhexyl version, and under the most optimized conditions, an overall improvement of more 50% was achieved.
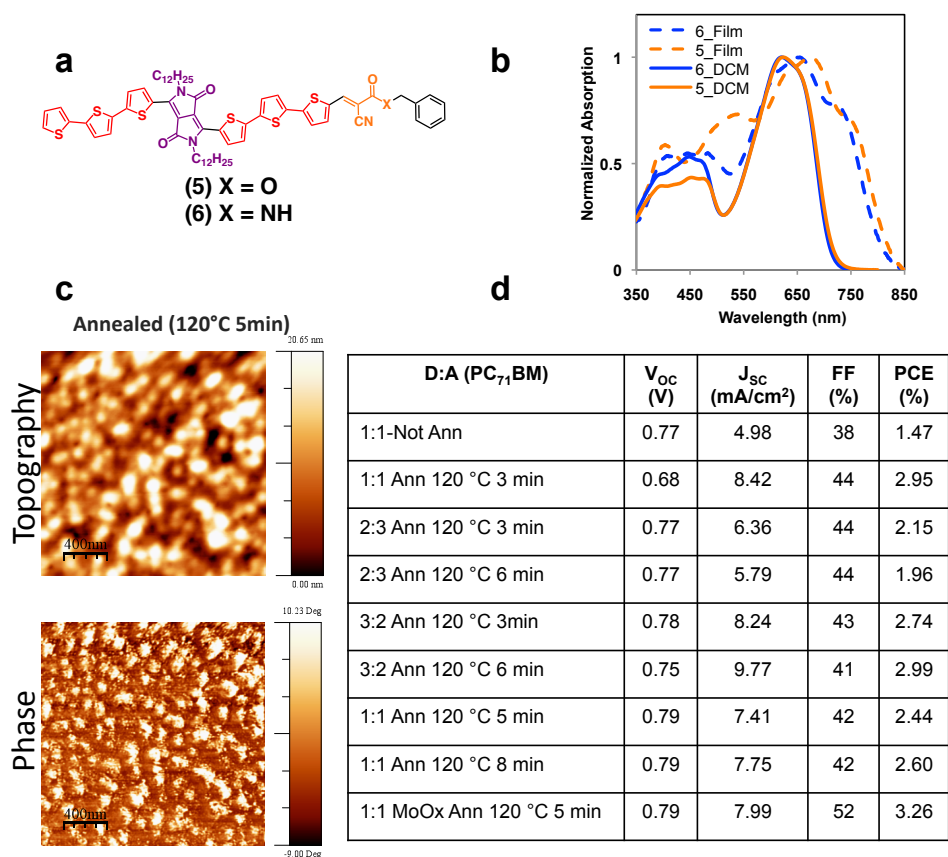
Figure 2.4.Summary of results for the butyloctyl-solubilized H-bonding modified asymmetric design. a) Molecular strucuture; b) UV-Vis absorption spectrum; c) AFM topology (top) and phase (bottom) images of amide after annealing; d) table of OPV device results.

D:A (PC$_{71}$BM)	V$_{OC}$ (V)	J$_{SC}$ (mA/cm^2)	FF (%)	PCE (%)
1:1-Not Ann	0.77	4.98	38	1.47
1:1 Ann 120 °C 3 min	0.68	8.42	44	2.95
2:3 Ann 120 °C 3 min	0.77	6.36	44	2.15
2:3 Ann 120 °C 6 min	0.77	5.79	44	1.96
3:2 Ann 120 °C 3min	0.78	8.24	43	2.74
3:2 Ann 120 °C 6 min	0.75	9.77	41	2.99
1:1 Ann 120 °C 5 min	0.79	7.41	42	2.44
1:1 Ann 120 °C 8 min	0.79	7.75	42	2.60
1:1 MoOx Ann 120 °C 5 min	0.79	7.99	52	3.26

As with previous molecules, the morphology was studied with AFM. Figure 2.4c shows the unannealed and annealed samples of molecule **6**. In the case of the annealed sample, the nanowires are not as clearly visible as before. In the ethylhexyl version, the nanowires (or nanofibers) reached lengths of ~400 nm, whereas in the butyloctyl version, they are reduced to sub 100 nm. This decrease of domain size was the expected result of having increased the solubility of the molecule, and as it will be seen in upcoming sections, played an important role in defining this project.

Discovery of Instability

Although the accidental discovery of the asymmetry of molecules **5** and **6** became an interesting journey, it also came with detrimental consequences. Before additional experiments could be performed, it was observed that over time, the device efficiencies, and more precisely, the V_{OC} was progressively lost, under no different conditions than before. Qualitatively speaking, the instability of a molecule can be indirectly predicted from its reactivity, and in this case, by studying other systems, we found that the loss of V_{OC} was due to the molecules decomposing under illumination. A previous publication in the group[147] mentioned that irreversible oxidation waves in a cyclic voltammetry (CV) graph (a voltammogram) are a sign of decomposition from the unprotected 2 or 5 positions in a thiophene ring. Another publication more correctly describes this phenomenon as oxidative dimerization,[182] which can be used in systems that have a relatively acidic position (or a position that can be deprotonated with a strong base, as is the case of thiophene). The voltammogram in Figure 2.5a shows an irreversible oxidation wave at ~2.4 V (see arrow), which grew in intensity after repeated cycling. This is an indication that the molecules most likely dimerized from the position with an arrow in Figure 2.5b, and in doing so became insoluble and precipitated on the surface of the electrode, a phenomenon described in the previously mentioned publications.

a

b
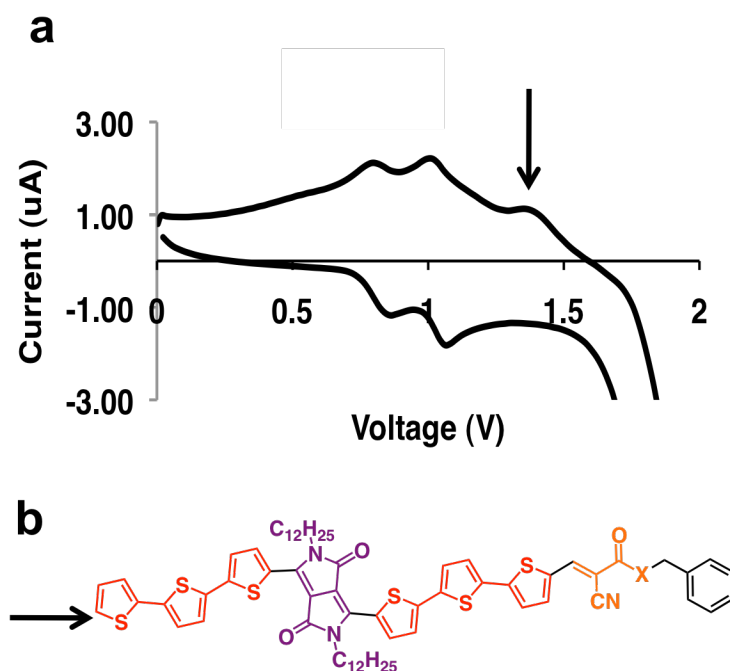
Figure 2.5. a) Voltammogram showing irreversible oxidation wave (arrow); b) position of molecule most likely responsible for the instability.

2.3 The Start of a Journey: The Real Symmetric Molecules

Synthesis

Having found the reason for the instability of molecules **5** and **6**, the main challenge became modifying the synthetic pathway to produce a fully symmetric molecule. The previous synthesis involved introduction of the aldehyde moieties via a Vilsmeier reagent (see Scheme 2.1). This reaction was able to produce both the mono and dialdehyde, but the latter was produced in small amounts. Unfortunately, other ways of introducing aldehydes would most likely also attack the DPP core (i.e. BuLi/DMF or reduction of a carboxylic acid to the aldehyde). The solution became to have the aldehyde prior to the coupling with DPP, but that by itself also presented a

challenge. In order to be able to run a stille coupling, two parts are necessary (in addition to the catalyst): the halogenated part (DPP in this case), and the trans-metallating unit (a trialkylstannyl-containing molecule), and most stannylations involve litiation, followed by quenching with trialkylstannyl chloride. Lithiations cannot be run with an unprotected aldehyde, but formation of the cyclic acetal would also not be convenient since the deprotection would involve refluxing in a strong acid, which the DPP unit is sensitive to. Finally, a strategy involving pseudo-protection of the aldehyde by turning it into the enamide, followed by the usual stannylation procedure, afforded the stannylated bithiophene carboxaldehyde after hydrolysis of the enamide in dilute acid, in good yields.[183]

Having solved the synthetic part, the fully symmetric molecules were synthesized as shown in Scheme 2.2. The coupling of two electron deficient units (DPP and the aldehyde) did come with some consequences, as it affected the yield, from ~70% to <50% by going from bithiophene, to bithiophenecarboxaldehyde. Nevertheless, the simplified coupling reduced the number of purification steps, and saved enourmous amounts of time. In addition, as will be seen in later sections, this strategy became very useful in streamlining the synthesis of different molecular designs.
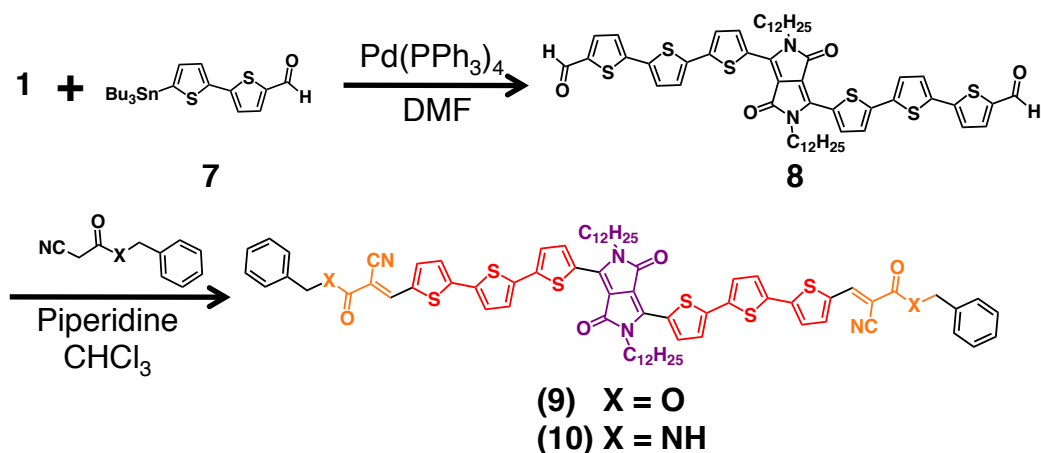
Scheme 2.2. Synthesis of the actual symmetric molecule initially designed.

New Problems in Symmetric Molecules

Molecules **9** and **10** exhibited radically different properties to its asymmetric predecesors. The first difference is in absorbance, where the now symmetric molecules showed enhanced absorption in the π-π* band and more defined red-shifted vibronic features on films, which indicate J-aggregation (Figure 2.6b).[184] The other major difference, and perhaps the most important, is that as designed, the symmetric molecules were barely soluble in most solvents. Given that the solubility was so low, these molecules were not studied any further, since it was clear that they would not work to any appreciable extent in OPV devices.
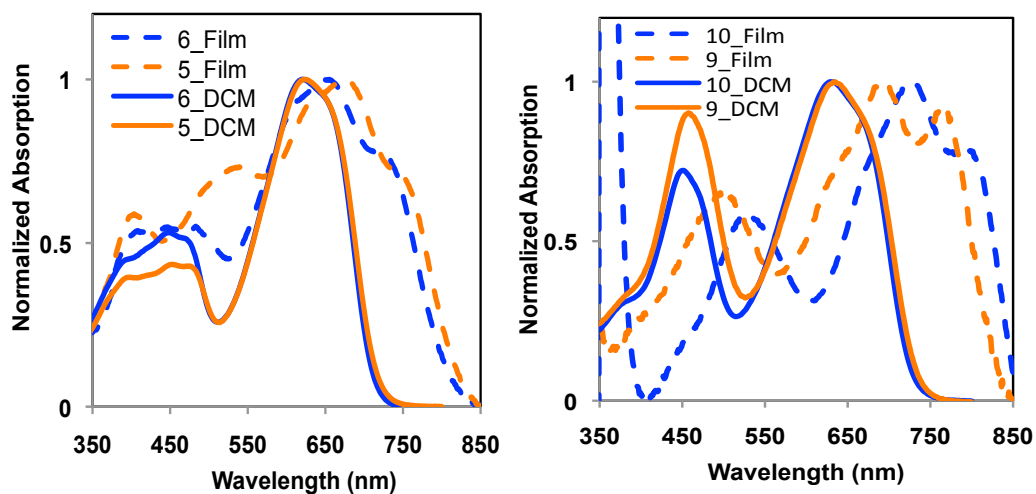
Figure 2.6. UV-Vis spectra comparison of asymmetric, butyloctyl solubilized (left) and symmetric molecules (right).

2.4 Increasing the Solubility of Symmetric DPP H-Bonding Molecules

Synthesis

Having solved, or at least so it was believed, the stability problem, a new challenge appeared, which was solubility. Fortunately, the previously discussed molecules **5** and **6** solved a solubility issue in a design, and so the same strategy was applied here. The problem was that molecules **9** and **10** already had butyloctyl tails in the DPP core, so it was decided that maybe alkyl tails should be incorporated on the extremes of the molecule, but in order to be able to do that, the benzylcyanoacetate or acetamide groups had to be modified. This was one time where having a modular design became very useful. Since the last step of any molecule discussed so far is the Knoevenagel condensation; that means that any molecule having the cyano group beta to an ester or amide could be used under the same conditions. Looking at the work of previous colleagues, one functional group in particular stood out: gallic acid. It consists

of a single trisubstituted benzene ring that was modified to be able to condense with the aldehyde. Although it required around six steps, having a single benzene ring with three alkyl tails was very helpful. The synthesis (shown in Scheme 2.3) started with reduction of a previously reported trialkylated gallic acid methyl ester to the alcohol. The alcohol was used directly to couple to cyanoacetic acid, which was used to make molecule **18**. The alcohol was converted into the chloride with $SOCl_2$, then to the azide with NaN_3, then to the amine with PPh_3. The amine was coupled to cyanoacetic acid, and the product condensed with the dialdehyde **8** to make molecule **19**.
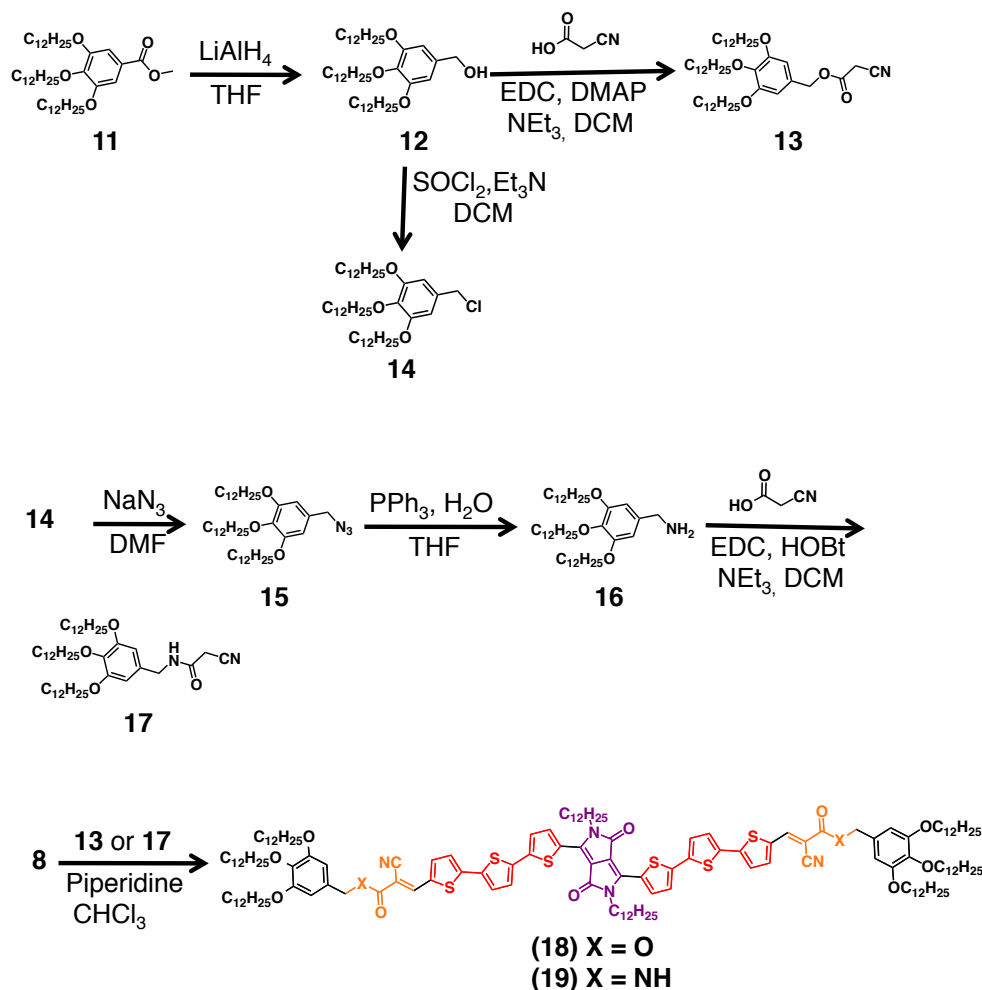
Scheme 2.3. Modified design of symmetric molecules to enhance solubility.

Absorption and Morphological Studies

The absorption of molecules **18** and **19** is shown in Figure 2.7a**.** The absorbance in solution remains essentially unchanged from that of molecules **9** and **10**, but the film absorption is quite different. Whereas **9** and **10** exhibited strong vibronic broadening (an indication of J-aggregation), **18** and **19** show only slight broadening of the CT band at λ_{Max} ~600 nm. The amide **19** seems to have J-type aggregation, while the ester **18** shows a slightly blue-shifted λ_M, which is characteristic of H-type aggregation. Given that molecules **18** and **19** were significantly more soluble than **9** and **10**, it was expected that their aggregation on film would be diminished, but the fact that the CT ban still broadens is an indication that the molecules, though very soluble, were still able to aggregate on film, which is necessary for proper electronic communication between them.
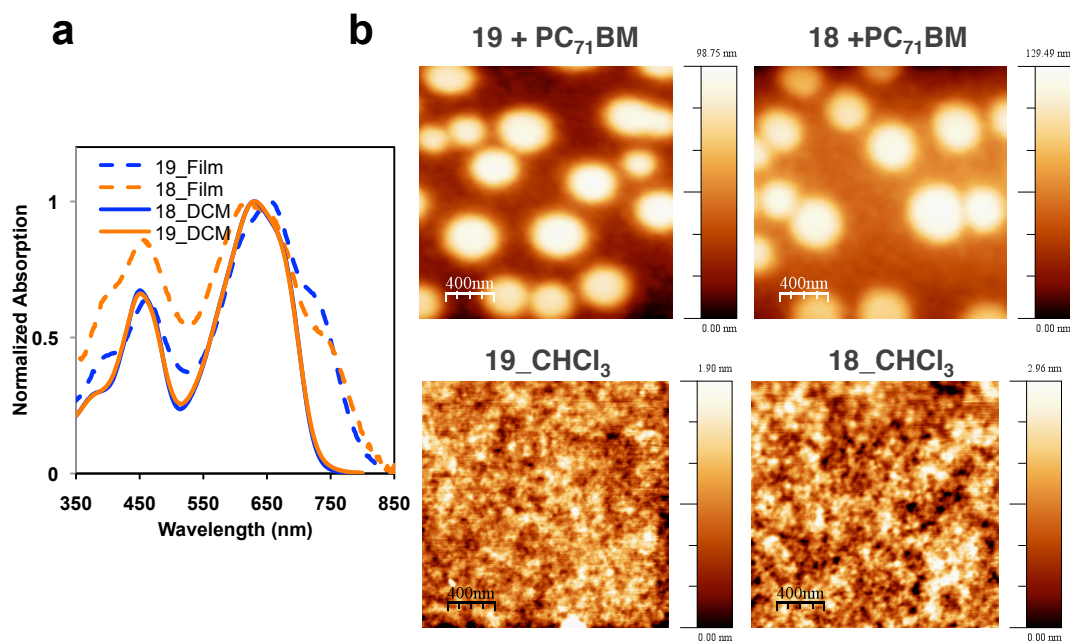
Figure 2.7. a)Absorption spectra of molecules **18-19**; b) AFM images showing molecules **18-19** with PCBM (top) and by themselves.

The morphology of the active layer was observed with AFM (Figure 2.7b, top row). When spin cast from $CHCl_3$, it was observed that as the solvent began drying, there was visible spinoidal decomposition (phase segregation); the color of the film went from dark green, to having brown and green patches (brown from PCBM and green from either **18** or **19**). From Figure 2.7b, it is clear why the active layer was visibly phase-segregated. The large clusters observed in the micrograph are PCBM aggregates of size > 400 nm. Not surprisingly, due to the strong phase segregation, devices performed poorly when compared to their asymmetric counterparts. The amide **19** topped at 0.3% PCE and the ester **18** at 0.1%, in the most optimized conditions. Although it was somewhat comforting to see that the amide performed better than the ester, the dramatic drop in efficiency posed a new problem that needed to be resolved.

The immediate thing to do would be change the solvent from $CHCl_3$ to CB, as solvents can have a significant impact in the aggregation of molecules. Unfortunately, the CB devices also showed strong aggregation; though somewhat better morphologies were achieved, the device efficiency was far too low to be of any significance. At this point, it became necessary to check the morphology of molecules **18** and **19**, before any further device optimization was attempted. Surprisingly, as the bottom pictures of Figure 2.7b show, both **18** and **19** show smooth films (in this case from $CHCl_3$, but CB was also similar), and annealing did not have a particularly significant effect either.

Device Performance

Given that the native films of **18** and **19** were not patchy, as when mixed with PCBM, it seemed that the phase segregation problem had its roots in how the donors and acceptors interacted on the films. It was clear from the AFM that there was a very

strong repulsion of donor and acceptor molecules on the films, and by considering the surface energy of the D:A couples, the fact that alkly tails are low-energy and PCBM is high energy gave clues as to why segregation was occurring. Although all solution-processable OPV designs have alkyl tails, molecules **18** and **19** had three long alkyl tails right next to each other, which definitely became excessive and caused the segregation problem and consequently, the poor photovoltaic performance (see Table 2.1). It was necessary to modify the design again to decrease segregation between the D:A couples.

Table 2.1. Summary of device results for molecules **18-19.**

D:A (PC71BM)	VOC (V)	JSC (mA/cm2)	FF (%)	PCE (%)
18_1:1 (no DIO) 120 °C 2 min	0.89	0.31	35	0.096
18_2:3 (0.4% DIO) 120 °C 2 min	0.91	0.35	34	0.11
18_1:1 (0.4% DIO) 120 °C 2 min	0.91	0.28	37	0.10
19_2:3 (0.4% DIO) 120 °C 2 min	0.89	0.85	43	0.32
19_1:1 (0.4% DIO) 120 °C 2 min	0.89	0.75	46	0.3

2.5. Reducing the Aggregation of Symmetric H-Bonding Donors and PCBM

Synthesis

The strong segregation of **18** and **19** with PCBM was an unexpected and disappointment finding, but there were a few lessons learned up to that point. First, the instability initially encountered in the asymmetric versions was undoubtedly resolved;

second, the ideal alkyl tail content was somewhere between the insoluble **9**-**10** molecules, and the strongly segregating **18**-**19**, so the challenge was slightly simplified by knowing what the limits of solubility should be. Once again, the core of the extended DPP could remain untouched, and the modifications of the cyanoacetate-containing amide or ester molecules could be done separately. Since the gallic acid represented too many alkyl tails, and the lonely benzene represented too little, it was decided to remove the benzene ring entirely and replace it with a single alkyl tail. The problem was that branched alky tails help increase solubility, while straight tails tend to increase crystallinity, so the branched alkyl tail was chosen and the synthesis of the modified cyano-containing part is shown in Scheme 2.4. Starting with 2-butyl-1-octanol, the ester **20** was made with EDC and condensed with dialdehyde **8** to make molecule **25**. A separate batch of the alcohol was tosylated, then the tosyl substituted for an azide with NaN3, then the azide reduced to the amine with PPh3, and the amine couple to cyanoacetic acid to make molecule **24**, which was condensed with aldehyde **8** to yield the amide **26**.

Scheme 2.4. Synthesis of the modified design of the symmetric donors to prevent segregation from PCBM.

Absorption, Morphological and Device Studies

The new molecules **25** and **26** had solubility as desired, in between molecules **9**-**10** and **18**-**19,** but trending more towards strong aggregation. The absorption shows essentially unchanged solution behavior as the two previous versions, but the film did change (Figure 2.8a). Molecules **18** and **19** had just a slight broadening in film, but **25**-**26** showed a significantly enhanced broadening and red-shift of the CT band particularly. Fortunately, the broadening is not as much as to overlap with the one from

molecules **9**-**10**, so molecules **25**-**26** did have intermediate solubility and absorption properties. Interestingly, despite having essentially identical absorption onsets, the absolute absorption of amide **26** is significantly higher than that of ester **25** (about 50% higher).

device	V_{OC} (V)	J_{SC} (mA/cm^2)	FF (%)	PCE (%)
S-Amide	0.86 ± 0.01	1.1 ± 0.1	40 ± 3	0.37 ± 0.05
S-Ester	0.63 ± 0.03	0.7 ± 0.1	32 ± 1	0.15 ± 0.03

^{a}Average performance of four devices.
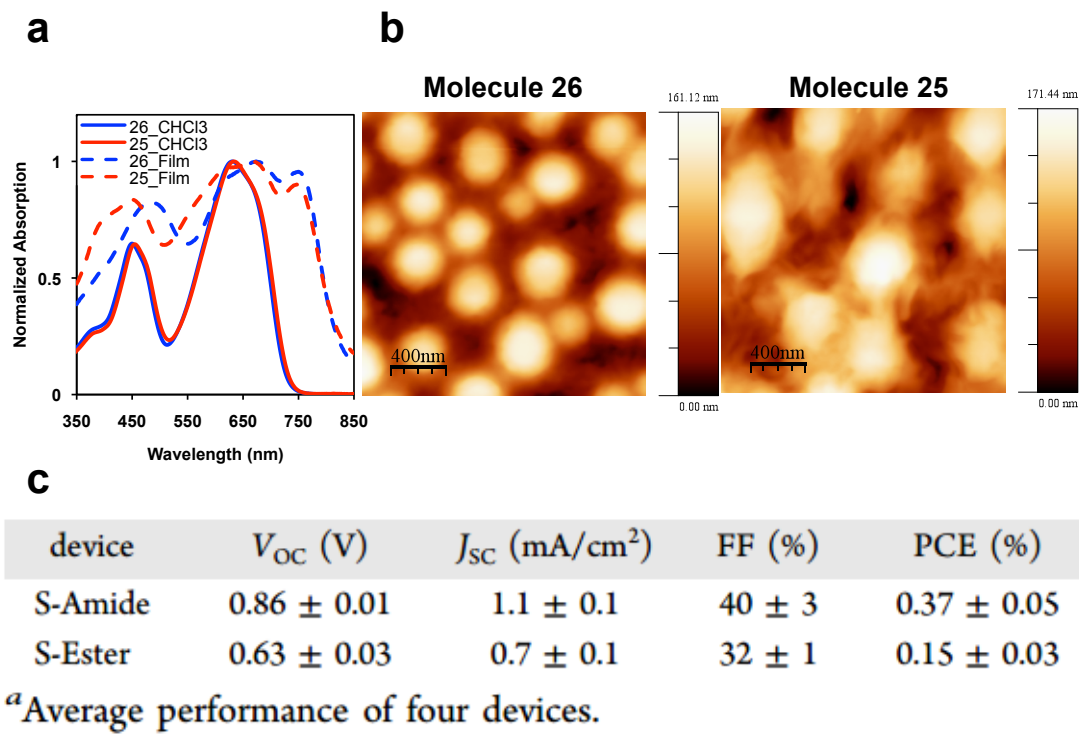
Figure 2.8. a) Absorption spectrum of molecules **25**-**26**; b) AFM micrographs showing the morphology of molecules **25**-**26** with PCBM and c) optimized device results. Retrieved from ref 185.

Having checked the optical properties, devices were then fabricated by using donor/PC$_{71}$BM blends at a 1:1 weight ratio, in CB. and the topology summary of devices is shown in Figure 2.8b**.** Though the molecules were still stable and soluble at relatively high concentrations, the morphology still indicated phase segregation, as can be seen from the AFM images. A rough surface with large spherical features is observed in the topography images of both donor/PC$_{71}$BM blends. The aggregate size

is smaller for **25** than **24,** which correlates with the higher efficiency and higher V_{OC} observed in the devices (Figure 2.8c). Although solvent additives were used to improve the device performance, there was little to no improvement in performance.   As shown in Figure 2.10c, and as has been the case for all previous molecules, the PCE of the amide **25** is higher than the ester **24**; both symmetric donor molecules show reasonable V_{oc} and FF, but the low J_{sc}s caused by phase segregation limit their performance to sub 1% values.

2.6 Revisiting Asymmetric H-Bonding Donors

Synthesis

The experiences encountered with the three different versions of symmetric H-bonding donors left a few lessons. First, tuning the aggregation/solubility is quite challenging, since molecules **24** and **25**, despite being soluble, also segregated strongly from PCBM, but not as strongly as their predecessors, molecules **18** and **19**. Second, up to this point, there was no unambiguous evidence that H-bonding was occurring. There is a simple way to figure that issue, and that is FTIR, but it was considered that before any in-dept study was performed, it was first necessary to find a pair of molecules that behaved as intended at the beginning of the project. The accidental discovery of the asymmetric molecules opened a way to finding such a pair of molecules. Since the symmetric versions were all underperforming the original asymmetric design, the next strategy attempted was to make use of the superior properties of the asymmetric designs, while at the same time find a way to fix the instability problem first encountered. The fully symmetric versions all had no instability

issues, which suggested that blocking the α-carbon to the sulfur on the thiophene opposite to the H-bonding group would be a way that could increase the stability of the molecule (that was after all the only difference between molecules **5**-**6** and **9**-**10**). The synthesis of the proposed molecule is shown in Scheme 2.5. The flexibility of the design cannot be overstated as an advantageous trait. Most of the molecules had already been synthesized in previous designs. For example, intermediate **27** was a byproduct of the reaction to make dialdehyde **8**, so there was plenty of what at the time seemed like useless material to start with. After purification, intermediate **27** was coupled to a stannylated thianapthene **28**, to make the protected asymmetric aldehyde **29**. Thianapthene was chosen because the fused thiophene can be stannylated, but the benzene cannot, and phenyl rings do not have positions that can be deprotonated, not even with bases such as n-BuLi. Since the electrochemical studies of Section 2.2 never mentioned oxidative dimerization cases in phenyl rings, choosing those rings to protect a vulnerable position seemed like the best informed decision possible at the time. To finish the synthesis, the aldehyde **29** was condensed with either benzylcyanoacetate or N-benzylcyanoacetamide to make amide **31** or ester **30**.
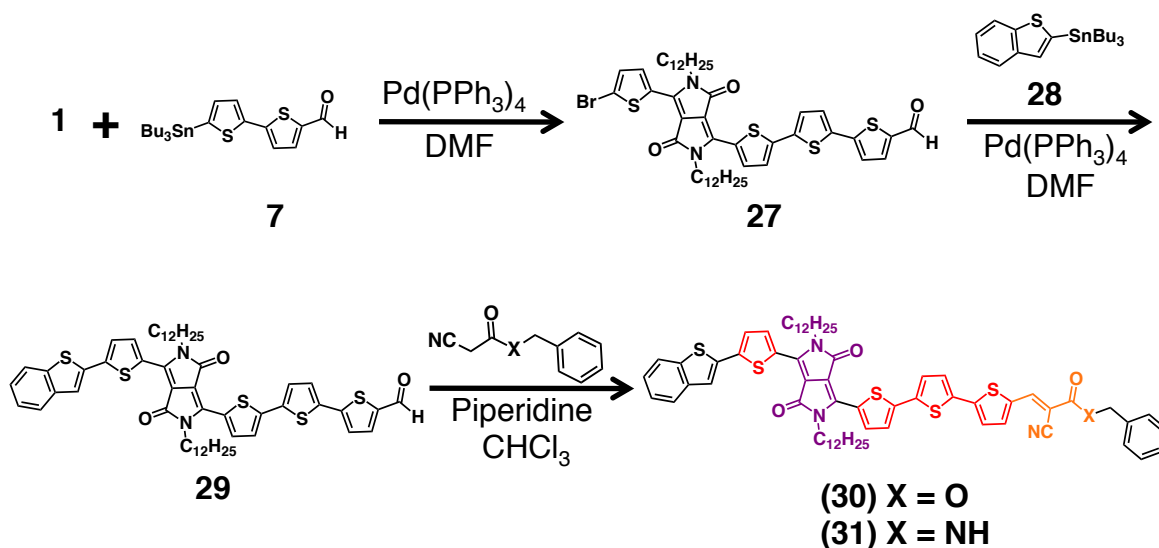
Scheme 2.5. Redesigned asymmetric H-bonding donor with thianaphene blocking the position thought to be the one responsible for initial instability

Absorption and Morphological Studies

The absorption of the improved asymmetric H-bonding donors is shown in Figure 2.9a. Compared to their symmetric counterparts, there are some differences in their light-absorbing properties. In solution, molecules **30**-**31** show a weaker π-π* band, but the CT band remains essentially unchanged. The film absorption reveals a weaker aggregation tendency than molecules **24**-**25**. In fact, the film absorption is reminiscent of molecules **18**-**19**, but the important thing to remember was that in that case, there was an excessive amount of alkyl tails, which was not the case for these new asymmetric molecules.

a **b**
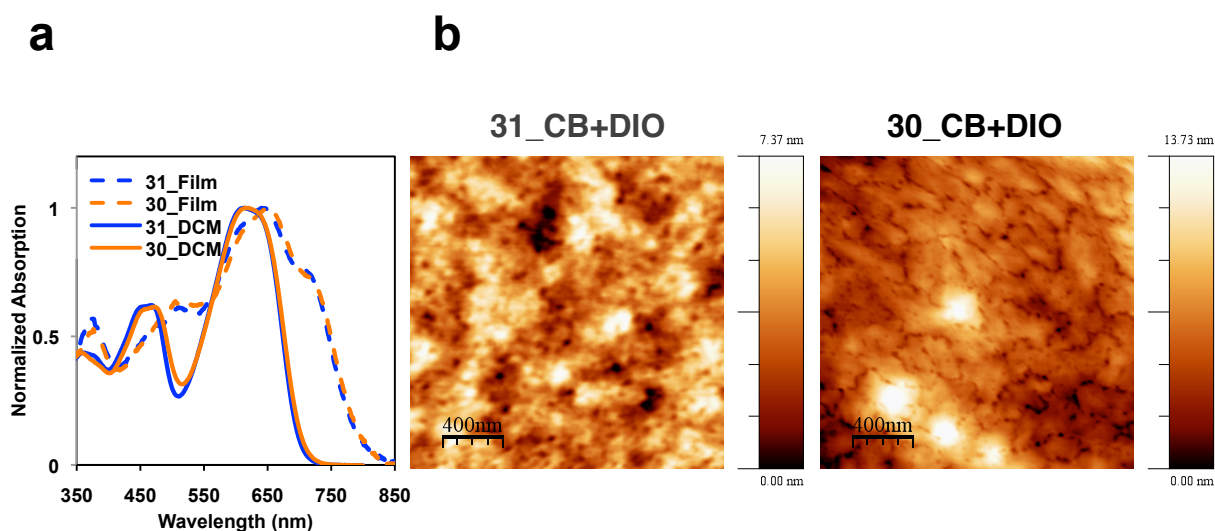
Figure 2.9. Absorption spectrum of molecules **30-31** by themselves (a) and AFM images of molecules **30-31** with PCBM (b).

As it had become customary, devices were built and the morphology studied with AFM. The very first asymmetric designs worked better with $CHCl_3$ as solvent, and so it became the solvent of choice for the improved design. The initial devices still showed large and spherical aggregates both in the non-annealed and annealed films. Switching solvents to CB helped in the past, but in order to have smooth films, the D:A couple was mixed, then heated overnight at 100°C to ensure proper dissolution. As before, MoOx was the HTL of choice. Finally, to help even further with optimization of the morphology and to decrease the surface tension between the D:A, 0.2-0.3 v/v% of DIO to solutions of **30**-**31** in CB resulted in significant increase in the device performance and morphology. The optimized morphologies are shown in Figure 2.9b, and for both amide **31** and ester **30**, large aggregates are not observed anymore, a sign that the films are well mixed.

Device Performance

The initial devices were promising, resulting in 1% efficiency for ester **30** and 2% efficiency for the amide **31**, so far higher than any symmetric design tested. The culprit for the increased performance was a higher current. After switching solvents and adding DIO, ester **30** achieved a PCE of 2.78% and the amide **31** increased up to 3.65%. The improvement in performance stemmed from the enhanced morphology and smaller aggregates in the active layers of such devices (see Table 2.2). It was believed that these two molecules were finally going to be published, but unfortunately, just like it happened with the unprotected asymmetric version, over time, there was a progressive loss of V_{oc}, that as experience could tell, was a sign of instability.

Table 2.2. Conditions attempted at optimizing the devices of molecules **30-31**.

D:A	Solvent	Spin rate (rpm)	Annealing	V_{OC} (V)	J_{SC} (mA/cm^2)	FF (%)	PCE (%)
30_1:1	CHCl$_3$	2000	None	0.89	2.45	46	0.99
30_1:1	CHCl$_3$	2000	100 °C 5 min	0.91	2.55	44	1.01
30_1:1	CB	1500	100 °C 5 min	0.93	3.89	44	1.61
30_1:1	CB+DIO	1500	100 °C 5 min	0.89	5.56	56	2.78
30_1:1	CB+DIO	1500	100 °C 7 min	0.89	5.61	53	2.64
30_1:1	CB+DIO	1500	100 °C 3 min	0.85	5.35	53	2.43
30_1:1	CB+DIO	1200	100 °C 5 min	0.87	5.21	49	2.21
31_1:1	CHCl$_3$	2000	None	0.91	3.14	40	1.13
31_1:1	CHCl$_3$	2000	100 °C 5 min	0.91	5.13	46	2.12
31_1:1	CB	1500	100 °C 5 min	0.91	7.98	43	3.16
31_1:1	CB+DIO	1500	100 °C 5 min	0.81	9.51	47	3.65
31_1:1	CB+DIO	1500	100 °C 5 min	0.83	5.91	53	2.61
31_1:1	CB+DIO	1500	100 °C 7 min	0.81	6.98	53	2.99

Finding the Reason for Instability

Unlike the previous case where there was literature precedence for knowing what the source of instability was, this time the answer came from an alternative synthesis. Intermediate **27** was initially synthesized by first coupling the stannylated thianaphtene unit **28**, to a monobrominated DPP core (not shown). Following the coupling, the DPP core was brominated, and it was during that bromination step that something happened. During the silica gel column to purify the brominated product, two fractions of different color were isolated, and the mass spectrum revealed they were isomers. Since it was too difficult to separate them, the next step was thought to be more useful for separation, and so the bithiophene carboxaldehyde **7** was coupled, and sure enough, during the column, two fractions of different color were isolated. After analyzing the NMR spectrum in detail, one of the isomers was found to be desired aldehyde **29**, and the other, being an isomer, had the same molecular weight, but one signal in particular was missing: the singlet that the proton on the thianaphtene unit (shown with an arrow in Figure 2.10). So it appeared that by fusing the benzene and thiophene rings, that special position became almost as acidic as a regular **2** or **5** position in a thiophene, and that was the reason for the instability. Fortunately, there was a very simple synthetic way to fix the instability problem, which gave way to the final modification of the asymmetric design, published in 2015.[185]
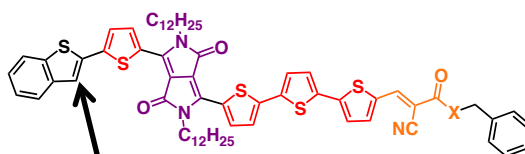
Figure 2.10. Position most likely responsible for the instability of molecules **30-31** (see arrow).

2.7 The Unfused-Ring Protected Asymmetric H-Bonding Donor

Synthesis

After discovering the reason for the instability of molecules **30**-**31**, it was necessary to find a blocking group with a phenyl group flanking one side of a thiophene ring, and leave the other side exposed for subsequent steps. Fortunately, such group was commercially available, 2-phenylthiophene. The synthesis of the improved design was identical to that of molecules **30**-**31**, except that intermediate **27** was coupled to a stannylated 2-phenylthiophene **32**, to make the monoaldehyde **33**, which was once again condensed with benzylcyanoacetate or N-benzylcyanoacetamide to make **34** or **35**, respectively (Scheme 2.6). Yet again, the flexibility of the design cannot be overstated. Throughout this project, having a few pieces of a molecule be interchangeable with other designs simplified the synthesis enormously and saved a significant amount of time, which was vital to be able to streamline the molecule-making process.
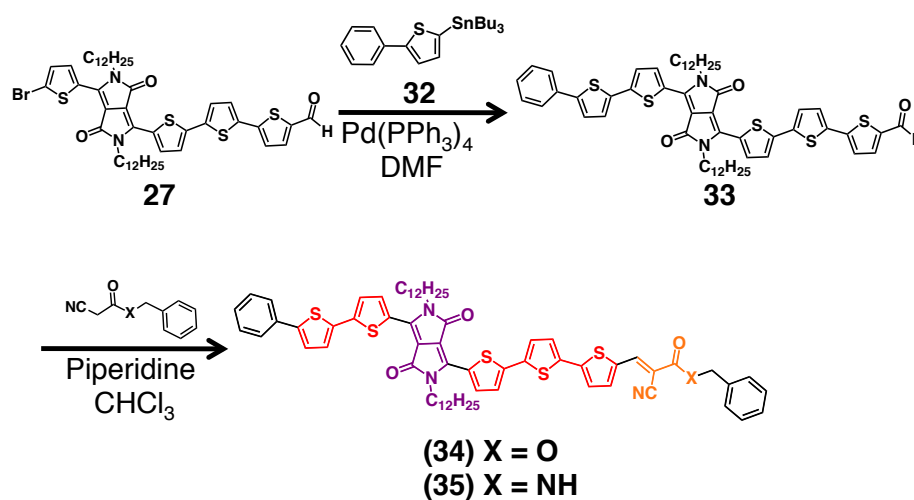
Scheme 2.6. Second modification of the asymmetric H-bonding donor with unfused rings to improve stability.

Absorption Studies

Despite being so similar to molecules **30**-**31**, the new asymmetric protected molecules **34**-**35** showed significant differences in absorption. In Figure 2.11a, to start with, it can be seen that the π-π* band in **34**-**35** diminished in intensity with respect to the previous design. Also, there is a dramatic difference in the aggregation on films between the amide **35**, and the ester **34**. In no other previous design had there been such differing behavior. The amide **35** film absorption resembles that of the gallate derivative **19**, but the ester **34** shows quite a significant red-shift in absorption, signaling a strong tendency to aggregate. This pair of molecules was the first case where the color of the films could be assigned to either the amide or ester, which was a very good sign, given that in the past, device performance favored lower aggregation and smaller domains over large crystalline ones. For the sake of having a more complete story, the best performing molecules, both symmetric a asymmetric were compared side-by-side, that is the pairs of molecules **25**-**26** (symmetric) and **34**-**35** (asymmetric).

a

(34) X = O
(35) X = NH

b

c

Molecule	λ$_M$ Sol (nm)	λ$_M$ Film (nm)	ε at λ$_M$ x 10^4 (M^{-1}cm^{-1})	E$_g$ (eV)	HOMO (eV)	LUMO (eV)
26	630	664	9.10	2.04	-5.44	-3.4
25	633	656	5.53	1.68	-5.39	-3.71
35	621	633	6.20	1.86	-5.33	-3.47
34	624	666	5.58	1.71	-5.28	-3.57
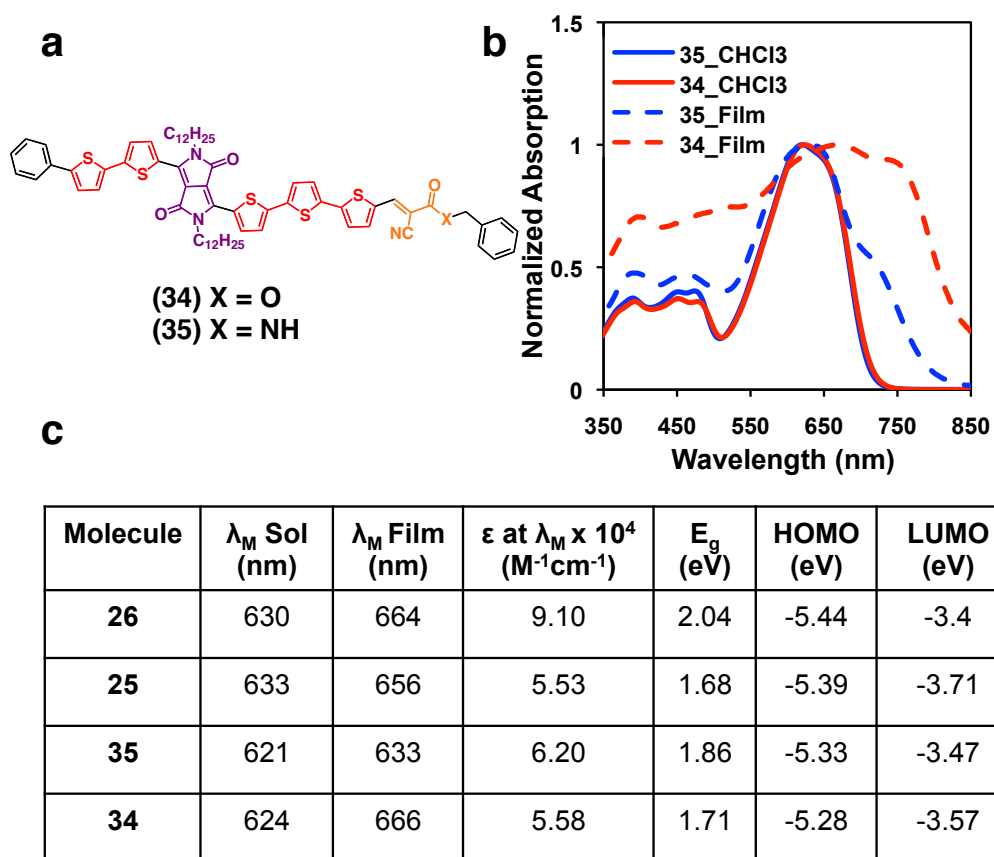
Figure 2.11. Molecular structure of **34-35**, their absorption spectrum (b) and table of electronic properties, comparing the optimized asymmetric and symmetric designs (c). Retrieved from Ref. 185.

Determination of Frontier Orbitals

The frontier molecular orbitals were calculated by performing cyclic voltammetry (CV) on films deposited on the working electrode from 10 mM CHCl$_3$ solutions. The HOMO and LUMO levels were calculated from the first oxidation and reduction potentials, respectively. The HOMO – LUMO gap (Eg) was determined from the orbital energy difference. Oxidation potentials are reported versus the nonaqueous reference electrode Ag/AgNO$_3$ and calibrated against the F$_c$/F$_c^+$ redox couple (assigned an energy level of -4.8 eV vs. vacuum).[186] The CV traces for all four molecules show

quasireversible oxidation waves in the region of 0.5-1 V. The reduction potentials occur in the -1 V region and present reversible behavior for all four molecules, but **26** presented a pre-reduction wave that made assigning a reduction potential difficult; for this reason, the difference in Eg reported in the manuscript for **26** and **25** is approximately 0.4 eV, even though their onset absorption would seem to indicate they should have nearly identical values for Eg (Figure 2.12).
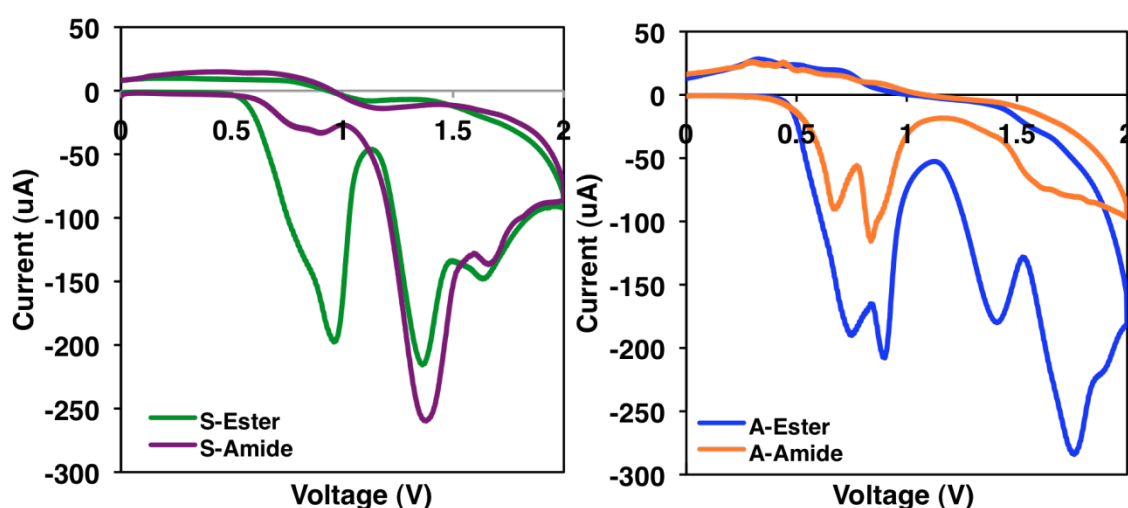
Figure 2.12. Cyclic voltammograms of molecules **25** (green on the left), **26** (purple on the left), **34** (blue on the right) and **35** (orange of the right). Retrieved from ref. 185.

The HOMO levels were determined by the equation HOMO = -4.8 + ($E_{oxFc/Fc+}$ - E_{oxM}) where $E_{oxFc/Fc+}$ and E_{oxM} are the onset oxidation potentials of ferrocene and M, where M = **26** (S-Amide), **25** (S-Ester), **35** (A-Amide), **34** (A-Ester), respectively. The LUMO levels were obtained by the equation LUMO = -4.8 + ($E_{oxFc/Fc+}$ - E_{RedM}), where E_{RedM} are the onset reduction potentials of M. In order for molecules to be stable in air, they need a HOMO of at least -5.2 eV or lower, and in this case, all four molecules fulfilled the requirements. Interestingly, molecules **5**-**6** also had safe HOMO levels, but

the instability in that case was not due to air, but rather due to redox reactions happening in the active layer. For the four molecules published, the summarized electronic properties are shown in Figure 2.11c.

Evidence of H-bonding

The presence of hydrogen bonding was established using FTIR spectra of films cast from 10 mM $CHCl_3$ solutions on an ATR Ge crystal (Figure 2.13). Hydrogen bonding can be detected by FTIR when the C=O and N-H stretching vibrations shift to lower wavenumbers when hydrogen bonding is present. The C=O stretch could not be unambiguously assigned, as three peaks of similar intensity appear in the region of 1650 cm-1. The N-H stretching peak is the weak peak at 3440 cm-1 for **26** and 3360 cm^{-1} for **35 (**Figure 2.16**)**. Based the free NH stretching band at 3440 cm^{-1} for **26**, it was concluded that assemblies of this compound in the films do not h-bond significantly.[187] On the other hand, the NH stretching frequency of 3360 cm − 1 in the **35** indicates the presence of significant hydrogen bonding in these films.[153] Measurements on blends of $PC_{71}BM$ and the four molecules were also performed, and in this case the 1:1 D:A molecules were drop-cast from CB at 10 mg/mL. The N–H stretch peak in both **35** and **26** remained unchanged. Both ester versions, not surprisingly, show no ability to hydrogen bond. Although all amides were expected to be able to hydrogen bond, it is believed **26** was not able to do so because the π-π stacking dominated the assembly; also, the termini alkyl tails were branched, and being flexible, could have interfered with the otherwise favorable hydrogen bonding.
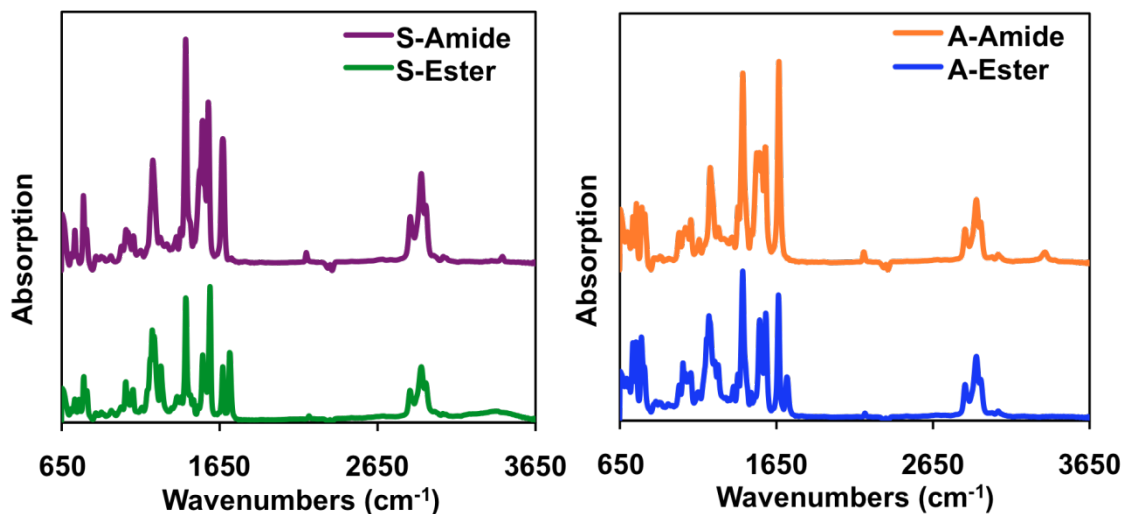
Figure 2.13. FTIR spectra of molecules **25** (green on the left), **26** (purple on the left), **34** (blue on the right) and **35** (orange of the right). Retrieved from ref. 185.

Device Performance

Photovoltaic devices from the four molecules were fabricated using donor/PC$_{71}$BM blends at 1:1 weight ratio in CB. Devices from the asymmetric molecules show superior performance compared to the symmetric ones. The PCE of **35** reached 3.65 ± 0.04%, significantly higher than **34** (1.45 ± 0.10%). Given that the pair of molecules **34**-**35** had similar frontier orbitals, the observed V$_{OC}$ was the same. Molecule **34** has slightly higher FF, but much lower J$_{SC}$ than **35**, which translates into lower PCE (Figure 2.14c). The difference in J$_{SC}$ can be directly observed by analyzing the EQE plot (Figure 2.14b). Ester **34** has lower EQE values at almost every wavelength than the amide **35**, and at λ$_{Max}$ 630 nm, the EQE value is ~ 20% for **34**, while it is 60% for **35**. The effect of solvent additives on device performance was also studied, and DIO was chosen again, because of its ability to dissolve PC$_{71}$BM selectively, while nitrobenzene was chosen because it is a non-solvent for both phases and improves the crystallinity.[110,188] For **35**, nitrobenzene (0.2 v/v%) resulted in improved FF and J$_{SC}$

values, which resulted in PCE values of 4.57± 0.13%, while DIO (0.2 v/v%) improved J_{SC} and FF in devices of **34**, reaching PCEs of 2.83 ± 0.20%. Interestingly, PCE did not significantly improve when the additives were switched (i.e nitrobenzene for **34** and DIO for **35**). Addition of a higher amount of solvent additives was observed to decrease the device performance. Under the best performing conditions, **35** shows 50% improvement in PCE compared to **34**, which stems mainly from superior J_{SC} and photon-to-electron conversion over the visible range. On the other hand, **34** has a higher FF value due to a larger R_{SH} compared to **35**. A higher R_{SH} is a sign of less charge recombination and fewer defects in the active layer.[189] However, a lower R_S for **35** is an indication of having lower intrinsic resistance in the active layer and a better morphology, assuming similar contact resistance due to similar energy levels.[190] Improvement in device morphology of **35** upon addition of nitrobenzene should increase hole mobility, which would explain the decrease in R_S. In addition, an increase in the hole mobility of devices from **35** can explain the higher device efficiency compared to **34**. The device hole mobilities were measured using the space charge limited current (SCLC) method, and the results support photovoltaic devices. Films of **35** have higher hole mobility (1.3 ± 0.5 × 10^{-5} cm^2/Vs) than those of **34** (6.4 ± 0.8×10^{-6} cm^2/Vs). A higher hole mobility can result in larger J_{SC} due to increased generation of free charge carriers, and higher FF values due to better conduction of charge carriers (refer to Figure 2.14c).
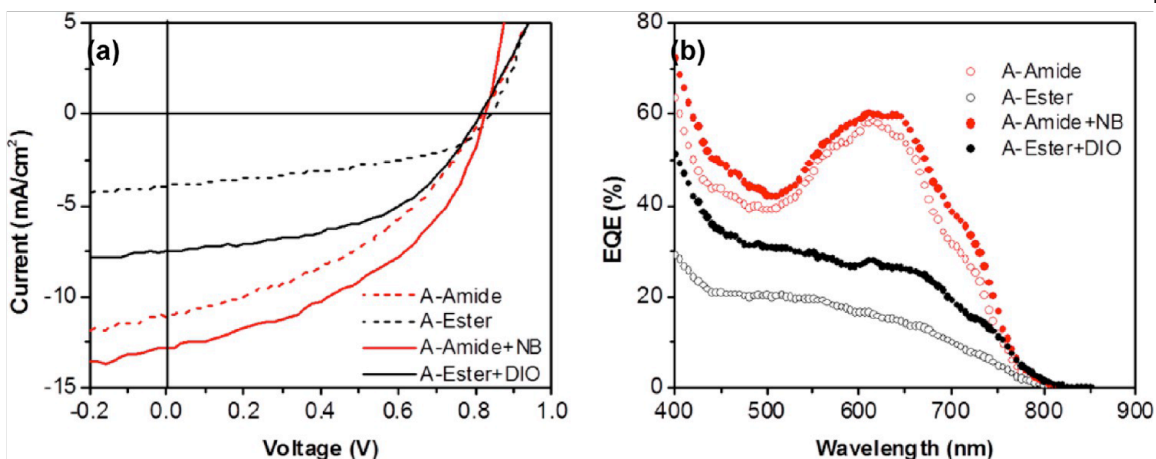
c

Device	V$_{OC}$ (V)	J$_{SC}$ (mA/cm^2)	FF (%)	PCE (%)	R$_{SH}$ (Ωcm^2)	R$_S$ (Ωcm^2)	μ$_h$ (cm^2/Vs^{-1})
35	0.82± 0.01	11.0±0.3	41±1	3.65± 0.04	-217± 13	23.3± 2.9	1.3±0.5 x10^{-5}
34	0.84± 0.01	3.9±0.2	44±1	1.45± 0.10	524± 10	39.7± 3.7	6.4±0.8 x10^{-6}
35+NB	621± 0	12.6±0.2	44±1	4.57± 0.13	215± 27	14.1± 2.2	3.2±0.6 x10^{-5}
34+DIO	624± 0	7.0±0.4	50±1	2.83± 0.20	570± 66	34.9± 5.6	1.1±0.3 x10^{-5}

Figure 2.14. a) J-V curve of molecules **34** (black line) and **35** (red line) and with the optimized additive (dashed lines, respectively); b) EQE spectra using the same color coding; c) table of optimized device results. Retrieved from ref. 185.

Morphological Studies

As pointed out earlier, optimized active layer morphology with a small domain size is extremely important for organic photovoltaic efficiency. Segregation of active layer components at the nanoscale is required to achieve high performance due to the limited exciton diffusion length in organic materials.[159] Thus, the nanoscale morphology of the photovoltaic devices was investigated with AFM and TEM. The AFM micrographs of the active layers of **35** and **34** show major differences in domain size. Films of **35** (Figure 2.15a) have a smoother surface with smaller features than **34**, which shows

large spherical aggregates (around 200 nm in Figure 2.15d), and this in turn explains the lower J_{SC} and PCE than **35**. The use of nitrobenzene as additive in films of **35** results in an interpenetrated morphology with reduced domain size, but the opposite happens when DIO is used (Figure 2.15b and c). Thus, the effect DIO has on PCE of devices made from **35** can be attributed to changes in domain size (larger domain sizes reduce J_{SC}). In the case of **34**, nitrobenzene does not improve morphology or device performance, while DIO improves both greatly (Figure 2.15e and f) by reducing the size aggregate size, yielding a more interpenetrated morphology.
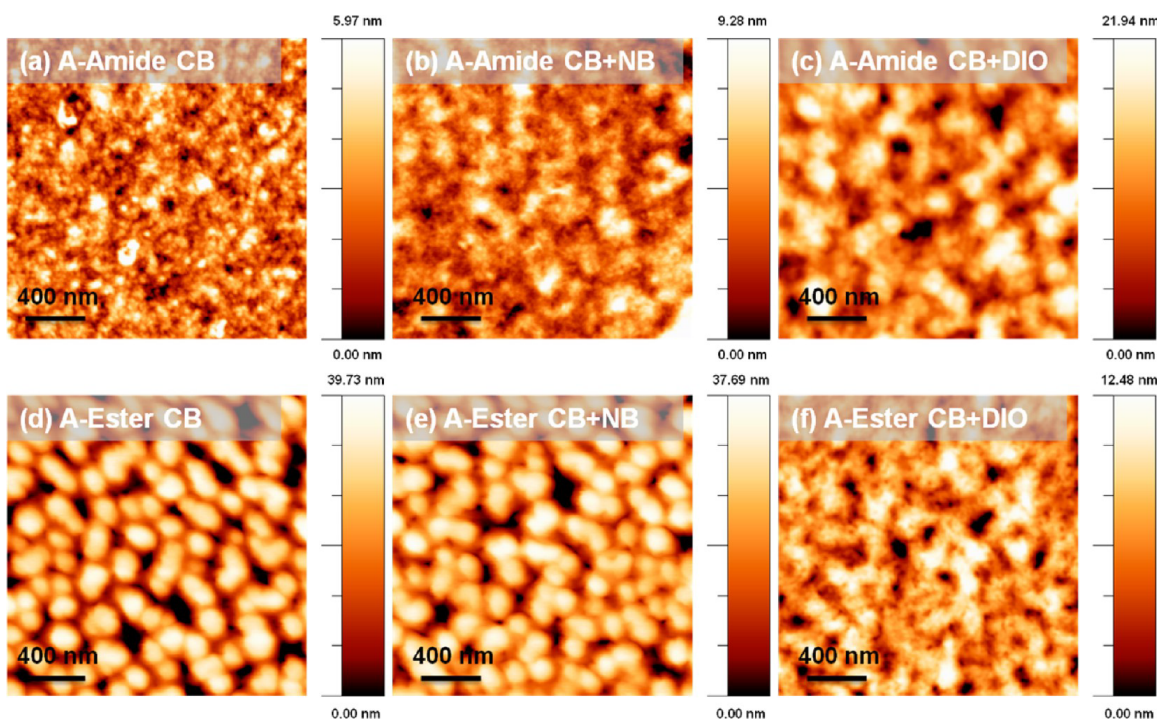
Figure 2.15. AFM images of molecules **34** (d-f) and **35** (a-c) under different processing conditions. Retrieved from ref. 185.

The thin films were also characterized with TEM, and just like it was observed in AFM, films of **35** cast from CB show small aggregates (**Figure 2.16**). In addition, the films show more connected domains with addition of NB and much larger domains with

DIO (Figure 2.16c). In the case of ester **34**, spherical aggregates observed in AFM appear as dark spots in TEM, which indicate aggregated $PC_{71}BM$ domains.[102] Once again, as observed by AFM in films of **34**, nitrobenzene increases aggregate size (200 – 300 nm), while DIO decreases it (Figure 2.16e and f, respectively).
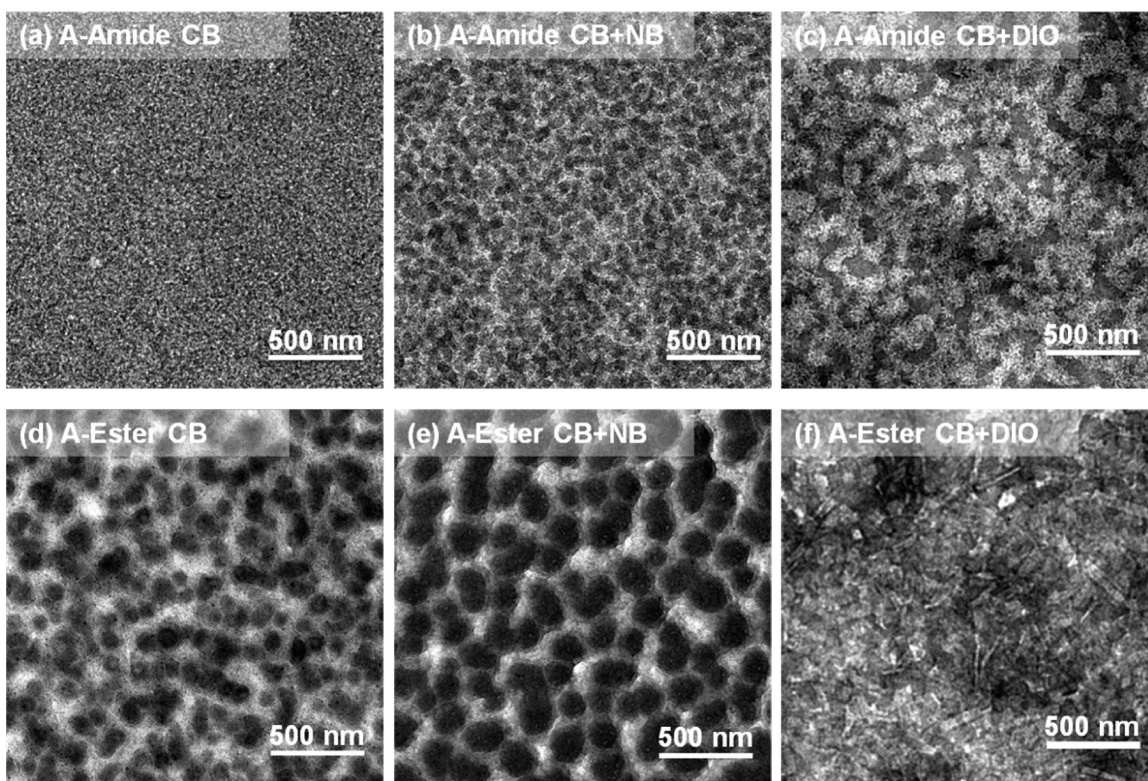
Figure 2.16. TEM images of molecules 34 (d-f) and 35 (a-c) under different processing conditions. Retrieved from ref. 185.

X-Ray Studies on the Morphology

Grazing incidence X-ray diffraction (GIXD) was used to determine the packing and orientation of molecules within the active layer (Figure 2.17). GIXD samples were prepared on silicon chips by spin coating donor/acceptor solutions with the same conditions used for devices. All samples were illuminated with X-ray for 1-2 s with an incident angle of 0.2°. The ring around 1.35 $Å^{-1}$ (0.47 nm) in all images corresponds to

the molecular dimensions of $PC_{71}BM$.[191] When cast from only CB, **34** and **35** show a significant difference in diffraction rings. In films of **35** alone (Figure 2.17a), the (100) ring can be observed around 0.45 $Å^{-1}$ (1.4 nm), which is the distance expected for alkyl groups on adjacent stacked molecules. The use of solvent additives only decreases slightly the alkyl-alkyl distance in **35** (Figure 2.17b and c). Films of **34** reveal higher crystallinity with the presence higher-order peaks for the (100) ring, which indicate a higher degree of stacking. The spacing corresponding to the (100) ring is very similar to that of **35** (~1.4 nm), which was not surprising given the similarity of the two molecules. The (010) peak observed in films of **34** around 1.73 $Å^{-1}$ (0.37 nm) is the characteristic spacing for π-π stacking (Figure 2.17d). Addition of nitrobenzene does not change the shape or position of the rings in films of **34**, but DIO appears to induce diffraction at certain angles and loss of circular shape of the rings (Figure 2.17e and f). This edge-on crystalline order is characteristic of most organic semiconductors including polythiophene.[105] GIXD results were analyzed in order to quantitatively compare the differences between the active layers.
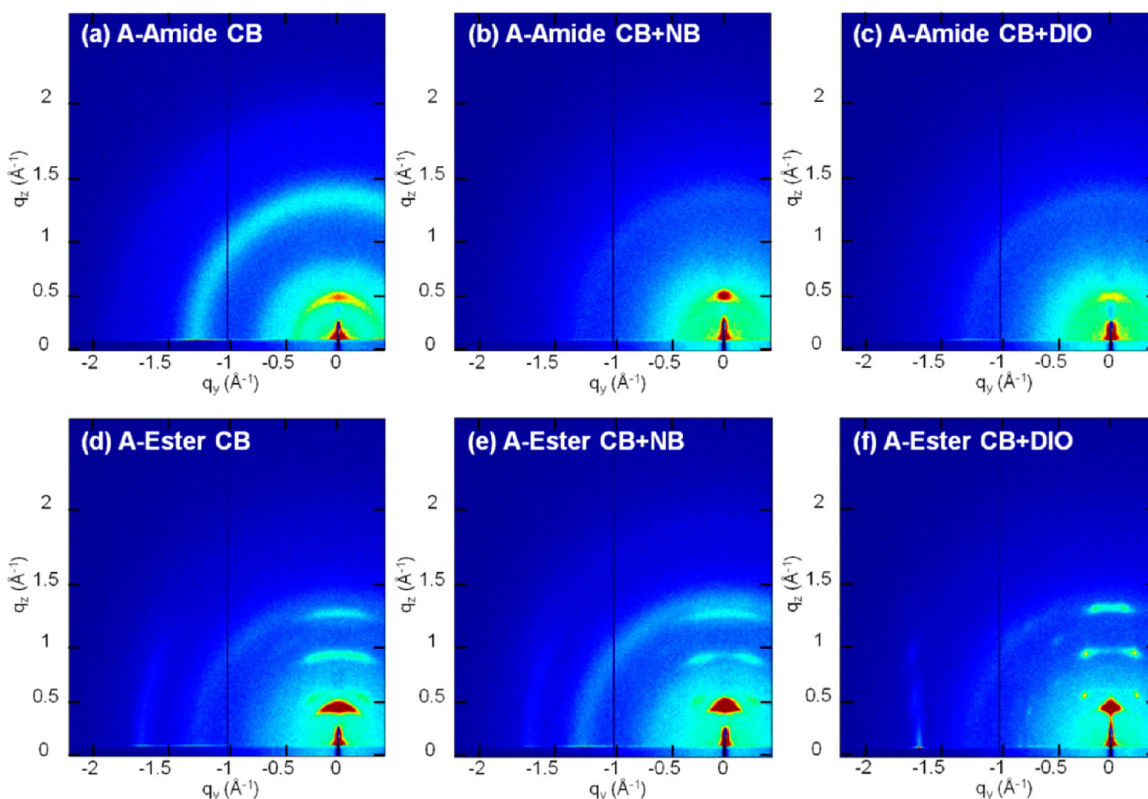
Figure 2.17 GIWAXS scattering patterns of molecules **34** (d-f) and **35** (a-c) under different conditions. Retrieved from ref. 185.

The quantitative data for paracrystallinity (g), crystal size (La), and Herman's orientation parameter (S) are shown in Table 2.3. Values for g and La were calculated using three rings when available, and otherwise they were calculated using only one ring as previously described.[192] In the g scale, 0% corresponds to a perfect crystal, 10% to a paracrystal, and 100% corresponds to a gaseous state with maximum disorder.[193,194] For g(100), the amide **35** is more amorphous (crystal size of 7 – 8 nm) than **34** (crystal size up to 18 nm). Solvent additives affect crystallinity in the alkyl stacking direction; nitrobenzene improves the crystallinity of **35** slightly, while DIO maximizes crystallinity of the **34**. DIO also enhances the π–π stacking of **34** and results in a smaller g(010) value and higher La(010) value. Although DIO has previously been

shown to increase crystallinity for DPP-based polymers,[195] in the case of amide **35**, it does not, mainly because aggregation is dominated by H-bonding. The greater crystallinity of **34** upon DIO addition is likely the reason for the higher FF and J_{SC} values observed. The orientation of (100) rings was also assessed with the S parameter. S scales lie in the range of 1 to −0.5, 1 being completely in-plane, 0 being isotropic, and −0.5 being out-of-plane.[196] Films of **35** have S values of 0.4–0.5, which indicate an alkyl–alkyl stacking orientation between isotropic and in-plane. Films of **34**, on the other hand, have S values of 0.8 and higher, which indicate more stacking in-plane direction.

Table 2.3. Table of paracrystallinity parameters calculated for molecules **34** and **35**. Retrieved from ref. 185.

Film	$g_{(100)}$ (%)	$La_{(100)}$ (nm)	$g_{(010)}$ (%)	$La_{(010)}$ (nm)	$S_{(100)}$ Orientation
35_CB	15.9	7.1	N/A	N/A	0.36
35_CB+NB	14.3	8.6	N/A	N/A	0.52
35_CB+DIO	15.9	7.0	N/A	N/A	0.48
34_CB	8.7	15,2	8.9	6.4	0.83
34_CB_NB	8.5	18.3	8.8	6.6	0.81
34_CB_DIO	7.6	16.3	6.5	12.2	0.79

It is surprising that the more amorphous **35** blends result in better performing devices. Although the initial intention of the project was fulfilled, i.e. to use H-bonding to improve photovoltaic device efficiency, these results contradict recent studies using similar end groups, where the performance is lowered due to a molecule's ability to

hydrogen bond.[159,160] It has been suggested that the most important feature for device performance is the presence of interconnected aggregates, even if they are small and disordered.[135] For this system, molecules of **35** can assemble into short fiber-like structures (especially after nitrobenzene addition) that are interconnected over longer distances, which can help with charge transport across the film. Another recent study has shown that amorphous donor domains can form better (more diffuse) interfaces with amorphous PCBM domains and enhance the charge separation.[197] For that reason, the use of molecules that are weakly crystalline yet possess some aggregation tendency (in this case through H-bonding) can be favorable for solar cell active layers.

To conclude, this chapter presented a series of symmetric and asymmetric DPP-based donors with and without the ability to h-bond and and the effect that this would cause on solar cell active layer morphologies and device performance. In general, while the optoelectronic properties of amide and ester derivatives were found to be similar in solution, the behavior on film was different, and much more in asymmetric derivatives than symmetric ones. The morphological differences in solar cell active layers were attributed to H-bonding interactions. It was concluded that H-bonding interactions compete effectively with long-range π–π stacking of the conjugated molecules, which results in interconnected and smaller nanoscale donor domains relative to the ester derivatives. This effect nearly doubles the efficiency of solar cells containing **35** as opposed to **34**. Given that π–π stacking is a ubiquitous interaction in organic photovoltaics that can generate long-range crystallinity, the general strategy of a competing intermolecular interaction is a valuable strategy to optimize function.

2.8 Synthesis and Additional Information

Synthetic Methods

Unless otherwise specified, all reagents were used without further purification. 2-phenylthiophene, butyllithium, tributyltin chloride, 2-butyl-1-octanol, p-tolunesulfonyl chloride, benzyl cyanoacetate, cyanoacetic acid, N-methylpiperazine, tetrakistriphenylphosphine palladium [Pd(PPh3)4], triphenylphosphine, anhydrous acetonitrile, anhydrous dimethylsulfoxide (DMSO), sodium azide, triethylamine (NEt$_3$) and piperidine (vacuum distilled over NaOH pellets and stored under nitrogen) were obtained from Sigma-Aldrich; 2-2-bithiophene carboxaldehyde was obtained from TCI America; N-benzyl-2-cyanoacetate was obtained from Santa Cruz Biotechnology; dimethylformamide (DMF), dichloromethane (DCM), hexanes, ethyl acetate (EtOAc) and hydrochloric acid (HCl) were obtained from Avantor Performance Materials; pyridine was obtained from Alfa Aesar; CHCl$_3$, tetrahydrofuran (THF) and methanol (MeOH) were obtained from BDH; 1- Ethyl-3-(3 dimethylaminopropyl)carbodiimide (EDC) and hydroxybenzotriazole hydrate (HOBt) were obtained from Advanced Chemtech. 4-(Dimethylamino)pyridinium-4 toluenesulfonate (DPTS) was prepared according to previously published procedure. Anhydrous solvents were degassed on a Vacuum Atmospheres 103991 system. Proton NMR spectra were performed on a Varian Inova 500 or Agilent DD MR-400 with working frequencies of 500 and 400 Mhz, respectively. Carbon NMR spectra were obtained using a Bruker Avance III 500 spectrometer, with working frequency of 125.6 MHz for ^{13}C nuclei. Chemical shifts are reported in parts per million (ppm) and referenced to the residual nondeuterated solvent frequencies (CDCl$_3$: δ 7.26 ppm for 1H, δ 77.36 ppm for ^{13}C). High-resolution mass

spectra were recorded on an Agilent Model 6210 LC-TOF multimode ionization (MMI) or a Bruker Autoflex III MALDI mass spectrometers. Ultraviolet−visible (UV-vis) spectra were recorded on a Perkin Elmer LAMBDA 1050 spectrophotometer. Cyclic voltammetry was performed using an EG&G Princeton Applied Research Potentiostat (Model 263A), using a three- electrode system, with a Au disk working electrode, Pt wire counter electrode, a $Ag/AgNO_3$ non-aqeous reference electrode (Bioanalytical Systems, Inc., models MF-2014, mF-2062 and MW-1032, repectively). Working electrodes were polished with a suspension of aluminum particles and on a nylon pad (Bioanalytical Systems, Inc. model MF-2060). Infrared spectra were obtained using a Thermo Nicolet, Nexus 870 spectrometer. Photovoltaic measurements were done while the devices were illuminated by an Oriel Xe solar simulator equipped with and Oriel 130 monochromator and a Keithley 2400 source meter. Filters were used to cut off grating overtones. The solar spectrum was simulated using an AM 1.5 filter with 100 mW/cm_2 power density. A calibrated silicon reference solar cell with a KG5 filter certified by the National Renewable Energy Laboratory was used to confirm the measurement conditions. AFM characterization was performed using a Bruker Dimension ICON atomic force microscope (Bruker Co.) at ambient conditions. Tapping mode was utilized with single-beam silicon cantilevers with a nominal oscillation frequency of 300 kHz. Conventional TEM of the samples were imaged using Hitachi HT-7700 TEM at 80-100 kV. 2D-GIXD measurements were performed at Beamline 8ID of the Advanced Photon Source at Argonne National Laboratory. An x-ray wavelength of λ = 1.6868 Å was used and data were collected using a 1-2 s exposure at a sample-detector distance of 204 mm with a Pilatus photodiode array.

BrTDPPTBrC12 (1). Molecule **1** was synthesized following a previously published procedure.[174]

2TSnBu3 (2). Molecule **2** was synthesized following a previously reported procedure.[147]

3TDPPT3TC12 (3). A 250 mL oven-dried Schlenk flask containing **1** (0.400 g, 0.503 mmol), **2** (0.505 g, 1.11 mmol) and $Pd(PPh_3)_4$ (0.114 g, 0.0985 mmol) was degassed by three vacuum/nitrogen cycles. Degassed DMF (20 mL) was then injected into the flask and the solution mixture was stirred for 12 h at 100 °C under nitrogen. After cooling to room temperature, the reaction mixture was poured into water (300 mL) with brine (30 mL). The precipitate was filtered over Celite, washed with additional water (100 mL) and the Celite was then washed with DCM until the washings were faint blue color. Residual water was removed in a separatory funnel. DCM was removed under vacuum and the product was purified by column chromatography (DCM/Hexanes 1:1) to afford **3** as a dark blue solid (0.300 g, 62%). 1H-NMR (499 MHz; $CDCl_3$): δ 8.92 (d, J = 4.2 Hz, 2H), 7.29 (d, J = 4.1 Hz, 2H), 7.26 (q, J = 1.7 Hz, 2H), 7.22 (d, J = 3.8 Hz, 4H), 7.13 (d, J = 3.8 Hz, 2H), 7.05 (dd, J = 5.0, 3.7 Hz, 2H), 4.04 (d, J = 7.8 Hz, 4H), 1.99-1.95 (m, 2H), 1.38-1.21 (m, 32H), 0.86 (dt, J = 16.8, 6.9 Hz, 12H). MALDI-MS (m / z): $[M + H]^+$ calc for $C_{54}H_{64}N_2O_2S_6$ 965.3371, found 965.219.

CHO3TDPP3TC12 (4). A Vilsmeier reagent was prepared by adding phosphorus oxychloride (0.502 mL, 5.40 mmol) to anhydrous DMF (3 mL), and once the solution turned slightly red, the reagent was added to a solution of **3** in DMF (30mL) and heated overnight at 70 C°. After cooling to room temperature, 100 mL of dilute potassium carbonate was added and the mixture extracted in DCM. The DCM layer was collected and dried under vacuum. The product was isolated by column chromatography

(DMC/Hexanes 1:1) to obtain **4** as a dark green/blue solid (0.060 g, 17%). 1H-NMR (499 MHz; CDCl3): δ 9.87 (s, 1H), 8.95 (d, J = 4.2 Hz, 1H), 8.89 (d, J = 4.1 Hz, 1H), 7.68 (d, J = 3.9 Hz, 1H), 7.33 (d, J = 4.1 Hz, 1H), 7.31 (d, J = 3.9 Hz, 1H), 7.29-7.27 (m, 2H), 7.27-7.25 (m, 2H), 7.23-7.21 (m, 2H), 7.13 (d, J = 3.8 Hz, 1H), 7.05 (dd, J = 5.0, 3.6 Hz, 1H), 4.04 (d, J = 7.7 Hz, 4H), 1.98-1.96 (m, 2H), 1.35-1.31 (m, 11H), 1.28-1.25 (m, 22H), 0.89-0.88 (m, 6H), 0.84 (t, J = 6.7 Hz, 6H). MALDI-MS (m / z): $[M]^+$ calc for $C_{55}H_{64}N_2O_3S_6$ 992.3241, found 992.885.

3TDPP3TCNOBn (5). Compound **4** (0.080 g, 0.0806 mmol) dissolved in $CHCl_3$ (10 mL), then benzylcyanoacetate (0.144 mL, 0.940 mmol) and triethylamine (0.217 mL, 1.57 mmol) were then added and the solution was stirred at 70 °C for 12 hrs. After cooling to room temperature, the solution was diluted with DCM (100 mL) and washed with 1 M HCl (30 mL). The organic phase was collected and the solvent removed under vacuum. The product was purified by column chromatography (DCM) to afford the product as a dark green solid (xxx g, xx%). MALDI-MS (m / z): $[M + H]^+$ calc for $C_{65}H_{71}N_3O_4S_6$ 1150.3848, found 1150.305.

3TDPP3TNHBn (6). Compound **4** (0.060 g, 0.0604 mmol) dissolved in $CHCl_3$ (10 mL), then N-benzylcyanoacetamide (0.102 g, 0.585mmol) and triethylamine (0.164 mL, 1.18 mmol) were then added and the solution was stirred at 70 °C for 12 hrs. After cooling to room temperature, the solution was diluted with DCM (100 mL) and washed with 1 M HCl (xx mL). The organic phase was collected and the solvent removed under vacuum. The product was purified by column chromatography (2%MeOH/ DCM) to afford the product as a dark green solid (0.018g, 26%). 1H-NMR (499 MHz; CDCl3): δ 8.94 (t, J = 6.4 Hz, 1H), 8.90-8.89 (m, 1H), 8.38-8.37 (m, 1H), 7.62-7.61 (m, 1H), 7.40-7.36 (m, 2H),

7.35-7.31 (m, 4H), 7.31-7.28 (m, 1H), 7.26-7.24 (m, 3H), 7.23-7.20 (m, 2H), 7.14-7.11 (m, 1H), 7.05-7.04 (m, 1H), 6.55-6.52 (m, 1H), 4.60 (t, J = 4.9 Hz, 2H), 4.06-4.02 (m, 4H), 2.00-1.94 (m, 2H), 1.41-1.17 (m, 32H), 0.92-0.81 (m, 12H). MALDI-MS (m / z): [M + H]$^+$ calc for $C_{65}H_{72}N_4O_3S_6$ 1149.4008, found 1149.361.

SnBu32TCHO (7). was synthesized using a modified procedure from the literature. 2,2-Bithiophene-5-carboxaldehyde (0.5 g, 2.57 mmol) was placed in an oven-dried 250 mL Schlenk flask. The flask was degassed by three vacuum/nitrogen cycles. Anhydrous THF (30 mL) was injected and the solution was cooled to -78°C. N-methylpiperazine (0.313 mL, 2.83 mmol) was then injected, followed by n-butyllithium (1.13 mL, 2.5M in hexane, 2.83 mmol), after which the reaction was stirred for 20min. The reaction was then warmed to -20°C, followed by a second addition of n-butyllithium (1.13 mL, 2.5M in hexane, 2.83 mmol) and left stirring for another 30 min. Tributyltin chloride was then added (0.831 mL, 3.08 mmol) and the cooling bath was removed. After warming to room temperature, the reaction was quenched with 1 M HCl 135 (20 mL). The crude was concentrated under vacuum, diluted in water (200 mL) and extracted with hexanes. The organic phase was separated and dried over magnesium sulfate (MgSO4), followed by solvent removal under vacuum. Column chromatography in 1:1 DCM/hexanes afforded **7** as a yellow liquid (1.05 g, 85%). 1H-NMR (500 MHz; CDCl3): δ 9.85 (s, 1H), 7.66 (d, J = 4.0 Hz, 1H), 7.47 (d, J = 3.4 Hz, 1H), 7.25 (d, J = 4.0 Hz, 1H), 7.11 (d, J = 3.4 Hz, 1H), 1.61-1.54 (m, 6H), 1.35 (m, 6H), 1.15-1.12 (m, 6H), 0.91 (t, J = 7.3 Hz, 9H). 13C-NMR (126 MHz; CDCl3): δ 183.0, 147.9, 141.61, 141.53, 141.3, 137.9, 136.9, 127.6, 124.3, 29.3, 27.6, 14.0, 11.3 HRMS calc m/z for $C_{21}H_{32}OS_2Sn$: [M+H]+ 485.0997, found 485.0993.

CHO3TDPP3TCHOC12 (8). In a 250 mL oven-dried Schlenk flask, 1 (0.240 g, 0.302 mmol), 2 (0.321 g, 0.664 mmol) and $Pd(PPh_3)_4$ (0.068 g, 0.0601 mmol) were placed. The flask was then degassed by three vacuum/nitrogen cycles. Degassed DMF, 40 mL was then injected into the flask and the solution mixture was stirred for 12h at 120 °C under nitrogen. After cooling to room temperature, the reaction mixture was poured into water (300 mL) with brine (30 mL). The precipitate was filtered over Celite, washed with additional water (100 mL) and the Celite was then washed with DCM until the washings were faint blue color. Residual water was removed in a separatory funnel. DCM was removed under vacuum and the product was purified by column chromatography (100% DCM) to afford **8** as a dark green solid (0.229 g, 74%). 1H-NMR (500 MHz; CDCl3): δ 9.78 (s, 2H), 8.84 (d, J = 4.1 Hz, 2H), 7.59 (d, J = 3.9 Hz, 2H), 7.22 (d, J = 3.9 Hz, 4H), 7.17 (t, J = 4.5 Hz, 4H), 3.95 (d, J = 7.6 Hz, 4H), 1.87 (m, 2H), 1.27-1.17 (m, 36H), 0.82-0.77 (m,12H). 13C-NMR (126 MHz; CDCl3): δ 182.7, 161.7, 146.4, 142.4, 141.8, 139.5, 137.9, 137.7, 137.1, 136.6, 129.2, 127.4, 126.3, 125.6, 124.8, 109.0, 46.6, 38.3, 32.2, 31.7, 31.4, 30.1, 28.9, 26.7, 23.5, 23.0,14.5 HRMS calc m/z for C56H64N2O4S6: 1020.319, found 1020.317.

BnCNO3TDPP3TC12 (9). Compound **8** (0.254 g, 0.249 mmol) was dissolved in $CHCl_3$ (30 mL), then benzylcyanoacetate (0.152 mL, 0.996 mmol) and triethylamine (0.347 mL, 2.49 mmol) were then added and the solution was refluxed for 12 hrs. After cooling to room temperature, the solution was diluted with DCM (100 mL) and washed with 1 M HCl (30 mL). The organic phase was collected and the solvent removed under vacuum. The product was purified by column chromatography (1%EtOAc in DCM) to afford the product as a dark green solid (0.060 g, 18%). MALDI-MS (m / z): $[M]^+$ calc for

C76H78N4O6S6 1334.4246, found 1334.507.

BnCNNH3TDPP3TC12 (10). Compound **8** (0.139 g, 0.136 mmol) was dissolved in CHCl$_3$ (20 mL), then N-benzylcyanoacetamide (0.142 g, 0.814 mmol) and piperidine (0.190 mL, 1.36 mmol) were then added and the solution was stirred at 70 °C for 12 hrs. After cooling to room temperature, the solution was diluted with DCM (100 mL) and washed with 1 M HCl (30 mL). The organic phase was collected and the solvent removed under vacuum. The product was purified by column chromatography (first EtOAc, then 4:1 DCM/EtOAc) to afford the product as a dark green solid (0. 0112 g, 11%). ^{1}H-NMR (500 MHz; CDCl$_3$): MALDI-MS (m / z): [M + H]+ calc for C76H80N604S6 1333.4664, found 1333.058.

GACOOMe (11). Molecule **11** was prepared according to a previously published procedure.[153]

GACOH (12). Molecule **11** (2.00 g, 2.90 mmol) was dissolved in anhydrous THF (10 mL), then a solution of lithium aluminum hydride (2M in THF, 1.45 mL, 2.90 mmol) was added dropwise and the reaction was left stirring for one hour. Water (5mL) and 1M HCl (5 mL) were then added slowly and the reaction was concentrated under vacuum. The crude was then diluted with water (100 mL) and extracted in DCM. The DCM layer wa then collected, dried with MgSO4 and the solvent evaporated under vacuum to give **11** as a waxy white solid (2.168 g, 99%). 1H-NMR (499 MHz; CDCl3): δ 6.56 (s, 2H), 4.59 (s, 2H), 1.49-1.44 (m, 6H), 1.36-1.25 (m, 30H), 0.89 (t, J = 6.9 Hz, 9H). HRMS-ESI (m / z): [M + H]+ calc for C43H8004 661.6136 m/z , found 661.6132

GACOCOCN (13). Cyanoacetic acid (0.125 g, 1.47 mmol) was dissolved in DCM (15 mL), then triethylamine was added (0.205 mL, 1.47 mmol), followed by EDC (0.281 g,

1.47 mmol) and DMAP (0.180 g, 1.47 mmol). The solution was stirred for 2 minutes before adding compound **12** (0.647 g, 0.979 mmol) in DCM (5 mL). The reaction as left stirring overnight at room temperature. The solvent was then evaporated and molecule **13** isolated by column chromatography (DCM) as a waxy white solid (0.670 g, 94%). 1H-NMR (499 MHz; CDCl3): δ 6.56 (s, 2H), 6.56 (s, 2H), 5.12 (s, 2H), 5.12 (s, 2H), 3.96 (dt, *J* = 9.2, 6.6 Hz, 6H), 3.49 (s, 2H), 3.49 (s, 2H), 1.81-1.72 (m, 6H), 1.46 (q, *J* = 7.6 Hz, 6H), 1.46 (q, *J* = 7.6 Hz, 6H), 1.37-1.27 (m, 50H), 1.37-1.27 (m, 50H), 0.89 (t, *J* = 6.9 Hz, 8H), 0.89 (t, *J* = 6.9 Hz, 8H). MALDI-MS (m / z): [M]+ calc for $C_{46}H_{81}NO_5$ 727.6115, found 727.576

GACCI (14). Compound **12** (1.005 g, 1.53 mmol) and tryethylamine (1.07 mL, 7.65 mmol) were dissolved in DCM (15 mL), then a solution of thionyl chloride (0.222 mL, 3.05 mmol) in DCM (5 mL) was slowly added and the reaction was heated at 40 C for 2 hours. After cooling to room temeperature, water was added and the mixture was extracted. The DCM layer was collected and dried under vacuum. A silica plug (DCM) afforded **14** as a waxy light-yellow solid (0.840 g, 81%) 1H-NMR (499 MHz; CDCl3): δ 6.58 (s, 2H), 4.52 (s, 2H), 3.96 (dt, *J* = 14.3, 7.0 Hz, 6H), 1.80 (t, *J* = 7.5 Hz, 3H), 1.75 (dd, *J* = 16.0, 8.7 Hz, 3H), 1.47 (q, *J* = 7.6 Hz, 6H), 1.37-1.27 (m, 53H), 0.89 (t, *J* = 6.9 Hz, 9H). MALDI-MS (m / z): [M]+ calc for $C_{43}H_{79}ClO_3$ 678.5718, found 678.503

GACN3 (15). Compound **14** (2.58 g, 3.81 mmol) was dissolved in DMSO (10 mL), then sodium azide (0.372 g, 5.72 mmol) was added and the suspension was left stirring overnight at 70 C. Water was then added (300 mL) and the mixture extracted in EtOAc (100 mL). The organic layer was collected, dried over MgSO4 and the solvent removed to afford **15** as a white waxy solid (1.51 g, 58%). 1H-NMR (499 MHz; CDCl3): δ 6.48 (s,

2H), 4.24 (s, 2H), 3.96 (dt, *J* = 13.4, 6.7 Hz, 6H), 1.81-1.72 (m, 6H), 1.46 (q, *J* = 7.6 Hz, 6H), 1.36-1.26 (m, 54H), 0.88 (t, *J* = 6.9 Hz, 9H). HRMS−ESI (m / z): [M + Na]+ calc for C43H79N3O3 708.6019, found 708.6022

GACNH2 (16). Compound **15** (1.51 g, 2.21 mmol) was dissolved in THF/H2O (10:1), then triphenylphosphine (0.696 g, 2.65 mmol) was added and the solution was left refluxing for 12 hrs. After cooling to room temperature, the solvent was removed under vaccum, and compound **16** was isolated by column chromatography (5% MeOH, DCM, then 10% MeOH/DCM) as a waxy white solid (1.13 g, 78%). 1H-NMR (499 MHz; CDCl3): δ 6.56 (s, 2H), 3.94 (dt, *J* = 21.9, 6.5 Hz, 7H), 3.84 (s, 2H), 1.80-1.72 (m, 6H), 1.47-1.43 (m, 6H), 1.32-1.27 (m, 53H), 0.88 (t, *J* = 6.9 Hz, 9H). MALDI-MS (m / z): [M]+ calc for C43H81NO3 659.6216, found 659.611

GACNHCOCN (17). Cyanoacetic acid (0.146 g, 1.70 mmol) was dissolved in DCM (15 mL), then triethylamine was added (0.476 mL, 3.42 mmol), followed by EDC (0.393 g, 2.05 mmol) and HOBt (0.314 g, 2.05 mmol). The solution was stirred for 2 minutes before adding compound **16** (1.13 g, 1.71 mmol) in DCM (5 mL). The reaction as left stirring overnight at room temperature. The solvent was then evaporated and molecule **17** isolated by column chromatography (1% MeOH/DCM) as a white solid (0.700 g, 56%). 1H-NMR (400 MHz; CDCl3): δ 6.68 (s, 1H), 6.34 (s, 2H), 4.28 (d, *J* = 5.5 Hz, 2H), 3.88 (q, *J* = 6.4 Hz, 5H), 3.38 (s, 2H), 1.83-1.66 (m, 6H), 1.44-1.21 (m, 42H), 0.86 (d, *J* = 13.7 Hz, 7H). HRMS−ESI (m / z): [M + H]+ calc for C46H82N2O4 727.6354, found 727.6344

GAOCO3TDPP3TC12 (18). Compound **13** (0.670 g, 0.920 mmol) and **8** (0.365 g, 0.357 mmol) were dissolved in CHCl₃ (30 mL), then piperidine (0.177 mL, 1.79 mmol) was

added and the solution was stirred at 70 °C for 12 hrs. After cooling to room temperature, the solution was diluted with DCM (100 mL) and washed with 1 M HCl (30 mL). The organic phase was collected and the solvent removed under vacuum. The product was purified by column chromatography (DCM) to afford the product as a dark green solid (0. 353 g, 40%). 1H-NMR (400 MHz; CDCl3): δ 8.90 (d, J = 4.2 Hz, 2H), 8.22 (s, 2H), 7.62 (dd, J = 3.1, 0.8 Hz, 2H), 7.31-7.28 (m, 4H), 7.24-7.22 (m, 3H), 6.61 (s, 4H), 5.20 (s, 5H), 4.10 (q, J = 7.1 Hz, 9H), 4.02-3.92 (m, 16H), 1.82-1.71 (m, 14H), 1.49-1.42 (m, 13H), 1.33-1.22 (m, 123H), 0.84 (dt, J = 15.9, 7.5 Hz, 26H). MALDI-MS (m / z): [M]+ calc for $C_{148}H_{222}N_4O_{12}S_6$ 2439.5209, found 2439.694.

GANHCO3TDPP3TC12 (19). Compound **17** (0.720 g, 0.963 mmol) and **8** (0.230 g, 0.225 mmol) were dissolved in $CHCl_3$ (30 mL), then piperidine (0.476 mL, 4.81 mmol) was added and the solution was stirred at 70 °C for 12 hrs. After cooling to room temperature, the solution was diluted with DCM (100 mL) and washed with 1 M HCl (30 mL). The organic phase was collected and the solvent removed under vacuum. The product was purified by column chromatography (30% EtOAc/Acetone, then DCM) to afford the product as a dark green solid (0. 369 g, 67%). 1H-NMR (400 MHz; CDCl3): δ 8.89 (d, J = 4.2 Hz, 2H), 8.35 (s, 2H), 7.59 (d, J = 4.1 Hz, 2H), 7.29 (d, J = 2.0 Hz, 5H), 7.22 (t, J = 5.0 Hz, 3H), 6.49 (s, 4H), 6.49-6.46 (m, 3H), 4.46 (d, J = 5.6 Hz, 4H), 3.95 (dd, J = 12.5, 6.3 Hz, 11H), 1.95-1.92 (m, 3H), 1.81-1.69 (m, 15H), 1.49-1.39 (m, 16H), 1.33-1.22 (m, 145H), 0.90-0.80 (m, 32H). MALDI-MS (m / z): [M]+ calc for $C_{148}H_{224}N_6O_{10}S_6$ 2437.5528, found 2437.292.

CNCOBuOc (20). In a 250 mL flask, cyanoacetic acid (1.37 g, 16.1 mmol) was suspended in DCM (10 mL), then 4-(dimethylamino)pyridinium-4-toluenesulfonate

(DPTS, 4.83 g, 16.1 mmol) was added. Once all acid was dissolved, EDC (3.09 g, 16.1 mmol) was added. After approximately one minute, a solution of 2-butyl-1-octanol (2 g, 10.73 mmol) in DCM (5 mL) was added in one portion, after which the reaction was left stirring for 12 h. The crude was diluted with DCM, and extracted with water. After collecting the organic phase, the solvent was removed under vacuum and the product was purified by column chromatography (20% EtOAc/hexane) to give **20** as a colorless liquid (2.60 g, 96%). 1H-NMR (500 MHz; CDCl3): δ 4.12 (d, J = 5.8 Hz, 2H), 3.46 (s, 2H), 1.67 (m, 1H), 1.34-1.27 (m, 16H), 0.89 (q, J = 7.0 Hz, 6H). 13C-NMR (126 MHz; CDCl3): δ 163.4, 113.3, 77.4, 70.1, 37.5, 32.1, 31.3, 31.0, 29.9, 29.2, 26.9, 25.1, 23.3, 23.0, 14.45, 14.39 HRMS calc m/z for C15H27NO2: [M+Na]+ 276.1934, found 276.1931.

TsBuOct (21). In a 250 mL flask, 2-butyl-1-octanol (20 g, 107 mmol) was dissolved in 40 mL of pyridine and cooled to 0 °C. p-Toluenesulfonyl chloride (19.4 g,102 mmol) was then added and the solution was left stirring for 12 h. The crude was poured onto 150 mL of 4 M HCl and extracted with hexane. The organic phase was dried over MgSO4, and the solvent was removed under vacuum to afford **21** as a colorless liquid (34.88g, 96%).1H-NMR (500 MHz; CDCl3): δ 7.79 (d, J = 8.3 Hz, 2H), 7.34 (d, J = 8.0 Hz, 2H), 3.91 (d, J = 5.3 Hz, 2H), 2.45 (s, 3H), 1.58 (m, 1H), 1.25-1.11 (m, 16H), 0.85 (m, 6H). 13C-NMR (126 MHz; CDCl3): δ 144.9, 133.4, 130.1, 128.3, 73.2, 37.9, 32.1, 30.9, 30.6, 29.8, 29.0, 26.8, 23.2, 23.0, 22.0, 14.45, 14.34 HRMS calc m/z for C19H32O3S: [M+Na]+ 363.1964, found 363.1964.

BuOcN3 (22). In a 100 mL flask, **21** (5 g, 14.68 mmol) was dissolved in DMSO (20 mL); sodium azide was then added (1.91 g, 29.4 mmol) and the solution was heated to 70 °C

for 12 h. After cooling to room temperature, the crude was diluted with water (200 mL) and extracted with ethyl acetate. The organic phase was collected, dried over MgSO4, and the solvent was removed under vacuum to afford **21** as a colorless liquid (3.10 g, 99%). 1H-NMR (500 MHz; CDCl3): δ 3.23 (d, J = 5.9 Hz, 2H), 1.55 (m, 1H), 1.28 (m, 16H), 0.91-0.88 (m, 6H). 13C-NMR (126 MHz; CDCl3): δ 55.3, 38.2, 31.85, 31.79, 31.5, 29.6, 28.9, 26.6, 23.0, 22.7, 14.15, 14.11 HRMS not possible due to sample fragmentation under several conditions. Elemental analysis: C: calc 68.20%, found 67.85±1.5%; N: calc 19.88%, found 19.79±1.3%.

BuOctNH2 (23). In a 100 mL flask, **22** (3.10 g, 14.68 mmol) and triphenylphosphine (4.62 g, 17.6 mmol) were dissolved in THF (20 mL). The solution was heated at 70 °C for 12 h, then 5 mL of water were added and the solution was left stirring for another hour. After cooling to room temperature, the crude was concentrated under vacuum, diluted with water and extracted with DCM. The product was purified by column chromatography (5% MeOH/DCM, then 5% MeOH/ 5% NEt$_3$/ DCM) to afford **23** as a colorless liquid (2.44 g, 90%). 1H-NMR (500 MHz; CDCl3): δ 2.60 (d, J = 5.2 Hz, 2H), 1.45 (m, 2H), 1.26 (m, 16H), 0.91 (m, 6H). 13C-NMR (126 MHz; CDCl3): δ 45.5, 41.1, 32.3, 31.9, 31.6, 31.3, 30.1, 29.3, 27.1, 23.5, 23.0, 14.5 HRMS calc m/z for C12H27N: [M+H]+ 186.2223, found 186.2216.

CONHBuOct (24). In a 250 mL flask, cyanoacetic acid (1.38 g, 16.1 mmol) was suspended in DCM (10 mL), then Et3N (2.25 mL, 16.2 mmol) was added. Once all acid was dissolved, EDC, (3.1 g, 16.2 mmol) and HOBt (1.65 g, 16.2 mmol) were added in succession. After approximately one minute, a solution of 10 (2 g, 10.78 mmol) in DCM (5 mL) was added in one portion, after which the reaction was left stirring for 12 h. The

crude was diluted with DCM, and extracted with water. After collecting the organic phase, the solvent was removed under vacuum and the product was purified by column chromatography (1% MeOH/DCM) to give **24** as a clear yellow liquid (2.55 g, 94%). 1H-NMR (500 MHz; CDCl3): δ 6.04 (s, 1H), 3.38 (s, 2H), 3.24 (t, J = 6.0 Hz, 2H), 1.53 (m, 1H), 1.27 (m, 16H), 0.89 (m, 6H). 13C-NMR (126 MHz; CDCl3): δ 161.0, 115.2, 77.4, 44.0, 38.1, 32.13, 32.04, 31.7, 29.9, 29.1, 26.9, 26.2, 23.3, 23.0, 14.45, 14.40 HRMS calc m/z for C15H28N2O: 252.2202, found 252.2199.

S-Ester (25). 8 (0.110 g, 0.108 mmol) was placed in a 100 mL flask and dissolved in CHCl3 (20 mL). **20** (0.068mL, 0.268 mmol) and piperidine (0.106 mL, 1.08 mmol) were then added and the solution was stirred at 70 °C for 12 h. After cooling to room temperature, the solution was diluted with DCM (100 mL) and washed with 1 M HCl (30 mL). The organic phase was collected and the solvent removed under vacuum. The product was purified by column chromatography (DCM) to afford **25** as a dark green solid (0.120 g, 74%). 1H-NMR (500 MHz; CDCl3): δ 8.92 (d, J = 4.2 Hz, 2H), 8.21 (s, 2H), 7.64 (d, J = 4.1 Hz, 2H), 7.31 (d, J = 4.0 Hz, 2H), 7.28 (d, J = 4.1 Hz, 2H), 7.23 (d, J = 3.9 Hz, 4H), 4.19 (d, J = 5.8 Hz, 4H), 4.02 (d, J = 7.6 Hz, 4H), 1.95 (m, 2H), 1.76 (m, 2H), 1.34-1.24 (m, 64H), 0.88 (m, 24H). 13C-NMR (126 MHz; CDCl3): δ 163.4, 161.9, 146.6, 146.2,141.8, 139.7, 139.3, 138.2, 137.1, 136.3, 135.2, 129.4, 127.8, 126.5, 125.7, 125.0, 116.1, 109.1, 98.5, 46.7, 38.3, 37.6, 32.2, 31.64, 31.51, 31.36, 31.18, 30.08, 29.95, 29.2, 28.9, 27.0, 26.7, 23.46, 23.31, 23.02, 23.00, 14.5. HRMS calc m/z for C86H114N4O6S61490.706, found 1490.707.

S-Amide (26). 8 (0.120 g, 0.117 mmol) was placed in a 100 mL flask and dissolved in CHCl3 (20 mL). **24** (0.074 g, 0.293 mmol) and piperidine (0.116 mL, 1.17 mmol) were

then added and the solution was stirred at 70 °C for 12 h. After cooling to room temperature, the solution was diluted with DCM (100 mL) and washed with 1 M HCl (30 mL). The organic phase was collected and the solvent removed under vacuum. The product was purified by column chromatography (1%MeOH/ 1%Et3N/ DCM) to afford **26** as a dark green solid (0. 080 g, 46%). 1H-NMR (500 MHz; CDCl3): δ 8.93 (d, J = 4.2 Hz, 2H), 8.34 (s, 2H), 7.61 (d, J = 4.2 Hz, 2H), 7.34 (t, J = 3.9 Hz, 4H), 7.27 (d, J = 3.9 Hz, 2H), 7.25 (d, J = 4.0 Hz, 2H), 6.23 (t, J = 5.8 Hz, 2H), 4.04 (d, J = 7.6 Hz, 4H), 3.35 (t, J = 6.0 Hz, 4H), 1.96 (m, 2H), 1.62-1.58 (m, 2H), 1.24 (m, 64H), 0.91 (m, 24H). 13C-NMR (126 MHz; CDCl3): δ 161.9, 160.8, 145.2, 144.3, 141.9, 139.6, 138.6, 137.9, 137.1, 136.6, 135.6, 129.3, 127.5, 126.5, 125.8, 125.0, 117.7, 109.1, 100.0, 46.7, 44.3, 38.3, 32.19, 32.17, 31.82, 31.65, 31.4, 30.08, 29.97, 29.2, 29.0, 27.0, 26.7, 23.47, 23.34, 23.02, 23.00, 14.48, 14.44 HRMS calc m/z for $C_{86}H_{116}N_6O_4S_6$ 1488.738, found 1490.736.

BrTDPP3TCHOC12 (27). In a 250 mL oven-dried Schlenk flask, **1** (0.510 g, 0.642 mmol), **8** (0.310 g, 0.578 mmol) and $Pd(PPh_3)_4$ (0.073 g, 0.065 mmol) were placed. The flask was then degassed by three vacuum/nitrogen cycles. Degassed DMF (60 mL) was then injected into the flask and the solution mixture was stirred for 12h at 100 °C under nitrogen. After cooling to room temperature, the reaction mixture was poured into water (300 mL) with brine (30 mL). The precipitate was filtered over Celite, washed with additional water (100 mL) and the Celite was then washed with DCM until the washings were faint blue color. Residual water was removed in a separatory funnel. DCM was removed under vacuum and the product was purified by column chromatography (30%hexane/DCM) to afford **27** as a dark blue solid (0.230 g, 39%). 1H-NMR (400 MHz;

CDCl3): δ 9.87 (s, 1H), 8.89 (d, J = 4.2 Hz, 1H), 8.61 (d, J = 4.2 Hz, 1H), 7.68 (d, J = 4.0 Hz,1H), 7.32 (m, J = 11.7 Hz, 2H), 7.27 (d, J = 3.5 Hz, 1H), 7.25 (d, J = 4.2 Hz, 1H), 7.21 (d, J = 4.2 Hz, 1H), 4.01 (d, J = 7.7 Hz, 2H), 3.94 (d, J = 7.8 Hz, 2H), 1.90 (m, 2H), 1.26 (m, 32H), 0.85 (m, 12H). 13C-NMR (126 MHz; CDCl3): δ 182.8, 161.87, 161.68, 146.4, 142.4, 142.0, 140.2, 139.2, 137.84, 137.66, 137.1, 136.7, 135.5, 131.7, 131.5, 129.1, 127.5, 126.4, 125.7, 124.9, 119.2, 108.70, 108.62, 46.64, 46.60, 38.3, 38.1, 32.17, 32.11, 31.62, 31.45, 31.33, 31.17, 30.07, 30.01, 28.90, 28.71, 26.66, 26.47, 23.44, 23.39, 23.0, 14.46, 14.39. HRMS calc m/z for C47H59BrN2O3S4: 906.2592, found 906.2586.

PhTSnBu3 (28). Thianaphtene (2.00 g, 14.9 mmol) was placed in an oven-dried 100 mL Schlenk flask and degassed by three vacuum/nitrogen cycles. Anhydrous THF (30 mL) was injected and the solution was cooled to -78 °C. N-butyllithium (1.6 M in hexanes, 11.1 mL, 17.8 mmol) was then injected, and the reaction was left stirring for 30 min. Tributyltin chloride (6.03 mL, 22.35 mmol) was then injected and the cooling bath was removed. After warming to room temperature, the reaction was quenched by adding water (5 mL). The crude was then concentrated under vacuum, diluted with water (200 mL), 1 M NaOH (20 mL) and extracted with hexanes. The organic phase was collected, dried under MgSO₄, followed by solvent removal under vacuum to afford **28** as a colorless liquid (7.00 g, 99% plus excess SnBu3Cl), which was used without further purification. 1H-NMR (499 MHz; CDCl3): δ 7.90-7.88 (m, 1H), 7.82 (d, J = 7.7 Hz, 1H), 7.39-7.27 (m, 4H), 1.64-1.57 (m, 9H), 1.40-1.33 (m, 12H), 1.17 (dd, J = 9.4, 6.8 Hz, 7H), 0.94-0.86 (m, 22H). MALDI-MS (m / z): [M + Na]+ calc for C20H32SSn 447.1145, found 447.250.

Ph2TDPP3TCHOC12 (29). Compound **27** (0.210 g, 0.231 mmol), **28** (0.117 g, 0.276 mmol) and Pd(PPh$_3$)$_4$ (0.026 g, 0.0225 mmol) degassed by three vacuum/nitrogen cycles, then degassed DMF (20 mL) was injected into the flask and the solution was stirred for 12hrs at 100 °C under nitrogen. After cooling to room temperature, the reaction mixture was poured into water (300 mL) with brine (30 mL). The precipitate was filtered over Celite, washed with additional water (100 mL) and the Celite was then washed with DCM until the washings were faint blue color. Residual water was removed in a separatory funnel. DCM was removed under vacuum and the product was purified by column chromatography (1:1 DCM/Hexanes) to afford **29** as a dark blue solid (0.160 g, 52%). 1H-NMR (499 MHz; CDCl3): δ 9.85 (s, 1H), 8.92 (dd, J = 10.0, 4.1 Hz, 2H), 7.79 (d, J = 7.6 Hz, 1H), 7.75-7.73 (m, 1H), 7.65 (d, J = 3.9 Hz, 1H), 7.51 (s, 1H), 7.47-7.43 (m, 1H), 7.39 (d, J = 4.1 Hz, 1H), 7.35 (td, J = 6.8, 1.2 Hz, 2H), 7.31 (d, J = 4.2 Hz, 1H), 7.29 (d, J = 3.9 Hz, 1H), 7.24 (d, J = 3.9 Hz, 2H), 7.18 (t, J = 7.6 Hz, 1H), 4.03 (q, J = 7.0 Hz, 4H), 1.99-1.94 (m, 2H), 1.39-1.14 (m, 40H), 0.90-0.80 (m, 15H). MALDI-MS (m / z): [M]+ calc for C55H64N2O3S5 960.3520, found 960.908.

Ph2TDPP3TCNC12control (30). Compound **29** (0.080 g, 0.0832 mmol) dissolved in CHCl$_3$ (20 mL), then benzylcyanoacetate (0.0190 mL, 0.124 mmol) and piperidine (0.0160 mL, 0.161 mmol) were then added and the solution was stirred at 70 °C for 12 hrs. After cooling to room temperature, the solution was diluted with DCM (100 mL) and washed with 1 M HCl (30 mL). The organic phase was collected and the solvent removed under vacuum. The product was purified by column chromatography (1:1 DCM/Hexanes) to afford **30** as a dark green solid (0.077 g, 83%). 1H-NMR (400 MHz; CDCl3): δ 8.96-8.90 (m, 2H), 8.96-8.90 (m, 2H), 8.24-8.21 (m, 1H), 8.24-8.21 (m, 1H),

7.81-7.77 (m, 1H), 7.82-7.73 (m, 2H), 7.77-7.73 (m, 1H), 7.65-7.63 (m, 1H), 7.65-7.63 (m, 1H), 7.54-7.51 (m, 1H), 7.54-7.51 (m, 1H), 7.47-7.30 (m, 8H), 7.47-7.30 (m, 8H), 7.25-7.21 (m, 4H), 7.25-7.21 (m, 4H), 4.08-4.00 (m, 4H), 4.08-4.00 (m, 4H), 2.02-1.92 (m, 2H), 2.02-1.92 (m, 2H), 1.65-1.46 (m, 10H), 1.65-1.46 (m, 10H), 1.42-1.17 (m, 33H), 1.42-1.17 (m, 33H), 0.92-0.78 (m, 12H), 0.92-0.78 (m, 12H). MALDI-MS (m / z): [M+H]+ calc for $C_{65}H_{71}N_3O_4S_5$ 1118.4842, found 1118.327.

Ph2TDPP3TCNC12 (31). Compound **29** (0.106 g, 0.110 mmol) was dissolved in $CHCl_3$ (20 mL), then N-benzylcyanoacetamide(0.030mL, 0.172 mmol) and piperidine (0.022 mL, 0.222 mmol) were then added and the solution was stirred at 70 °C for 12 hrs. After cooling to room temperature, the solution was diluted with DCM (100 mL) and washed with 1 M HCl (30 mL). The organic phase was collected and the solvent removed under vacuum. The product was purified by column chromatography (Acetone, then 5%EtOAc/DCM) to afford **31** as a dark green solid (0.055 g, 45%). 1H-NMR (499 MHz; CDCl3): δ 8.93-8.91 (m, 2H), 8.37 (s, 1H), 7.80-7.79 (m, 1H), 7.75 (dd, *J* = 6.8, 1.7 Hz, 1H), 7.61 (d, *J* = 4.1 Hz, 1H), 7.53 (s, 1H), 7.40 (d, *J* = 4.1 Hz, 1H), 7.39-7.31 (m, 9H), 7.26-7.23 (m, 5H), 7.05 (s,), 6.53 (dd, *J* = 6.6, 4.7 Hz, 1H), 4.59 (d, *J* = 5.8 Hz, 2H), 4.05 (dd, *J* = 10.3, 5.4 Hz, 4H), 2.01-1.93 (m, 3H), 1.42-1.20 (m, 39H), 0.90-0.82 (m, 13H). MALDI-MS (m / z): [M + H]+ calc for $C_{65}H_{72}N_4O_3S_5$ 1117.4287, found 1117.396.

Ph-TSnBu3 (32). 2-Phenylthiophene (0.5 g, 3.12 mmol) was placed in an oven-dried 100 mL Schlenk flask and degassed by three vacuum/nitrogen cycles. Anhydrous THF (30 mL) was injected and the solution was cooled to -78 °C. N-butyllithium (1.25 mL, 2.5M in hexanes, 3.12 mmol) was then injected, and the reaction was left stirring for 30

min. Tributyltin chloride (0.841 mL, 3.12 mmol) was then injected and the cooling bath was removed. After warming to room temperature, the reaction was quenched by adding water (5 mL). The crude was then concentrated under vacuum, diluted with water (200 mL), 1 M NaOH (50 mL) and extracted with hexanes. The organic phase was collected, dried under MgSO4, followed by solvent removal under vacuum to afford **32** as a colorless liquid (1.35 g, 96%). This compound was found to be unstable to column chromatography; if isolated, this product should be used in subsequent steps without further purification. 1H-NMR (500 MHz; CDCl3): δ 7.63 (d, J = 7.2 Hz, 2H), 7.43 (d, J = 3.3 Hz, 1H), 7.36 (t, J = 7.8 Hz, 3H), 7.14 (d, J = 3.3 Hz, 1H), 1.59 (m, 6H), 1.36 (m, 6H), 1.14-1.11 (m, 6H), 0.89 (m, 9H). 13C-NMR (126 MHz; CDCl3): δ 150.3, 137.2, 136.8, 134.9, 129.22, 129.12, 127.4, 126.28, 126.25, 124.6, 77.4, 29.3, 27.6, 14.0, 11.2 HRMS calc m/z for $C_{22}H_{34}SSn$: 450.1403, found 450.1410.

Ph-2TDPP3TCHOC12 (33). 27 (0.230 g, 0.242 mmol), **32** (0.130 g, 0.290 mmol) and tetrakistriphenylphosphine palladium(0) (0.027 g, 0.024 mmol) were placed in an oven-dried 250 mL Schlenk flask. The flask was the degassed by three vacuum/nitrogen cycles. Degassed DMF (40 mL) was then injected into the flask and the solution mixture was stirred for 12h at 100 °C under inert atmosphere. After cooling to room temperature, the reaction mixture was poured into water (300 mL) with brine (30 mL). The precipitate was filtered over Celite, washed with additional water (100 mL) and the Celite was then washed with DCM until the washings were faint blue color. Residual water was removed in a separatory funnel. DCM was removed under vacuum and the product was purified by column chromatography (30%hexane/DCM) to afford **33** as a dark blue solid (0.194 g, 81%). 1H-NMR (500 MHz; CDCl3): δ 9.86 (s, 1H), 8.96 (d, J =

4.1 Hz, 1H), 8.88 (d, J = 4.1 Hz, 1H), 7.67 (d, J = 3.8 Hz,1H), 7.61 (d, J = 7.8 Hz, 2H), 7.40 (t, J = 7.6 Hz, 2H), 7.32-7.28 (m, 7H), 7.25 (d, J = 3.6 Hz, 1H), 4.04 (d, J = 5.9 Hz, 4H), 1.97 (m, 2H), 1.35-1.24 (m, 36H), 0.89-0.84 (m, 12H). 13C-NMR (126 MHz; CDCl3): δ 182.8, 161.97, 161.81, 146.5, 145.6, 143.3, 142.4, 141.4, 140.2, 139.0, 138.0, 137.7, 137.4, 136.70, 136.51, 135.6, 133.9, 129.4, 128.4, 128.2, 127.5, 126.5, 126.2, 126.0, 125.7, 124.92, 124.83, 124.5, 109.1, 108.65, 108.62, 46.6, 38.3, 32.2, 31.7, 31.4, 30.1, 28.9, 26.7, 23.5, 23.0, 14.5 HRMS calc m/z for C57H66N2O3S5: 986.368, found 986.371.

A-Ester (34). 27 (0.0940 g, 0.0952 mmol) was placed in a 100 mL flask and dissolved in CHCl3 (20 mL). Benzyl-cyanoacetate (0.077mL, 0.500 mmol) was added, followed by piperidine (0.200 mL, 2.00 mmol). The solution was stirred at 70 °C for 12 h. After cooling to room temperature, the solution was diluted with DCM (100 mL) and washed with 1 M HCl (30 mL). The organic phase was collected and the solvent removed under vacuum. The crude was suspended in acetonitrile and filtered, to remove excess starting material. The product was purified by column chromatography (5%hexane/DCM, then DCM) to afford **34** as a dark blue solid (0.0423g, 21%). 1H-NMR (500 MHz; CDCl3): δ 8.96 (d, J = 4.2 Hz, 1H), 8.89 (d, J = 4.1 Hz, 1H), 8.26 (s, 1H), 7.67 (d, J = 3.9 Hz, 1H), 7.62 (d, J = 7.2 Hz, 2H), 7.45-7.27 (m, 16H), 5.34 (s, 2H), 4.05 (d, J = 7.0 Hz, 4H), 1.98 (m, 2H), 1.34-1.24 (m, 36H), 0.87-0.84 (m, 12H). 13C-NMR (126 MHz; CDCl3): δ 162.7, 161.54, 161.40, 146.7, 146.2, 145.2, 143.0, 141.0, 139.74, 139.71, 139.4, 138.55, 138.53, 138.1, 137.2, 136.5, 135.8, 135.3, 135.1, 134.6, 133.5, 129.17, 129.08, 128.71, 128.57, 128.26, 128.11, 127.92, 127.5,126.13, 125.99, 125.7, 125.4, 124.64, 124.56, 124.2, 115.9, 108.8, 108.3, 97.59, 97.56, 67.9, 46.3, 38.07,

38.03, 31.9, 31.4, 31.1, 29.82, 29.80, 28.67, 28.64, 26.4, 23.2, 22.7, 14.2 HRMS calc

m/z for $C_{67}H_{73}N_3O_4S_5$:1143.421, found 1143.423.

A-Amide (35). 27 (0.100 g, 0.101 mmol) was placed in a 100 mL flask and dissolved in

CHCl3 (20 mL). N-benzylcyanoacetate (0.088 g, 0.505 mmol) was added, followed by

piperidine (0.200 mL, 2.00 mmol). The solution was stirred at 70 °C for 4 h. After cooling

to room temperature, the solution was diluted with DCM (100 mL) and washed with 1 M

HCl (30 mL). The organic phase was collected and the solvent removed under vacuum.

The crude was suspended in acetonitrile and filtered, to remove excess starting

material. The product was purified by column chromatography (DCM, then

1%MeOH/DCM) to afford **35** as a dark blue solid (0. 0383 g, 33%). 1H-NMR (400 MHz;

CDCl3): δ 8.96 (d, J = 4.2 Hz, 1H), 8.89 (d, J = 4.2 Hz, 1H), 8.37 (s, 1H), 7.62-7.61 (m,

3H), 7.42-7.27 (m, 13H), 7.24 (t, J = 2.9 Hz, 2H), 6.54 (t, J = 5.8 Hz, 1H), 4.60 (d, J =

5.7 Hz, 2H), 4.04 (d, J = 7.1 Hz, 4H), 1.97 (m, 2H), 1.35-1.24 (m, 36H), 0.85 (m, 12H).

13C-NMR (126 MHz; CDCl3): δ 161.90, 161.76, 160.8, 145.65, 145.55, 144.7, 143.3,

141.4, 140.1, 138.95, 138.87, 138.1, 137.51, 137.47, 136.8, 136.3, 135.6, 135.4, 133.9,

129.39, 129.24, 128.43, 128.28,127.5, 126.44, 126.29, 126.0, 125.7, 124.92, 124.89,

124.5, 117.5, 109.1, 108.6, 99.4, 46.6, 44.9, 38.34, 38.31, 32.21, 32.19, 31.7, 31.4,

30.12, 30.09, 30.06, 28.97, 28.95, 26.7, 23.5, 23.0, 14.5 HRMS calc m/z for

$C_{67}H_{74}N_4O_3S_5$: 1142.436, found 1142.435.

Devices

Experimental conditions for active later deposition such as solvent, concentration

and solvent composition were optimized. Pre-patterned indium-doped tin oxide (ITO) on

glass was used as the transparent bottom electrode. The ITO was scrubbed with soapy

water and cleaned by ultrasonicating sequentially in hexanes, soapy water, water, and a 1:1:1 solution of acetone/methanol/2- propanol. The electrode was then blown dry in a N2 stream and transferred into a N_2 glovebox (O2 and H2O < 0.1 ppm). Before active layer coating, MoOx (10 nm) was thermally evaporated on ITO surface as the interfacial layer. Bulk heterojunction photovoltaic devices were fabricated from blends of donor small molecule and acceptor phenyl-C71-butyric acid methyl ester ($PC_{71}BM$). In the optimized conditions, donor/acceptor ratio is fixed to 1:1, with a total solution concentration of 22 mg/ml in CB. Films were cast by spin-coating at 2000 rpm in the glovebox for 60s and annealed on a hot plate at 100°C for 5 minutes. Total organic layer thickness ranged from 60-70 nm as determined by AFM. Devices were completed by thermally evaporating 1 nm of LiF then 100 nm of Al through a shadow mask at 1 x 10-6 mbar to yield devices of 4 mm2 in area and sealed with a UV-curable epoxy if needed. The devices for space-charge-limited-current (SCLC) measurements were fabricated with a similar procedure. Hole transport layer were replaced with PEDOT:PSS (Clevios P VP Al 4083) and the top electrode is replaced with Au (50 nm) rather than LiF/Al in order to suppress electron injection.

Hole mobility were estimated using the data showed in equation 3, where in the equation J is current, ε is relative permittivity of the material (assumed as 3 for most organic materials), L is the thickness of the film, V is the applied voltage and μ is the mobility. For the absolute voltage, the voltage drop across the ITO due to series resistance (VRS) and built in voltage (VBI) was subtracted from the applied voltage.[92] The only remaining unknown L, the thickness of active layer, was measured with AFM. These results were used to determine the hole mobility of each active layer.

$$(3) \quad J = \frac{9}{8} \frac{\varepsilon \mu_0}{L^3} V^2$$

Microscopy

AFM measurements were either performed on the fabricated solar cell device or on a separate sample prepared with the same spin coating parameters used for device on a freshly cleaved mica substrate. AFM images are processed with WSxM software. Samples for conventional transmission electron microscopy (TEM) were prepared by fishing the active layer that floats on water onto a copper TEM grid. To float the active layer in water a sacrificial PEDOT:PSS layer is coated on a glass and active layer is spin coated on PEDOT:PSS layer.

GIXD

Orientational distribution of the crystallographic features can be quantitatively described in terms of an orientational order parameter S (Herman's orientation parameter). Where separate orientational parameters $f\perp$ and $f\parallel$ used to represent the orientation of polymeric crystallites, respectively, along the plane of the film surface and along the axis normal to the surface are determined from the geometrically corrected scattered intensity. S can be calculated by knowing $f\perp$ (eq.1) which is calculated with the cosine function (eq. 2) as given below.

$$S = \frac{1}{2}(3f_\perp - 1)$$

$$3f_\perp = \langle \cos^2\chi \rangle \frac{\int_0^{\pi/2} I(\chi)(\cos^2\chi)(\sin\chi)d\chi}{\int_0^{\pi/2} I(\chi)(\sin\chi)d\chi}$$

From a practical perspective, S is a quantity that varies between -0.5 and 1, where value of 1 (-0.5) indicates parallel (orthogonal) orientation of the normal of a crystallographic plane relative to substrate normal. Conversely, a completely isotropic distribution of the crystallographic planes leads to an S value of 0.

Chapter 3 Supramolecular Organic Frameworks for High Efficiency Photovoltaics

3.1 Introduction

Before the asymmetric molecules were discovered, the premise of this project was that H-bonding could be used to help organize, and in a way program molecules to arrange themselves in a certain way, and that by doing so, the device performance could be enhanced. Chapter two discussed the story behind a pair of asymmetric molecules, one amide and one ester, where the amide **35** was able to h-bond, and although that ability ultimately increased its performance above that of ester **34**, the mechanism by which that happened was though competition of intermolecular forces. The ester was observed to behave similar to the organic donors normally found in the literature, but because the amide **35** could h-bond, that ended up dominating the assembly and compete with the otherwise favorable pi-pi stacking observed almost in any other donor. This finding was actually contradictory to the studies in references 154 and 155, but the different results can be attributed to the difference in designs.

In spite of the bitter sweet result (i.e. increased PCE upon h-bond at the cost of more disorganized domains) the idea of being able to direct molecules into specific assemblies was still something of extreme interest. For that reason it was decided that in order to keep pursuing that goal, some changes would have to be made. The DPP system allowed for the rapid modification of the design, given that the extended core, whether it was symmetric or asymmetric, was almost left unmodified, so it was possible to transition from greatly soluble molecules to greatly insoluble ones by modifying the

end groups, and that was something highly desirable. The drawback with the DPP core is that the absorption properties changed quite dramatically by making slight modifications. For example, intermediate **1** was red, but addition of a single thiophene ring to each side would make it blue, which represents a batochromic shift in absorbance of hundreds of nm, so there was no possibility of fine-tuning absorption. Also, the latest high performance designs are A-D-A type (see Figure 1.11) whereas the DPP-based amide and ester designs are essentially A-A-A (DPP is itself electron poor, and at each end there is the cyanovinyl group, another electron deficient unit). The importance of having alternating electron rich and poor units was recently studied and found that having two neighboring TT decreased the amount of cationic and CT states, which ultimately units was detrimental to the performance of a PTB7 analogue,[198] and even though molecules **34-35** did not have adjacent accepting moieties, it was still possible that a similar effect could take place, but to a lesser degree.

3.2 Attempts at Improving the Electronic Properties of H-Bonding Donors

Synthesis

It became clear that a DPP core, while it provided great light absorbing properties, was perhaps not the most electronically optimized molecule, for the reasons explained above. Consequently, it was necessary to modify the design for one that allow for intramolecular CT outwards. One candidate for substituting the DPP was BDT, which was discussed earlier. Benzothiadiazole (BTD) was selected as the "pull" unit of the design. The intention was to design a molecule with a BDT core, surrounded by BTD units, and with aldehydes in the ends, to be able to run the Knoevenagel

condensation with the H-bonding groups. Instead of butyloctyl tails, the core would be solubilized with ethylethyl, and additional tails would be added to the thiophene π-spacers. The synthesis of the π-spacers and BDT cores is shown in Scheme 3.1.
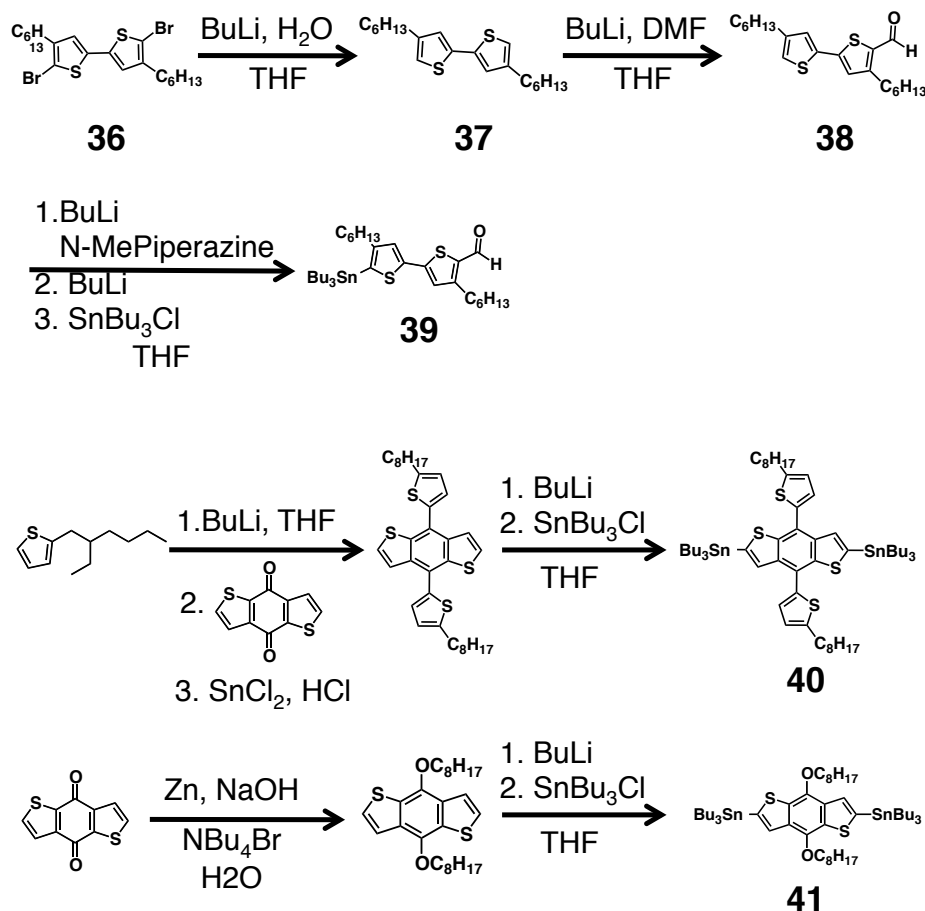
Scheme 3.1. Synthesis of alkylated thiophene spacers (top) and BDT cores (middle and bottom).

The new BDT-containing molecule synthesis is shown in Scheme 3.2; it consisted of first coupling an alkylated bithiophene aldehyde **39** to a dibrominated BTD unit. Instead of coupling the other brominated side of BDT to the stannylated BDT core, one additional thiophene was coupled for the purpose of creating sufficient area for fullerene intercalation, which it has been suggested as one way to create strong D:A

interaction.[199] Intermediate **43** was then brominated, and the product coupled to the distannylated BDT unit **40**. The resulting dialdehyde **45** was condensed with benzylcyanoacetate or acetamide, as were molecules **34**-**35**. It was mentioned that one of the objectives of the design was to improve on the electronic properties of the DPP units, but synthetically, one of the additional aims was to construct a symmetric molecule because it reduces the number of steps, thus simplifying the overall synthetic load. Nevertheless, molecules **46**-**47** ended up doubling the number of steps of the DPP predecessors, which was somewhat inconvenient, but this became another design where being able to assemble different parts separately was advantageous.
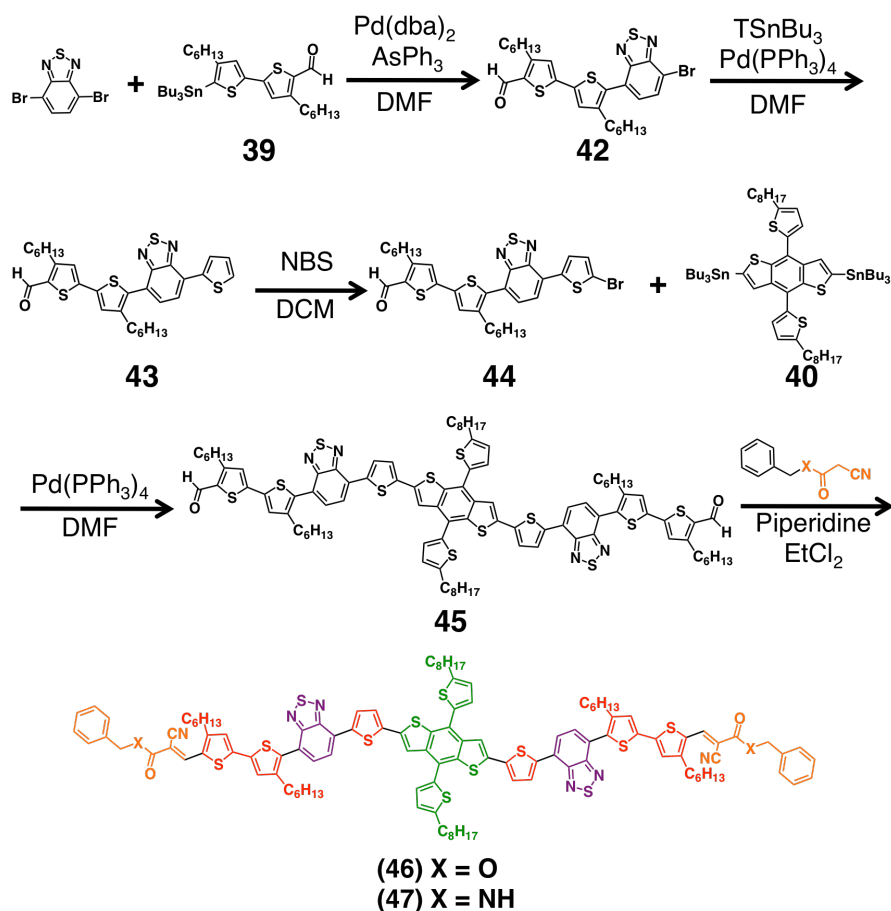
Scheme 3.2. Synthesis of BDT-containing H-bonding donor.

Absorption Studies

The absorption of molecules **46**-**47** is shown in Figure 3.1a. The spectra are notoriously different from its DPP analogues. The first thing to note is that the π-π* and CT bands are not distinguishable, but rather merged. The implications of this remain unknown, but it is not uncommon to see spectra like that. Some of the BDT-containing high efficiency OPV designs also do not show two clear bands and are still able to perform well.[33] The behavior on film is also different, but the pair of molecules does share some similarities with the DPP designs. As expected from a conjugated molecule, there is a significant absorption red-shift upon drying, but unlike the DPP donors, there is no significant vibronic broadening of the absorption bands, they just shift. Fortunately, the film absorption covers the majority of the visible spectrum. Although not shown, the extinction coefficient does decrease, however, that has not been an impediment for other BDT small molecules to achieve high PCEs.

Sample	J_{SC} (mA/cm^2)	V_{OC} (V)	FF (%)	PCE (%)
46:PC$_{71}$BM_CHCl3	3.51	0.99	38	1.30
46:PC$_{71}$BM_CHCl3	4.15	0.81	28	0.95
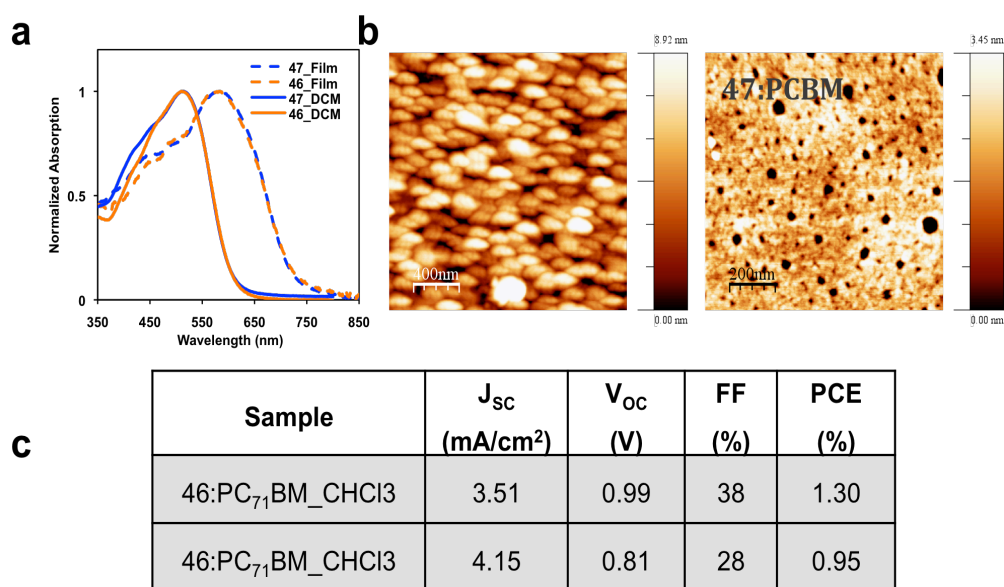
Figure 3.1. a) Absorption spectrum of molecules **46-47**; b) AFM images of the morphology of molecules **46-47** with PCBM and table of summarized device results (c).

Morphological Studies

Per tradition, devices were made with these molecules, and the morphology was studied with AFM (Figure 3.1b). The ester **46** show spherical aggregates of about 200 nm in size, while the amide **47** exhibited film dewetting (a different type of aggregation problem). It was disappointing to see the quality of films being poor, and not ideal, but that problem had been seen before, just only when there was an excess of alkyl tails. In the past, segregation problems were dealt by modifying the design, but before going to those extremes, the performance of the devices was measured.

Device Performance

A brief summary of the device performance is shown in Figure 3.1c. At the time of testing, the amide **47** was in short supply, so devices were built mostly of the ester **46**, and unfortunately, were not promising. Given the morphology of the active layer, it was not surprising that the devices did not perform extraordinary either, with maximum PCEs of 1.3%. One of the major obstacles to optimizing devices was the solubility of the molecules. Before completely modifying the design, and because there was still enough of intermediate **45**, the design was quickly modified to enhance solubility.

3.3 Increasing Solubility in Symmetric BDT-Based Symmetric Designs

Synthesis

The need to increase solubility of molecules had fortunately been encountered before, and there was one simple solution, increase the alkyl tail content. However,

there were some specific facts that had to be accounted for. First, when the gallate derivatives were synthesized, the large number of alkyl tails increased solubility dramatically, but they also created a strong segregation problem. The second thing to keep in mind is that when a single branched alkyl tail replaced the excessive number of alkyl tails, the segregation problem was not particularly solved, but did allow for decent solubility. With that in mind, and considering the fact that molecules **46**-**47** did not have a segregation problem as the DPP designs, it was decided to replace the benzyl groups with a straight alkyl tail. The synthesis is shown in Scheme 3.3. The intermediate **45**, just like it was intended from the beginning, did not have to be modified, so it was condensed with the octylcyanoacetate or acetamide groups, respectively, to make the modified molecules **50**-**51**.
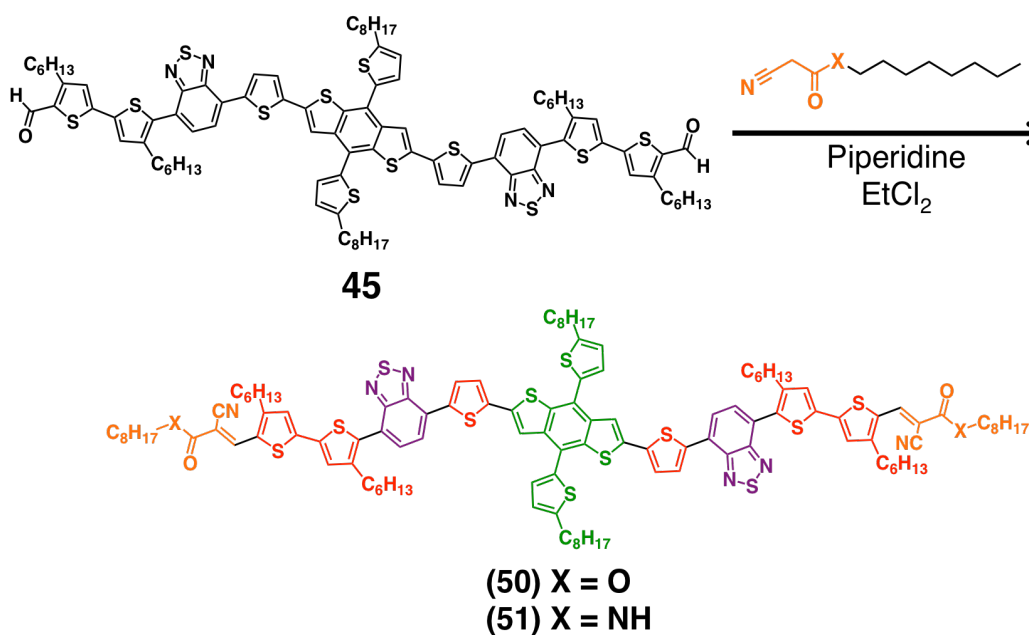
Scheme 3.3. Modified BDT donor to enhance solubility.

Absorption Properties

The absorption of the modified molecules is not surprisingly identical to molecules **46**-**47**. The absorption in solution remains unchanged, but there is a slight change in the films. It was initially expected that because there is less conjugation in the modified molecules, the red-shift in absorption upon drying on a film would be affected (dimished), but it was a pleasant surprise to see that the onset of absorbance and interval of absorption still covered most of the visible spectrum. In molecules **46**-**47**, both amide and ester had the exact same absorption on film, but molecules **50**-**51** have only a slight difference, and that is that amide **51** has a slightly less red-shifted absorption than ester **50** (Figure 3.2a). Although the difference is small enough that would probably not be statistically significant, it could also mean that the amides are again competing with π-π stacking, which reduces crystallinity, thus a lesser degree of red-shift.
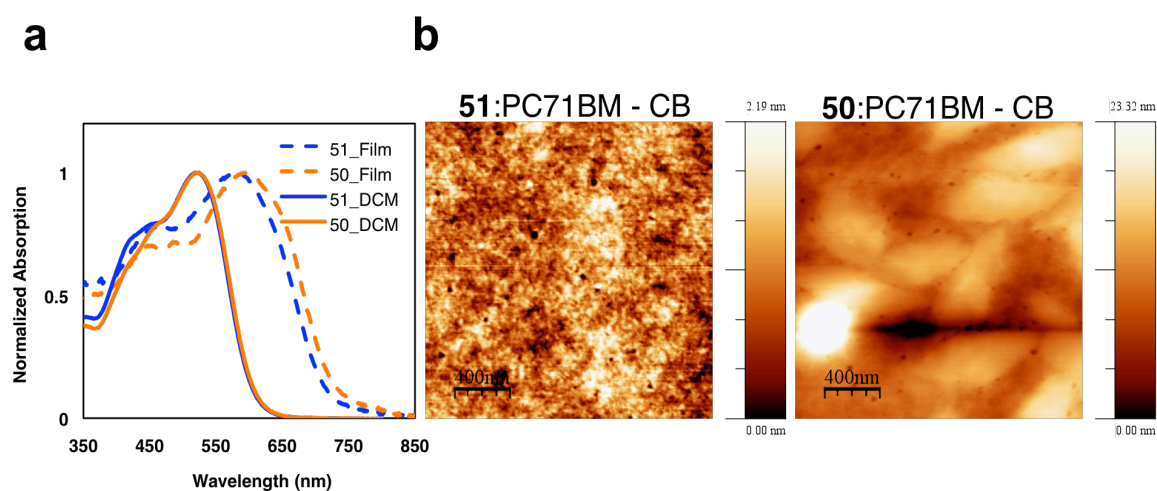
Figure 3.2. Absorption of molecules **50-51** (a) and AFM images of the morphology with PCBM (b).

Morphological Studies

With improved solubility, it was expected that the morphology of the devices built was going to show smaller aggregates, as it occurred in the case of the DPP molecules. The initial films were spin-coated from $CHCl_3$ solutions, but it was soon noticed that because the solvent evaporates so fast, the quality of the films was very poor. In CB, there were slight improvements, and judging by the AFM micrographs of Figure 3.2b**,** molecules **50**-**51** have very distinct morphologies. Amide **51** forms relatively well-mixed films, but with holes, which is an indication of film dewetting. The ester **50** shows large aggregates, not spherical as it normally happens, but these aggregates appear to be crystalline, at least by first look. It would appear that the increased solubility still did not help in improving the active layer morphology.

Device Performance

The newly improved, or at least solubility-wise, molecules **50**-**51** were tested in OPV devices. The performance for several conditions is summarized in Table 3.1. When spin-cast from $CHCl_3$, the ester **50** performs slightly better than the amide **51**, possibly due to better crystallinity, but when the solvent is CB, the amide outperforms the ester. The latter drops in efficiency almost half of that in $CHCl_3$. In both solvents, the devices were annealed, so a quick test revealed than annealing was actually detrimental to the device, since as-cast devices more than doubled in PCE, mainly due to increased current and a much better morphology. Another aspect that was tested was if the acceptor had any effect. The initial devices were made with $PC_{71}BM$, but it was interesting to know whether the smaller $PC_{61}BM$ would be able to interact better

with the donors. Devices were made with the amide only, but there was no improvement observed.

Table 3.1 Summary of device results for molecules **50-51.**

D:A (PC71BM)	J_{SC} (mA/cm²)	V_{OC} (V)	FF (%)	PCE (%)
50_1:1_CB (2000 rpm) 100 °C 2 min	1.6	0.93	29	0.43
50_1:1_CB (4000 rpm) 100 °C 2 min	2.93	0.97	27	0.82
51_1:1_CB (2000 rpm) 100 °C 2 min	2.37	0.97	26	0.6
51_1:1_CB (4000 rpm) 100 °C 2 min	1.90	0.93	30	0.53
51_1:1 (PC$_{61}$BM) CB (4000 rpm) 100 °C 2 min	1.79	0.99	24	0.42
51_1:1 (PC$_{61}$BM) CB (4000 rpm) 100 °C 2 min	4.88	0.91	36	1.59

Many more conditions were tested in an attempt to optimize the performance of the devices, but the PCE peaked at <1.6%. It was possible that the film quality was responsible, but it became necessary to analyze the molecular structure as well. In dye-sensitized solar cells, strongly electron withdrawing units are generally not placed next to another electron-withdrawing unit because they can create electron traps and prevent efficient electron transfer,[200,201] and it is possible that in molecules **50**-**51**, such a phenomenon was happening. As disappointing as it was, a lot of time was invested without success, so it was decided that the design should be modified. The first issue was obviously synthetic, and it became necessary to reduce the number of steps.

3.4 Discovery of Isomers in Symmetric BDT-Based H-Bonding Donors

Synthesis

The initial testing of BDT-BTD-containing donors revealed potential problems with the electronic properties of the molecules, some kind of electron-trap, or high recombination rates, that prevented an otherwise good molecule from having high efficiency. The synthesis of molecules **46**-**47** was 14 steps until intermediate **45**, so in the interest of time, the next design had to be simpler. It was decided that the BTD unit should be removed since it was believed to be the cause of low efficiency in molecules **46**-**51**. Another issue that had to be considered was solubility. In the past, both DPP and BDT-based molecules had problems being soluble enough for device fabrication, but experience showed that there is a limit to the number of alkyl tails possible before they cause segregation problems, so an alternative way of imparting solubility, without adding excessive numbers of alkyl tails, was needed. Having considered that, the new design was based on the high performing BDT designs, i.e. BDT core, with π-bridges and cyanovinyl electron withdrawing groups (see Figure 1.11). The design was much more in accordance with the push-pull design mentioned in previous sections.

Since the intention was to impart solubility, but not with excess alkyl tails, it was decided to use sterics, in particular torsion angle between a phenyl ring and a thiophene one, to weaken π-π stacking. Such strategy has been used in DPP-based polymers to be able to modify the mobility.[202] The synthesis of the modified BDT donor is shown in Scheme 3.4. It consisted on llithiation of 3-hexylthiophene, followed by transmetallation with magnesium bromide ethyl ethereate to make the Grignard reagent, then couple that to 1,6-dibromobenzene via a Kumada coupling to make intermediate **52**.

Formylation followed, and the aldehyde **54** was brominated with NBS, then coupled to distannylated BDT **40** to make the symmetric aldehyde **56**, which was condensed with octylcyanoactetate or cyanoacetamide to make **57** or **58**, respectively. In this case, the core BDT design had to be changed, but the cyano-containing groups could still be used, along with BDT. The number of steps was reduced to 11 up to intermediate **56**. It was not originally intended to produce molecules **57**-**58**, but rather the isomers with the alkyl tails on the 3,3' positions. Careful analysis of the NMR spectra revealed that intermediate **52** had splitting patterns not corresponding to what they should be, but since the molecules were already made, now it was possible to compare the effect of regioisomerism on device performance.
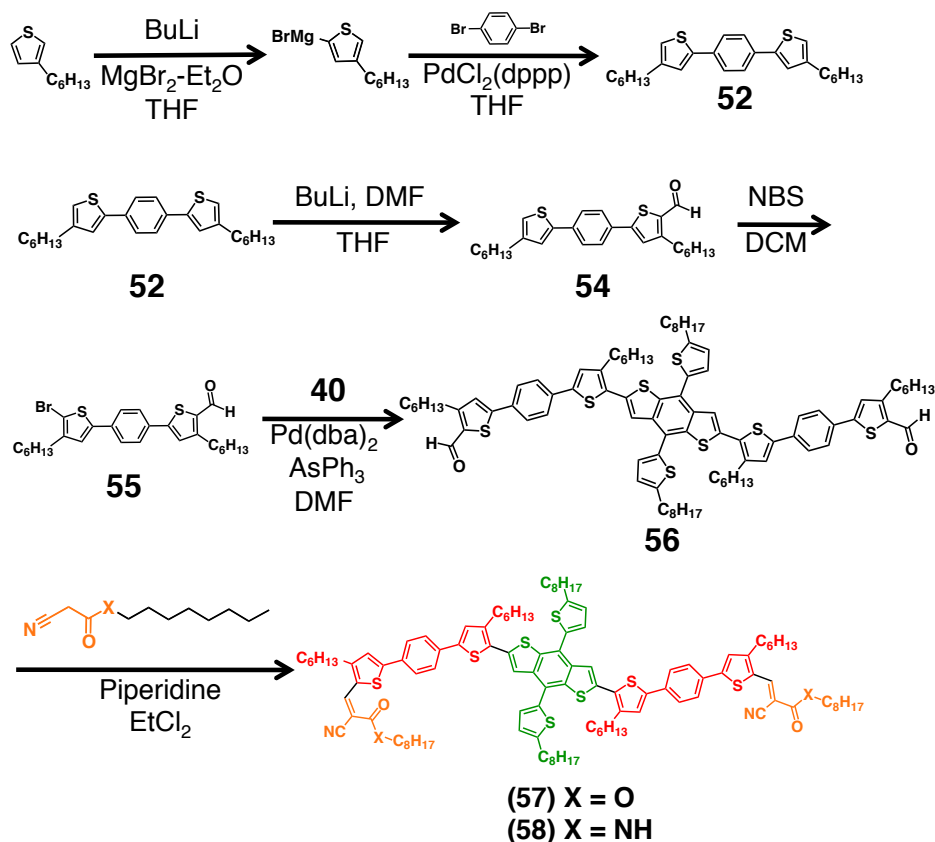
Scheme 3.4. Unintentional synthesis of the 4,4'-alkylated isomer of the modified BDT H-bonding donor.

Absorption Studies

The absorbance of the modified molecules is shown in Figure 3.3a. Compared to molecules **50**-**51**, the modified donors absorb significantly less light. In this case, only a single absorption band can be detected in the visible spectrum, if there is a π-π* band, it is most likely located in the UV range. The broadness of the band also decreases, and now the red region of the visible spectrum is not covered. Upon drying on a film, there is still a batochromic shift in absorbance, but the onset is about 100 nm blue-shifted than molecules **50**-**51**. Amide **58** and ester **57** show similar absorption, both in solution and film. In the DPP designs, the H-bonding effect was more noticeable in asymmetric designs, where it seems that the π-π stacking was not strong enough to dominate the assembly and H-bonding could interfere and decrease the domain size, but so far, all symmetric designs, whether DPP or BDT-based, do not show significant differences in aggregation in amide vs ester film absorption.
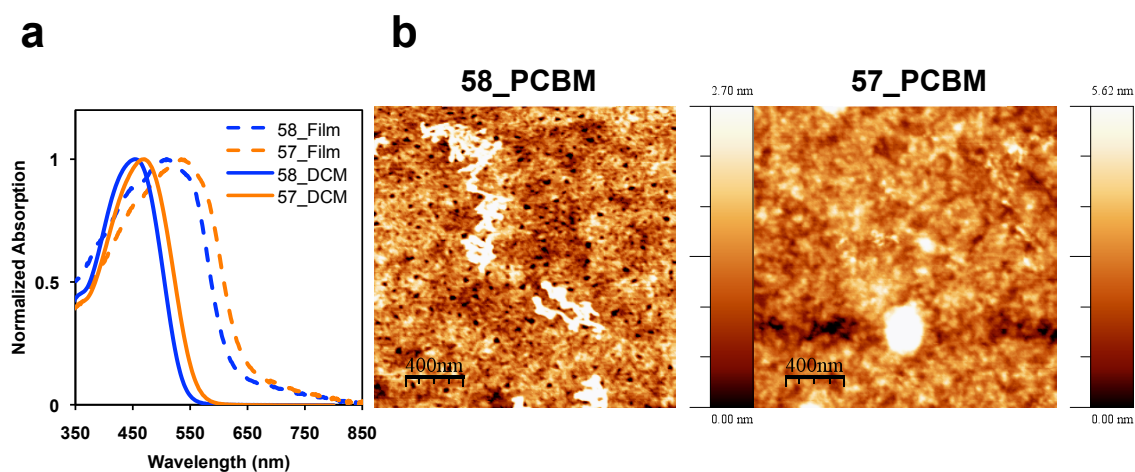
Figure 3.3. a) Absorption spectrum of molecules **57-58** and device morphology AFM image with PCBM (b).

Morphological Studies

The morphology of the films was analyzed with AFM and the micrographs are shown in Figure 3.3b. When mixed with PCBM, the ester **57** shows spherical domains, just like it has been observed before. On the other hand, the amide **58** shows short fibrous structures with less than 50-100 nm width, which was promising, but the domains needed to be reduced further. The films were also analyzed with GIXS and it was found that the Amide **58** w/PCBM film is essentially amorphous, since there are barely visible diffraction signals. The ester **57** w/PCBM film still shows strong diffraction peaks off-plane, indicative of alky-alkyl stacking and a strong in-plane diffraction peak that correlates with π-π stacking.

Device Performance

The device performance for molecules **57**-**58** was tested, as with any other design. The films were spin-coated from $CHCl_3$, but after initial testing, it was changed to CB. The results are shown in Table 3.2. This time, annealing had no significant effect on the device performance, and although for both amide **58** and ester **57** the Voc was relatively high, the current was very small, as it was the FF, ending up in a low performance. Solvent additives, contrary to most designs so far, have deleterious effect on device performance. Normally, amides work better than esters since they tend to have smaller domains on films, but in this case, the ester **57** worked better, yet still with low PCE. Since this design had the alkyl tails in an unintended position, it became interesting to see how the molecules would perform if the design were corrected.

Table 3.2. Device results for molecules **57-58.**

D:A	J_{SC} (mA/cm^2)	V_{OC} (V)	FF (%)	PCE (%)
57_1:1 PC$_{61}$BM_CB 1250 rpm, 100 °C 10 min	3.65	0.95	0.40	1.39
57_1:1 PC$_{61}$BM_CB 2000 rpm, 100 °C 10 min	2.52	0.93	0.46	1.07
57_1:1 PC$_{61}$BM_CB 2000 rpm, 100 °C 5 min	2.13	0.95	0.34	0.68
57_1:1 PC$_{71}$BM_CB 2000 rpm, 100 °C 5 min	2.02	0.95	0.36	0.69
57_1:1 PC$_{61}$BM_CB 1250 rpm, 100 °C 2 min	2.73	0.95	0.34	0.89
57_1:1 PC$_{61}$BM_CB 1250 rpm, 100 °C 10 min	2.39	0.95	034	0.74
58_1:1 PC$_{61}$BM_CB 1250 rpm, 100 °C 5 min	0.67	0.96	0.27	0.16

3.5 Fixing Alkyl Tail Positions in New BDT-Based Isomer H-Bonding Donor

Synthesis

Although the previous molecules were unintentionally made, it was still surprising that the efficiency did not increase over that of molecules **50**-**51**. The BTD unit was removed because it was believed to be creating electron traps in the core of the molecule. Before further conclusions could be drawn, it was decided that the correct isomers should be synthesized first, then it would be possible to fully compare the different designs. The synthesis of the correct isomers (Scheme 3.5) was identical except for one step. Instead of lithiating 3-hexylthiophene and transmetallating with magnesium, the Grignard of 2-bromo-3-hexylthiophene was prepared directly, and

coupled via a Kumada coupling to 1,4-dibromobenzene. The remaining steps were identical. The ability of being able to assemble the molecule in parts was once again an important factor in saving time.
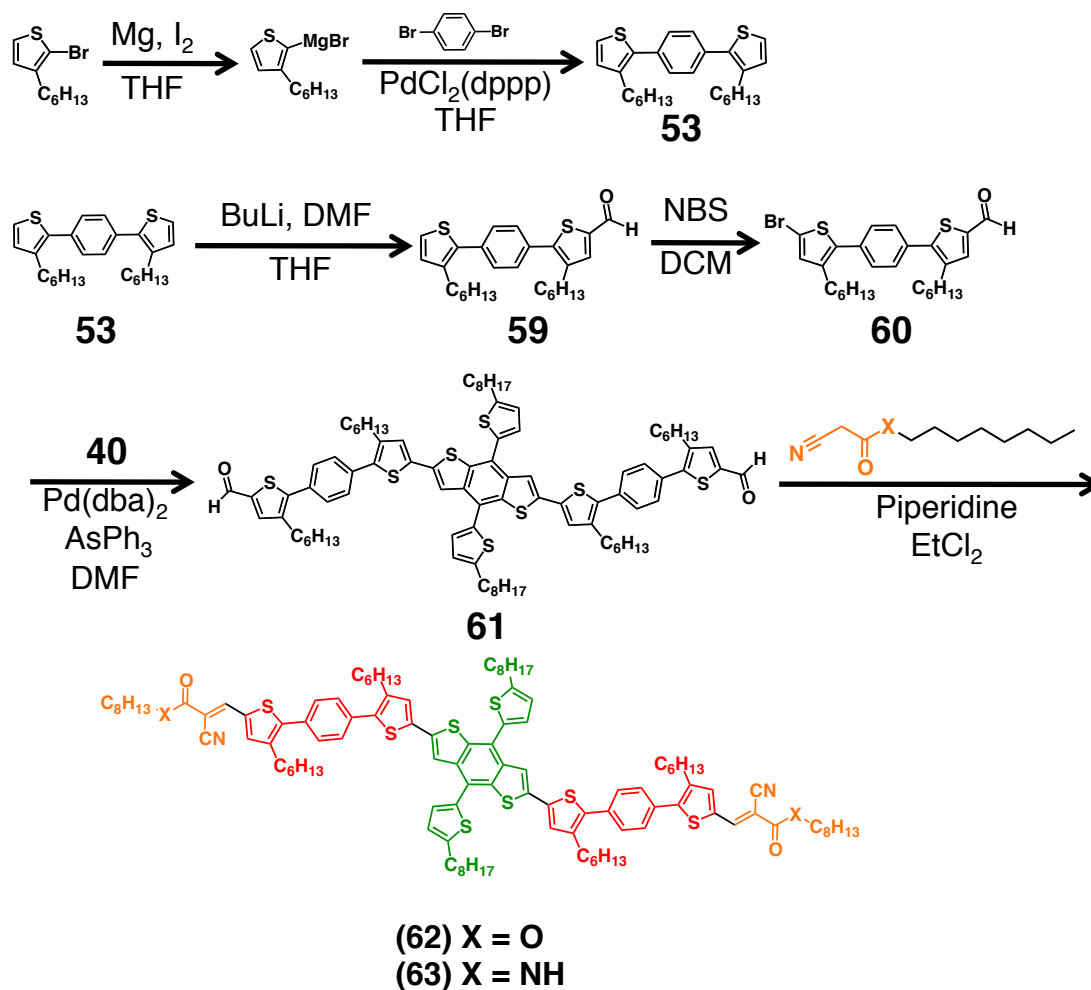
Scheme 3.5. Synthesis of the correct 3,3'-alkylated isomer of the BDT H-bonding donor.

Absorption Properties

The absorption of the now correct regioisomers is shown in Figure 3.4. Contrary to what it was initially hoped for, the new molecules **62**-**63** were actually more hindered, and this was causing much less light absorption than in the previous isomer. The absorption band was now narrower than in the previous isomers, but it did show some

vibronic shoulder in solution. Upon drying, the new isomers did not absorb as much as before. As could be expected, there was a red-shifted absorption, and in this case visible vibronic broadening indicative of J-aggregation in both amide **62** and ester **63**, but the onset of absorption was now ~50 nm blue-shifted over molecules **57**-**58**. At this time it was indirectly implied that the presence of the phenyl ring between two thiophenes was preventing strong π-π stacking, which was in a way the desired effect, but it was too much hindrance, and that was causing the poor light absorption, and possibly even affected excited state lifetimes.

a **b**

D:A	J_{SC} (mA/cm^2)	V_{OC} (V)	FF (%)	PCE (%)
63 1:1 PCBM 1250 rpm 100 C 10 min	0.88	0.99	0.23	0.20
63 1:1 PCBM 1250 rpm 100 C 10 min	2.58	1.01	0.49	1.28
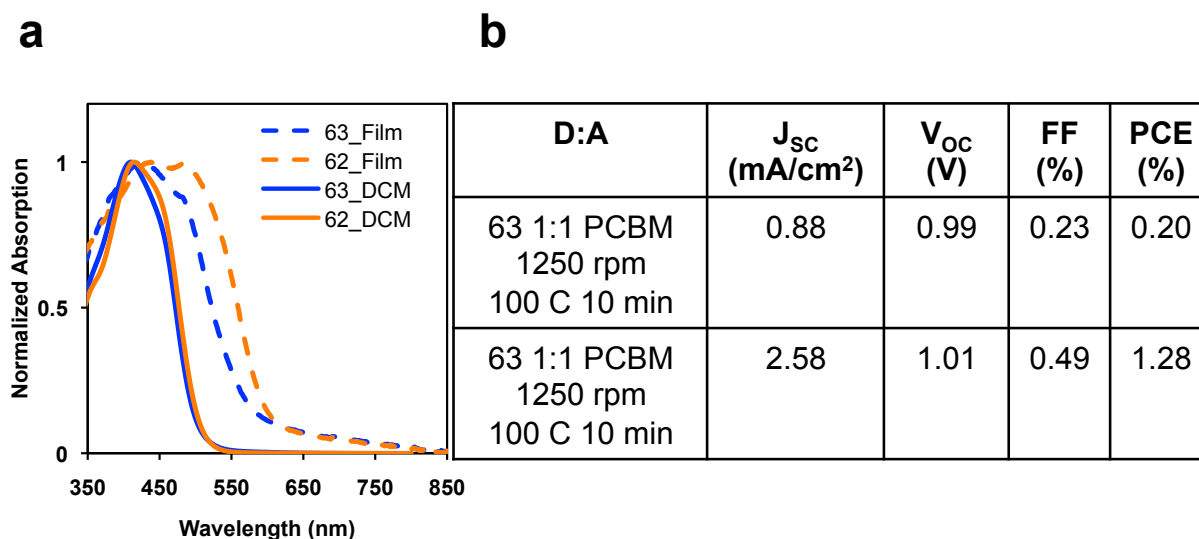
Figure 3.4. Absorption spectrum of molecules **62-63** (a) and device results (b).

Device Performance

Before studying the morphology in detail, devices were built with the new molecules from solutions in CB. Since molecules **62-63** were regioisomers of molecules **57-58**, the conditions were not substantially changed. Given that the absorbance was negatively affected by the new positions of the alkyl tails, there was little possibility that

the performance of the devices was going to be improved, and unfortunately, it was not (see Figure 3.4b). Only amide **63** was tested because after that it became clear that the alkyl tails created even more steric hindrance and the molecules basically did not stack, so it was not surprising that the PCE remained <<1%. Although the result was discouraging, now it was clear that having a phenyl ring in between two thiophenes was also creating electronic problems, perhaps not electron traps, but rather electronic decoupling within the molecule, so the design had to be modified again.

3.6 Attempt at Replacing BDT Core in H-Bonding Donors

Synthesis

The lesson molecules **57**-**58** and their isomers **62**-**63** left was that a phenyl ring is effective at increasing solubility in small molecules indeed, but not overall PCE. Perhaps the reason it worked better in polymers is because of how much longer the conjugated chain is in a polymer than in a small molecule, so breaking the conjugation could help solubilize more monomers. In small molecules, however, it greatly reduces the light absorption ability and overall OPV performance. The other lesson learned was that the original fears of the molecule having solubility problems may have been unsubstantiated, after all, the designs shown in Figure 1.11 shared many similarities to the BDT isomers. For that reason, the design was modified again, this time incorporating the dithienylthiophene arm (essentially a 3-thiophene **pi**-bridge). One important issue to keep in mind was that the proposed design had already been published, so to have a more original design, the core BDT was replaced by an alkylated anthracene. Synthetically, this made sense because the anthracene core

required less number of steps to be synthesized (Scheme 3.6). The synthesis consisted on first making intermediate **64**, then stannylated it and couple it to a previously reported alkylated anthracene core **66**, to make intermediate **67**, which was formylated to make dialdehyde **68**. The reason formylation using a Vilsmeier reagent was necessary again was because the bromines in the anthracene core **66** could not be stannylated, so the alternative route became to attach the arms first, then prepare the aldehyde from the extended core. Sadly, intermediate **68** was as far as this synthesis was able to go. It was found that during the Knoevenagel condensation, the molecules quickly decomposed. As a matter of fact, it is possible that they began decomposing even after the coupling.
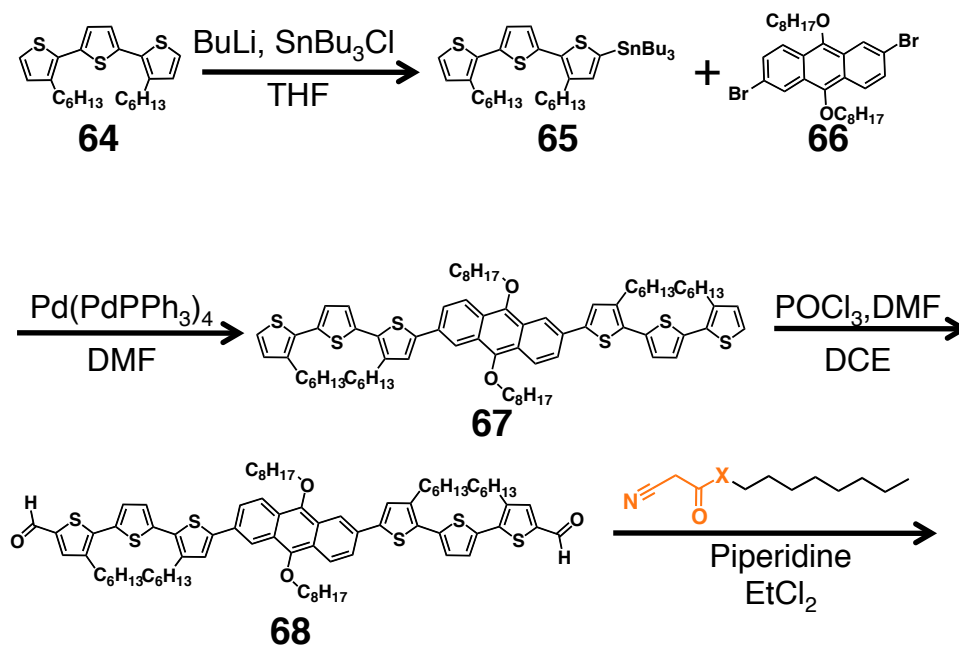
Scheme 3.6. Attempted synthesis of a BDT core substitute, anthracene.

3.7 The Path Towards Creating a Supramolecular Organic Framework

Synthesis

The previous designs were all aimed at improving the electronic properties of the original DPP donors, and unfortunately, the attempts were unsuccessful. In addition, the DPP system worked due to competition between H-bonding and π-π stacking. One of the goals of this project was to program molecules to create the morphology from Figure 1.20, by means of having H-bonding and π-π interactions in a conjugated small molecule donor work cooperatively to form a porous, supramolecular polymer (a supramolecular organic framework, SOF) where potentially fullerenes could fit. Such a framework would align ideally in a face-on fashion. While to date there is no direct evidence that a molecule that packs face-on will have higher PCE than if it packed edge-on, the mobility of OPV devices where face-on orientation predominates is usually higher than that of edge-on orientations.[87,203,204]

When thinking of porous, organized materials, there are a few established fields that come to mind. The oldest one would be metal-coordination polymers[205] or the more recent metal-organic frameworks (MOFs);[206] there are also h-bonded porous organic crystals,[207–209] some have shown C_{60} binding affinity,[210] but neither MOFs nor crystals, despite being h-bonded, have been used for OPV devices. There are only a handful of SOFs, and most are based on host-guest chemistries of water soluble charged molecules,[211–213] with the exception of an h-bonded co-crystal;[214] as before, they have not been used in OPV devices. A more viable alternative was to base the design on covalent organic frameworks (COFs). Chemically speaking, COFs are made or aromatic units already,[215–217] some relevant to OPVs such as porphyrin[218] or thiophene-based;[219]

what is more important, they have been shown to form porous frameworks and transfer charge to fullerenes trapped in their cavities.[220,221] Although OPV devices made with COFs have been unsuccessful,[222] COFs only served to point out the need to have a symmetric molecule with multi-directional H-bonding for the purposes of this project. Since COFs are covalently bonded, highly stacked polymer materials, it is no surprise that they are insoluble powders, but in a supramolecular setting, the stacking would be greatly reduced.

Having gained a little more confidence in a SOF, there were still some major challenges to address. Despite the confidence that a SOF would stack less than a COF, solubility would still be the most difficult challenge to solve because it is hard to predict how effective alkyl tails will be at modulating the stacking ability of an OPV donor by just looking at its structure (COFs do not have alkyl tails, so again, it is not surprising that they are insoluble powders). In addition, solvents for OPVs are limited to what dissolves PCBM, i.e. $CHCl_3$, CB or DCB, which may not be entirely suitable for an H-bonding donor. In order to be able to address the processing problems faster, the conjugated part of the design was based on high performance BDT small molecules,[33] with modifications that will be discussed later. The H-bonding part, as mentioned, needed to be bidirectional to be able to create an interconnected framework. A popular H-bonding group that is also compatible with Knoevenagel condensations is barbituric acid,[173] which is known to form networks when mixed with the complementary H-bonding unit melamine.[223] To further avoid work, even simpler conjugated cores, and after digging through past results, one symmetric aldehyde was chosen, the by-product of the reaction to make intermediate **42**, i.e. the disubstituted product. The reaction is shown in

Scheme 3.7, and it was good news that it worked. Nevertheless, there was little time for celebration, given that the final product was incredibly insoluble, in anything but DMF and DMSO, none of which are compatible with PCBM. It looked like the original concern of solubility was correct, there is a major problem when a bidirectional H-bonding group is added to a conjugated core.
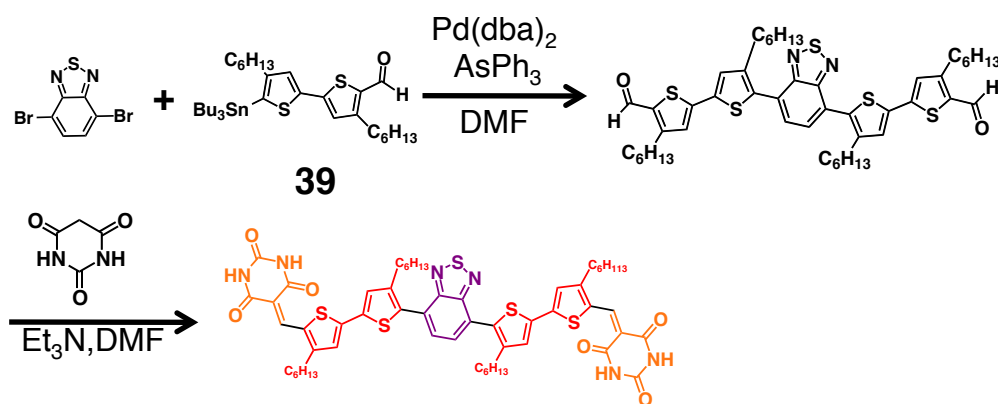
Scheme 3.7. Attempted synthesis of a BTD-core multidirectional H-bonding donor for SOF formation.

The only good thing about the insoluble powder was that it was a molecule that would not have any use anyway, and no significant time was lost. The dialdehyde of **42** was incredibly soluble and turned completely insoluble by barbituric acid, which meant that perhaps additional solubilizing groups were needed, but once again, experience from past molecules indicates there is a limit to the number of alkyl tails present in a design before it segregates from PCBM, so the next issue on the agenda was to find a way to increase solubility that does not involve adding more alkyl tails. Fortunately, another past molecule was able to do just that, dialdehyde **61**, so once again the Knoevenagel condensation was attempted, and just like before, it resulted in an

incredibly insoluble molecule (Scheme 3.8). Though some improvements in solubility were observed, the low solubility indicated that a different design was needed.
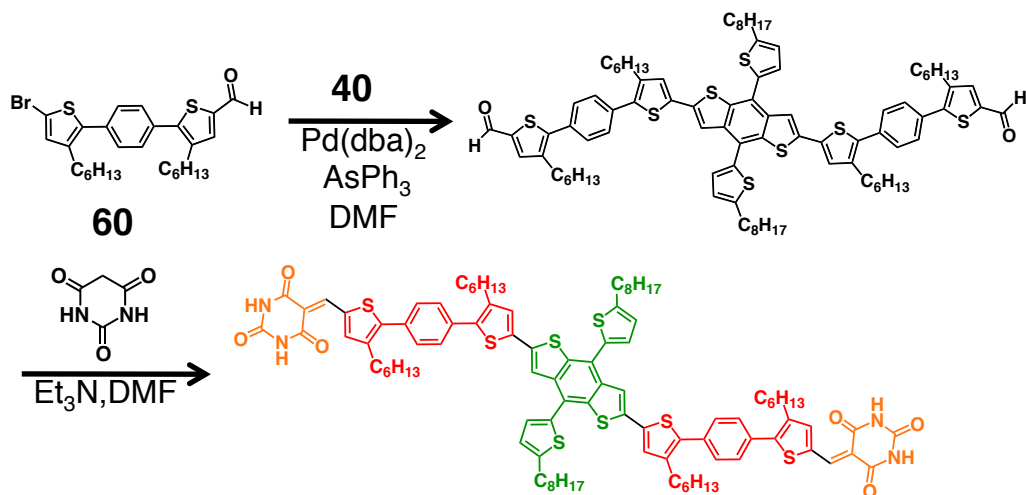
Scheme 3.8. Attempted synthesis of a BDT-core multidirectional H-bonding donor for SOF formation.

3.8 Supramolecular Organic Frameworks for OPVs

Synthesis

The experiences from the previous sections taught a few lessons: the BDT core is the most stable, and intermediate **69** does not interfere with electronic coupling of the molecule. Lastly, coupling a multidirectional H-bonding group to a conjugated core makes it very insoluble. For this reason, the updated SOF design is shown in Scheme 3.9. Sadly, there was not enough time to synthesize this molecule, but the design will consist of two different BDT cores, one with alkoxy tails and one with alkylated thiophene tails. Intermediate **69** will act as the π-bridge and a modified uracil, coupled to a six-carbon linker will be attached to provide the pulling effect. Since one of the positions from uracil will used to attach the linker, the end result will be a H-bonding in a

single direction, but one that will occur on both sides, which should still allow the formation of a porous framework.
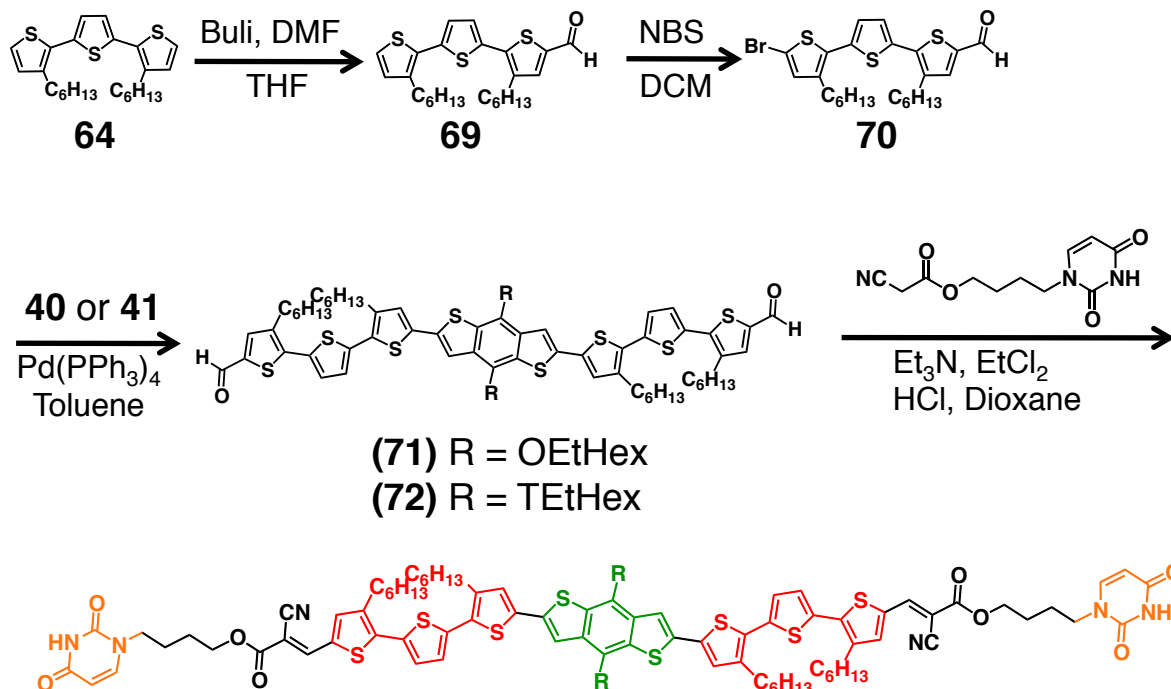
Scheme 3.9. Proposed new design for a multidirectional H-bonding donor capable of SOF formation.

3.9 Synthetic Methods

Br2TBrC6 (36). Molecule **36** was prepared according to a previously published procedure.

2TC6 (37). Compound **36** (1.33 g, 2.70 mmol) was placed in an oven-dried 100 mL Schlenk flask and degassed by three vacuum/nitrogen cycles. Anhydrous THF (15 mL) was injected and the solution was cooled to -78 °C. N-butyllithium (2.5 M in hexanes, 2.70 mL, 6.75 mmol) was then injected, and the reaction was left stirring for 30 min. Water (5 mL) was then injected and the cooling bath was removed. After warming to room temperature, the reaction was diluted in water (100 mL) and extracted with

hexanes (100 mL). The organic phase was collected, dried under MgSO$_4$, followed by solvent removal under vacuum to afford **37** as a colorless liquid (0.808 g, 89%). 1H-NMR (400 MHz; CDCl3): δ 6.98 (d, J = 1.4 Hz, 2H), 6.76 (d, J = 1.2 Hz, 2H), 2.56 (t, J = 7.7 Hz, 4H), 1.65-1.58 (m, 4H), 1.38-1.26 (m, 12H), 0.91-0.87 (m, 6H). HRMS−ESI (m / z): [M]+ calc for C20H30S2 334.1789, found 334.1797.

2TC6CHO (38). Compound **37** (1.00g, 2.98 mmol) was placed in an oven-dried 100 mL Schlenk flask and degassed by three vacuum/nitrogen cycles. Anhydrous THF (15 mL) was injected and the solution was cooled to -78 °C. N-butyllithium (2.5M in hexanes, 1.43 mL, 3.58 mmol) was then injected, and the reaction was left stirring for 30 min. Anhydrous DMF (0.348 mL, 4.51 mmol) was then injected and the cooling bath was removed. After warming to room temperature, the reaction was diluted with water (200 mL), 1 M HCl (30 mL) and extracted with hexanes. The organic phase was collected and dried under MgSO$_4$. Compound **38** was isolated by column chromatography (1:1:DCM/Hexanes) to afford a clear yellow liquid (0.842 g, 78%). 1H-NMR (499 MHz; CDCl3): δ 9.97 (s, 1H), 7.16 (d, J = 0.8 Hz, 1H), 7.02 (s, 1H), 6.93 (s, 1H), 2.91 (t, J = 7.7 Hz, 2H), 2.59 (t, J = 7.7 Hz, 2H), 1.70-1.65 (m, 2H), 1.63-1.60 (m, 2H), 1.39-1.31 (m, 12H), 0.89 (t, J = 6.3 Hz, 6H). HRMS−ESI (m / z): [M + H]+ calc for C21H30OS2 363.1817, found 363.1818.

 SnBu32TC6CHO (39). Compound **38** (1.17 g, 3.23 mmol) was placed in an oven-dried 250 mL Schlenk flask and degassed by three vacuum/nitrogen cycles. Anhydrous tetrahydrofuran (THF, 30 mL) was injected and the solution was cooled to -78°C. N-methylpiperazine (0.394 mL, 3.55 mmol) was then injected, followed by n-butyllithium (2.5M in hexane, 1.42 mL, 3.55 mmol), after which the reaction was stirred for 20min.

The reaction was then warmed to -20°C, followed by a second addition of n-butillithium (2.5M in hexane, 1.42 mL, 3.55 mmol) and left stirring for another 30 min. Tributyltin chloride was then added (1.05 mL, 3.88 mmol) and the cooling bath was removed. After warming to room temperature, the reaction was quenched with 1 M HCl (20 mL). The crude was concentrated under vacuum, diluted in water (200 mL) and extracted with hexanes. The organic phase was separated and dried over magnesium sulfate (MgSO$_4$), followed by solvent removal under vacuum. Column chromatography in 1:1 DCM:hexanes afforded **39** as a yellow liquid (1.89 g, 90%). 1H-NMR (499 MHz; CDCl3): δ 9.97 (s, 1H), 7.30-7.29 (m, 1H), 7.03 (s, 1H), 2.90 (t, J = 7.7 Hz, 2H), 2.54 (t, J = 8.0 Hz, 2H), 1.68 (dt, J = 15.2, 7.5 Hz, 2H), 1.62-1.51 (m, 15H), 1.40-1.25 (m, 25H), 1.14 (dd, J = 9.7, 6.8 Hz, 5H), 0.94-0.85 (m, 22H). HRMS−ESI (m / z): [M + H]+ calc for C33H56OS2Sn 653.2874, found 653.2848.

SnBu3BDTO2TC8SnBu3 (40). Molecule **40** was synthesized according to a published procedure.

SnBu3BDTC8SnBu3 (41). Molecule **41** was synthesized according to a published procedure.

CHO2TC6BTDBr (42). 2,1,3-benzothiadiazole (0.955 g, 3.25 mmol), **39** (2.12 g, 3.25 mmol), bis(dibenzylidineacetone)palladium (0) (0.093 g, 0.163 mmol) and triphenylarsine (0.1g, 0.325 mmol) were placed in an oven-dried and degassed by three vacuum/nitrogen cycles. Degassed DMF (30 mL) was then injected into the flask and the solution mixture was stirred for 12hrs at 100 °C under inert atmoshphere. After cooling to room temperature, the reaction mixture was poured into water (300 mL) with potassium fluoride (1 M, 30 mL). The precipitate was filtered over Celite, washed with

additional water (100 mL) and the Celite was then washed with DCM until the washings were faint red color. Residual water was removed in a separatory funnel. DCM was removed under vacuum and the product was purified by column chromatography (1:1 DCM/Hexane, then 100% DCM) to afford **42** as a red liquid (0.910 g, 49%). 1H-NMR (400 MHz; CDCl3): δ 10.00 (s, 1H), 7.92 (d, *J* = 7.5 Hz, 1H), 7.50 (d, *J* = 7.5 Hz, 1H), 7.31 (s, 1H), 7.10 (s, 1H), 2.93 (t, *J* = 7.7 Hz, 2H), 2.59 (t, *J* = 7.9 Hz, 2H), 1.71 (dd, *J* = 15.0, 7.4 Hz, 2H), 1.61 (ddd, *J* = 22.8, 9.4, 5.7 Hz, 3H), 1.37-1.29 (m, 6H), 1.27-1.16 (m, 6H), 0.91-0.86 (m, 3H), 0.83 (q, *J* = 6.3 Hz, 3H). HRMS−ESI (m / z): [M + H]+ calc for C27H31BrN2OS3 575.0861, found 575.0853.

CHO2TC6BTDT (43). Compound **42** (0.910 g, 1.58 mmol), 2-tributylstannylthiophene (0.552 mL, 1.74 mmol) and tetrakistriphenylphosphine palladium(0) (0.185 g, 0.160 mmol) were placed in a Schlenk flask and degassed by three vacuum/nitrogen cycles. Degassed dimethylformamide (DMF, 20 mL) was then injected into the flask and the solution mixture was stirred for 4 hrs at 100 °C under nitrogen. After cooling to room temperature, the reaction mixture was poured into water (300 mL) with 1 M potassium fluoride (30 mL). The precipitate was filtered over Celite, washed with additional water (100 mL) and the Celite was then washed with DCM until the washings were faint red color. Residual water was removed in a separatory funnel. DCM was removed under vacuum and the product was purified by column chromatography (1:1 DCM/Hexanes) to afford 4**3** as a waxy red liquid (0.553 g, 60%). 1H-NMR (400 MHz; CDCl3): δ 10.00 (d, *J* = 3.1 Hz, 1H), 8.17 (dd, *J* = 3.7, 1.1 Hz, 1H), 7.93 (d, *J* = 7.4 Hz, 1H), 7.66 (d, *J* = 7.5 Hz, 1H), 7.50 (dd, *J* = 5.1, 1.0 Hz, 1H), 7.33 (s, 1H), 7.26-7.23 (m, 2H), 7.12 (s, 1H), 2.94 (t, *J* = 7.7 Hz, 2H), 2.65 (dd, *J* = 10.2, 5.5 Hz, 2H), 1.75-1.68 (m, 2H), 1.67-1.62 (m,

2H), 1.39-1.30 (m, 6H), 1.29-1.19 (m, 6H), 0.92-0.89 (m, 3H), 0.84-0.79 (m, 3H).

HRMS−ESI (m / z): [M + H]+ calc for C31H34N2OS4 579.1633, found 579.1626.

CHO2TC6BTDTBr (44). Compound **43** (0.553 g, 0.955 mmol) was disoolved in DCM

(25 mL) and covered with aluminum foil, then N-bromosuccinimide (0.190 g, 1.07 mmol)

was added in one portion and the reaction was left stirring for 12 hrs. The reaction was

then diluted in DCM (100 mL), then washed with 1 M NaOH (50 mL). The DCM layer

was then collected and dried under MgSO4 to afford 0.515 mg of crude (mixture of **43**

and **44**, roughly 50% yield), which was used without further purification. 1H-NMR (499

MHz; CDCl3): δ 8.18-8.17 (m, 1H), 7.94 (d, *J* = 7.5 Hz, 1H), 7.86-7.85 (m, 2H), 7.65

(dd, *J* = 7.4, 5.3 Hz, 2H), 7.50 (dd, *J* = 5.0, 0.9 Hz, 1H), 7.33 (d, *J* = 1.1 Hz, 2H), 7.26-

7.23 (m, 5H), 7.18 (d, *J* = 4.0 Hz, 1H), 7.12 (s, 2H), 2.94 (t, *J* = 7.7 Hz, 4H), 2.65 (td, *J* =

7.7, 0.8 Hz, 3H), 1.74-1.69 (m, 4H), 1.68-1.60 (m, 4H), 1.41-1.18 (m, 29H), 0.91-0.80

(m, 16H). MS-MALDI (m / z): [M]+ calc for C31H33BrN2OS4 656.0659, found 656.092.

CHO2TC6BTDTBDTO2TC8 (45). Compound **44** (0.515 g, 0.587 mmol [taking into

account that it is a mixture]), **40** (0.310 g, 0.268 mmol) and tetrakistriphenylphosphine

palladium(0) (0.070 g, 0.0605 mmol) were degassed by three vacuum/nitrogen cycles.

Degassed dimethylformamide (DMF, 20 mL) was then injected into the flask and the

solution mixture was stirred for 4 hrs at 100 °C under nitrogen. After cooling to room

temperature, the reaction mixture was poured into water (300 mL) with 1 M potassium

fluoride (30 mL). The precipitate was filtered over Celite, washed with additional water

(100 mL) and the Celite was then washed with DCM until the washings were faint red

color. Residual water was removed in a separatory funnel. DCM was removed under

vacuum and the product was purified by column chromatography (20% Hexane/DCM)

to afford **45** as a dark red solid (0.430 g, 42%). 1H-NMR (400 MHz; CDCl3): δ 9.99-9.97 (s, 2H), 8.08-8.05 (d, 2H), 7.91-7.87 (d, 2H), 7.76-7.74 (s, 2H), 7.64-7.61 (d, 2H), 7.37 (d, J = 3.8 Hz, 2H), 7.37-7.33 (m, 2H), 7.31-7.29 (s, 2H), 7.10-7.08 (s, 2H), 6.98-6.95 (d, 2H), 2.95-2.87 (m, 8H), 2.68-2.60 (m, 4H), 1.79-1.57 (m, 16H), 1.43-1.14 (m, 54H), 1.04-0.75 (m, 40H). MS-MALDI (m / z): [M+H]+ calc for $C_{96}H_{106}N_4O_2S_{12}$ 1731.5043, found 1731.387.

BnO2TC6BTDTBDTO2TC8 (46). Compound **45** (0.019 g, 0.0110 mmol) was dissolved in $CHCl_3$ (10 mL), then benzylcyanoacetate (0.008 mL, 0.0509 mmol) and triethylamine (0.015 mL, 0.108 mmol) were then added and the solution was stirred at 70 °C for 4 hrs. After cooling to room temperature, the solution was diluted with DCM (100 mL) and washed with 1 M HCl (30 mL). The organic phase was collected and the solvent removed under vacuum. The product was purified by size-exclusion chromatography to afford dark red solid (0.015 g, 66%). 1H-NMR (499 MHz; CDCl3): δ 8.42-8.39 (s, 2H), 8.11-8.08 (d, 2H), 7.92-7.89 (d, 2H), 7.76 (s, 2H), 7.66-7.62 (d, 2H), 7.47-7.42 (m, 4H), 7.42-7.34 (m, 12H), 7.14 (s, 2H), 6.98-6.98 (d, 2H), 5.35-5.33 (m, 4H), 2.96-2.90 (m, 4H), 2.80-2.74 (m, 4H), 2.68-2.64 (m, 6H), 1.79-1.74 (m, 2H), 1.70-1.58 (m, 10H), 1.44-1.14 (m, 58H), 1.06-0.77 (m, 38H). MS-MALDI (m / z): [M]+ calc for $C_{116}H_{120}N_6O_4S_{12}$ 2044.6020, found 2044.590.

BnNH2TC6BTDTBDTO2TC8 (47). Compound **45** (0.012 g, 0.00693 mmol) was dissolved in $CHCl_3$ (10 mL), then N-benzylcyanoacetamide (0.006 g, 0.0344 mmol) and piperidine (0.007 mL, 0.0725 mmol) were then added and the solution was stirred at 70 °C for 4 hrs. After cooling to room temperature, the solution was diluted with DCM (100 mL) and washed with 1 M HCl (30 mL). The organic phase was collected and the

solvent removed under vacuum. The product was purified by size-exclusion chromatography to afford dark red solid (0.010 g, 69%). 1H-NMR (500 MHz; CDCl3): δ 8.53 (s, 2H), 8.09 (d, J = 3.9 Hz, 2H), 7.91 (d, J = 7.5 Hz, 2H), 7.77 (s, 2H), 7.65 (t, J = 3.6 Hz, 2H), 7.39-7.30 (m, 16H), 7.14 (s, 2H), 6.98 (d, J = 3.4 Hz, 2H), 6.58 (dd, J = 7.6, 3.9 Hz, 2H), 4.61 (d, J = 5.7 Hz, 4H), 2.96-2.91 (m, 6H), 2.81-2.78 (m, 4H), 2.68-2.64 (m, 6H), 1.79-1.72 (m, 4H), 1.71-1.62 (m, 10H), 1.44-1.35 (m, 16H), 1.36-1.30 (m, 16H), 1.30-1.18 (m, 20H), 0.99-0.93 (m, 8H), 0.92-0.87 (m, 8H), 0.87-0.80 (m, 10H). MS-MALDI (m / z): [M]+ calc for $C_{116}H_{122}N_8O_2S_{12}$ 2042.6339, found 2042.662.

C8OCOCN (48). Molecule **48** was prepared according to a literature procedure. 1H-NMR (499 MHz; CDCl3): δ 4.20 (t, J = 6.8 Hz, 2H), 3.45 (s, 2H), 1.68 (quintet, J = 7.2 Hz, 2H), 1.37-1.27 (m, 10H), 0.88 (t, J = 7.0 Hz, 3H). HRMS−ESI (m / z): [M + NH4]+ calc for $C_{11}H_{19}NO_2$ 215.1754, found 215.1768.

C8NHCOCN (49). Cyanoacetic acid (1.00 g, 11.7 mmol) was suspended in DCM (20 mL), then triethylamine (2.45 mL, 17.6 mmol) was added, followed by 1-Ethyl-3-(3-dimethylaminopropyl)carbodiimide (2.69 g, 14.0 mmol) and hydroxybenzotriazole (2.15 g, 14.0 mmol). The solution was stirred for 2 minutes before adding 1-octylamine (2.32 mL, 14.0 mmol). The reaction was stirred for 1 hour before adding 1 M HCl (10 mL), then extracting in DCM (50 mL). The DCM layer was collected and the solvent removed under vacuum. Molecule **49** was isolated by column chromatography (1% MeOH/DCM) to give a white solid (2.24 g, 98%). 1H-NMR (499 MHz; CDCl3): δ 6.39 (dd, J = 1.7, 0.9 Hz, 1H), 3.29 (q, J = 6.7 Hz, 2H), 1.54 (quintet, J = 7.1 Hz, 2H), 1.31-1.28 (m, 11H), 0.88 (t, J = 9.8 Hz, 3H). HRMS−ESI (m / z): [M + Na]+ calc for $C_{11}H_{20}N_2O$ 219.1477, found 219.1465.

C8CNO2TC6BTDTBDTO2TC8 (50). Compound **45** (0.090 g, 0.0520 mmol) was dissolved in EtCl2 (20 mL), then **48** (0.5 g, 2.53 mmol) and piperidine (1.00 mL, 7.17 mmol) were then added and the solution was stirred at 80 °C for 4 hrs. After cooling to room temperature, the solvent was removed under vacuum. The crude was suspended in MeOH (30 mL) then filtered through Celite, followed by addition of more MeOH (50 mL). The washings were discarded and the Celite pad was washed with DCM until the washings were faint red. The solvent was removed under vacuum and the product was isolated by gel permeation chromatography to afford a dark red solid (0.070 g, 64%). 1H-NMR (400 MHz; CDCl3): δ 8.38-8.36 (s, 2H), 8.09-8.06 (d, 2H), 7.92-7.88 (d, 2H), 7.78-7.74 (s, 2H), 7.65-7.61 (d, 3H), 7.40-7.36 (m, 4H), 7.36-7.33 (d, 2H), 7.14-7.12 (s, 2H), 6.98-6.94 (d, 2H), 4.33-4.22 (m, 5H), 4.22-4.12 (m, 4H), 2.96-2.89 (m, 5H), 2.81-2.72 (m, 5H), 2.72-2.61 (m, 6H), 1.81-1.71 (m, 7H), 1.70-1.57 (m, 10H), 1.50-1.17 (m, 49H), 1.05-0.78 (m, 27H). MALDI-MS (m / z): [M]+ calc for $C_{118}H_{140}N_6O_4S_{12}$ 2088.7585, found 2088.702.

C8CNNH2TC6BTDTBDTO2TC8 (51).Compound **45** (0.090 g, 0.0520 mmol) was dissolved in EtCl2 (20 mL), then **49** (0.5 g, 2.55 mmol) and piperidine (1.00 mL, 7.17 mmol) were then added and the solution was stirred at 80 °C for 4 hrs. After cooling to room temperature, the solvent was removed under vacuum. The crude was suspended in MeOH (30 mL) then filtered through Celite, followed by addition of more MeOH (50 mL). The washings were discarded and the Celite pad was washed with DCM until the washings were faint red. The solvent was removed under vacuum and the product was isolated by gel permeation chromatography to afford a dark red solid (0.065 g, 59%). 1H-NMR (400 MHz; CDCl3): δ 8.46-8.44 (s, 2H), 8.10-8.05 (d, 2H), 7.92-7.86 (d, 2H),

7.77-7.73 (s, 2H), 7.65-7.60 (d, 2H), 7.39-7.35 (d, 2H), 7.36-7.30 (m, 4H), 7.13-7.10 (s, 2H), 6.98-6.94 (d, 2H), 6.27-6.20 (m, 2H), 3.44-3.32 (m, 5H), 2.96-2.88 (m, 4H), 2.80-2.72 (m, 4H), 2.69-2.60 (m, 4H), 1.81-1.72 (m, 3H), 1.71-1.58 (m, 12H), 1.44-1.17 (m, 40H), 1.05-0.78 (m, 24H). MALDI-MS (m / z): [M]+ calc for $C_{118}H_{142}N_8O_2S_{12}$ 2086.7904, found 2086.873.

TC6PhTC6 (52). A Schlenk flask containing 3-hexylthiophene (5.00 g, 29.7 mmol) was degassed by three nitrogen/vacuum cycles. Anhydrous THF (40 mL) was then injected and the solution was cooled to -78 °C. N-butyllithium (2.5 M in hexane, 13.1 mL, 32.8 mmol) was then added dropwise under nitrogen and the reaction was left stirring for 30 minutes before adding magnesium bromide ethyl ethereate (7.71 g, 29.9 mmol) and removing the cooling bath. Once the flask warmed to room temperature, 1,4-dibromobenzene (2.80 g, 11.9 mmol) was added, followed by dichloro[1,3-bis(diphenyphosphino)propane]palladium(II) (0.855 g, 1.49 mmol). The reaction was then refluxed under nitrogen for 4 hours. After cooling to room temperature, hexane was added to the crude and the suspension filtered. The solid residue was discarded and the hexane/THF were evaporated under vacuum. The product was isolated by column chromatography (Hexane) to give **52** as a white solid (2.11 g, 35%). 1H-NMR (499 MHz; CDCl3): δ 7.58 (s, 3H), 7.17 (d, *J* = 1.1 Hz, 2H), 6.87 (s, 2H), 2.62 (t, *J* = 7.7 Hz, 4H), 1.66 (dt, *J* = 15.1, 7.5 Hz, 4H), 1.32-1.25 (m, 13H), 0.91 (d, *J* = 6.3 Hz, 6H). HRMS-ESI (m / z): [M+H]+ calc for $C_{26}H_{34}S_2$ 411.2181, found 411.2178.

C_TC6PhTC6 (53). A Schlenk flask containing 2-bromo-3-hexylthiophene (5.00 g, 20.2 mmol) was degassed, then dissolved in anhydrous THF (30 mL). Freshly polished magnesium (0.736 g, 30.7 mmol) was then added, followed by iodine (0.120 g, 0.472

mmol). The suspension was heated until the color of iodine disappeared. The flask was then submerged in an ice-bath for a few minutes, then taken out, to maintain a gentle boiling of THF. When the reaction cooled to room temperature, the Grignard reagent was cannulated into a flask containing 1,4-dibromobenzene (2.17 g, 9.2 mmol) and dichloro[1,3-bis(diphenyphosphino)propane]palladium(II) (0.530 g, 0.920 mmol) dissolved in anhydrous THF (20 mL) under nitrogen. The reaction was then refluxed for 2hrs. After cooling to room temperature, hexane was added to the crude and the suspension filtered. The solid residue was discarded and hexane/THF were evaporated under vacuum. The product was isolated by column chromatography (Hexane) to give **53** as a colorless liquid (2.52 g, 67%).1H-NMR (499 MHz; CDCl3): δ 7.26 (d, J = 5.2 Hz, 2H), 7.01 (d, J = 5.2 Hz, 2H), 2.71 (t, J = 7.9 Hz, 4H), 1.65 (dd, J = 15.2, 7.4 Hz, 4H), 1.34-1.28 (m, 14H), 0.91-0.87 (m, 7H). MALDI-MS (m / z): [M]+ calc for $C_{26}H_{34}S_2$ 410.2102, found 410.385.

TC6PhTC6CHO (54). Compound **52** (1.00g, 2.43 mmol) was placed in an oven-dried 100 mL Schlenk flask and degassed by three vacuum/nitrogen cycles. Anhydrous THF (15 mL) was injected and the solution was cooled to -78 °C. N-butyllithium (2.5M in hexanes, 1.17 mL, 2.93 mmol) was then injected, and the reaction was left stirring for 30 min. Anhydrous DMF (0.280 mL, 3.63 mmol) was then injected and the cooling bath was removed. After warming to room temperature, the reaction was diluted with water (200 mL), 1 M HCl (30 mL) and extracted with hexanes. The organic phase was collected and dried under $MgSO_4$. Compound **54** was isolated by column chromatography (1:1:DCM/Hexanes) to afford a yellow solid (0.400 g, 38%). 1H-NMR (400 MHz; CDCl3): δ 10.02 (s, 1H), 7.67-7.63 (m, 4H), 7.23-7.21 (m, 2H), 6.91 (d, J =

0.5 Hz, 1H), 2.96 (t, *J* = 7.7 Hz, 2H), 2.63 (d, *J* = 7.5 Hz, 2H), 1.72 (dt, *J* = 14.2, 6.7 Hz, 2H), 1.66 (dd, *J* = 12.7, 6.3 Hz, 2H), 1.40-1.32 (m, 12H), 0.90 (d, *J* = 6.9 Hz, 6H). HRMS−ESI (m / z): [M]+ calc for C27H34OS2 438.2051.

BrTC6PhTC6CHO (55). Compound **54** (0.400 g, 0.912 mmol) was dissolved in DCM (25 mL) and covered with aluminum foil, then N-bromosuccinimide (0.195 g, 1.10 mmol) was added in one portion and the reaction was left stirring for 24 hrs. The reaction was then diluted in DCM (100 mL) and washed with 1 M NaOH (50 mL). The DCM layer was collected and dried under vacuum. Product **55** was isolated after passing though a silica plug (DCM) to afford 0.657 g (72%) of a yellow solid. 1H-NMR (400 MHz; CDCl3): δ 9.86 (s, 1H), 7.65 (s, 1H), 7.48-7.42 (m, 4H), 6.94 (s, 1H), 2.69 (t, *J* = 7.8 Hz, 2H), 2.61 (t, *J* = 7.8 Hz, 2H), 1.64-1.58 (m, 4H), 1.29-1.23 (m, 13H), 0.88-0.83 (m, 7H). HRMS−ESI (m / z): [M + H]+ calc for C27H33BrOS2 519.1215, found 519.1218.

CHOTC6PhTC6BDTO2TC8 (56). Compound **40** (0.232 g, 0,200 mmol) and **55** (0.238 g, 0.441 mmol) were degassed by three vacuum/nitrogen cycles, then dissolved in degassed DMF (30 mL). To this solution, a previously degassed solution of bis(dibenzylidineacetone)palladium(0) (0.012 g, 0.0209 mmol) and triphenylphosphine (0.021 g, 0.0800 mmol) was added. The solution was stirred for 2 hrs at 100 °C under nitrogen. After cooling to room temperature, the reaction mixture was poured into water (300 mL) with 1 M potassium fluoride (30 mL). The precipitate was filtered over Celite, washed with additional water (100 mL) and the Celite was then washed with DCM until the washings were faint red color. Residual water was removed in a separatory funnel. DCM was removed under vacuum and the product was purified by column chromatography (60%hexane/40% DCM) to afford **56** as a waxy orange solid. The solid

was further washed with hexane and the precipitate isolated by filtration (0.088 g, 40%).1H-NMR (499 MHz; CDCl3): δ 10.02 (s, 2H), 7.69 (s, 2H), 7.65-7.62 (m, 7H), 7.36 (d, *J* = 3.5 Hz, 2H), 7.25-7.23 (m, 4H), 6.92 (t, *J* = 3.2 Hz, 2H), 2.96 (t, *J* = 7.7 Hz, 4H), 2.89 (d, *J* = 6.8 Hz, 4H), 1.73-1.69 (m, 10H), 1.41-1.27 (m, 46H), 0.92-0.88 (m, 24H). MALDI-MS (m / z): [M]+ calc for C88H106O2S8 1450.5958, found 1450.5958.

C8CNOTC6PhTC6BDTO2TC8 (57). Compound **56** (0.035 g, 0.0241 mmol) was dissolved in EtCl2 (15 mL), then **48** (0.050 g, 0.261 mmol) and triethylamine (0.5 mL, 3.59 mmol) were then added and the solution was stirred at 80 °C for 4 hrs. After cooling to room temperature, the solvent was removed under vacuum and the crude was suspended in MeOH (30 mL), then filtered through Celite, followed by addition of more MeOH (50 mL). The washings were discarded and the Celite pad was washed with DCM until the washings were faint red. The solvent was removed under vacuum and the product was isolated by gel permeation chromatography to afford a red solid (0.0078 g, 18%). 1H-NMR (400 MHz; CDCl3): δ 8.42-8.40 (m, 2H), 7.72-7.66 (m, 6H), 7.63-7.59 (m, 6H), 7.36-7.33 (m, 3H), 7.29-7.26 (m, 3H), 6.92-6.90 (m, 2H), 4.31-4.27 (m, 4H), 2.89-2.80 (m, 12H), 1.76-1.61 (m, 19H), 1.44-1.25 (m, 77H), 0.95-0.87 (m, 31H). MALDI-MS (m / z): [M]+ calc for C110H136N2O4S8 1804.8266, found 18089.915.

C8CNNHTC6PhTC6BDTO2TC8 (58). Compound **56** (0.053 g, 0.0365 mmol) was dissolved in EtCl2 (15 mL), then **49** (0.071 g, 3.62 mmol) and piperidine (0.5 mL, 5.06 mmol) were then added and the solution was stirred at 80 °C for 4 hrs. After cooling to room temperature, the solvent was removed under vacuum and the crude was suspended in MeOH (30 mL), then filtered through Celite, followed by addition of more MeOH (50 mL). The washings were discarded and the Celite pad was washed with

DCM until the washings were faint red. The solvent was removed under vacuum and the product was isolated by gel permeation chromatography to afford a red solid (0.016 g, 24%). 1H-NMR (400 MHz; CDCl3): δ 8.51-8.47 (m, 2H), 7.71-7.57 (m, 10H), 7.36-7.31 (m, 2H), 7.25 (s, 2H), 7.24-7.21 (m, 6H), 6.93-6.91 (m, 2H), 6.28-6.24 (m, 2H), 3.40 (dt, *J* = 10.6, 5.0 Hz, 4H), 2.90-2.78 (m, 12H), 1.71-1.59 (m, 15H), 1.38-1.23 (m, 57H), 0.93-0.80 (m, 30H). MALDI-MS (m / z): [M]+ calc for $C_{110}H_{134}N_4O_2S_8$ 1802.8585, found 1806.917.

C_TC6PhTC6CHO (59). Compound **53** (1.25g, 3.04 mmol) was placed in an oven-dried 100 mL Schlenk flask and degassed by three vacuum/nitrogen cycles. Anhydrous THF (15 mL) was injected and the solution was cooled to -78 °C. N-butyllithium (2.5M in hexanes, 1.46 mL, 4.00 mmol) was then injected, and the reaction was left stirring for 30 min. Anhydrous DMF (0.355 mL, 4.60 mmol) was then injected and the cooling bath was removed. After warming to room temperature, the reaction was diluted with water (200 mL), 1 M HCl (30 mL) and extracted with hexanes. The organic phase was collected and dried under $MgSO_4$. Compound **59** was isolated by column chromatography (1:1:DCM/Hexanes) to afford a clear yellow solid (0.900 g, 67%) 1H-NMR (499 MHz; CDCl3): δ 9.87 (s, 1H), 7.67 (s, 1H), 7.53-7.48 (m, 4H), 7.27 (s, 1H), 7.01 (d, *J* = 5.2 Hz, 1H), 2.71 (q, *J* = 7.9 Hz, 4H), 1.68-1.60 (m, 5H), 1.34-1.25 (m, 17H), 0.87 (dd, *J* = 7.2, 3.5 Hz, 7H). HRMS calc m/z for $C_{27}H_{34}OS_2$ 438.2051.

C_BrTC6PhTC6CHO (60). Compound **59** (0.900 g, 2.05 mmol) was dissolved in DCM (25 mL) and covered with aluminum foil, then N-bromosuccinimide (0.438 g, 2.46 mmol) was added in one portion and the reaction was left stirring for 24 hrs. The reaction was then diluted in DCM (100 mL), then washed with 1 M NaOH (50 mL). The DCM layer

was then collected and dried under vacuum. Product 60 was isolated after passing

through a silica plug (1:1:DCM/Hexane) to afford a yellow solid (0.743 g, 70%). 1H-NMR

(400 MHz; CDCl3): δ 9.86 (d, *J* = 2.3 Hz, 1H), 7.65 (d, *J* = 1.8 Hz, 1H), 7.48-7.42 (m,

4H), 6.94 (s, 1H), 2.70 (d, *J* = 7.7 Hz, 2H), 2.62 (d, *J* = 7.7 Hz, 2H), 1.65-1.56 (m, 4H),

1.31-1.23 (m, 12H), 0.85 (dd, *J* = 6.8, 2.0 Hz, 6H). HRMS−ESI (m / z): [M + H]+ calc for

C27H33BrOS2 519.1215, found 519.1219.

C_CHOTC6PhTC6BDTO2TC8 (61). Compound **40** (0.770 g, 1.33 mmol) and **60** (0.700

g, 0.606 mmol) were degassed by three vacuum/nitrogen cycles, then dissolved in

degassed DMF (30 mL). To this solution, a previously degassed solution of

bis(dibenzylidineacetone)palladium(0) (0.080 g, 0.139 mmol) and triphenylarsine (0.085

g, 0.278 mmol) was added. The reaction was stirred for 2 hrs at 100 °C under nitrogen.

After cooling to room temperature, the reaction mixture was poured into water (300 mL)

with 1 M potassium fluoride (30 mL). The precipitate was filtered over Celite, washed

with additional water (100 mL) and the Celite was then washed with DCM until the

washings were faint red color. Residual water was removed in a separatory funnel.

DCM was removed under vacuum and the product was purified by column

chromatography (60%hexane/40% DCM) to afforda waxy orangeliquid, which was

further washed with hexane, and **61** was isolated by filtration as an orange solid (0.350

g,18%). 1H-NMR (400 MHz; CDCl3): δ 9.86 (s, 2H), 7.65 (d, *J* = 5.1 Hz, 4H), 7.53-7.47

(m, 8H), 7.32 (d, *J* = 3.5 Hz, 2H), 7.18 (s, 2H), 6.92 (d, *J* = 3.5 Hz, 2H), 2.88 (dd, *J* =

6.6, 3.9 Hz, 4H), 2.68 (dt, *J* = 12.0, 7.9 Hz, 8H), 1.70-1.60 (m, 10H), 1.39-1.25 (m, 37H),

0.94-0.90 (m, 6H), 0.86 (td, *J* = 6.8, 4.3 Hz, 16H). MALDI-MS (m / z): [M]+ calc for

C88H106O2S8 1450.5958, found 1450.663.

C_C8CNOTC6PhTC6BDTO2TC8 (62). Compound **61** (0.066 g, 0.0455 mmol) was dissolved in EtCl2 (15 mL), then **48** (0.090 g, 0.471 mmol) and triethylamine (0.5 mL, 3.59 mmol) were then added and the solution was stirred at 80 °C for 4 hrs. After cooling to room temperature, the solvent was removed under vacuum and the crude was suspended in MeOH (30 mL), then filtered through Celite, followed by addition of more MeOH (50 mL). The washings were discarded and the Celite pad was washed with DCM until the washings were faint red. The solvent was removed under vacuum and the product was isolated by gel permeation chromatography to afford a red solid (0.049 g, 60%). 1H-NMR (400 MHz; CDCl3): δ 8.25 (s, 2H), 7.66 (d, J = 7.6 Hz, 4H), 7.52 (s, 6H), 7.32 (d, J = 3.5 Hz, 2H), 7.18 (s, 2H), 6.96 (s, 2H), 6.92 (d, J = 3.5 Hz, 2H), 4.28 (t, J = 6.8 Hz, 4H), 2.88 (dd, J = 6.4, 4.1 Hz, 4H), 2.69 (dt, J = 17.2, 8.4 Hz, 8H), 1.76-1.70 (m, 6H), 1.66-1.61 (m, 6H), 1.36-1.23 (m, 46H), 0.98-0.93 (m, 8H), 0.90-0.84 (m, 16H). MALDI-MS (m / z): [M]+ calc for C110H136N2O4S8 1804.8266, found 1808.841.

C_C8CNNHTC6PhTC6BDTO2TC8 (63). Compound **61** (0.066 g, 0.0455 mmol) was dissolved in EtCl2 (15 mL), then **49** (0.090 g, 0.459 mmol) and piperidine (0.5 mL, 5.06 mmol) were then added and the solution was stirred at 80 °C for 4 hrs. After cooling to room temperature, the solvent was removed under vacuum and the crude was suspended in MeOH (30 mL), then filtered through Celite, followed by addition of more MeOH (50 mL). The washings were discarded and the Celite pad was washed with DCM until the washings were faint red. The solvent was removed under vacuum and the product was isolated by gel permeation chromatography to afford a red solid (0.039 g, 48%). 1H-NMR (400 MHz; CDCl3): δ 8.34 (s, 2H), 7.66 (s, 2H), 7.60 (s, 2H), 7.53 (s,

8H), 7.34 (d, J = 3.5 Hz, 2H), 7.20 (s, 2H), 6.94 (d, J = 3.5 Hz, 2H), 6.24 (t, J = 5.7 Hz, 2H), 3.42 (t, J = 6.6 Hz, 4H), 2.90 (dd, J = 6.6, 3.9 Hz, 4H), 2.70 (dt, J = 14.9, 7.6 Hz, 10H), 1.65 (dd, J = 15.4, 7.1 Hz, 11H), 1.60-1.56 (m, 15H), 1.37-1.28 (m, 57H), 0.98-0.86 (m, 31H). MALDI-MS (m / z): [M]+ calc for $C_{110}H_{134}N_4O_2S_8$ 1802.8585, found 1806.917.

TC6TTC6 (64). A Schlenk flask containing 2-bromo-3-hexylthiophene (5.00 g, 20.2 mmol) was degassed, then dissolved in anhydrous THF (30 mL). Freshly polished magnesium (0.736 g, 30.7 mmol) was then added, followed by iodine (0.256 g, 1.01 mmol). The suspension was heated until the color of iodine disappeared. The flask was then submerged in an ice-bath for a few minutes, then taken out, to maintain a gentle boiling of THF. When the reaction cooled to room temperature, the Grignard reagent was cannulated into a flask containing 2,5-dibromothiophene (1.25 mL, 9.2 mmol) and dichloro[1,3-bis(diphenyphosphino)propane]palladium(II) (0.520 g, 0.900 mmol) dissolved in anhydrous THF (20 mL) under nitrogen. The reaction was then refluxed for 2hrs. After cooling to room temperature, hexane was added to the crude and the suspension filtered. The solid residue was discarded and hexane/THF were evaporated under vacuum. The product was isolated by column chromatography (Hexane) to give **53** as a colorless liquid (2.55 g, 67%). 1H-NMR (400 MHz; CDCl3): δ 7.18-7.17 (m, 2H), 7.05 (s, 2H), 6.94 (d, J = 5.2 Hz, 2H), 2.78 (t, J = 7.9 Hz, 4H), 1.69-1.63 (m, 4H), 1.40-1.36 (m, 4H), 1.32-1.29 (m, 8H), 0.89 (qd, J = 4.1, 3.2 Hz, 6H). HRMS−ESI (m / z): [M]+ calc for $C_{24}H_{32}S_3$ 416.1666, found 416.1668.

TC6TTC6SnBu3 (65). Compound **64** (1.00 g, 2.40 mmol) was placed in an oven-dried 100 mL Schlenk flask and degassed by three vacuum/nitrogen cycles. Anhydrous THF

(30 mL) was injected and the solution was cooled to -78 °C. N-butyllithium (2.5 M in hexanes, 1.06 mL, 2.64 mmol) was then injected, and the reaction was left stirring for 30 min. Tributyltin chloride (0.712 mL, 2.64 mmol) was then injected and the cooling bath was removed. After warming to room temperature, the reaction was diluted in water (100 mL), 1 M NaOH (20 mL) and extracted with hexanes. The organic phase was collected, dried under $MgSO_4$, followed by solvent removal under vacuum to afford **65** as a yellow liquid (1.63 g, 96%), which was used without further purification. 1H-NMR (400 MHz; CDCl3): δ 7.18-7.15 (m, 1H), 7.04 (q, *J* = 1.9 Hz, 2H), 6.96-6.92 (m, 2H), 2.82-2.78 (m, 4H), 1.68-1.56 (m, 9H), 1.43-1.27 (m, 19H), 1.15-1.09 (m, 4H), 0.94-0.85 (m, 15H). MALDI-MS (m / z): [M]+ calc for $C_{36}H_{58}S_3Sn$ 706.2723, found 706.341.

Br2AntC8 (66). Br2COAnt (reference! 2.00 g, 5.62 mmol) was suspended in THF/H2O (4:1 ratio, 20 mL), then sodium dithionite (2.45 g, 14.5 mmol) was added and the mixture was stirred for 10 minutes before adding 6M NaOH (5 mL), 2-ethylhexyl bromide (5.00 mL, 28.1 mmol) and tetrabutylammonium bromide (2.00 g, 61.8 mmol) in sequence. The reaction was left refluxing for 12 hrs. After cooling to room temperature, the reaction was diluted in water (200 mL) and extracted in hexanes. The product was purified by column chromatography (5% DCM/Hexane) to give **66** as a yellow liquid (1.35 g, 36%). MALDI-MS (m / z): [M]+ calc for $C_{38}H_{44}Br_2S_2$ 590.1395, found 590.200.

TC6TTC6AntC8 (67). A Schlenk flask containing compound **66** (0.420 g, 0.645 mmol), **65** (1.00 g, 1.42 mmol) and tetrakistriphenylphosphine palladium(0) (0.154 g, 0.133 mmol) was degassed by three vacuum/nitrogen cycles. Degassed dimethylformamide (DMF, 15 mL) was then injected into the flask and the solution mixture was stirred for 2 hrs at 100 °C under nitrogen. After cooling to room temperature, the reaction mixture

was poured into water (300 mL) with 1 M potassium fluoride (30 mL). The precipitate was filtered over Celite, washed with additional water (100 mL) and the Celite was then washed with DCM until the washings were faint yellow color. Residual water was removed in a separatory funnel. DCM was removed under vacuum and the product was purified by column chromatography (20% DCM/Hexanes) to afford **67** as a yellow solid (0.290 g, 59%). ^{1}H-NMR (500 MHz; CDCl$_3$): HRMS−ESI (m / z): [M]+ calc for C78H102O2S6 1262.6204, found sample decomposes.

CHOTC6TTC6AntC8 (68). Phosphorus oxychloride (0.030 mL, 0.261 mmol) was added to anhydrous DMF (1 mL) and heated under nitrogen until the solution turned red. The Vilsmeier reagent was added to a solution of 67 (0.110 g, 0.0870 mmol) in EtCl2 (20 mL) and heated to 60 C for four hours. Once cooled to room temperature, the reaction was poured onto saturated sodium bicarbonate solution (50 mL), the extracted, and the EtCl2 layer collected and dried under vacuum. The product was purified by column chromatography (DCM) to give a red solid (0.032 g, 28%). HRMS−ESI (m / z): [M]+ calc for C80H102O4S66 1318.6102, found sample decomposes.

TC6TTC6CHO (69). A Schlenk flask containing compound **64** (0.920g, 2.21 mmol) was degassed by three vacuum/nitrogen cycles. Anhydrous THF (15 mL) was injected and the solution was cooled to -78 °C. N-butyllithium (2.5M in hexanes, 1.06 mL, 2.65 mmol) was then injected, and the reaction was left stirring for 30 min. Anhydrous DMF (0.260 mL, 3.32 mmol) was then injected and the cooling bath was removed. After warming to room temperature, the reaction was diluted with water (200 mL), 1 M HCl (30 mL) and extracted with hexanes. The organic phase was collected and dried under MgSO$_4$. Compound **69** was isolated by column chromatography (1:1:DCM/Hexanes) to afford a

clear yellow liquid (0.670, 68%). 1H-NMR (400 MHz; CDCl3): δ 9.83 (s, 1H), 7.60 (s, 1H), 7.24 (d, *J* = 3.8 Hz, 1H), 7.24-7.21 (m, 1H), 7.10 (d, *J* = 3.8 Hz, 1H), 6.96 (d, *J* = 5.2 Hz, 1H), 2.85-2.79 (m, 4H), 1.69 (dt, *J* = 15.5, 7.7 Hz, 4H), 1.43-1.30 (m, 12H), 0.89 (dq, *J* = 6.9, 3.5 Hz, 6H).HRMS−ESI (m / z): [M + H]+ calc for C25H32OS3 445.1694, found 445.1696.

BrTC6TTC6CHO (70). Compound **69** (0.900 g, 2.02 mmol) was dissolved in DCM (25 mL) and covered with aluminum foil, then N-bromosuccinimide (0.432 g, 2.43 mmol) was added in one portion and the reaction was left stirring for 12 hrs. The reaction was then diluted in DCM (100 mL) and washed with 1 M NaOH (50 mL). The DCM layer was then collected and dried under vacuum. The product was isolated after running through a silica plug (DCM) to give a dark yellow liquid (0.860 g, 81% yield). 1H-NMR (500 MHz; CDCl3): δ 9.83 (s, 1H), 7.60 (d, *J* = 4.6 Hz, 1H), 7.22 (d, *J* = 3.8 Hz, 1H), 7.05 (d, *J* = 3.8 Hz, 1H), 6.92 (s, 1H), 2.82 (t, *J* = 6.5 Hz, 2H), 2.72 (t, *J* = 7.8 Hz, 2H), 1.69 (dd, *J* = 7.6, 3.2 Hz, 2H), 1.63-1.60 (m, 2H), 1.33-1.25 (m, 12H), 0.89 (t, *J* = 6.3 Hz, 6H). HRMS−ESI (m / z): [M + H]+ calc for C25H31BrOS3 523.0799, found 523.0794.

CHOTC6TTC6BDTC8 (71). A Schlenk flask containing compound **41** (0.525 g, 0.512 mmol), **70** (0.590 g, 1.13 mmol) and tetrakistriphenylphosphine palladium(0) (0.120 g, 0.102 mmol) was then degassed by three vacuum/nitrogen cycles. Degassed toluene (20 mL) was then injected into the flask and the solution mixture was stirred for 3 hrs at 100 °C under nitrogen. After cooling to room temperature, the reaction mixture was poured into water (300 mL) with 1 M potassium fluoride (30 mL). The toluene layer was collected and dried under vacuum and the product was purified by column

chromatography (20% Hexanes in DCM)) to afford **71** as a dark red solid (0.142 g,

21%). MALDI-MS (m / z): [M + H]+ calc for C76H98O4S8 1330.5310, found 1331.506.

CHOTC6TTC6BDTO2TC8 (72). A Schlenk flask containing compound **40** (0.542 g,

0.469 mmol), **70** (0.540 g, 1.03 mmol) and tetrakistriphenylphosphine palladium(0)

(0.110 g, 0.0938 mmol) was then degassed by three vacuum/nitrogen cycles. Degassed

toluene (20 mL) was then injected into the flask and the solution mixture was stirred for

3 hrs at 100 °C under nitrogen. After cooling to room temperature, the reaction mixture

was poured into water (300 mL) with 1 M potassium fluoride (30 mL). The toluene layer

was collected and dried under vacuum and the product was purified by column

chromatography (20% Hexanes in DCM)) to afford **72** as a dark red solid, which was

further washed with acetone, and the acetone-insoluble fraction collected and dried

(0.347 g, 34%). 1H-NMR (499 MHz; CDCl3): δ 9.86-9.85 (m, 3H), 7.66 (d, *J* = 2.8 Hz,

1H), 7.63-7.62 (m, 2H), 7.34 (t, *J* = 2.3 Hz, 2H), 7.27-7.26 (m, 2H), 7.16-7.15 (m, 4H),

6.96 (td, *J* = 2.3, 0.8 Hz, 2H), 2.94-2.91 (m, 4H), 2.88-2.84 (m, 6H), 2.82-2.77 (m, 6H),

1.74-1.70 (m, 11H), 1.46-1.35 (m, 43H), 1.01-0.92 (m, 27H). MALDI-MS (m / z): [M]+

calc for C84H102O2S10 1462.5087, found 1462.515.

Chapter 4 Additive-Like Alkyl Tails on DPP-Based Donors

4.1 Introduction

Within the field of OPVs, the processing conditions can sometimes have more impact on the performance of a design than its actual structure. The proof lies in observing the polymer designs from ten years ago to the ones used today, and it can be observed that there are not that many differences. For example the high performance polymer PTB7 was first reported in 2008;[224] it was a polymer of <20 kg/mol and two years later, after fluorination of one position on the TT unit and almost five-fold increase in molecular weight, it had almost doubled in PCE. Over the years, the synthetic methods have evolved because the effects of impurities and high polydispersity were understood better. Yet, more than synthetic methods, the processing conditions have changed; Chapter 1 discussed the different strategies used to optimize performance of OPV devices, as well as to improve the morphology of the active layer. Solvent

additives in particular, are known to dramatically improve morphology and enhance performance.

There are many reports stating importance and impact of solvent additives on morphology of the active layer,[110,225–227] but one recent study went further, by studying what happens when the solvent additive leaves the active layer, and found that the effect additives have on the active layer can be reversed, and if they prevent segregation, then it will be detrimental to the device if the additives evaporate. The recommendations the authors leave are either incorporate the additive character on the molecule, or seal the devices.[228] For practical applications, it obviously makes sense to seal the device, but the other suggestion, to incorporate the additive onto the design, is a fundamentally attractive idea. Something to keep in mind is that for industrial applications, the simpler the processing the better, so removing the need to add additives and do post-treatments is also an attractive idea. Incorporating a third component into a BHJ solution is not a new idea, many ternary blend system have been reported,[229] but most focus on complementing the absorption spectra of the primary donor, similar to tandem cells. This chapter will discuss the attempts aimed at introducing an additive-like character to OPV donors, for the purpose of improving morphology and performance of devices.

4.2 Evidence of Additive-Like Character in a Simple DPP-Based Donor

One of the lessons learned from past molecules was that starting with a simple design can save valuable time, especially when it has to be modified. With that said, the idea was to design a molecule, and have the design be flexible enough to allow for post-

modification of a specific part, where a functional group could be introduced, and that functional group would give the modified molecule the ability to act as an additive. The important thing to remember about additives is that they are used in fractions of a percent, so the devices of molecule one would be spiked with the additive one. The challenge became to make that idea happen synthetically. One of the additives discussed here and in many other OPV donors is DIO, but the iodine is prone to be hydrolyzed since it is such a good leaving group, so it quickly became necessary to maybe instead of looking for the actual additives, look for molecules than can have a similar effect. By looking at how the previous molecules were prepared, it was observed that upon using CB or DCB, the morphology of the active layers tended to improve, so if somehow CB, or a derivative of it could be incorporated into the design of an OPV, it could act as an additive. The iodo- version would probably work better, but the concern of its reactivity was still prevalent, and since this was a design to prove a concept, it was not immediately necessary to add more complexity to the design. The first design was synthesized by an undergraduate student in the lab; it consisted of a BDT core, immediately coupled to a symmetric DPP unit on both sides. The alkyl tails in the DPP cores were initially terminated in a bromo, which was displaced in an S_{N2}-type reaction with phenol, or chlorophenol (Figure 4.1a).

a

b

c

Donor	J_{sc} (mA/cm²)	V_{oc} (V)	FF (%)	η (%)
PhH (100%)	3.68	0.81	51	1.52
PhH:PhCl (75:25)	7.96	0.81	58	3.76
PhH:PhCl (50:50)	8.42	0.85	50	3.55
PhH:PhCl (25:75)	8.01	0.83	53	3.52
PhCl (100%)	3.30	0.83	45	1.24
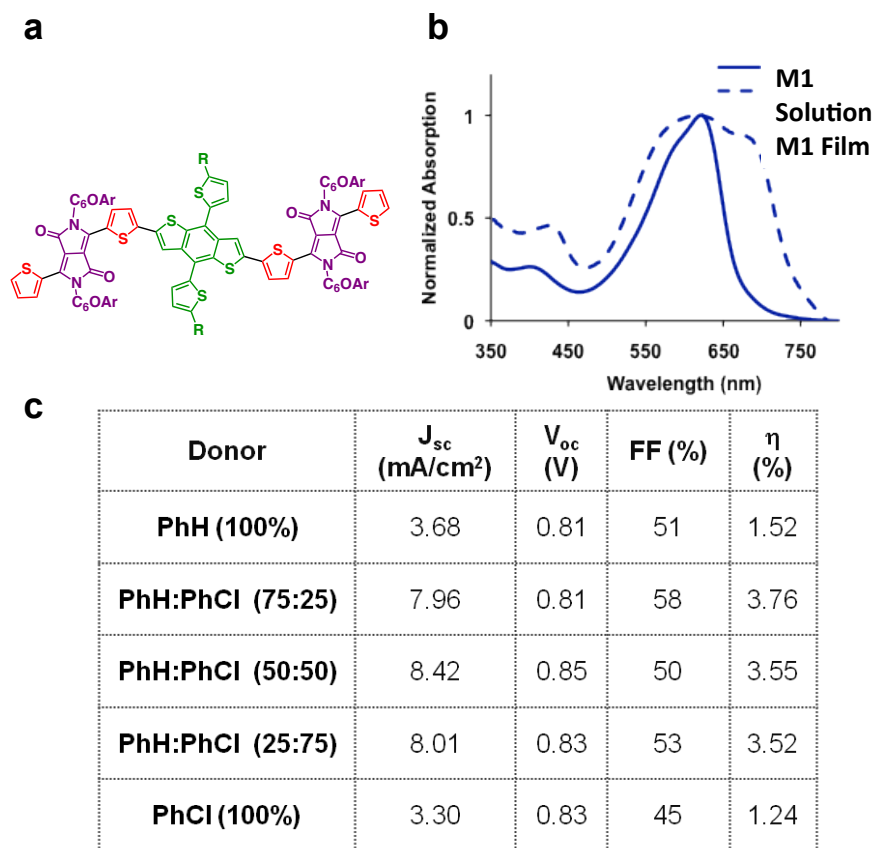
Figure 4.1. a) First design of an additive-containing BDT-DPP donor and its absorption spectrum (b); c) Summary of devices (Conditions. Acceptor: $PC_{61}BM$ (D:A 1-1) Chloroform – 5000rpm – Additive: 0.3vol% DIO – No Annealing).

The absorbance in solution and film are shown in Figure 4.1b. As expected from a molecule having DPP, the absorbance is strong in the visible region. In previous designs there was a single DPP unit, but since in this case there are two, the absorbance shifts to the red region. Also due to DPP's propensity to aggregate, the film absorption shows strong vibronic features that cover regions of the near-IR, all the way up to the UV. There was no significant difference in absorption of PhCl and PhH, so only the latter is shown.

Devices were fabricated with varying ratios of the chloro- (PhCl) version (ranging from 0-100%), along with the control (PhH). The mixtures were spin-coated from $CHCl_3$ solutions at 5000 rpm and not annealed. The devices summary is shown in Figure 4.1c. Devices of either pure PhH or PhCl, respectively showed an efficiency barely surpassing 1%, but as soon as some PhCl is added to PhH devices, the PCE increased and peaked at 25% **PhCl** content in a **PhH** device. The morphologies of the blends were studied with AFM but they do not offer an acceptable explanation of the improvement upon **PhCl** addition. Nevertheless, these results were encouraging since they shed evidence that a minority component could have a significant effect in the overall device performance. In this case, 25% of **PhCl** tripled the efficiency of the cell, which was quite noteworthy. Obviously, ideally it would preferred to lower the spike content to less than 5%, but for a first design, it was very exciting.

Although the initial objective was to use a molecule as an additive substitute, during the exploratory stages of this project, it became necessary to use DIO for the sake of reproducibility. In any case, all the blends had the exact same quantity of DIO and were processed the same, so there was still a way to compare the effect PhCl had on the devices. More studies were required, but since after some time both PhH and PhCl began developing stability problems, and the solubility needed to be improved, it was thought that perhaps a different design could address those two issues and provide more material for testing.

4.3 Asymmetric DPP Cores in Additive-Like Donors

Synthesis

In Chapter 2, it was mentioned that studies suggest having one thiophene spacer in between electron-rich or poor units can help increase the area of contact with fullerenes.[199] For that reason, it was desirable to have such a spacer between the BDT and DPP units for future designs. In order to be able to have a thiophene spacer, one of the positions from the DPP core had to be unreactive, or blocked, because otherwise there would be a statistical mixture of isomers that would become nearly impossible to separate. The way this problem was addressed is shown in Scheme 4.1 was by starting off with an asymmetric DPP core **75**, alkylate it with 1,6-dibromohexane, then brominate it with NBS, followed by Stille coupling of the thiophene spacer, then a second bromination to make the intermediate **79**, which was coupled to the stannylated BDT core **40** to make the tetrabromo BDT-DPP compound **80**. Lastly, the phenol and chlorophenol groups were attached to **80** to make the Ph (**81**) and PhCl (**82**) extended versions of the original molecule.
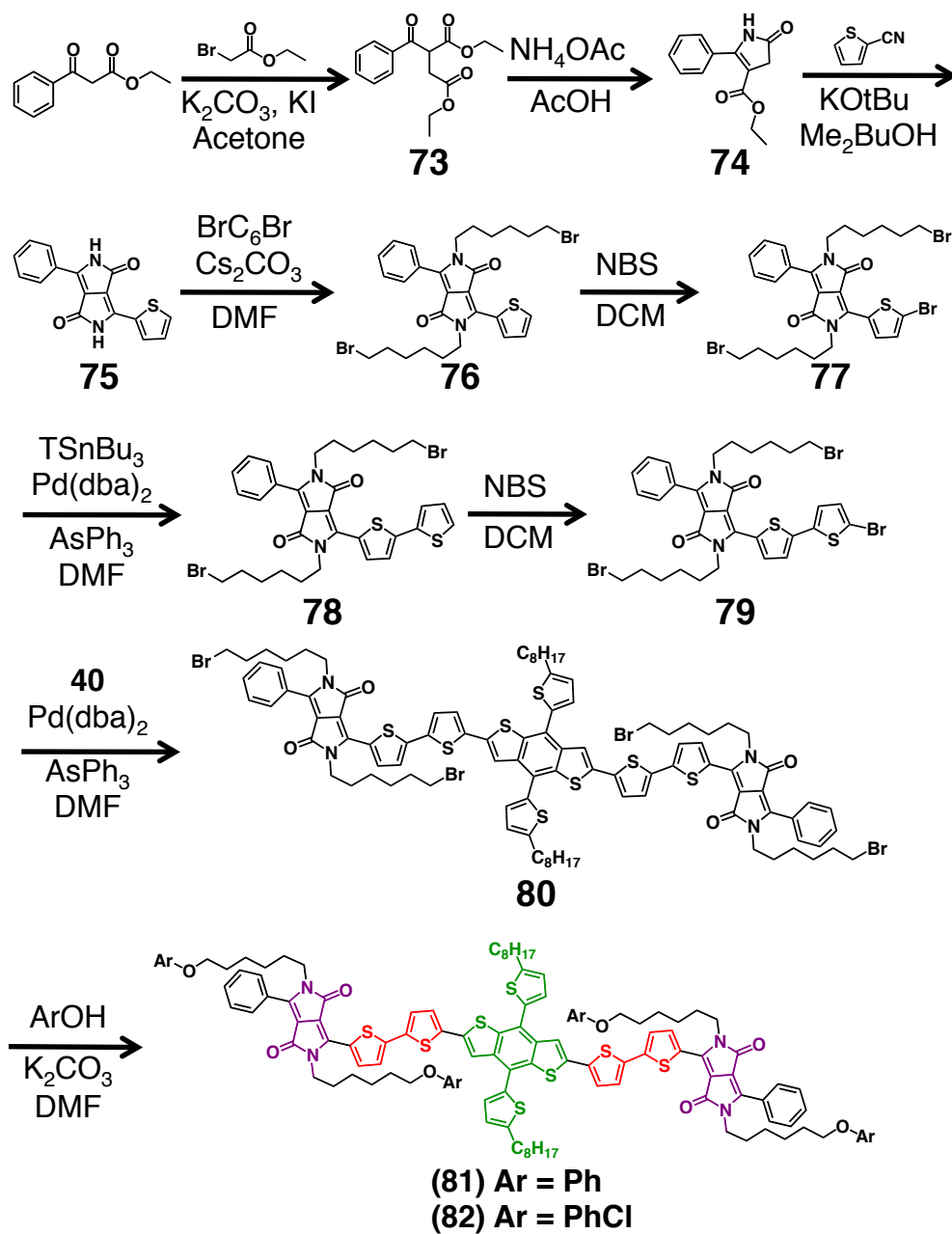
Scheme 4.1. Synthesis of an asymmetric DPP core for the additive-containing donor.

Absorption Studies

The absorbance of the two molecules is shown in Figure 4.2b. The extended core shows a few differences than the previous version. First, there are two absorption

bands, one possibly π-π* at 375 nm and another CT band at 550 nm, covering most of the visible, except for the red, but there is an improvement over the previous design. The absorption of film, however, does not show the enhanced vibronic broadening of the previous design. In fact, even though the solution absorption of molecules **81**-**82** is better than the first design, the film absorption is not. This can be understood by the fact that the DPP core is asymmetric, and one of the sides has a phenyl ring, which in the previous chapter was thought to decrease electronic coupling (in that case it was thiophenes, but DPP is two fused rings, so the torsion angle might be larger).

a

(81) Ar = Ph
(82) Ar = PhCl

b

c

D:A	J_{SC} (mA/cm²)	V_{OC} (V)	FF (%)	PCE (%)
81_PC61BM CHCl3 5000 rpm 100 °C 1 min	3.69	0.83	0.41	1.25
81_1:1 PC61BM CHCl3 5000 rpm No anneal	5.11	0.78	0.44	1.75
81 (10% 82): PC61BM CHCl3 5000 rpm MoOx No anneal	4.27	0.81	0.38	1.30
81 (10% 82): PC61BM CHCl3 5000 rpm No anneal	4.94	0.79	0.44	1.72
82 1:1 PC61BM CHCl3 5000 rpm MoOX no anneal	5.66	0.85	0.47	2.26
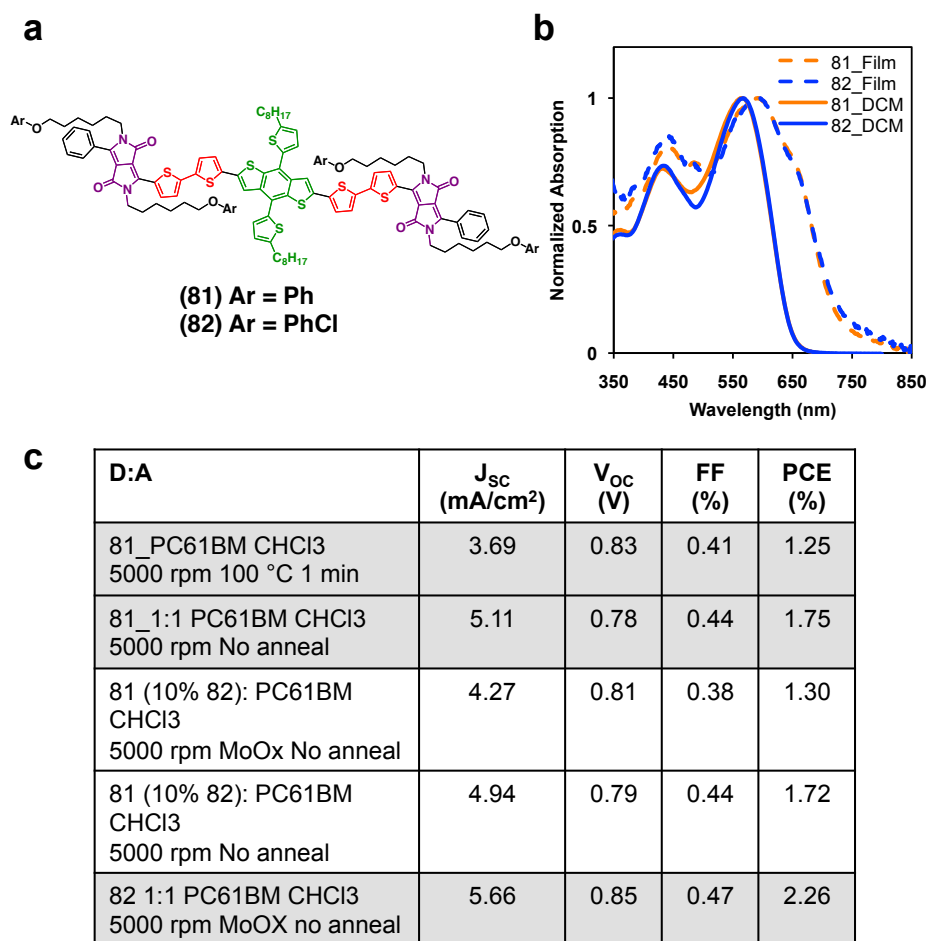
Figure 4.2. Molecular structure (a) and absorption spectrum (b) of molecules **81-82**; c) summary of device results.

Device Performance

To test the effect of the design modifications, devices were made from CHCl$_3$ solutions. As with the previous design, the efficiency of molecules **81**-**82** was first tested separately, and a summary of the conditions tested is presented in Figure 4.2c. The control molecule **81** exhibits a PCE of 1.25-1.75%, while the additive molecule **82** is just above 2%. Annealing the samples lowers the efficiency somewhat considerably, as does the use of additional solvent additives such as DIO, the latter dramatically lowers the performance of the molecules (see Figure 4.2c). The initial testing revealed comparable, if not slightly better performance of the molecules alone than in the previous case, and it was time to find out if the co-mixtures worked better. Devices were built with 10% content of **82** in devices of **81**, and sadly, this time the spiking did not yield a significantly better performance as it did in the previous design.

During device fabrication, it was observed that these molecules lacked some solubility. Although the asymmetry of the DPP core did indeed help in solubilizing the molecule better than the previous design, the additional thiophene spacers did the contrary. Molecules **81**-**82** were more conjugated and had a tendency to aggregate at high concentrations, so it became necessary to modify the design to be able to improve solubility.

4.4 Increasing the Solubility of the Extended Additive-Like Design

Synthesis

Solubility problems had been encountered many times before, so it did not take a long time to propose a strategy to fix it. Since the asymmetric DPP core has less

stacking ability than the fully symmetric one, there was no need to add large alkyl tails. Branched tails would be required definitely, but not butyloctyl for example. It was found that ethylhexyl tails were enough to dramatically increase the solubility of the core. The synthesis was analogous to molecules **81-82** (see Scheme 4.2), except that in this case there was no additive version, just molecule **87**. The objective of the project had not changed, but the new idea was to build devices out of the more soluble molecule **87**, and spike them with molecule **82**.
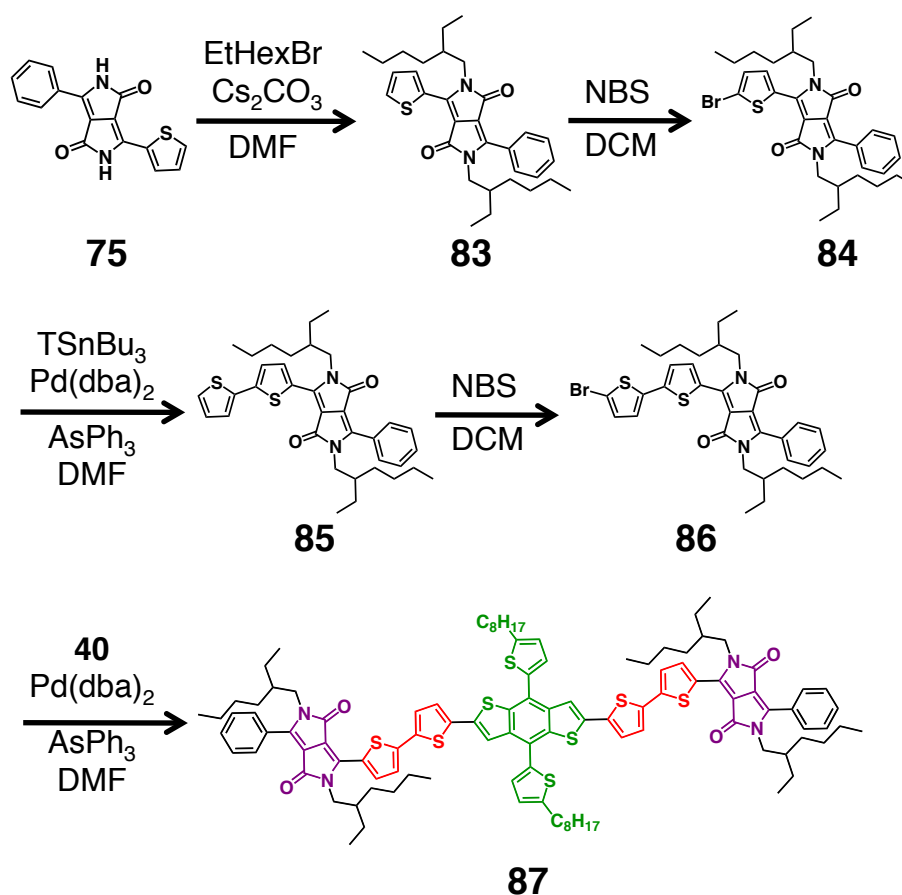
Scheme 4.2. Modification of the asymmetric-DPP core design to enhance solubiity

Absorption Studies and Device Performance

The absorption of molecule **87** is not surprisingly identical to that of molecules **81-82** (Figure 4.3a). What was more interesting was whether the more soluble version was able to perform better when spiked with the PhCl molecule **82**. By itself, molecule **87** outperformed the previous two molecules and it maintained efficiency in the mid 3% range, which was very promising. Unlike the previous molecules, **87** increased in efficiency after being annealed, and that fact became the challenge. When mixed with 10% of **82**, the efficiency of devices built dropped to just above 3%, and content up to 50% of **82** continued to drop the efficiency. Whether devices were annealed or not, the conditions only worked in favor of one molecule, while the other decreased in efficiency (Figure 4.4c). It became clear that the design either had to be consistent in straight or branched alkyl tails, but it could not be a combination of the two because the annealing conditions would be detrimental to either one, no matter what. Synthetically, only the linear tails allowed for introduction of the spiking group, so the design had to be modified again to be able to address the potential electronic problems of the molecule.

a

87

b

c

D:A	J_{SC} (mA/cm^2)	V_{OC} (V)	FF (%)	PCE (%)
87 1:1 PC61BM CHCl3 5000 rpm Anneal 100 °C 5 min	7.29	0.95	0.50	3.49
87 1:1 PC61BM CHCl3 5000 rpm No Anneal	6.78	0.91	0.53	3.27
87 1:1 PC61BM CHCl3 5000 rpm Anneal 100 °C 2 min	7.14	0.93	0.51	3.38
87 1:1 PC61BM CHCl3 Inverted 5000 rpm Anneal 110 °C 2 min	5.76	0.87	0.44	2.20
87/82 1:1:1 PC61BM CHCl3 Inverted 5000 rpm Anneal 100 °C 5 min	5.58	0.85	0.38	1.80
87/82 1:1:1 PC61BM CHCl3 MoOx 5000 rpm No Anneal	6.89	0.89	0.49	3.01
87/82 1:0.1:1 PC61BM CHCl3 MoOx 5000 rpm No Anneal	6.81	0.87	0.54	3.18

Figure 4.3. Molecular structure (a) and absorption spectrum (b) of molecule **87**; c) summary of device results.

4.5 Attempts at Restoring Efficient Electronic Coupling in DPP-BDT Systems

Synthesis

The asymmetry of the DPP core in molecules **81**-**82** and **87** was required because the addition of the thiophene spacer needed to be regioselective, and although the molecules ended up still giving decent efficiencies, the lack of strong absorption on film was concerning, and it was believed to be the result of inefficient intermolecular electronic coupling. To test this hypothesis, two strategies were attempted. The first was to use a more electron rich molecule, in this case an alkoxy-alkylated BDT unit, to more efficiently distribute charge outwards of the molecule. The synthesis of such a molecule was analogous to molecules **81**-**82**, and it is shown in Scheme 4.3. Before any further study, devices were built out molecules **89**-**90**, but performed considerably below 1% PCE.
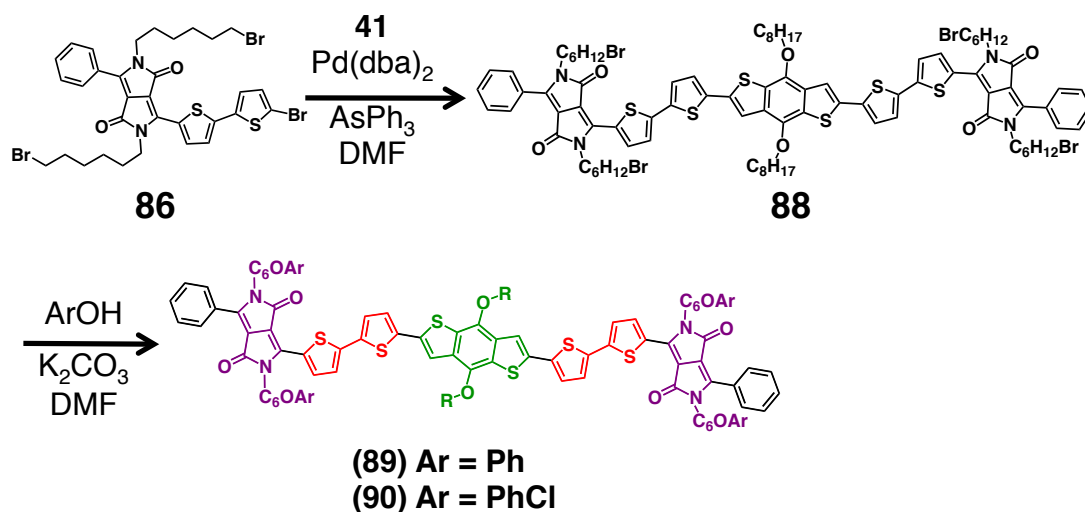
Scheme 4.3. Attempt to increase the electronic coupling of the molecule by using a more electron rich molecule.

After the results from molecules **89-90**, it became necessary to use a fully symmetric DPP core, to emulate molecule M1 from Section 4.1. The problem, as mentioned before, was that a symmetric molecule can react from both sides indiscriminately, unless some kind of blocking group is used. The blocking group used for molecules **34-35** was a simple phenyl group, so the same strategy was used in this case. The synthesis is shown in Scheme 4.4. Most of the intermediates were easy to purify, simple precipitation in methanol allowed the impurities to be washed out, but at intermediate **95**, the molecule became incredibly insoluble, and there was no point in continuing with the synthesis since the final product would be nearly impossible to characterize.
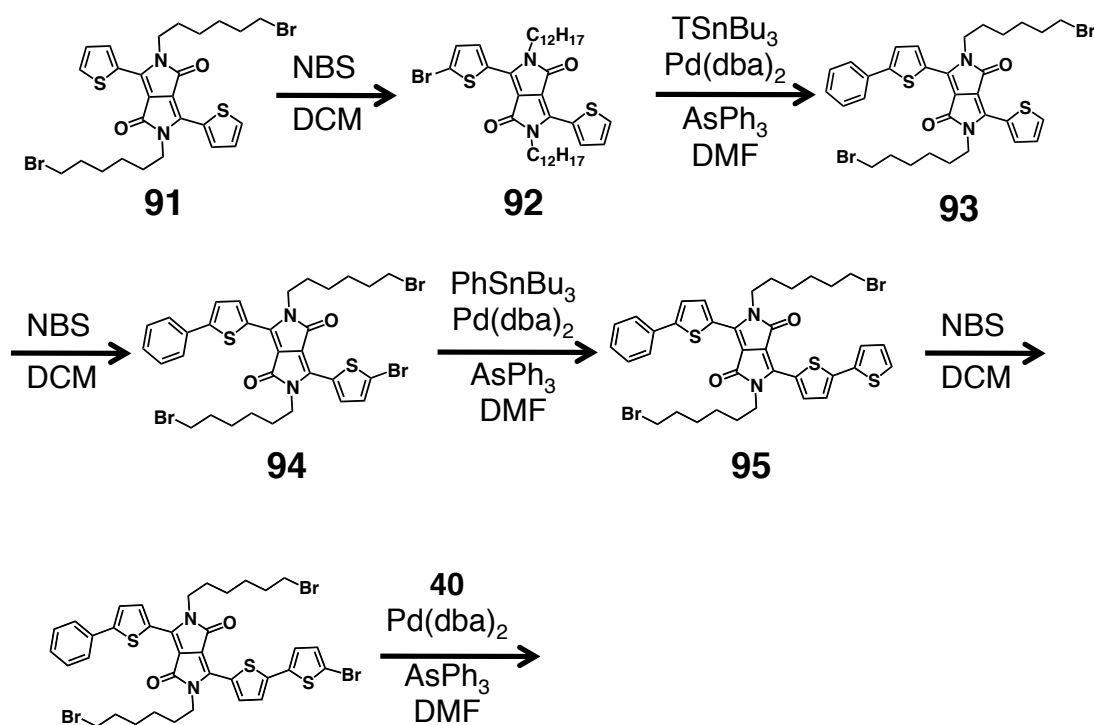
Scheme 4.4. Attempted synthesis of a symmetric-DPP core for the additive containing donor.

4.6 Improving Solubility of Symmetric DPP Core in Additive-Like Designs

Synthesis

Although unsuccessful, all past designs taught a few things: the symmetric DPP core was better at absorbing light and packing on solid films than the asymmetric one (also higher in PCE); linear tails in either core worked better non-annealed, while branched worked better annealed, for that reason they should not be used in conjunction. Lastly, using a phenyl group to block one reactive position of the symmetric DPP core was an effective strategy to create selectivity for the other side, but the design would require more solubility. Taking all the lessons learned, one observation was made, and that was that up to this point, the sides of the molecule had been left empty, and with the appropriate chemistry, they could be used to introduce a functional group, while branched tails could give the symmetric DPP core the necessary solubility.

The new design was aimed at using the facts mentioned above, and try to materialize them all into a molecule. The proposed design is shown in Scheme 4.5. The Instead of a phenyl group being used as a blocking group, a thiophene with a four-carbon linker carboxylic acid was used to block the symmetric DPP core, which was alkylated with butyloctyl tails for enhanced solubility. First, the carboxylic acid was reduced to the alcohol **96**, then protected with a benzyl group, then stanylated and coupled to the monobrominated symmetric DPP core to make intermediate **100**. The other side of the DPP core was then brominated, followed by coupling of the thiophene spacer, which was brominated again and coupled to the BDT core **40**.
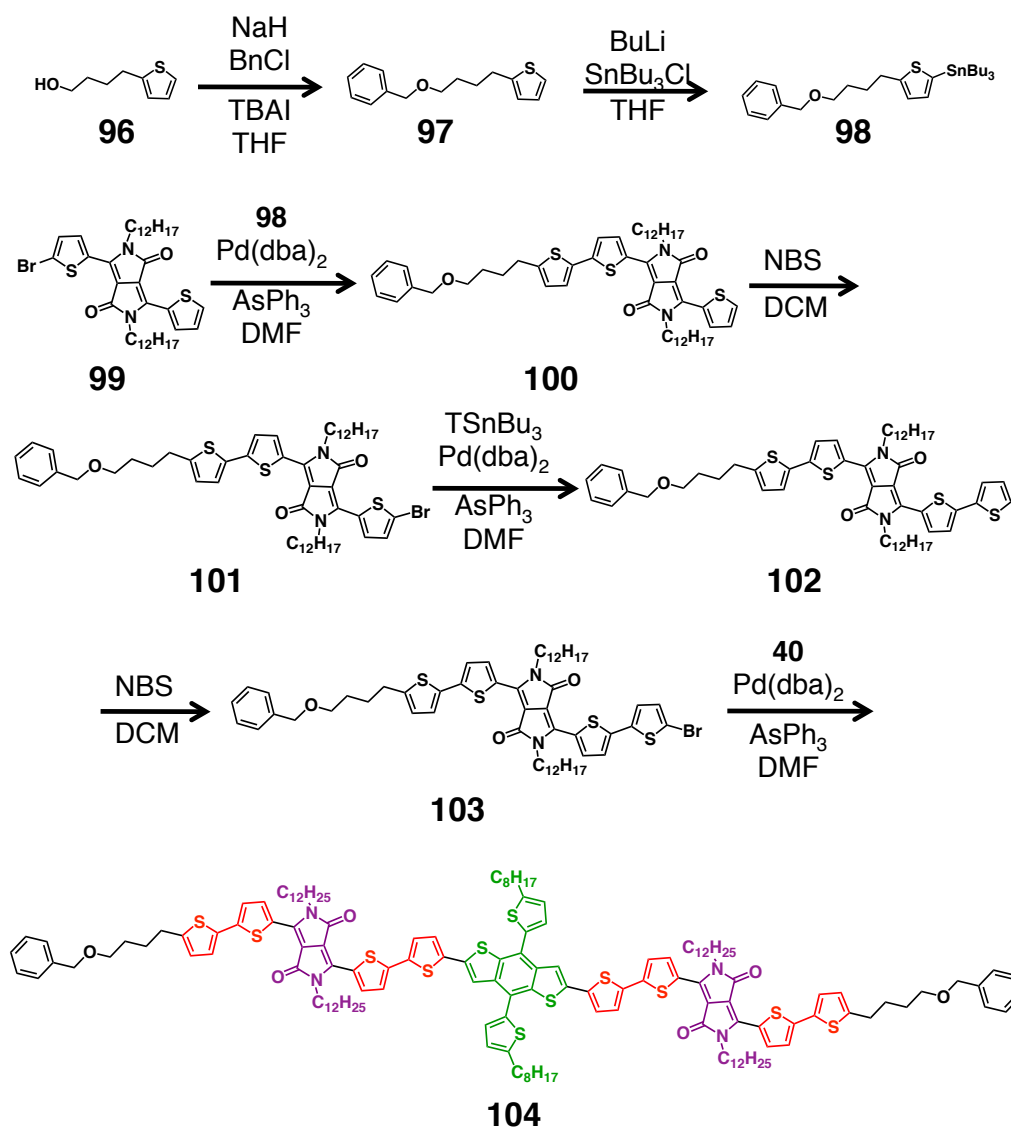
Scheme 4.5. Modification of the symmetric-DPP core for the additive containing donor, with enhanced solubility.

Absorption Properties and Device Performance

Molecule **104** was notoriously soluble, which immediately raised some flags since in the past, the molecules had to have a solubility intermediate between being oils and crystalline powders. Nevertheless, the absorption spectrum showed some promise. The color of the molecule was intense green; though not measured, it was clear that the extinction coefficient was higher than the asymmetric DPP core. The absorption in

solution showed two π-π* (or one π-π* and a S_0-S_2 band possibly) bands in the UV region, and one intense CT band in the blue-to-red regions, covering a large portion of the visible range (Figure 4.4b). The concern over its solubility was sadly backed by a weak red-shifted absorption and though the vibronic features were enhanced (a good sign of electronic coupling), they didn't occur as strong as molecules M1. When devices were built with molecule **104**, they unfortunately worked poorly, with PCEs <<1%, and the films showed strong segregation from PCBM, which confirmed the original concern of the molecule having too many alkyl tails.

a

104
Ar = Benzyl
R = Ethylhexyl

b

c

D:A	J_{SC} (mA/cm²)	V_{OC} (V)	FF (%)	PCE (%)
104 1:1 PC71BM CHCl3 4000 rpm MoOx Anneal 100 °C 5 min	1.47	0.67	0.40	0.39
104 1:1 PC71BM CHCl3 4000 rpm MoOx No Anneal	0.71	0.65	0.27	0.12
104 1:1 PC71BM CHCl3 (3% DIO) 4000 rpm MoOx Anneal 100 °C 2 min	0.025	0.77	0.217	0.004
104 1:1 PC71BM CHCl3 (5%DIO) 4000 rpm MoOx Anneal 100 °C 5 min	0.065	0.350	0.281	0.006
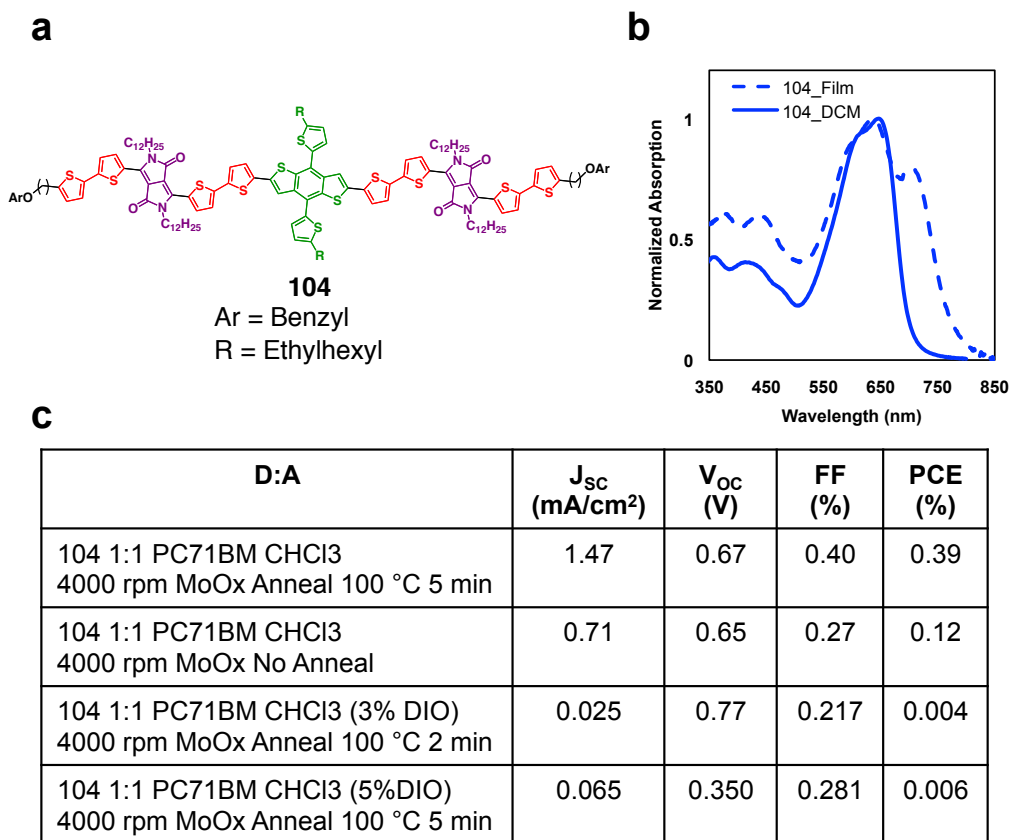
Figure 4.4. Molecular structure (a) and absorption spectrum (b) of molecule **104**; c) summary of device results.

4.7 Latest Modifications and Future Work

Synthesis

It was never easy to have a molecule not work after taking so long to synthesize, but the one thing molecule **104** had was two side-arms that could be further functionalized. All the previous designs were meant to fix the initial solubility problem of molecule M1, and so it was thought that perhaps the sides of the molecule could provide better solubility, while the core could be the extended one, similar to molecules **81-82**, but with a symmetric DPP. Scheme 4.6 shows the modified synthesis of the design, which turned out to be even more challenging given that this time, the core DPP had to be synthesized with a side-arm, as opposed to being coupled one to it like in the previous designs. The key was to be able to synthesize the modified 2-ethyl-hexyl-5-thiophenecarbonitrile **109** and intermediate **107**, then condense those two to make the side-alkylated, symmetric DPP core **110**. From there, the synthesis was similar as that of molecules **81-82**. After the coupling to make intermediate **115**, the only step left to do was to displace the bromine groups at the end of the alkyl tails in the DPP core with either phenol or dichlorophenol, but for some unknown reason, intermediate **115** decomposes under the reaction conditions, which happened to be the exact same as those for molecules **81-82**.
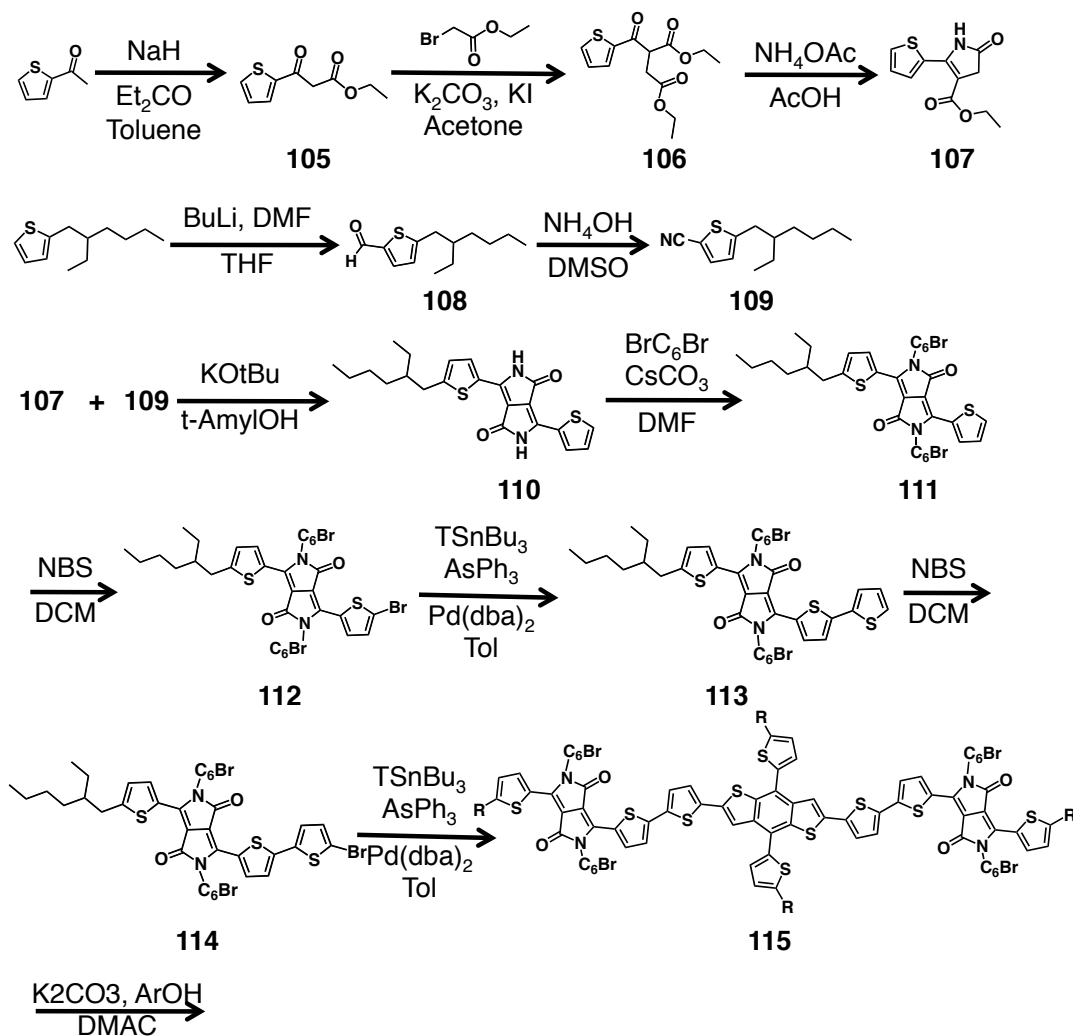
Scheme 4.6. Attempted synthesis of an alkylated, symmetric DPP core for the additive-containing donor.

The instability of intermediate **115** was a major drawback since that molecule had good solubility/crystallinity properties and very good absorption, and it was even more difficult finding the reason for its decomposition. Mass spectrometry indicated was not helpful, and sadly NMR would not be of any use since intermediate **115** was mixed with the homocoupling of **114**. As difficult as it sounded, the design had to be modified. Since an alkylated thiophene was the only different element of this designs, it was to be

removed, or as molecule **104** showed, to be coupled to the DPP core. The future design of this project, which may end up being the last, is shown in Figure 4.5. Synthesis will be reported soon.
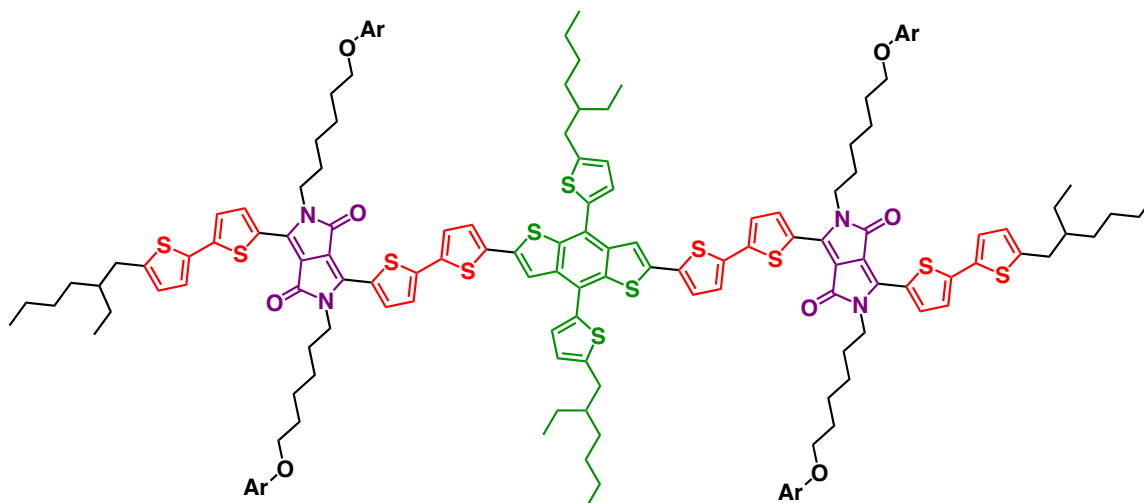
Figure 4.5. Last possible design of the additive-containing donor.

4.8 Synthetic Methods

PhCOC(COOEt)2 (73). Ethyl benzoylacetate (40.0 mL, 232 mmol), ethyl bromoacetate (32.0 mL, 278 mmol), potassium carbonate (33.0 g, 239 mmol), potassium iodide (7.00 g, 42.2 mmol) were mixed in acetone (100 mL) and refluxed for 6 hrs. After cooling to room temperature, the reaction was diluted in water (300 mL) and extracted in diethyl ether (200 mL). The ether layer was collected and dried under vacuum. The crude of the reaction was used for the next step without purification.

PhPyrCOOEt (74). The crude mixture of product **73** was dissolved in glacial acetic acid (150 mL). Ammonium acetate (70.0 g, 908 mmol) was added in one portion and the reaction was refluxed for 4 hrs. After cooling to room temperature, the crude was poured over ice and the precipitate filtered, then washed with diethyl ether until washings were faint brown color. Compound **74** was dried under vacuum overnight to

give a light yellow solid (26.5 g, 57% over the previous two steps). 1H-NMR (400 MHz; DMSO-d6): δ 7.55-7.52 (m, 2H), 7.44-7.39 (m, 3H), 3.96 (q, J = 7.1 Hz, 2H), 3.35 (s, 2H), 1.05 (t, J = 7.1 Hz, 3H). HRMS−ESI (m / z): [M + Na]+ calc for $C_{13}H_{13}NO_3$ 254.0792, found 254.0792.

PhDPPTH (75). A Schlenk flask containing compound **74** (10.0 g, 43.3 mmol) and 2-thiophene carbonitrile (6.00 mL, 64.8 mmol) was degassed by one vacuum/nitrogen cycle, then 2-methyl-2-butanol (was added 80 mL) and the mixture was heated to 120 C. Potassium tert-butoxide (14.6 g, 130 mmol) was then added in small portions, making sure the bubbling was not too violent. The reaction was stirred in open air for another 15 minutes before letting cool down to room temperature. Glacial acetic acid (30 mL) was then added, and the reaction was diluted with hexane (100 mL). The resulting precipitate was filtered, and then washed with water (200 mL) and MeOH (300 mL) until washings were faint brown color. The resulting filtrate was left drying under vacuum for 12 hrs and was isolated as a dark red solid (10.5 g, 85%). 1H-NMR (400 MHz; DMSO-d6): δ 11.20 (s, 1H), 11.12 (s, 1H), 8.31 (dd, J = 7.5, 2.1 Hz, 2H), 8.15 (dd, J = 3.8, 1.0 Hz, 1H), 7.87 (dd, J = 4.9, 1.0 Hz, 1H), 7.47-7.42 (m, 3H), 7.20 (dd, J = 4.9, 3.9 Hz, 1H). HRMS−ESI (m / z): [M + H]+ calc for $C_{16}H_{10}N_2O_2S$ 295.0542, found 295.0536.

PhDPPTC6Br (76). A Schlenk flask containing compound **75** (5.00 g, 16.6 mmol) and 1,6-dibromohexane (15.0 mL, 98.0 mmol) was degassed by one vacuum/nitrogen cycle. Anhydrous DMF (30 mL) was then added, along with cesium carbonate (16.0 g, 49.0 mmol) and the reaction was heated to 120 C for 2 hours under nitrogen. After cooling to room temperature, water (100 mL) and 1 M HCl (30 mL) were added. The mixture was

filtered through Celite and washed with water (200 mL). The Celite was then washed with DCM until the washings were faint red color. Residual water was removed in a separatory funnel, and DCM was evaporated under vacuum. The product was purified by column chromatography (30% hexanes/DCM) to give a dark red solid (1.54 g, 15%). 1H-NMR (499 MHz; CDCl3): δ 8.96-8.96 (m, 1H), 7.81-7.79 (m, 2H), 7.69 (d, J = 5.0 Hz, 1H), 7.55 (quintet, J = 6.4 Hz, 3H), 7.32 (dd, J = 4.8, 4.1 Hz, 1H), 4.03 (t, J = 7.7 Hz, 2H), 3.85 (t, J = 7.5 Hz, 2H), 3.41 (d, J = 6.8 Hz, 2H), 3.36 (d, J = 6.8 Hz, 2H), 1.88 (d, J = 7.1 Hz, 2H), 1.81-1.76 (m, 4H), 1.66 (d, J = 7.4 Hz, 2H), 1.51-1.39 (m, 8H), 1.32-1.28 (m, 2H). MALDI-MS (m / z): [M]+ calc for $C_{28}H_{32}Br_2N_2O_2S$ 618.0551, found 618.068.

PhDPPTBrC6Br (77). Compound **76** (1.21 g, 1.96 mmol) was dissolved in DCM (25 mL) and covered with aluminum foil, then N-bromosuccinimide (0.340 g, 1.91 mmol) was added in one portion and the reaction was left stirring for 12 hrs. The reaction was then diluted in DCM (100 mL) and washed with 1 M NaOH (50 mL). The DCM layer was then collected and dried under vacuum. The product was isolated after running through a silica plug (DCM) to give a dark red solid (0.655 g, 48% yield). 1H-NMR (400 MHz; CDCl3): δ 8.67 (t, J = 4.0 Hz, 1H), 7.77-7.73 (m, 2H), 7.54-7.47 (m, 3H), 7.23 (s, 1H), 3.92 (t, J = 7.7 Hz, 2H), 3.85-3.79 (m, 2H), 3.41-3.37 (m, 2H), 3.32 (q, J = 6.3 Hz, 2H), 1.84 (dd, J = 8.8, 5.8 Hz, 2H), 1.76-1.68 (m, 4H), 1.60 (dd, J = 15.1, 7.6 Hz, 2H), 1.51-1.34 (m, 8H), 1.29-1.21 (m, 2H). MALDI-MS (m / z): [M]+ calc for $C_{28}H_{31}Br_3N_2O_2S$ 695.9656, found 695.945.

PhDPP2TC6Br (78). A Schlenk flask containing compound **77** (0.643 g, 0.923 mmol), 2-(tributylstannyl)thiophene (0.360 mL, 1.11 mmol) and tetrakistriphenylphosphine palladium(0) (0.107 g, 0.0923 mmol) was then degassed by three vacuum/nitrogen

cycles. Degassed DMF (15 mL) was then injected into the flask and the solution mixture was stirred for 2 hrs at 100 °C under nitrogen. After cooling to room temperature, the reaction mixture was poured into water (300 mL) with 1 M potassium fluoride (30 mL). The precipitate was filtered over Celite, washed with additional water (100 mL) and the Celite was then washed with DCM until the washings were faint red color. Residual water was removed in a separatory funnel. DCM was removed under vacuum and the product was purified by column chromatography (30% hexane/DCM) to afford **78** as a dark red solid (0.375 g, 58%). 1H-NMR (499 MHz; CDCl3): δ 8.97-8.95 (m, 1H), 7.79 (t, J = 5.2 Hz, 2H), 7.57-7.51 (m, 3H), 7.39-7.35 (m, 3H), 7.10 (dd, J = 4.6, 4.1 Hz, 1H), 4.06-4.03 (m, 2H), 3.88-3.85 (m, 2H), 3.42-3.40 (m, 2H), 3.35 (dd, J = 8.6, 5.0 Hz, 2H), 1.91-1.87 (m, 2H), 1.82-1.77 (m, 4H), 1.69-1.66 (m, 2H), 1.54-1.46 (m, 4H), 1.43-1.39 (m, 2H), 1.33-1.28 (m, 2H). MALDI-MS (m / z): [M]+ calc for C32H34Br2N2O2S2 700.0428, found 700.052.

PhDPP2TBrC6Br (79). Compound **78** (0.670 g, 0.957 mmol) was dissolved in DCM (25 mL) and covered with aluminum foil, then N-bromosuccinimide (0.204 g, 1.15 mmol) was added in one portion and the reaction was left stirring for 12 hrs. The reaction was then diluted in DCM (100 mL) and washed with 1 M NaOH (50 mL). The DCM layer was then collected and dried under vacuum. The product was isolated after running through a silica plug (DCM) to give a dark red solid (0.625 g, 83% yield). 1H-NMR (400 MHz; CDCl3): δ 8.88 (d, J = 4.1 Hz, 1H), 7.76 (ddt, J = 6.0, 4.2, 2.0 Hz, 2H), 7.54-7.48 (m, 3H), 7.42-7.38 (m, 1H), 7.09-7.07 (m, 1H), 7.03 (d, J = 3.9 Hz, 1H), 3.99 (t, J = 7.7 Hz, 2H), 3.83 (d, J = 7.4 Hz, 2H), 3.39-3.36 (m, 2H), 3.36-3.29 (m, 3H), 1.86 (dd, J = 14.0,

7.2 Hz, 2H), 1.80-1.73 (m, 3H), 1.50-1.36 (m, 8H), 1.27-1.24 (m, 4H). MALDI-MS (m / z): [M + H]+ calc for C32H33Br3N2O2S2 778.9613, found 778.930.

PhDPP2TBDTO2TC8C6Br (80). A Schlenk flask containing compound **79** (0.330 g, 0.424 mmol), compound **40** (0.223 g, 0.193 mmol) was degassed by three vacuum/nitrogen cycles. Degassed DMF (15 mL) was then injected into the flask, and a degassed DMF solution (5mL) of bis-(dibenzylidineacetone)palladium(0) (0.011 g, 0.0191 mmol) and triphenylarsine (0.020 g, 0.0653 mmol) was also injected. The reaction mixture was stirred for 2 hrs at 100 °C under nitrogen. After cooling to room temperature, the reaction mixture was poured into water (300 mL) with 1 M potassium fluoride (30 mL). The precipitate was filtered over Celite, washed with additional water (100 mL) and the Celite was then washed with DCM until the washings were faint red color. Residual water was removed in a separatory funnel. DCM was removed under vacuum and the product was purified by column chromatography (30% hexane/DCM) and gel permeation chromatography to afford **80** as a dark purple solid (0.160 g, 42%). 1H-NMR (499 MHz; CDCl3): δ 8.96-8.95 (m, 2H), 7.79-7.78 (m, 4H), 7.67-7.65 (m, 2H), 7.55-7.49 (m, 8H), 7.34 (d, J = 3.5 Hz, 2H), 7.31-7.29 (m, 2H), 7.25-7.22 (m, 2H), 6.98 (t, J = 3.1 Hz, 2H), 4.03-3.99 (m, 4H), 3.87-3.83 (m, 4H), 3.42 (q, J = 3.7 Hz, 4H), 3.37-3.34 (m, 4H), 2.95 (dd, J = 3.6, 0.7 Hz, 2H), 1.92-1.88 (m, 4H), 1.81-1.76 (m, 9H), 1.54-1.39 (m, 38H), 1.33-1.28 (m, 8H), 1.04-1.00 (m, 8H), 0.99-0.95 (m, 8H). MALDI-MS (m / z): [M+H]+ calc for C98H106Br4N4O4S8 1975.3507, found 1975.457.

PhDPP2TBDTO2TC8Ph (81). Compound **80** (0.031 g, 0.0157 mmol), phenol (0.030 g, 0.314 mmol) and potassium carbonate (0.043 g, 0.314 mmol) were dissolved in N,N-dimethylacetamide (10 mL) and heated to 60 C for 3 hrs. After cooling to room

temperature, the crude was diluted with water (100 mL) and 1 M HCl (10 mL), then filtered over Celite. The Celite pad was then washed with methanol until the washings were colorless, then DCM was added to the Celite pad until the washings were faint purple color. The solvent was then removed under vacuum. The product was purified by gel permeation chromatography (CHCl3) to give a dark purple solid (0.015 g, 46%). 1H-NMR (400 MHz; CDCl3): δ 8.97-8.92 (m, 2H), 7.79-7.76 (m, 2H), 7.70-7.65 (m, 2H), 7.55-7.46 (m, 6H), 7.34-7.29 (m, 4H), 7.28-7.26 (m, 9H), 7.24-7.20 (m, 6H), 7.18-7.12 (m, 2H), 6.99-6.82 (m, 10H), 4.06-3.96 (m, 4H), 3.96-3.79 (m, 9H), 2.93-2.85 (m, 4H), 1.82-1.58 (m, 15H), 1.50-1.25 (m, 32H), 1.22-1.13 (m, 4H), 1.02-0.89 (m, 12H), 0.89-0.76 (m, 6H). HRMS−ESI (m / z): [M]+ calc for C122H126N4O8S8 2030.7341, found 2030.958.

PhDPP2TBDTO2TC8PhCl (82). Compound **80** (0.048 g, 0.0203 mmol), 4-chlorophenol (0.063 g, 0. mmol) and potassium carbonate (0.043 g, 0.314 mmol) were dissolved in N,N-dimethylacetamide (10 mL) and heated to 60 C for 3 hrs. After cooling to room temperature, the crude was diluted with water (100 mL) and 1 M HCl (10 mL), and filtered over Celite. The Celite pad was then washed with methanol until the washings were colorless, then DCM was added to the Celite pad until the washings were faint purple color. The solvent was then removed under vacuum. The product was purified by gel permeation chromatography (CHCl3) to give a dark purple solid (0.016 g, 36%). 1H-NMR (499 MHz; CDCl3): δ 8.97-8.95 (m, 2H), 7.80-7.77 (m, 4H), 7.67-7.66 (m, 2H), 7.54-7.49 (m, 6H), 7.35-7.33 (m, 2H), 7.33-7.30 (m, 2H), 7.25-7.15 (m, 12H), 6.98-6.96 (m, 2H), 6.81-6.75 (m, 8H), 4.06-4.00 (m, 4H), 3.93-3.90 (m, 4H), 3.88-3.84 (m, 8H),

2.94-2.91 (m, 4H), 1.83-1.65 (m, 20H), 1.54-1.30 (m, 39H), 1.03-0.95 (m, 13H). MALDI-MS (m / z): [M]+ calc for $C_{122}H_{122}Cl_4N_4O_8S_8$ 2166.5782, found 2166.904.

PhDPPTC8 (83). A Schlenk flask containing compound **75** (5.20 g, 17.7 mmol) was degassed by one vacuum/nitrogen cycle. Anhydrous DMF (30 mL) was then added, along with cesium carbonate (14.4 g, 44.2 mmol) and the reaction was heated to 120 C for 30 miutes before adding 2-ethylhexyl bromide (7.90 mL, 44.2 mmol) . After cooling to room temperature, water (100 mL) and 1 M HCl (50 mL) were added. The mixture was filtered through Celite and washed with water (200 mL). The Celite was then washed with DCM until the washings were faint red color. Residual water was removed in a separatory funnel, and DCM was evaporated under vacuum. The product was purified by column chromatography (50% hexanes in DCM) to give a red waxy solid (4.86 g, 53%). 1H-NMR (400 MHz; CDCl3): δ 8.89 (dd, J = 3.9, 1.1 Hz, 1H), 8.89 (dd, J = 3.9, 1.1 Hz, 1H), 7.75-7.71 (m, 2H), 7.75-7.71 (m, 2H), 7.64-7.62 (m, 1H), 7.64-7.62 (m, 1H), 7.52-7.46 (m, 3H), 7.52-7.46 (m, 3H), 7.28-7.26 (m, 1H), 7.28-7.26 (m, 1H), 3.96-3.90 (m, 2H), 3.96-3.90 (m, 2H), 3.83-3.78 (m, 2H), 3.83-3.78 (m, 2H), 3.47-3.42 (m, 2H), 3.47-3.42 (m, 2H), 1.53-1.48 (m, 2H), 1.53-1.48 (m, 2H), 1.27 (td, J = 7.5, 3.7 Hz, 12H), 1.27 (td, J = 7.5, 3.7 Hz, 12H), 1.11-1.06 (m, 6H), 1.11-1.06 (m, 6H), 0.80-0.73 (m, 4H), 0.80-0.73 (m, 4H), 0.73-0.64 (m, 4H), 0.73-0.64 (m, 4H), 0.05 (s, 4H). MALDI-MS (m / z): [M]+ calc for $C_{32}H_{42}N_2O_2S$ 518.2967, found 518.410.

PhDPPTBrC8 (84). Compound **83** (1.53 g, 2.95 mmol) was dissolved in DCM (30 mL) and covered with aluminum foil, then N-bromosuccinimide (0.525 g, 2.95 mmol) was added in one portion and the reaction was left stirring for 12 hrs. The reaction was then diluted in DCM (100 mL) and washed with 1 M NaOH (50 mL). The DCM layer was then

collected and dried under vacuum. The product was isolated after running through a silica plug (DCM) to give a dark red solid (0.360 g, 20%). 1H-NMR (400 MHz; CDCl3): δ 8.63 (d, *J* = 4.2 Hz, 1H), 7.72 (dt, *J* = 5.9, 1.8 Hz, 2H), 7.52-7.46 (m, 3H), 7.21 (d, *J* = 4.2 Hz, 1H), 3.84 (dd, *J* = 7.7, 4.5 Hz, 2H), 3.79 (td, *J* = 7.0, 3.3 Hz, 2H), 1.30-1.22 (m, 8H), 1.11-1.06 (m, 5H), 0.90-0.81 (m, 10H), 0.76 (t, *J* = 6.7 Hz, 3H), 0.68 (td, *J* = 7.4, 1.3 Hz, 3H). MALDI-MS (m / z): [M]+ calc for C32H41BrN2O2S 596.2072, found 596.290.

PhDPP2TC8 (85). A Schlenk flask containing compound **84** (0.360 g, 0.602 mmol), 2-(tributylstannyl)thiophene (0.230 mL, 0.723 mmol) and tetrakistriphenylphosphine palladium(0) (0.070 g, 0.0602 mmol) was then degassed by three vacuum/nitrogen cycles. Degassed DMF (15 mL) was then injected into the flask and the solution mixture was stirred for 2 hrs at 100 °C under nitrogen. After cooling to room temperature, the reaction mixture was poured into water (300 mL) with 1 M potassium fluoride (30 mL). The precipitate was filtered over Celite, washed with additional water (100 mL) and the Celite was then washed with DCM until the washings were faint red color. Residual water was removed in a separatory funnel. DCM was removed under vacuum and the product was purified by column chromatography (1:1 hexane/DCM) to afford **85** as a dark red solid (0.260 g, 72%). 1H-NMR (499 MHz; CDCl3): δ 8.95 (d, *J* = 4.1 Hz, 1H), 8.95 (d, *J* = 4.1 Hz, 1H), 7.77-7.76 (m, 2H), 7.77-7.76 (m, 2H), 7.54-7.49 (m, 3H), 7.54-7.49 (m, 3H), 7.36-7.33 (m, 3H), 7.36-7.33 (m, 3H), 7.09 (dd, *J* = 5.0, 3.8 Hz, 1H), 7.09 (dd, *J* = 5.0, 3.8 Hz, 1H), 3.97 (t, *J* = 7.2 Hz, 2H), 3.97 (t, *J* = 7.2 Hz, 2H), 3.86-3.82 (m, 2H), 3.86-3.82 (m, 2H), 1.90-1.88 (m, 1H), 1.90-1.88 (m, 1H), 1.57-1.51 (m, 4H), 1.57-1.51 (m, 4H), 1.40-1.33 (m, 4H), 1.40-1.33 (m, 4H), 1.30-1.27 (m, 4H), 1.30-1.27 (m,

4H), 1.11 (t, *J* = 6.5 Hz, 4H), 1.11 (t, *J* = 6.5 Hz, 4H), 0.92-0.85 (m, 8H), 0.92-0.85 (m, 8H), 0.79 (t, *J* = 6.5 Hz, 3H), 0.79. MALDI-MS (m / z): [M+H]+ calc for $C_{36}H_{44}N_2O_2S_2$ 701.0507, found 701.225.

PhDPP2TBrC8 (86). Compound **85** (0.260 g, 0.433 mmol) was dissolved in DCM (30 mL) and covered with aluminum foil, then N-bromosuccinimide (0.092 g, 0.519 mmol) was added in one portion and the reaction was left stirring for 12 hrs. The reaction was then diluted in DCM (100 mL) and washed with 1 M NaOH (50 mL). The DCM layer was then collected and dried under vacuum. The product was isolated after running through a silica plug (DCM) to give a dark red solid (0.180 g, 61% yield). 1H-NMR (400 MHz; CDCl3): δ 8.87 (d, *J* = 4.1 Hz, 1H), 7.75-7.71 (m, 2H), 7.51-7.45 (m, 3H), 7.22 (dd, *J* = 6.8, 3.6 Hz, 1H), 7.04 (t, *J* = 3.5 Hz, 1H), 7.02 (q, *J* = 3.1 Hz, 1H), 3.93 (dd, *J* = 9.9, 5.1 Hz, 2H), 3.82-3.78 (m, 2H), 1.86-1.81 (m, 1H), 1.52-1.46 (m, 1H), 1.28-1.24 (m, 5H), 1.07 (q, *J* = 6.1 Hz, 5H), 0.91-0.83 (m, 8H), 0.81-0.76 (m, 4H), 0.69 (qd, *J* = 7.1, 1.4 Hz, 4H). MALDI-MS (m / z): [M]+ calc for $C_{36}H_{43}BrN_2O_2S_2$ 678.1949, found 678.232.

PhDPP2TC8BDTO2TC8 (87). A Schlenk flask containing compound **86** (0.130 g, 0.191 mmol), compound **40** (0.100 g, 0.0861 mmol), tetrakistriphenylphosphine palladium(0) (0.044 g, 0.0382 mmol) and copper iodide (0.007 g, 0.0382 mmol) was degassed by three vacuum/nitrogen cycles. Degassed DMF (15 mL) was then injected into the flask and the solution mixture was stirred for 2 hrs at 100 °C under nitrogen. After cooling to room temperature, the reaction mixture was poured into water (300 mL) with 1 M potassium fluoride (30 mL). The precipitate was filtered over Celite, washed with additional water (100 mL) and the Celite was then washed with DCM until the washings were faint purple color. Residual water was removed in a separatory funnel. DCM was

removed under vacuum and the product was purified by gel permeation chromatography (CHCl3) to afford **87** as a dark purple solid (0.060 g, 39%). 1H-NMR (499 MHz; CDCl3): δ 8.96 (d, *J* = 4.1 Hz, 2H), 7.76 (d, *J* = 6.7 Hz, 4H), 7.70 (s, 2H), 7.53-7.49 (m, 6H), 7.34-7.33 (m, 4H), 7.27-7.25 (m, 4H), 6.97 (d, *J* = 3.4 Hz, 2H), 3.98-3.96 (m, 4H), 3.86-3.83 (m, 4H), 2.93 (dd, *J* = 6.7, 3.4 Hz, 4H), 1.74 (d, *J* = 6.3 Hz, 2H), 1.42-1.37 (m, 14H), 1.31-1.26 (m, 12H), 1.15-1.09 (m, 13H), 1.02-0.99 (m, 8H), 0.97 (t, *J* = 4.7 Hz, 5H), 0.93-0.87 (m, 16H), 0.81-0.78 (m, 7H), 0.72 (ddd, *J* = 8.6, 6.3, 1.9 Hz, 7H). MALDI-MS (m / z): [M]+ calc for $C_{106}H_{126}N_4O_4S_6$ 1774.7545, found 1774.956.

PhDPP2TC6BrBDTC8 (88). A Schlenk flask containing compound **79** (0.340 g, 0.436 mmol), compound **41** (0.203 g, 0.200 mmol) and tetrakistriphenylphosphine palladium(0) (0.050 g, 0.0400 mmol) was degassed by three vacuum/nitrogen cycles. Degassed DMF (15 mL) was then injected into the flask and the solution mixture was stirred for 2 hrs at 100 °C under nitrogen. After cooling to room temperature, the reaction mixture was poured into water (300 mL) with 1 M potassium fluoride (30 mL). The precipitate was filtered over Celite, washed with additional water (100 mL) and the Celite was then washed with DCM until the washings were faint purple color. Residual water was removed in a separatory funnel. DCM was removed under vacuum and the crude was used for the next step without further purification.

PhDPP2TBDTC8Ph (89). Compound **88** (0.038 g, 0.0206 mmol), phenol (0.040 g, 0.413 mmol) and potassium carbonate (0.057 g, 0.413 mmol) were dissolved in N,N-dimethylacetamide (10 mL) and heated to 60 C for 3 hrs. After cooling to room temperature, the crude was diluted with water (100 mL) and 1 M HCl (10 mL), then filtered over Celite. The Celite pad was then washed with methanol until the washings

were colorless, then DCM was added to the Celite pad until the washings were faint purple color. The solvent was then removed under vacuum. The product was purified by gel permeation chromatography (CHCl3) to give a dark purple solid (0.006 g, 15%). 1H-NMR (400 MHz; CDCl3): δ 8.97-8.90 (m, 2H), 7.80-7.69 (m, 4H), 7.53-7.41 (m, 7H), 7.31-7.28 (m, 2H), 7.28-7.26 (m, 3H), 7.24-7.20 (m, 9H), 7.18-7.12 (m, 2H), 6.94-6.79 (m, 8H), 4.22-4.11 (m, 4H), 4.09-3.97 (m, 4H), 3.99-3.91 (m, 3H), 3.91-3.78 (m, 6H), 1.87-1.26 (m, 53H), 1.11-1.03 (m, 6H), 1.02-0.93 (m, 6H). MALDI-MS (m / z): [M+H]+ calc for C114H122N4O10S6 1899.7564, found 1899.939.

PhDPP2TBDTC8PhCl (90). Compound **88** (0.0210 g, 0.0114 mmol), 4-chlorophenol (0.030 g, 0.228 mmol) and potassium carbonate (0.030 g, 0.228 mmol) were dissolved in N,N-dimethylacetamide (10 mL) and heated to 60 C for 3 hrs. After cooling to room temperature, the crude was diluted with water (100 mL) and 1 M HCl (10 mL), then filtered over Celite. The Celite pad was then washed with methanol until the washings were colorless, then DCM was added to the Celite pad until the washings were faint purple color. The solvent was then removed under vacuum. The product was purified by gel permeation chromatography (CHCl3) to give a dark purple solid (0.011 g, 47%). 1H-NMR (400 MHz; CDCl3): δ 8.97-8.90 (m, 2H), 8.97-8.90 (m, 2H), 7.79-7.70 (m, 4H), 7.79-7.70 (m, 4H), 7.54-7.40 (m, 8H), 7.54-7.40 (m, 8H), 7.38-7.26 (m, 3H), 7.38-7.26 (m, 3H), 7.23-7.12 (m, 9H), 7.23-7.12 (m, 9H), 6.81-6.67 (m, 7H), 6.81-6.67 (m, 7H), 4.22-4.12 (m, 4H), 4.22-4.12 (m, 4H), 4.07-3.98 (m, 4H), 4.07-3.98 (m, 4H), 3.93-3.88 (m, 3H), 3.93-3.88 (m, 3H), 3.85-3.83 (m, 4H), 3.85-3.83 (m, 4H), 1.88-1.74 (m, 8H), 1.74-1.60 (m, 14H), 1.57-1.50 (m, 13H), 1.47-1.41 (m, 10H), 1.35-1.19 (m, 9H), 1.10-

1.04 (m, 6H), 1.10-1.04 (m, 6H), 1.00-0.96 (m, 6H), 1.00-0.96 (m, 6H). MALDI-MS (m / z): [M + H]+ calc for $C_{114}H_{118}Cl_4N_4O_{10}S_6$ 2035.6005, found 2035.798.

TDPPTC6Br (91). A Schlenk flask containing compound **75** (5.00 g, 16.6 mmol) and 1,6-dibromohexane (15.0 mL, 98.0 mmol) was degassed by one vacuum/nitrogen cycle. Anhydrous DMF (30 mL) was then added, along with cesium carbonate (16.0 g, 49.0 mmol) and the reaction was heated to 120 C for 2 hours under nitrogen. After cooling to room temperature, water (100 mL) and 1 M HCl (30 mL) were added. The mixture was filtered through Celite and washed with water (200 mL). The Celite was then washed with DCM until the washings were faint red color. Residual water was removed in a separatory funnel, and DCM was evaporated under vacuum. The product was purified by column chromatography (30% hexanes/DCM) to give a dark red solid (1.54 g, 15%). 1H-NMR (400 MHz; CDCl3): δ 8.91-8.89 (m, 2H), 7.63 (dd, *J* = 5.0, 1.0 Hz, 2H), 7.29-7.27 (m, 2H), 4.08 (dd, *J* = 8.6, 3.6 Hz, 4H), 3.39 (dd, *J* = 6.8, 3.6 Hz, 4H), 1.87-1.83 (m, 4H), 1.77-1.73 (m, 4H), 1.47-1.42 (m, 8H). MALDI-MS (m / z): [M]+ calc for $C_{26}H_{30}Br_2N_2O_2S_2$ 624.0115, found 624.105.

TDPPTBrC6Br (92). Compound **91** (3.28 g, 5.25 mmol) was dissolved in DCM (30 mL) and covered with aluminum foil, then N-bromosuccinimide (0.375 g, 2.10 mmol) was added in one portion and the reaction was left stirring for 12 hrs. The reaction was then diluted in DCM (100 mL) and washed with 1 M NaOH (50 mL). The DCM layer was then collected and dried under vacuum. The product was isolated by column chromatography (30% Hexane/DCM) to give a dark red solid (0.998 g, 68% yield). 1H-NMR (499 MHz; CDCl3): δ 8.93 (dd, *J* = 3.9, 1.0 Hz, 1H), 8.67 (t, *J* = 4.7 Hz, 1H), 7.67-7.66 (m, 1H), 7.30 (dd, *J* = 5.0, 4.0 Hz, 1H), 7.25-7.24 (m, 1H), 4.10-4.08 (m, 2H), 4.01

(t, *J* = 7.7 Hz, 2H), 1.90-1.84 (m, 6H), 1.79-1.72 (m, 5H), 1.52-1.44 (m, 11H). MALDI-MS (m / z): [M+H]+ calc for C26H29Br3N2O2S2 702.9300, found 702.951.

PhTDPPTC6Br (93). A Schlenk flask containing compound **92** (0.998 g, 1.42 mmol), and tributylphenylstannane (0.700 g, 2.13 mmol) was degassed by three vacuum/nitrogen cycles and dissolved in degassed toluene (25 mL). A degassed mixure of bis(benzylidineacetone)palladium(0) (0.082 g, 0.142 mmol) and triphenylarsine (0.130 g, 0.406 mmol) in toluene (5 mL) was then injected onto the flask and the reaction was heated to 100 C for 2 hrs under nitrogen. After cooling to room temperature, the reaction mixture was poured into water (300 mL) with 1 M potassium fluoride (30 mL). The toluene layer was collected and dried under vacuum. Methanol was then added (20 mL) and the suspension sonicated, then filtered over Celite, and washed with additional methanol (100 mL). The Celite pad was then washed with DCM until the washings were faint purple color. The solvent was removed under vacuum and the product was purified by column chromatography (DCM) to afford **93** as a dark purple solid (0.650 g, 65%). 1H-NMR (400 MHz; CDCl3): δ 8.96-8.95 (m, 1H), 8.91-8.89 (m, 1H), 7.69-7.67 (m, 2H), 7.64-7.61 (m, 1H), 7.48 (d, *J* = 4.2 Hz, 1H), 7.45-7.40 (m, 2H), 7.39-7.35 (m, 1H), 7.29-7.26 (m, 1H), 4.14-4.06 (m, 4H), 3.41-3.34 (m, 4H), 1.91-1.72 (m, 9H), 1.57-1.41 (m, 11H). MALDI-MS (m / z): [M]+ calc for C32H34Br2N2O2S2 700.0428.

PhTDPPTBrC6Br (94). Compound **93** (0.650 g, 0.925mmol) was dissolved in DCM (30 mL) and covered with aluminum foil, then N-bromosuccinimide (0.178 g, 1.00 mmol) was added in one portion and the reaction was left stirring for 12 hrs. The reaction was then diluted in DCM (100 mL) and washed with 1 M NaOH (50 mL). The DCM layer was

then collected and dried under vacuum. Methanol was then added (20 mL) and the suspension sonicated, then filtered over Celite, and washed with additional methanol (100 mL). The Celite pad was then washed with DCM until the washings were faint blue color. The solvent was removed under vacuum and the resulting dark blue solid used without further purification (0.590 g, 82%). 1H-NMR (499 MHz; CDCl3): δ 9.01 (t, J = 3.0 Hz, 1H), 9.01 (t, J = 3.0 Hz, 1H), 8.70-8.68 (m, 1H), 8.70-8.68 (m, 1H), 7.73-7.71 (m, 3H), 7.73-7.71 (m, 3H), 7.52-7.51 (m, 1H), 7.52-7.51 (m, 1H), 7.49-7.45 (m, 3H), 7.49-7.45 (m, 3H), 7.28-7.27 (m, 1H), 7.27 (dd, J = 5.6, 3.4 Hz, 1H), 4.18-4.15 (m, 3H), 4.18-4.15 (m, 3H), 4.08-4.03 (m, 2H), 4.08-4.03 (m, 2H), 3.46-3.41 (m, 6H), 3.46-3.41 (m, 6H), 1.95-1.88 (m, 7H), 1.95-1.88 (m, 7H), 1.88-1.76 (m, 7H), 1.88-1.76 (m, 7H). HRMS calc m/z for $C_{32}H_{33}BrN_2O_2S_2$ 777.9534.

PhTDPP2TC6Br (95). A Schlenk flask containing compound **94** (0.590 g, 0.755 mmol), and 2-(tributylstannyl)thiophene (0.360 mL, 1.13 mmol) was degassed by three vacuum/nitrogen cycles and dissolved in degassed toluene (25 mL). A degassed mixture of bis(benzylidineacetone)palladium(0) (0.043 g, 0.0748 mmol) and triphenylarsine (0.070 g, 0.227 mmol) in toluene (5 mL) was then injected onto the flask and the reaction was heated to 100 C for 2 hrs under nitrogen. After cooling to room temperature, the reaction mixture was poured into water (300 mL) with 1 M potassium fluoride (30 mL). The toluene layer was collected and dried under vacuum. Methanol was then added (20 mL) and the suspension sonicated, then filtered, and washed with additional methanol (100 mL). The product becomes too insoluble, so it was scratched from the filter paper. Due to its low solubility, this compound was not characterized.

TC4OH (96). A Schlenk flask containing 4-(2-thienyl)butyric acid (2.00 g, 11.5 mmol) was degassed by three vacuum/nitrogen cycles, then dissolved in anhydrous THF (25 mL). The flask was cooled to 0 C before adding lithium aluminum hydride (1 M in THF, 10.0 mL, 10.0 mmol) over 20 minutes. The reaction was then let warm up to room temperature before carefully adding water (5 mL). The reaction was diluted in water (100 mL) and filtered over Celite. The Celite pad was washed with DCM (200 mL) and residual water was removed in a separatory funnel. The DCM layer was collected, dried under MgSO4 and the solvent removed under vacuum to afford a colorless liquid (1.29 g, 72%). 1H-NMR (499 MHz; CDCl3): δ 7.14 (td, J = 5.5, 1.2 Hz, 1H), 6.96-6.93 (m, 1H), 6.82-6.81 (m, 1H), 3.71-3.68 (m, 2H), 2.91-2.88 (m, 2H), 1.83-1.76 (m, 2H), 1.70-1.64 (m, 2H). HRMS GC-TOF (m / z): [M]+ calc for C8H12OS 156.0609, found 156.0600.

TC4OBn (97). A Schlenk flask containing compound **96** (3.06 g, 19.6 mmol) was degassed by three vacuum/nitrogen cycles, then dissolved in anhydrous THF (15 mL). Sodium hydride (60% dispersion, 0.862 g, 21.6 mmol) was added in small portions under nitrogen; when no bubbling was observed, tetrabutylammonium iodide (1.45 g, 3.92 mmol) and benzyl chloride (2.71 mL, 23.5 mmol) were added in sequence. The reaction was left stirring for 12 hours at room temperature, under nitrogen. The solvent was evaporated under vacuum and the crude diluted in diethyl ether (100 mL) and extracted with water. The ether layer was collected and dried under vacuum. The product was isolated by column chromatography (1:1 hexane/DCM) to give a colorless liquid (2.61 g, 54%). 1H-NMR (400 MHz; CDCl3): δ 7.33-7.30 (m, 4H), 7.28-7.25 (m, 1H), 7.09 (dd, J = 5.1, 1.2 Hz, 1H), 6.89 (dd, J = 5.1, 3.4 Hz, 1H), 6.76 (dq, J = 3.3, 1.1

Hz, 1H), 4.48 (s, 2H), 3.48 (t, *J* = 6.3 Hz, 2H), 2.85-2.81 (m, 2H), 1.80-1.73 (m, 2H), 1.73-1.64 (m, 2H). HRMS GC-TOF (m / z): [M]+ calc for $C_{15}H_{18}OS$ 246.1078, found 246.1083.

SnBu3TC4OBn (98). A Schlenk flask comtaining compound **97** (1.51 g, 6.13 mmol) was degassed by three vacuum/nitrogen cycles and dissolved in anhydrous THF (20 mL), before cooling to -78 °C. N-butyllithium (2.5 M in hexanes, 2.70 mL, 6.74 mmol) was then slowly injected, and the reaction was left stirring for 30 min. Tributyltin chloride (1.82 mL, 6.74 mmol) was then injected and the cooling bath was removed. After warming to room temperature, the reaction was diluted in water (100 mL), 1 M NaOH (20 mL) and extracted with hexanes. The organic phase was collected, dried under $MgSO_4$, followed by solvent removal under vacuum to afford **98** as a colorless liquid (65% conversion by NMR), which was used without further purification. 1H-NMR (499 MHz; CDCl3): δ 7.36 (q, *J* = 2.8 Hz, 5H), 7.13-7.12 (m,), 7.00 (d, *J* = 3.2 Hz, 1H), 6.93-6.92 (m, 1H), 4.52 (d, *J* = 3.2 Hz, 3H), 3.54-3.51 (m, 3H), 2.92-2.86 (m, 3H), 1.89-1.86 (m, 1H), 1.83-1.78 (m, 3H), 1.75-1.70 (m, 3H), 1.64-1.58 (m, 6H), 1.41-1.31 (m, 11H), 1.13-1.07 (m, 8H), 0.96-0.86 (m, 18H). MALDI-MS (m / z): [M + H]+ calc for $C_{27}H_{44}OSSn$ 537.2214, found 537.149.

BrTDPPTC12 (99). A butyl-octyl DPP (from ref 174) (1.00 g, 1.57 mmol) was dissolved in DCM (35 mL) and covered with aluminum foil, then N-bromosuccinimide (0.140 g, 0.786 mmol) was added in one portion and the reaction was left stirring for 12 hrs. The reaction was then diluted in DCM (100 mL) and washed with 1 M NaOH (50 mL). The DCM layer was then collected and dried under vacuum. The product was isolated by column chromatography (50% Hexane/DCM) to give a dark red solid (0.600 g, 53%).

1H-NMR (499 MHz; CDCl3): δ 8.89 (d, *J* = 3.8 Hz, 1H), 8.62 (t, *J* = 4.0 Hz, 1H), 7.67-7.66 (m, 1H), 7.30 (d, *J* = 4.1 Hz, 1H), 7.24 (d, *J* = 4.2 Hz, 1H), 4.04-4.03 (m, 2H), 3.97 (s, 2H), 1.93-1.88 (m, 3H), 1.37-1.24 (m, 42H), 0.91-0.85 (m, 15H). MALDI-MS (m / z): [M]+ calc for C38H39BrN2O2S2 714.2888, found 714.305.

BnOC42TDPPTC12 (100). A Schlenk flask containing compound **99** (0.960 g, 1.34 mmol) and compound **98** (1.21 g, 1.47 mmol) was degassed by three vacuum/nitrogen cycles and dissolved in degassed toluene (25 mL). A degassed mixture of bis(benzylidineacetone)palladium(0) (0.080 g, 0.134 mmol) and triphenylarsine (0.082 g, 0.268 mmol) in toluene (5 mL) was then injected onto the flask and the reaction was heated to 100 C for 2 hrs under nitrogen. After cooling to room temperature, the reaction mixture was poured into water (300 mL) with 1 M potassium fluoride (30 mL). The toluene layer was collected, dried under vacuum and the product was purified by column chromatography (30% Hexanes/DCM) to afford **100** as a dark purple waxy solid (0.920 g, 79%). 1H-NMR (400 MHz; CDCl3): δ 8.94-8.89 (m, 1H), 8.85-8.82 (m, 1H), 7.62-7.59 (m, 1H), 7.37-7.32 (m, 3H), 7.32-7.27 (m, 3H), 7.24 (dd, *J* = 8.1, 2.8 Hz, 1H), 7.14 (t, *J* = 4.1 Hz, 1H), 6.74 (d, *J* = 3.6 Hz, 1H), 4.54-4.50 (m, 2H), 4.08-3.99 (m, 4H), 3.56-3.48 (m, 2H), 2.89-2.80 (m, 2H), 2.01-1.88 (m, 2H), 1.85-1.68 (m, 4H), 1.39-1.22 (m, 28H), 0.87-0.81 (m, 10H). MALDI-MS (m / z): [M + K]+ calc for C53H56N2O3S3 903.4436, found 903.508.

BnOC42TDPPTBrC12 (101). Compound **100** (1.29 g, 1.49 mmol) was dissolved in DCM (30 mL) and covered with aluminum foil, then N-bromosuccinimide (0.318 g, 1.79 mmol) was added in one portion and the reaction was left stirring for 12 hrs. The reaction was then diluted in DCM (100 mL) and washed with 1 M NaOH (50 mL). The

DCM layer was then collected and dried under vacuum. The product was purified by column chromatography (30%Hexanes/DCM) to give a purple waxy solid (0.580 g, 41%). 1H-NMR (499 MHz; CDCl3): δ 8.95 (d, *J* = 4.1 Hz, 1H), 8.59 (d, *J* = 4.2 Hz, 1H), 7.38-7.35 (m, 5H), 7.32-7.31 (m, 1H), 7.25-7.22 (m, 2H), 7.16 (d, *J* = 3.6 Hz, 1H), 6.77 (t, *J* = 4.5 Hz, 1H), 4.54 (s, 2H), 4.03 (d, *J* = 7.8 Hz, 2H), 3.96 (d, *J* = 7.7 Hz, 2H), 3.54 (t, *J* = 6.3 Hz, 2H), 2.87 (t, *J* = 7.4 Hz, 2H), 1.91 (t, *J* = 3.3 Hz, 1H), 1.85-1.82 (m, 2H), 1.77-1.73 (m, 2H), 1.35-1.25 (m, 42H), 0.91-0.84 (m, 16H). MALDI-MS (m / z): [M + K]+ calc for $C_{53}H_{55}BrN_2O_3S_3$ 981.3541, found 981.437.

BnOC42TDPP2TC12 (102). A Schlenk flask containing compound **101** (0.580 g, 0.614 mmol) and 2-(tributylstannyl)thiophene (0.300 mL, 0.921 mmol) was degassed by three vacuum/nitrogen cycles and the mixture dissolved in degassed toluene (25 mL). A degassed mixture of bis(benzylidineacetone)palladium(0) (0.035 g, 0.0614 mmol) and triphenylarsine (0.056 g, 0.184 mmol) in toluene (5 mL) was then injected onto the flask and the reaction was heated to 100 C for 2 hrs under nitrogen. After cooling to room temperature, the reaction mixture was poured into water (300 mL) with 1 M potassium fluoride (30 mL). The toluene layer was collected, dried under vacuum and the product was purified by column chromatography (30% Hexanes/DCM) to afford **102** as a dark blue waxy solid (0.480 g, 83%). 1H-NMR (400 MHz; CDCl3): δ 8.92 (d, *J* = 4.2 Hz, 1H), 8.88 (d, *J* = 4.1 Hz, 1H), 7.41 (q, *J* = 2.9 Hz, 1H), 7.35-7.33 (m, 4H), 7.32-7.30 (m, 3H), 7.22 (d, *J* = 4.1 Hz, 1H), 7.12 (t, *J* = 4.5 Hz, 1H), 7.07 (dd, *J* = 4.6, 4.1 Hz, 1H), 6.74 (d, *J* = 3.6 Hz, 1H), 4.51 (s, 2H), 4.03 (dd, *J* = 7.7, 1.8 Hz, 4H), 3.52 (t, *J* = 6.2 Hz, 2H), 2.85 (t, *J* = 7.4 Hz, 2H), 1.97-1.96 (m, 2H), 1.81 (td, *J* = 7.6, 3.0 Hz, 2H), 1.79-1.70 (m,

2H), 1.34-1.23 (m, 31H), 0.90-0.82 (m, 13H). MALDI-MS (m / z): [M + K]+ calc for C57H58N203S4 985.4313, found 985.608.

BnOC42TDPP2TBrC12 (103). Compound **102** (0.480 g, 0.507 mmol) was dissolved in DCM (30 mL) and covered with aluminum foil, then N-bromosuccinimide (0.100 g, 0.557 mmol) was added in one portion and the reaction was left stirring for 12 hrs. The reaction was then diluted in DCM (100 mL) and washed with 1 M NaOH (50 mL). The DCM layer was then collected and dried under vacuum. The product was purified by column chromatography (30%Hexanes/DCM) to give a purple waxy solid (0.190 g, 80%). 1H-NMR (499 MHz; CDCl3): δ 8.95 (d, J = 4.1 Hz, 1H), 8.85 (d, J = 4.1 Hz, 1H), 7.37-7.36 (m, 4H), 7.33-7.30 (m, 1H), 7.25 (dd, J = 4.0, 0.9 Hz, 2H), 7.16 (d, J = 3.6 Hz, 1H), 7.07 (d, J = 3.9 Hz, 1H), 7.05 (d, J = 3.9 Hz, 1H), 6.77 (d, J = 3.6 Hz, 1H), 4.54 (s, 2H), 4.06-4.03 (m, 4H), 3.54 (t, J = 6.2 Hz, 2H), 2.87 (t, J = 7.5 Hz, 2H), 1.99-1.96 (m, 2H), 1.85-1.80 (m, 2H), 1.77-1.73 (m, 3H), 1.65-1.62 (m, 1H), 1.54 (dd, J = 7.4, 4.6 Hz, 1H), 1.38-1.25 (m, 61H), 0.99 (d, J = 6.6 Hz, 3H), 0.92-0.85 (m, 34H). MALDI-MS (m / z): [M + K]+ calc for C57H57BrN2O3S4 1063.3418, found 1063.538.

BnOC42TDPP2TC12BDTO2TC8 (104). A Schlenk flask containing compound **103** (0.190 g, 0.185 mmol) and compound **40** (0.100 mL, 0.0882 mmol) was degassed by three vacuum/nitrogen cycles and the mixture dissolved in degassed toluene (25 mL). A degassed mixture of   bis(benzylidineacetone)palladium(0) (0.010 g, 0.0176 mmol) and triphenylarsine (0.011 g, 0.0353 mmol) in toluene (5 mL) was then injected onto the flask and the reaction was heated to 100 C for 2 hrs under nitrogen. After cooling to room temperature, the reaction mixture was poured into water (300 mL) with 1 M potassium fluoride (30 mL). The toluene layer was collected, dried under vacuum and

the product was purified by gel permeation chromatography(CHCl3) to afford **104** as a dark green solid (0.0575 g, 26%). 1H-NMR (499 MHz; CDCl3): δ 8.96-8.94 (m, 2H), 8.94-8.92 (m, 2H), 7.64-7.63 (m, 2H), 7.39-7.34 (m, 11H), 7.33-7.31 (m, 3H), 7.27-7.25 (m, 1H), 7.22-7.19 (m, 5H), 7.13 (q, J = 2.9 Hz, 2H), 6.99 (d, J = 3.4 Hz, 2H), 6.74-6.73 (m, 2H), 4.53 (s, 4H), 4.08-4.03 (m, 8H), 3.52 (q, J = 5.2 Hz, 5H), 2.98-2.93 (m, 4H), 2.86-2.83 (m, 4H), 2.02-1.95 (m, 6H), 1.84-1.78 (m, 7H), 1.78-1.69 (m, 7H), 1.46-1.20 (m, 92H), 1.07-0.97 (m, 14H), 0.93-0.82 (m, 29H). MALDI-MS (m / z): [M]+ calc for $C_{146}H_{186}N_4O_6S_{12}$ 2499.1021, found 2499.443.

References

(1)   Smalley, R. E. *MRS Bulletin.* **2005**, 38, 412-417.

(2)   International Energy Outlook 2013. Energy Information Administration. https://www.eia.gov/outlooks/ieo/pdf/0484(2013).pdf (accessed Aug 18, 2016).

(3)   Global Climate Change http://climate.nasa.gov/ (accessed Aug 18, 2016).

(4)   McGlade, C.; Ekins, P. *Nature* **2015**, *517* (7533), 187.

(5)   Lewis, N. S.; Nocera, D. G. *Proc. Natl. Acad. Sci.* **2006**, *103* (43), 15729.

(6)   Jean, J.; Brown, P. R.; Jaffe, R. L.; Buonassisi, T.; Bulović, V. *Energy Environ. Sci.* **2015**, *8* (4), 1200.

(7)   Herron, J. A.; Kim, J.; Upadhye, A. A.; Huber, G. W.; Maravelias, C. T. *Energy Environ. Sci.* **2014**, *8* (1), 126.

(8)   Cook, T.R.; Dogutan, D.K.;Reese, S.Y.; Surendranath, Y.;Teets, T.S.; Nocera, D.G. *Chem Rev*. **2010**, 110 (11), 6474-6502.

(9)   Weinstein, L. A.; Loomis, J.; Bhatia, B.; Bierman, D. M.; Wang, E. N.; Chen, G. *Chem. Rev.* **2015**, *115* (23), 12797.

(10)   The History of Solar. US Department of Energy. https://www1.eere.energy.gov/solar/pdfs/solar_timeline.pdf (accesssed Aug. 18, 2016).

(11)   Shirakawa, H.; Louis, E. J.; MacDiarmid, A. G.; Chiang, C. K.; Heeger, A. J. *J. Chem. Soc. Chem. Commun.* **1977**, No. 16, 578.

(12)   NREL: National Center for Photovoltaics Home Page http://www.nrel.gov/ncpv/ (accessed Aug 18, 2016).

(13)   SunShot Initiative | Department of Energy http://www.energy.gov/eere/sunshot/sunshot-initiative (accessed Aug 18, 2016).

(14)   Mazzio, K. A.; Luscombe, C. K. *Chem. Soc. Rev.* **2014**, *44* (1), 78.

(15)   Knapp, K.; Jester, T. *Sol. Energy* **2001**, *71* (3), 165.

(16)   Dou, L.; You, J.; Hong, Z.; Xu, Z.; Li, G.; Street, R. A.; Yang, Y. *Adv. Mater.* **2013**, *25* (46), 6642.

(17)   Heeger, A. J. *Chem. Soc. Rev.* **2010**, *39* (7), 2354.

(18)   Heeger, A. J. *Angew. Chem. Int. Ed.* **2001**, *40* (14), 2591.

(19)   Chamberlain, G. A. *Sol. Cells* **1983**, *8* (1), 47.

(20)   Tang, C. W. *Appl. Phys. Lett.* **1986**, *48* (2), 183.

(21)   Sariciftci, N. S.; Smilowitz, L.; Heeger, A. J.; Wudl, F. *Science* **1992**, *258* (5087), 1474.

(22)   Yu, G.; Gao, J.; Hummelen, J. C.; Wudl, F.; Heeger, A. J. *Science* **1995**, *270* (5243), 1789.

(23)   Brabec, C. J.; Gowrisanker, S.; Halls, J. J. M.; Laird, D.; Jia, S.; Williams, S. P. *Adv. Mater.* **2010**, *22* (34), 3839.

(24)   Padinger, F.; Rittberger, R. s.; Sariciftci, N. s. *Adv. Funct. Mater.* **2003**, *13* (1), 85.

(25)   Darling, S. B.; You, F. *RSC Adv.* **2013**, *3* (39), 17633.

(26)   Dou, L.; You, J.; Yang, J.; Chen, C.-C.; He, Y.; Murase, S.; Moriarty, T.; Emery, K.; Li, G.; Yang, Y. *Nat. Photonics* **2012**, *6* (3), 180.

(27)   Zhou, H.; Zhang, Y.; Mai, C.-K.; Collins, S. D.; Bazan, G. C.; Nguyen, T.-Q.; Heeger, A. J. *Adv. Mater.* **2015**, *27* (10), 1767.

(28)   Deibel, C.; Dyakonov, V.; Brabec, C. J. *IEEE J. Sel. Top. Quantum Electron.* **2010**, *16* (6), 1517.

(29)   Hu, L.; Iwasaki, A.; Suizu, R.; Yoshikawa, H.; Awaga, K.; Ito, H. *Chem. Phys. Lett.* **2010**, *484* (4–6), 177.

(30)   Zhao, W.; Qian, D.; Zhang, S.; Li, S.; Inganäs, O.; Gao, F.; Hou, J. *Adv. Mater.* **2016**, *28* (23), 4734.

(31)   You, J.; Dou, L.; Yoshimura, K.; Kato, T.; Ohya, Y.; Moriarty, T.; Emery, K.; Chen C-C.; Gao, J.; Li, G.; Yang, Y. *Nature Commun.* **2013**, 4, 1446-1456.

(32)   Kan, B.; Zhang, Q.; Liu, F.; Wan, X.; Wang, Y.; Ni, W.; Yang, X.; Zhang, M.; Zhang, H.; Russell, T. P.; Chen, Y. *Chem. Mater.* **2015** *27* (24), 8414-8423.

(33)   Liu, Y.; Chen, C.-C.; Hong, Z.; Gao, J.; (Michael) Yang, Y.; Zhou, H.; Dou, L.; Li, G.; Yang, Y. *Sci. Rep.* **2013**, *3*.

(34)   Shockley, W.; Queisser, H. J. *J. Appl. Phys.* **1961**, *32* (3), 510.

(35)   Giebink, N. C.; Wiederrecht, G. P.; Wasielewski, M. R.; Forrest, S. R. *Phys. Rev. B* **2011**, *83* (19), 195326.

(36)   Yip, H.-L.; Jen, A. K.-Y. *Energy Environ. Sci.* **2012**, *5* (3), 5994.

(37)   Lu, L.; Zheng, T.; Wu, Q.; Schneider, A. M.; Zhao, D.; Yu, L. *Chem. Rev.* **2015**, *115* (23), 12666.

(38)   Pingree, L. S. C.; MacLeod, B. A.; Ginger, D. S. *J. Phys. Chem. C* **2008**, *112* (21), 7922.

(39)   Wong, K. W.; Yip, H. L.; Luo, Y.; Wong, K. Y.; Lau, W. M.; Low, K. H.; Chow, H. F.; Gao, Z. Q.; Yeung, W. L.; Chang, C. C. *Appl. Phys. Lett.* **2002**, *80* (15), 2788.

(40)   Jung, J. W.; Lee, J. U.; Jo, W. H. *J. Phys. Chem. C* **2010**, *114* (1), 633.
(41)   Zhou, H.; Zhang, Y.; Mai, C.-K.; Collins, S. D.; Nguyen, T.-Q.; Bazan, G. C.; Heeger, A. J. *Adv. Mater.* **2014**, *26* (5), 780.

(42)   Steirer, K. X.; Ndione, P. F.; Widjonarko, N. E.; Lloyd, M. T.; Meyer, J.; Ratcliff, E. L.; Kahn, A.; Armstrong, N. R.; Curtis, C. J.; Ginley, D. S.; Berry, J. J.; Olson, D. C. *Adv. Energy Mater.* **2011**, *1* (5), 813.

(43)   Chen, C.-P.; Chen, Y.-D.; Chuang, S.-C. *Adv. Mater.* **2011**, *23* (33), 3859.

(44)   Xu, Q.; Wang, F.; Tan, Z.; Li, L.; Li, S.; Hou, X.; Sun, G.; Tu, X.; Hou, J.; Li, Y. *ACS Appl. Mater. Interfaces* **2013**, *5* (21), 10658.

(45)   Choi, H.; Kim, B.; Ko, M. J.; Lee, D.-K.; Kim, H.; Kim, S. H.; Kim, K. *Org. Electron.* **2012**, *13* (6), 959.

(46)   Tu, X.; Wang, F.; Li, C.; Tan, Z.; Li, Y. *J. Phys. Chem. C* **2014**, *118* (18), 9309.

(47)   Tan, Z. a.; Zhang, W.; Qian, D.; Cui, C.; Xu, Q.; Li, L.; Li, S.; Li, Y. *Phys. Chem. Chem. Phys.* **2012**, 14 (41), 14217-14223.

(48)   Sun, Y.; Takacs, C. J.; Cowan, S. R.; Seo, J. H.; Gong, X.; Roy, A.; Heeger, A. J. *Adv. Mater.* **2011**, *23* (19), 2226.

(49)   Park, S. H.; Roy, A.; Beaupré, S.; Cho, S.; Coates, N.; Moon, J. S.; Moses, D.; Leclerc, M.; Lee, K.; Heeger, A. J. *Nat. Photonics* **2009**, *3* (5), 297.

(50)   Park, B.; Shin, J. C.; Cho, C. Y. *Sol. Energy Mater. Sol. Cells* **2013**, *108*, 1.

(51)   Palilis, L. C.; Vasilopoulou, M.; Douvas, A. M.; Georgiadou, D. G.; Kennou, S.; Stathopoulos, N. A.; Constantoudis, V.; Argitis, P. *Solar Energy Materials and Solar Cells.* **2013**, 114, 205-213.

(52)   Wang, F.; Xu, Q.; Tan, Z.; Qian, D.; Ding, Y.; Li, L.; Li, S.; Li, Y. *Org. Electron.* **2012**, *13* (11), 2429.

(53)   Zhou, Y.; Fuentes-Hernandez, C.; Shim, J.; Meyer, J.; Giordano, A. J.; Li, H.; Winget, P.; Papadopoulos, T.; Cheun, H.; Kim, J.; Fenoll, M.; Dindar, A.; Haske, W.; Najafabadi, E.; Khan, T. M.; Sojoudi, H.; Barlow, S.; Graham, S.; Brédas, J.-L.; Marder, S. R.; Kahn, A.; Kippelen, B. *Science* **2012**, *336* (6079), 327.

(54)   Wang, H.; Zhang, W.; Xu, C.; Bi, X.; Chen, B.; Yang, S. *ACS Appl. Mater. Interfaces* **2013**, *5* (1), 26.

(55)   Halls, J. J. M.; Cornil, J.; dos Santos, D. A.; Silbey, R.; Hwang, D.-H.; Holmes, A. B.; Brédas, J. L.; Friend, R. H. *Phys. Rev. B* **1999**, *60* (8), 5721.

(56)   Cheng, Y.-J.; Yang, S.-H.; Hsu, C.-S. *Chem. Rev.* **2009**, *109* (11), 5868.

(57)   Brédas, J. L. *J. Chem. Phys.* **1985**, *82* (8), 3808.

(58)   Brédas, J. L.; Heeger, A. J.; Wudl, F. *J. Chem. Phys.* **1986**, *85* (8), 4673.

(59)   Kitamura, C.; Tanaka, S.; Yamashita, Y. *Chem. Mater.* **1996**, *8* (2), 570.

(60)   Brocks, G.; Tol, A. *J. Phys. Chem.* **1996**, *100* (5), 1838.

(61)   Roncali, J. *Acc. Chem. Res.* **2009**, *42* (11), 1719.

(62)   Sun, X.; Zhou, Y.; Wu, W.; Liu, Y.; Tian, W.; Yu, G.; Qiu, W.; Chen, S.; Zhu, D. *J. Phys. Chem. B* **2006**, *110* (15), 7702.

(63)   Roncali, J.; Leriche, P.; Cravino, A. *Adv. Mater.* **2007**, *19* (16), 2045.

(64)   Kopidakis, N.; Mitchell, W. J.; Lagemaat, J. van de; Ginley, D. S.; Rumbles, G.; Shaheen, S. E.; Rance, W. L. *Appl. Phys. Lett.* **2006**, *89* (10), 103524.

(65)   Ma, C.-Q.; Mena-Osteritz, E.; Debaerdemaeker, T.; Wienk, M. M.; Janssen, R. A. J.; Bäuerle, P. *Angew. Chem. Int. Ed.* **2007**, *46* (10), 1679.

(66)   Schmidt-Mende, L.; Fechtenkötter, A.; Müllen, K.; Moons, E.; Friend, R. H.; MacKenzie, J. D. *Science* **2001**, *293* (5532), 1119.

(67) Schmidt-Mende, L.; Fechtenkötter, A.; Müllen, K.; Friend, R. H.; MacKenzie, J. D. *Phys. E Low-Dimens. Syst. Nanostructures* **2002**, *14* (1–2), 263.

(68) Petritsch, K.; Dittmer, J. J.; Marseglia, E. A.; Friend, R. H.; Lux, A.; Rozenberg, G. G.; Moratti, S. C.; Holmes, A. B. *Sol. Energy Mater. Sol. Cells* **2000**, *61* (1), 63.

(69) Walker, B.; Tamayo, A. B.; Dang, X.-D.; Zalar, P.; Seo, J. H.; Garcia, A.; Tantiwiwat, M.; Nguyen, T.-Q. *Adv. Funct. Mater.* **2009**, *19* (19), 3063.

(70) Roquet, S.; Cravino, A.; Leriche, P.; Alévêque, O.; Frère, P.; Roncali, J. *J. Am. Chem. Soc.* **2006**, *128* (10), 3459.

(71) Sun, Y.; Welch, G. C.; Leong, W. L.; Takacs, C. J.; Bazan, G. C.; Heeger, A. J. *Nat. Mater.* **2012**, *11* (1), 44.

(72) Chen, Y.; Wan, X.; Long, G. *Acc. Chem. Res.* **2013**, *46* (11), 2645.

(73) Zhou, J.; Zuo, Y.; Wan, X.; Long, G.; Zhang, Q.; Ni, W.; Liu, Y.; Li, Z.; He, G.; Li, C.; Kan, B.; Li, M.; Chen, Y. *J. Am. Chem. Soc.* **2013**, *135* (23), 8484.

(74) Slooff, L. H.; Veenstra, S. C.; Kroon, J. M.; Moet, D. J. D.; Sweelssen, J.; Koetse, M. M. *Appl. Phys. Lett.* **2007**, *90* (14), 143506.

(75) Liang, Y.; Xiao, S.; Feng, D.; Yu, L. *J. Phys. Chem. C* **2008**, *112* (21), 7866.

(76) Hou, J.; Park, M.-H.; Zhang, S.; Yao, Y.; Chen, L.-M.; Li, J.-H.; Yang, Y. *Macromolecules* **2008**, *41* (16), 6012.

(77) Ye, L.; Zhang, S.; Huo, L.; Zhang, M.; Hou, J. *Acc. Chem. Res.* **2014**, *47* (5), 1595.

(78) de Leeuw, D. M.; Simenon, M. M. J.; Brown, A. R.; Einerhand, R. E. F. *Synth. Met.* **1997**, *87* (1), 53.

(79) Liang, Y.; Xu, Z.; Xia, J.; Tsai, S.-T.; Wu, Y.; Li, G.; Ray, C.; Yu, L. *Adv. Mater.* **2010**, *22* (20), E135.

(80) Cabanetos, C.; El Labban, A.; Bartelt, J. A.; Douglas, J. D.; Mateker, W. R.; Fréchet, J. M. J.; McGehee, M. D.; Beaujuge, P. M. *J. Am. Chem. Soc.* **2013**, *135* (12), 4656.

(81) Fang, L.; Zhou, Y.; Yao, Y.-X.; Diao, Y.; Lee, W.-Y.; Appleton, A. L.; Allen, R.; Reinspach, J.; Mannsfeld, S. C. B.; Bao, Z. *Chem. Mater.* **2013**, *25* (24), 4874.

(82)   Li, W.; Roelofs, W. S. C.; Wienk, M. M.; Janssen, R. A. J. *J. Am. Chem. Soc.*, **2012**, *134* (33), 13787–13795.

(83)   Dou, L.; Gao, J.; Richard, E.; You, J.; Chen, C.-C.; Cha, K. C.; He, Y.; Li, G.; Yang, Y. *J. Am. Chem. Soc.*, **2012**, *134* (24),10071–10079.

(84)   Huo, L.; Zhang, S.; Guo, X.; Xu, F.; Li, Y.; Hou, J. *Angew. Chem. Int. Ed.* **2011**, *50* (41), 9697.

(85)   Liao, S.-H.; Jhuo, H.-J.; Cheng, Y.-S.; Chen, S.-A. *Adv. Mater.* **2013**, *25* (34), 4766.

(86)   Ye, L.; Zhang, S.; Zhao, W.; Yao, H.; Hou, J. *Chem. Mater.*, **2014**, *26* (12), 3603–3605.

(87)   Nguyen, T. L.; Choi, H.; Ko, S.-J.; Uddin, M. A.; Walker, B.; Yum, S.; Jeong, J.-E.; Yun, M. H.; Shin, T. J.; Hwang, S.; Kim, J. Y.; Woo, H. Y. *Energy Environ. Sci.* **2014**, *7* (9), 3040.

(88)   Ho, C.-C.; Chen, C.-A.; Chang, C.-Y.; Darling, S. B.; Su, W.-F. *J. Mater. Chem. A* **2014**, *2* (21), 8026.

(89)   Scharber, M. C.; Mühlbacher, D.; Koppe, M.; Denk, P.; Waldauf, C.; Heeger, A. J.; Brabec, C. J. *Adv. Mater.* **2006**, *18* (6), 789.

(90)   Jakowetz, A. C.; Böhm, M. L.; Zhang, J.; Sadhanala, A.; Huettner, S.; Bakulin, A. A.; Rao, A.; Friend, R. H. *J. Am. Chem. Soc.* **2016**, *138* (36), 11672.

(91)   Po, R.; Bianchi, G.; Carbonera, C.; Pellegrino, A. *Macromolecules*, **2015**, *48* (3), 453–461.

(92)   Mihailetchi, V. D.; Xie, H. X.; de Boer, B.; Koster, L. J. A.; Blom, P. W. M. *Adv. Funct. Mater.* **2006**, *16* (5), 699.

(93)   Xin, H.; Guo, X.; Ren, G.; Watson, M. D.; Jenekhe, S. A. *Adv. Energy Mater.* **2012**, *2* (5), 575.

(94)   Liu, T.; Troisi, A. *Adv. Mater.* **2013**, *25* (7), 1038.

(95)   Wienk, M. M.; Turbiez, M.; Gilot, J.; Janssen, R. A. J. *Adv. Mater.* **2008**, *20* (13), 2556.

(96)   Zhao, G.; He, Y.; Li, Y. *Adv. Mater.* **2010**, *22* (39), 4355.

(97)   Matsuo, Y.; Sato, Y.; Niinomi, T.; Soga, I.; Tanaka, H.; Nakamura, E. *J. Am. Chem. Soc.*, **2009**, *131* (44), 16048–16050.

(98)   Cheng, P.; Ye, L.; Zhao, X.; Hou, J.; Li, Y.; Zhan, X. *Energy Environ. Sci.* **2014**, *7* (4), 1351.

(99)   Kozma, E.; Catellani, M. *Dyes Pigments* **2013**, *98* (1), 160.

(100)   Mori, D.; Benten, H.; Okada, I.; Ohkita, H.; Ito, S. *Energy Environ. Sci.* **2014**, *7* (9), 2939.

(101)   Huang, Y.; Kramer, E. J.; Heeger, A. J.; Bazan, G. C. *Chem. Rev.*, **2014**, *114* (14), 7006–7043.

(102)   Liu, F.; Wang, C.; Baral, J. K.; Zhang, L.; Watkins, J. J.; Briseno, A. L.; Russell, T. P. *J. Am. Chem. Soc.*, **2013**, *135* (51), 19248–19259.

(103)   Moon, J. S.; Lee, J. K.; Cho, S.; Byun, J.; Heeger, A. J. *Nano Lett.* **2009**, *9* (1), 230.

(104)   Kline, R. j.; McGehee, M. d.; Kadnikova, E. n.; Liu, J.; Fréchet, J. m. j. *Adv. Mater.* **2003**, *15* (18), 1519.

(105)   Müller-Buschbaum, P. *Adv. Mater.* **2014**, *26* (46), 7692.

(106)   Sirringhaus, H.; Brown, P. J.; Friend, R. H.; Nielsen, M. M.; Bechgaard, K.; Langeveld-Voss, B. M. W.; Spiering, A. J. H.; Janssen, R. A. J.; Meijer, E. W.; Herwig, P.; de Leeuw, D. M. *Nature.* **1999**, 401 (6754), 685-688.

(107)   Shaheen, S. E.; Brabec, C. J.; Sariciftci, N. S.; Padinger, F.; Fromherz, T.; Hummelen, J. C. *Appl. Phys. Lett.* **2001**, *78* (6), 841.

(108)   Peet, J.; Kim, J. Y.; Coates, N. E.; Ma, W. L.; Moses, D.; Heeger, A. J.; Bazan, G. C. *Nat. Mater.* **2007**, *6* (7), 497.

(109)   Lee, J. K.; Ma, W. L.; Brabec, C. J.; Yuen, J.; Moon, J. S.; Kim, J. Y.; Lee, K.; Bazan, G. C.; Heeger, A. J. *J. Am. Chem. Soc.* **2008**, *130* (11), 3619.

(110)   Lou, S. J.; Szarko, J. M.; Xu, T.; Yu, L.; Marks, T. J.; Chen, L. X. *J. Am. Chem. Soc.*, **2011**, *133* (51), 20661–20663.

(111)   Kim, Y.; Yeom, H. R.; Kim, J. Y.; Yang, C. *Energy Environ. Sci.* **2013**, *6* (6), 1909.

(112) Machui, F.; Maisch, P.; Burgués-Ceballos, I.; Langner, S.; Krantz, J.; Ameri, T.; Brabec, C. J. *ChemPhysChem* **2015**, *16* (6), 1275.

(113) Erb, T.; Zhokhavets, U.; Gobsch, G.; Raleva, S.; Stühn, B.; Schilinsky, P.; Waldauf, C.; Brabec, C. J. *Adv. Funct. Mater.* **2005**, *15* (7), 1193.

(114) Park, J. K.; Jo, J.; Seo, J. H.; Moon, J. S.; Park, Y. D.; Lee, K.; Heeger, A. J.; Bazan, G. C. *Adv. Mater.* **2011**, *23* (21), 2430.

(115) Peumans, P.; Uchida, S.; Forrest, S. R. *Nature* **2003**, *425* (6954), 158.

(116) Qian, D.; Liu, B.; Wang, S.; Himmelberger, S.; Linares, M.; Vagin, M.; Müller, C.; Ma, Z.; Fabiano, S.; Berggren, M.; Salleo, A.; Inganäs, O.; Zou, Y.; Zhang, F. *J. Mater. Chem. A* **2015**, *3* (48), 24349.

(117) Mihailetchi, V. D.; Xie, H.; Boer, B. de; Popescu, L. M.; Hummelen, J. C.; Blom, P. W. M.; Koster, L. J. A. *Appl. Phys. Lett.* **2006**, *89* (1), 12107.

(118) Lloyd, M. T.; Mayer, A. C.; Subramanian, S.; Mourey, D. A.; Herman, D. J.; Bapat, A. V.; Anthony, J. E.; Malliaras, G. G. *J. Am. Chem. Soc.* **2007**, *129* (29), 9144.

(119) Zhou, H.; Zhang, Y.; Seifter, J.; Collins, S. D.; Luo, C.; Bazan, G. C.; Nguyen, T.-Q.; Heeger, A. J. *Adv. Mater.* **2013**, *25* (11), 1646.

(120) Whitesides, G.M. *Scientific American.* **1995**, 146,149.

(121) Wang, C.; Dong, H.; Hu, W.; Liu, Y.; Zhu, D. *Chem. Rev.*, **2012**, *112* (4), 2208–2267.

(122) Schmidtke, J. P.; Friend, R. H.; Kastler, M.; Müllen, K. *J. Chem. Phys.* **2006**, *124* (17), 174704.

(123) Wong, W. W. H.; Singh, T. B.; Vak, D.; Pisula, W.; Yan, C.; Feng, X.; Williams, E. L.; Chan, K. L.; Mao, Q.; Jones, D. J.; Ma, C.-Q.; Müllen, K.; Bäuerle, P.; Holmes, A. B. *Adv. Funct. Mater.* **2010**, *20* (6), 927.

(124) Takeya, J.; Yamagishi, M.; Tominari, Y.; Hirahara, R.; Nakazawa, Y.; Nishikawa, T.; Kawase, T.; Shimoda, T.; Ogawa, S. *Appl. Phys. Lett.* **2007**, *90* (10), 102120.

(125) Seo, J. H.; Park, D. S.; Cho, S. W.; Kim, C. Y.; Jang, W. C.; Whang, C. N.; Yoo, K.-H.; Chang, G. S.; Pedersen, T.; Moewes, A.; Chae, K. H.; Cho, S. J. *Appl. Phys. Lett.* **2006**, *89* (16), 163505.

(126) Anthony, J. E.; Subramanian, S.; Parkin, S. R.; Park, S. K.; Jackson, T. N. *J. Mater. Chem.* **2009**, *19* (42), 7984.

(127) Winzenberg, K. N.; Kemppinen, P.; Fanchini, G.; Bown, M.; Collis, G. E.; Forsyth, C. M.; Hegedus, K.; Singh, T. B.; Watkins, S. E. *Chem. Mater.*, **2009**, *21* (24), 5701–5703.

(128) He, X.; Gao, F.; Tu, G.; Hasko, D. G.; Hüttner, S.; Greenham, N. C.; Steiner, U.; Friend, R. H.; Huck, W. T. S. *Adv. Funct. Mater.* **2011**, *21* (1), 139.

(129) Brady, M. A.; Su, G. M.; Chabinyc, M. L. *Soft Matter* **2011**, *7* (23), 11065.

(130) Watkins, P. K.; Walker, A. B.; Verschoor, G. L. B. *Nano Lett.* **2005**, *5* (9), 1814.

(131) Facchetti, A. *Chem. Mater.*, **2011**, *23* (3), 733–758.

(132) Zhang, W.; Smith, J.; Watkins, S. E.; Gysel, R.; McGehee, M.; Salleo, A.; Kirkpatrick, J.; Ashraf, S.; Anthopoulos, T.; Heeney, M.; McCulloch, I. *J. Am. Chem. Soc.*, **2010**, *132* (33), 11437–11439.

(133) Jung, J. W.; Liu, F.; Russell, T. P.; Jo, W. H. *Energy Environ. Sci.* **2012**, *5* (5), 6857.

(134) Dössel, L. F.; Kamm, V.; Howard, I. A.; Laquai, F.; Pisula, W.; Feng, X.; Li, C.; Takase, M.; Kudernac, T.; Feyter, S. D.; Müllen, K. *J. Am. Chem. Soc.*, **2012**, *134* (13), 5876–5886.

(135) Noriega, R.; Rivnay, J.; Vandewal, K.; Koch, F. P. V.; Stingelin, N.; Smith, P.; Toney, M. F.; Salleo, A. *Nat. Mater.* **2013**, *12* (11), 1038.

(136) Hedley, G. J.; Ward, A. J.; Alekseev, A.; Howells, C. T.; Martins, E. R.; Serrano, L. A.; Cooke, G.; Ruseckas, A.; Samuel, I. D. W. *Nat. Commun.* **2013**, *4*, 2867.

(137) Lin, Y.; Li, Y.; Zhan, X. *Chem. Soc. Rev.* **2012**, *41* (11), 4245.

(138) Thompson, B. C.; Fréchet, J. M. J. *Angew. Chem. Int. Ed.* **2008**, *47* (1), 58.

(139) You, J.; Dou, L.; Yoshimura, K.; Kato, T.; Ohya, K.; Moriarty, T.; Emery, K.; Chen, C.-C.; Gao, J.; Li, G.; Yang, Y. *Nat. Commun.* **2013**, *4*, 1446.

(140) Li, G.; Shrotriya, V.; Huang, J.; Yao, Y.; Moriarty, T.; Emery, K.; Yang, Y. *Nat. Mater.* **2005**, *4* (11), 864.

(141) Lin, Y.; Zhan, X. *Mater. Horiz.* **2014**, *1* (5), 470.

(142) Nielsen, C. B.; Holliday, S.; Chen, H.-Y.; Cryer, S. J.; McCulloch, I. *Acc. Chem. Res.* **2015**, *48* (11), 2803.

(143) Jackson, N. E.; Savoie, B. M.; Kohlstedt, K. L.; Olvera de la Cruz, M.; Schatz, G. C.; Chen, L. X.; Ratner, M. A. *J. Am. Chem. Soc.* **2013**, *135* (28), 10475.

(144) Jackson, N. E.; Kohlstedt, K. L.; Savoie, B. M.; Olvera de la Cruz, M.; Schatz, G. C.; Chen, L. X.; Ratner, M. A. *J. Am. Chem. Soc.* **2015**, *137* (19), 6254.

(145) Coughlin, J. E.; Zhugayevych, A.; Bakus, R. C.; van der Poll, T. S.; Welch, G. C.; Teat, S. J.; Bazan, G. C.; Tretiak, S. *J. Phys. Chem. C* **2014**, *118* (29), 15610.

(146) Heo, H.; Kim, H.; Lee, D.; Jang, S.; Ban, L.; Lim, B.; Lee, J.; Lee, Y. *Macromolecules* **2016**, *49* (9), 3328.

(147) Tsai, W.-W.; Tevis, I. D.; Tayi, A. S.; Cui, H.; Stupp, S. I. *J. Phys. Chem. B* **2010**, *114* (45), 14778.

(148) Tevis, I. D.; Tsai, W.-W.; Palmer, L. C.; Aytun, T.; Stupp, S. I. *ACS Nano* **2012**, *6* (3), 2032.

(149) Ruiz-Carretero, A.; Aytun, T.; Bruns, C. J.; Newcomb, C. J.; Tsai, W.-W.; Stupp, S. I. *J. Mater. Chem. A* **2013**, *1* (38), 11674.

(150) Hill, J. P.; Jin, W.; Kosaka, A.; Fukushima, T.; Ichihara, H.; Shimomura, T.; Ito, K.; Hashizume, T.; Ishii, N.; Aida, T. *Science* **2004**, *304* (5676), 1481.

(151) Sinks, L. E.; Rybtchinski, B.; Iimura, M.; Jones, B. A.; Goshe, A. J.; Zuo, X.; Tiede, D. M.; Li, X.; Wasielewski, M. R. *Chem Mater.* **2005**, 17 (25), 6295-6303.

(152) Tevis, I. D.; Palmer, L. C.; Herman, D. J.; Murray, I. P.; Stone, D. A.; Stupp, S. I. *J. Am. Chem. Soc.* **2011**, *133* (41), 16486.

(153) Stone, D. A.; Tayi, A. S.; Goldberger, J. E.; Palmer, L. C.; Stupp, S. I. *Chem. Commun.* **2011**, *47* (20), 5702.

(154) Schenning, A. P. H. J.; Jonkheijm, P.; Peeters, E.; Meijer, E. W. *J. Am. Chem. Soc.* **2001**, 123 (3), 409-416.

(155) Jonkheijm, P.; Hoeben, F. J. M.; Kleppinger, R.; van Herrikhuyzen, J.; Schenning, A. P. H. J.; Meijer, E. W. *J. Am. Chem. Soc.* **2003**, 125 (51), 15941-15949.

(156) Jonkheijm, P.; van Duren, J. K. J.; Kemerink, M.; Janssen, R. A. J.; Schenning, A. P. H. J.; Meijer, E. W. *Macromolecules.* **2006**, 39 (2), 784-788.

(157) Matmour, R.; De Cat, I.; George, S. J.; Adriaens, W.; Leclère, P.; Bomans, P. H. H.; Sommerdijk, N. A. J. M.; Gielen, J. C.; Christianen, P. C. M.; Heldens, J. T.; van Hest, J. C. M.; Löwik, D. W. P. M.; De Feyter, S.; Meijer, E. W.; Schenning, A. P. H. J. *J. Am. Chem. Soc.* **2008**, 130 (44), 14576-14583.

(158) Spada, G. P.; Lena, S.; Masiero, S.; Pieraccini, S.; Surin, M.; Samorì, P. *Adv. Mater.* **2008**, *20* (12), 2433.

(159) Kim, K.-H.; Yu, H.; Kang, H.; Kang, D. J.; Cho, C.-H.; Cho, H.-H.; Oh, J. H.; Kim, B. J. *J. Mater. Chem. A* **2013**, *1* (46), 14538.

(160) Xiao, Z.; Sun, K.; Subbiah, J.; Ji, S.; Jones, D. J.; Wong, W. W. H. *Sci. Rep.* **2014**, *4*.

(161) Yassin, A.; Leriche, P.; Allain, M.; Roncali, J. *New J. Chem.* **2013**, *37* (2), 502.

(162) Siram, R. B. K.; Stephen, M.; Ali, F.; Patil, S. *J. Phys. Chem. C*, **2013**, *117* (18), 9129–9136.

(163) Yao, K.; Chen, L.; Li, F.; Wang, P.; Chen, Y. *J. Phys. Chem. C.* **2012** *116* (1), 714-721.

(164) Li, F.; Yager, K. G.; Dawson, N. M.; Jiang, Y.-B.; Malloy, K. J.; Qin, Y. *Polym. Chem.* **2015**, *6* (5), 721.

(165) Li, F.; Yager, K. G.; Dawson, N. M.; Yang, J.; Malloy, K. J.; Qin, Y. *Macromolecules*, **2013**, *46* (22), 9021–9031.

(166) Lin, Y.; Lim, J. A.; Wei, Q.; Mannsfeld, S. C. B.; Briseno, A. L.; Watkins, J. J.*Chem. Mater.*, **2012**, *24* (3), 622–632.

(167) Lin, Y.-H.; Nie, W.; Tsai, H.; Li, X.; Gupta, G.; Mohite, A. D.; Verduzco, R. *RSC Adv.* **2016**, *6* (57), 51562.

(168) Kumar, R. J.; Subbiah, J.; Holmes, A. B. *Beilstein J. Org. Chem.* **2013**, *9*, 1102.

(169) Schulze, B. M.; Shewmon, N. T.; Zhang, J.; Watkins, D. L.; Mudrick, J. P.; Cao, W.; Zerdan, R. B.; Quartararo, A. J.; Ghiviriga, I.; Xue, J.; Castellano, R. K. *J. Mater. Chem. A* **2013**, *2* (5), 1541.

(170) Shewmon, N. T.; Watkins, D. L.; Galindo, J. F.; Zerdan, R. B.; Chen, J.; Keum, J.; Roitberg, A. E.; Xue, J.; Castellano, R. K. *Adv. Funct. Mater.* **2015**, *25* (32), 5166.

(171) Ouchi, H.; Lin, X.; Kizaki, T.; Prabhu, D. D.; Silly, F.; Kajitani, T.; Fukushima, T.; Nakayama, K.; Yagai, S. *Chem. Commun.* **2016**, *52* (50), 7874.

(172) Huang, C.-H.; McClenaghan, N. D.; Kuhn, A.; Bravic, G.; Bassani, D. M. *Tetrahedron* **2006**, *62* (9), 2050.

(173) Yagai, S.; Suzuki, M.; Lin, X.; Gushiken, M.; Noguchi, T.; Karatsu, T.; Kitamura, A.; Saeki, A.; Seki, S.; Kikkawa, Y.; Tani, Y.; Nakayama, K. *Chem. – Eur. J.* **2014**, *20* (49), 16128.

(174) Lee, O. P.; Yiu, A. T.; Beaujuge, P. M.; Woo, C. H.; Holcombe, T. W.; Millstone, J. E.; Douglas, J. D.; Chen, M. S.; Fréchet, J. M. J. *Adv. Mater.* **2011**, *23* (45), 5359.

(175) He, G.; Li, Z.; Wan, X.; Zhou, J.; Long, G.; Zhang, S.; Zhang, M.; Chen, Y. *J. Mater. Chem. A* **2013**, *1* (5), 1801.

(176) Tamayo, A. B.; Walker, B.; Nguyen*, T.-Q. *J. Phys. Chem. C* **2008**, *112* (30), 11545.

(177) Tamayo, A. B.; Tantiwiwat, M.; Walker, B.; Nguyen, T.-Q. *J. Phys. Chem. C* **2008**, *112* (39), 15543.

(178) Tamayo, A. B.; Dang, X.-D.; Walker, B.; Seo, J.; Kent, T.; Nguyen, T.-Q. *Appl. Phys. Lett.* **2009**, *94* (10), 103301.

(179) Lee, J. W.; Choi, Y. S.; Jo, W. H. *Org. Electron.* **2012**, *13* (12), 3060.

(180) Riggs, R. L.; Morton, C. J. H.; Slawin, A. M. Z.; Smith, D. M.; Westwood, N. J.; Austen, W. S. D.; Stuart, K. E. *Tetrahedron* **2005**, *61* (47), 11230.

(181) Luňák Jr., S.; Vyňuchal, J.; Vala, M.; Havel, L.; Hrdina, R. *Dyes Pigments* **2009**, *82* (2), 102.

(182) Cataldi, T. R. I.; Centonze, D.; Ricciardi, G. *Electroanalysis* **1995**, *7* (4), 312.

(183) Denat, F.; Gaspard-Iloughmane, H.; Dubac, J. *Synthesis* **1992**, *1992* (10), 954.

(184) Spano, F. C. *Acc. Chem. Res.* **2010**, *43* (3), 429.

(185) Aytun, T.; Barreda, L.; Ruiz-Carretero, A.; Lehrman, J. A.; Stupp, S. I. *Chem. Mater.*, **2015**, *27* (4), 1201–1209.

(186) Pommerehne, J.; Vestweber, H.; Guss, W.; Mahrt, R. F.; Bässler, H.; Porsch, M.; Daub, J. *Adv. Mater.* **1995**, *7* (6), 551.

(187) Skrovanek, D. J.; Howe, S. E.; Painter, P. C.; Coleman, M. M. *Macromolecules* **1985**, *18* (9), 1676.

(188) Chang, L.; Lademann, H. W. A.; Bonekamp, J.-B.; Meerholz, K.; Moulé, A. J. *Adv. Funct. Mater.* **2011**, *21* (10), 1779.

(189) Nikiforov, M. P.; Lai, B.; Chen, W.; Chen, S.; Schaller, R. D.; Strzalka, J.; Maser, J.; Darling, S. B. *Energy Environ. Sci.* **2013**, *6* (5), 1513.

(190) Qi, B.; Wang, J. *Phys. Chem. Chem. Phys.* **2013**, *15* (23), 8972.

(191) Szarko, J. M.; Guo, J.; Liang, Y.; Lee, B.; Rolczynski, B. S.; Strzalka, J.; Xu, T.; Loser, S.; Marks, T. J.; Yu, L.; Chen, L. X. *Adv. Mater.* **2010**, 22 (48), 5468-5472.

(192) Lilliu, S.; Agostinelli, T.; Pires, E.; Hampton, M.; Nelson, J.; Macdonald, J. E. *Macromolecules* **2011**, *44* (8), 2725.

(193) Rivnay, J.; Noriega, R.; Northrup, J. E.; Kline, R. J.; Toney, M. F.; Salleo, A. *Phys. Rev. B* **2011**, *83* (12), 121306.

(194) Hindeleh, A. M.; Hosemann, R. *J. Phys. C Solid State Phys.* **1988**, *21* (23), 4155.

(195) Gao, J.; Chen, W.; Dou, L.; Chen, C.-C.; Chang, W.-H.; Liu, Y.; Li, G.; Yang, Y. *Adv. Mater.* **2014**, *26* (19), 3142.

(196) Rogers, J. T.; Schmidt, K.; Toney, M. F.; Bazan, G. C.; Kramer, E. J. *J. Am. Chem. Soc.* **2012**, *134* (6), 2884.

(197) Collins, B. A.; Li, Z.; Tumbleston, J. R.; Gann, E.; McNeill, C. R.; Ade, H. *Adv. Energy Mater.* **2013**, *3* (1), 65.

(198) Carsten, B.; Szarko, J. M.; Son, H. J.; Wang, W.; Lu, L.; He, F.; Rolczynski, B. S.; Lou, S. J.; Chen, L. X.; Yu, L. *J. Am. Chem. Soc.*, **2011**, *133* (50), 20468–20475.

(199) Miller, N. C.; Cho, E.; Gysel, R.; Risko, C.; Coropceanu, V.; Miller, C. E.; Sweetnam, S.; Sellinger, A.; Heeney, M.; McCulloch, I.; Brédas, J.-L.; Toney, M. F.; McGehee, M. D. *Adv. Energy Mater.* **2012**, *2* (10), 1208.

(200) Wiberg, J.; Marinado, T.; Hagberg, D. P.; Sun, L.; Hagfeldt, A.; Albinsson, B. *J. Phys. Chem. C* **2009**, *113* (9), 3881.

(201) Li, C.; Yang, X.; Chen, R.; Pan, J.; Tian, H.; Zhu, H.; Wang, X.; Hagfeldt, A.; Sun, L. *Sol. Energy Mater. Sol. Cells* **2007**, *91* (19), 1863.

(202) Kanimozhi, C.; Naik, M.; Yaacobi-Gross, N.; Burnett, E. K.; Briseno, A. L.; Anthopoulos, T. D.; Patil, S. *J. Phys. Chem. C* **2014**, *118* (22), 11536.

(203) Warnan, J.; Cabanetos, C.; Labban, A. E.; Hansen, M. R.; Tassone, C.; Toney, M. F.; Beaujuge, P. M. *Adv. Mater.* **2014**, 26 (25), 4357-4362.

(204) Ide, M.; Saeki, A.; Koizumi, Y.; Koganezawa, T.; Seki, S. *J. Mater. Chem. A* **2015**, *3* (43), 21578.

(205) Yan, X.; Li, S.; Pollock, J. B.; Cook, T. R.; Chen, J.; Zhang, Y.; Ji, X.; Yu, Y.; Huang, F.; Stang, P. J. *Proc. Natl. Acad. Sci.* **2013**, *110* (39), 15585.

(206) Furukawa, H.; Cordova, K. E.; O'Keeffe, M.; Yaghi, O. M. *Science* **2013**, *341* (6149), 1230444.

(207) Mastalerz, M.; Oppel, I. M. *Angew. Chem. Int. Ed.* **2012**, *51* (21), 5252.

(208) Helzy, F.; Maris, T.; Wuest, J. D. *J. Org. Chem.* **2016**, *81* (8), 3076.

(209) Zhou, D.-D.; Xu, Y.-T.; Lin, R.-B.; Mo, Z.-W.; Zhang, W.-X.; Zhang, J.-P. *Chem. Commun.* **2016**, *52* (28), 4991.

(210) Hisaki, I.; Nakagawa, S.; Sato, H.; Tohnai, N. *Chem. Commun.* **2016**, *52* (63), 9781.

(211) Pfeffermann, M.; Dong, R.; Graf, R.; Zajaczkowski, W.; Gorelik, T.; Pisula, W.; Narita, A.; Müllen, K.; Feng, X. *J. Am. Chem. Soc.*, **2015**, *137* (45), 14525–14532.

(212) Tian, J.; Zhou, T.-Y.; Zhang, S.-C.; Aloni, S.; Altoe, M. V.; Xie, S.-H.; Wang, H.; Zhang, D.-W.; Zhao, X.; Liu, Y.; Li, Z.-T. *Nat. Commun.* **2014**, *5*, 5574.

(213) Zhang, K.-D.; Tian, J.; Hanifi, D.; Zhang, Y.; Sue, A. C.-H.; Zhou, T.-Y.; Zhang, L.; Zhao, X.; Liu, Y.; Li, Z.-T. *J. Am. Chem. Soc.*, **2013**, *135* (47), 17913–17918.

(214) Roy, S.; Titi, H. M.; Goldberg, I. *CrystEngComm* **2016**, *18* (19), 3372.

(215) Guo, J.; Xu, Y.; Jin, S.; Chen, L.; Kaji, T.; Honsho, Y.; Addicoat, M. A.; Kim, J.; Saeki, A.; Ihee, H.; Seki, S.; Irle, S.; Hiramoto, M.; Gao, J.; Jiang, D. *Nat. Commun.* **2013**, *4*, 2736.

(216) Côté, A. P.; Benin, A. I.; Ockwig, N. W.; O'Keeffe, M.; Matzger, A. J.; Yaghi, O. M. *Science* **2005**, *310* (5751), 1166.

(217) Colson, J. W.; Dichtel, W. R. *Nat. Chem.* **2013**, *5* (6), 453.

(218) Feng, X.; Chen, L.; Dong, Y.; Jiang, D. *Chem. Commun.* **2011**, 47 (7), 1979-1981.

(219) Bertrand, G. H. V.; Michaelis, V. K.; Ong, T.-C.; Griffin, R. G.; Dincă, M. *Proc. Natl. Acad. Sci.* **2013**, *110* (13), 4923.

(220) Chen, L.; Furukawa, K.; Gao, J.; Nagai, A.; Nakamura, T.; Dong, Y.; Jiang, D. *J. Am. Chem. Soc.*, **2014**, *136* (28), 9806–9809.

(221) Medina, D. D.; Werner, V.; Auras, F.; Tautz, R.; Dogru, M.; Schuster, J.; Linke, S.; Döblinger, M.; Feldmann, J.; Knochel, P.; Bein, T. *ACS Nano*, **2014**, *8* (4), 4042–4052.

(222) Dogru, M.; Handloser, M.; Auras, F.; Kunz, T.; Medina, D.; Hartschuh, A.; Knochel, P.; Bein, T. *Angew. Chem. Int. Ed.* **2013**, *52* (10), 2920.

(223) Whitesides, G. M.; Simanek, E. E.; Mathias, J. P.; Seto, C. T.; Chin, D.; Mammen, M.; Gordon, D. M. *Acc. Chem. Res.* **1995**, *28* (1), 37.

(224) Liang, Y.; Wu, Y.; Feng, D.; Tsai, S.-T.; Son, H.-J.; Li, G.; Yu, L. *J. Am. Chem. Soc.*, **2009**, *131* (1), 56–57.

(225) Schmidt, K.; Tassone, C. J.; Niskala, J. R.; Yiu, A. T.; Lee, O. P.; Weiss, T. M.; Wang, C.; Fréchet, J. M. J.; Beaujuge, P. M.; Toney, M. F. *Adv. Mater.* **2014**, *26* (2), 300.

(226) Perez, L. A.; Chou, K. W.; Love, J. A.; van der Poll, T. S.; Smilgies, D.-M.; Nguyen, T.-Q.; Kramer, E. J.; Amassian, A.; Bazan, G. C. *Adv. Mater.* **2013**, *25* (44), 6380.

(227) Wang, H.; Liu, F.; Bu, L.; Gao, J.; Wang, C.; Wei, W.; Russell, T. P. *Adv. Mater.* **2013**, *25* (45), 6519.

(228) Schaffer, C. J.; Palumbiny, C. M.; Niedermeier, M. A.; Burger, C.; Santoro, G.; Roth, S. V.; Müller-Buschbaum, P. *Adv. Energy Mater.* **2016**, 6 (19), 1600712.

(229) An, Q.; Zhang, F.; Zhang, J.; Tang, W.; Deng, Z.; Hu, B. *Energy Environ. Sci.* **2016**, *9* (2), 281.

(230) Choi, N.-S.; Chen, Z.; Freunberger, S. A.; Ji, X.; Sun, Y.-K.; Amine, K.; Yushin, G.; Nazar, L. F.; Cho, J.; Bruce, P. G. *Angew. Chem. Int. Ed.* **2012**, *51* (40), 9994.

(231) Simon, P.; Gogotsi, Y. *Nat. Mater.* **2008**, *7* (11), 845.

(232) Kötz, R.; Carlen, M. *Electrochimica Acta* **2000**, *45* (15–16), 2483.

(233) Pandolfo, A. G.; Hollenkamp, A. F. *J. Power Sources* **2006**, *157* (1), 11.

(234) Wang, G.; Zhang, L.; Zhang, J. *Chem. Soc. Rev.* **2012**, *41* (2), 797.

(235) Frackowiak, E.; Béguin, F. *Carbon* **2001**, *39* (6), 937.

(236) Liu, R.; Duay, J.; Lee, S. B. *Chem. Commun.* **2011**, *47* (5), 1384.

(237) Taberna, P. L.; Mitra, S.; Poizot, P.; Simon, P.; Tarascon, J.-M. *Nat. Mater.* **2006**, *5* (7), 567.

(238) Liu, R.; Duay, J.; Lane, T.; Lee, S. B. *Phys. Chem. Chem. Phys.* **2010**, *12* (17), 4309.

(239) Xu, C.; Kang, F.; Li, B.; Du, H. *J. Mater. Res.* **2010**, *25* (8), 1421.

(240) Rudge, A.; Davey, J.; Raistrick, I.; Gottesfeld, S.; Ferraris, J. P. *J. Power Sources* **1994**, *47* (1), 89.

(241) Yang, S.; Song, X.; Zhang, P.; Gao, L. *J. Mater. Chem. A* **2013**, *1* (45), 14162.

(242) El-Kady, M. F.; Ihns, M.; Li, M.; Hwang, J. Y.; Mousavi, M. F.; Chaney, L.; Lech, A. T.; Kaner, R. B. *Proc. Natl. Acad. Sci.* **2015**, *112* (14), 4233.

(243) Alhebshi, N. A.; Rakhi, R. B.; Alshareef, H. N. *J. Mater. Chem. A* **2013**, *1* (47), 14897.

(244) Li, Z.; Xu, Z.; Wang, H.; Ding, J.; Zahiri, B.; Holt, C. M. B.; Tan, X.; Mitlin, D. *Energy Environ. Sci.* **2014**, *7* (5), 1708.

(245) Liu, Y.; Ma, Y.; Guang, S.; Xu, H.; Su, X. *J. Mater. Chem. A* **2013**, *2* (3), 813.

(246) Shen, L.; Che, Q.; Li, H.; Zhang, X. *Adv. Funct. Mater.* **2014**, *24* (18), 2630.

(247) Yang, P.; Li, Y.; Lin, Z.; Ding, Y.; Yue, S.; Wong, C. P.; Cai, X.; Tan, S.; Mai, W. *J. Mater. Chem. A* **2013**, *2* (3), 595.

(248) Yu, X.; Lu, B.; Xu, Z. *Adv. Mater.* **2014**, *26* (7), 1044.

(249) Jiang, Y.; Wang, P.; Zang, X.; Yang, Y.; Kozinda, A.; Lin, L. *Nano Lett.* **2013**, *13* (8), 3524.

(250) Liu, W.; Lu, C.; Liang, K.; Tay, B. K. *J. Mater. Chem. A* **2014**, *2* (14), 5100.

(251) Zhang, H.; Cao, G.; Wang, Z.; Yang, Y.; Shi, Z.; Gu, Z. *Nano Lett.* **2008**, *8* (9), 2664.

(252) Jurewicz, K.; Delpeux, S.; Bertagna, V.; Béguin, F.; Frackowiak, E. *Chem. Phys. Lett.* **2001**, *347* (1–3), 36.

(253) Schnoor, T. I. W.; Smith, G.; Eder, D.; Koziol, K. K. K.; Tim Burstein, G.; Windle, A. H.; Schulte, K. *Carbon* **2013**, *60*, 229.

(254) Xiao, Q.; Zhou, X. *Electrochimica Acta* **2003**, *48* (5), 575.

(255) Fu, H.; Du, Z.; Zou, W.; Li, H.; Zhang, C. *J. Mater. Chem. A* **2013**, *1* (47), 14943.

(256) Zhou, Y.; Lachman, N.; Ghaffari, M.; Xu, H.; Bhattacharya, D.; Fattahi, P.; Abidian, M. R.; Wu, S.; Gleason, K. K.; Wardle, B. L.; Zhang, Q. M. *J. Mater. Chem. A* **2014**, *2* (26), 9964.

(257) Pham, D. T.; Lee, T. H.; Luong, D. H.; Yao, F.; Ghosh, A.; Le, V. T.; Kim, T. H.; Li, B.; Chang, J.; Lee, Y. H. *ACS Nano*, **2015**, *9* (2), 2018–2027

(258) Xu, Y.; Lin, Z.; Zhong, X.; Huang, X.; Weiss, N. O.; Huang, Y.; Duan, X. *Nat. Commun.* **2014**, *5*, 4554.

(259) Wang, H.; Xu, Z.; Kohandehghan, A.; Li, Z.; Cui, K.; Tan, X.; Stephenson, T. J.; King'ondu, C. K.; Holt, C. M. B.; Olsen, B. C.; Tak, J. K.; Harfield, D.; Anyia, A. O.; Mitlin, D. *ACS Nano*, **2013**, *7* (6), 5131–5141.

(260) Yoon, Y.; Lee, K.; Kwon, S.; Seo, S.; Yoo, H.; Kim, S.; Shin, Y.; Park, Y.; Kim, D.; Choi, J.-Y.; Lee, H. *ACS Nano*, **2014**, *8* (5), 4580–4590.

(261) Futaba, D. N.; Hata, K.; Yamada, T.; Hiraoka, T.; Hayamizu, Y.; Kakudate, Y.; Tanaike, O.; Hatori, H.; Yumura, M.; Iijima, S. *Nat. Mater.* **2006**, *5* (12), 987.

(262) Qiu, Y.; Li, G.; Hou, Y.; Pan, Z.; Li, H.; Li, W.; Liu, M.; Ye, F.; Yang, X.; Zhang, Y. *Chem. Mater.*, **2015**, *27* (4), 1194–1200.

(263) Chen, L.; Bai, H.; Huang, Z.; Li, L. *Energy Environ. Sci.* **2014**, *7* (5), 1750.

(264) Ren, Z. F.; Huang, Z. P.; Xu, J. W.; Wang, J. H.; Bush, P.; Siegal, M. P.; Provencio, P. N. *Science* **1998**, *282* (5391), 1105.

(265) Hasegawa, K.; Noda, S. *ACS Nano* **2011**, *5* (2), 975.

(266) Wang, B.; Qin, L.; Neumann, K. D.; Uppaluri, S.; Cerny, R. L.; DiMagno, S. G.
       Org. Lett. **2010**, *12* (15), 3352.

(267) Nemoto, H.; Nishiyama, T.; Akai, S. *Org. Lett.* **2011**, *13* (10), 2714.

(268) Pedersen, C. J. *J. Am. Chem. Soc.* **1967**, *89* (26), 7017.

(269) Hoey, M. D.; Dittmer, D. C. *J. Org. Chem.* **1991**, *56* (5), 1947.

(270) Illescas, B.; Martín, N.; Seoane, C.; de la Cruz, P.; Langa, F.; Wudl, F.
       Tetrahedron Lett. **1995**, *36* (45), 8307.

Appendix 1. Original Research Proposal: Study of Ion Diffusion Kinetics in Electrochemical Supercapacitors

Abstract

The development of energy storage systems will help transient technologies such as solar or wind to generate power at night or when there is no wind. Though there are several types energy storage systems, this proposal is focused on electric energy storage, more specifically supercapacitors. The field of supercapacitors attempts to bridge the gap between batteries (long term, low power energy delivery) and capacitors (short term, high power energy delivery), by creating high-surface area electrodes that can store large amounts of energy and are still able to deliver it at relatively large power quantities. There are two types of supercapcacitors, those that are more battery-like, called pseudocapacitors, and those that resemble capacitors, called double-layer capacitors. Both have advantages over each other, but for the purpose of this proposal, double-layer capacitors will be the subject of study.

The objective of this proposal is to modify the surface of vertically grown multi-walled carbon nanotubes on the surface of an double-layer capacitor electrode, with corresponding positive or negative ion-binding groups so that the kinetics of ion transport will be affected in such a way that the charging times will be considerably faster than the discharge rates. Since double-layer capacitors have a much larger lifetime than batteries or pseudocapacitors, this strategy address two drawbacks of this technology, low capacitance and fast discharge rates.

A.1.1 Introduction

The projected global energy consumption of the year 2050 is nearly three times the current one.[2] Although the current energy reserves are still more than enough for the foreseeable future, especially after the discovery of fracking technology, it is now common knowledge that burning fossil fuels over the last one and a half centuries has had a significant impact on the global climate. For that reason, the global tendency is to seek alternative sources of energy. Nevertheless, with the exception, of hydroelectric power, alternative energies such as solar and wind, are transient, meaning that the sun does not shine everyday and the wind does not blow constantly. Storing electrical energy for later use is now a new strategy that complements energy generation in renewable energy systems.[230]

The most well-known energy storage systems are batteries and capacitors, each having its own advantages and disadvantages. To better understand energy storage systems, the Ragonne plot in Figure 5.1 shows power density vs. energy density; batteries tend to be in the lower right region, meaning they can deliver a low amount of power for extended periods. Capacitors tend to be on the upper left region, meaning they can deliver large amounts of power, but only for a short period.[231] Ideally, a storage system should combine the advantages of both, i.e. be able to deliver high power for long periods. Essentially, an ideal energy storage system would be as close to the top right corner of the Ragonne plot as possible. The field of supercapacitors is currently attempting to do just that. Within the field of supercapacitors, there are two classes, electric double-layer capacitors and pseudocapacitors.
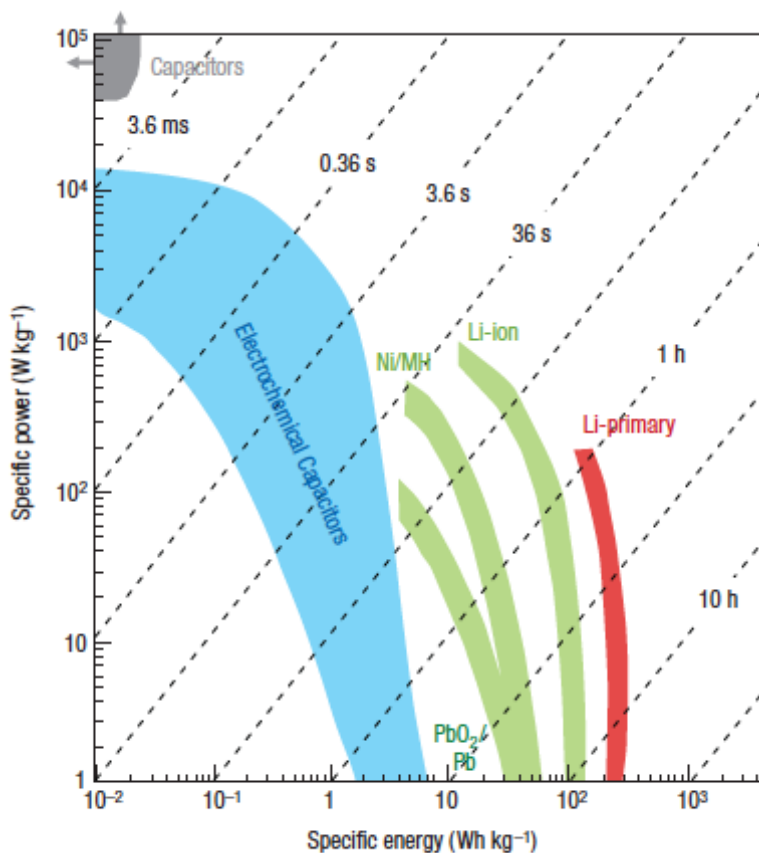
Figure A.1. Ragonne plot showing the energy and power densities of different storage systems. Retrieved from ref. 231.

Electric double layer capacitors (EDLs) store energy in the electrochemical double layer, also known as Helmholtz Layer, which forms at an electrode/electrolyte interface.[232] A schematic of an EDL is shown in Figure 5.2a;[233] it consists of a single cell with two high surface-area electrodes, which are immersed in an electrolyte, and are separated by a porous material (a separator).[234] The electrolyte solubilizes positive and negative ionic charges that accumulate at the surface of the electrode and compensates for the electronic charge at the electrode surface.[232] The mechanism of operation is purely by ion diffusion; during charging, electrons travel from the negative electrode to the positive one through an external circuit, but within the electrolyte, cations move

towards the negative electrode while anions move towards the positive one (Figure 5.2b). During discharge, the reverse processes take place;[234] consequently, there are no redox reactions, which eliminates volume changes during charge/discharge cycles, and allows for lifetimes of millions of cycles. In addition, the rapid ion diffusion allows very fast energy uptake and delivery, regardless of the solvent used, since the latter is not involved in the charge storage mechanism. The main drawback of EDLs is their limited energy density, where current research focuses on addressing.[231]
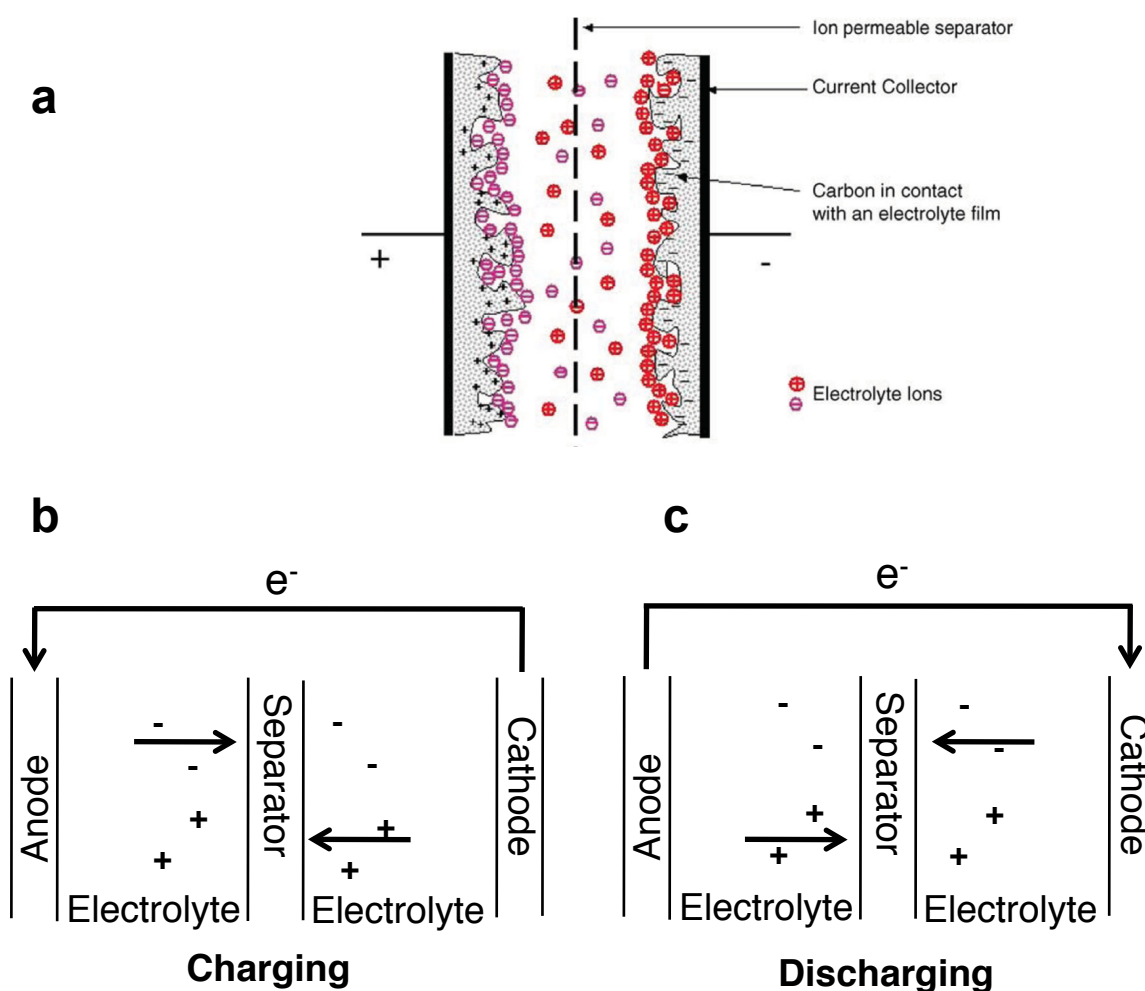
Figure A.2. a) Schematic of an EDL supercapacitor (Retrieved from Ref. 233) and the dynamics of ion exchange during charging (b) and discharging (c).

In pseudocapacitors, the energy is delivered by faradaic reactions, i.e. fast redox reactions that happen at the surface of the electrode.[231] Pseudocapacitance arises when, the charge required for the progression of an electrode process changes continuously as a function of potential; the rate of change of charge vs. potential corresponds to a faradaic-like capacitance, and the term 'pseudo' implies that the double-layer capacitance arises from quick faradaic reactions and not from ion diffusion as in EDLs.[235] Figure 5.3 shows a schematic of a pseudocapacitor;[236] most of the components in EDLs are also present in pseudocapacitors, with the exception that the latter use metal oxides such as Fe_3O_4,[237] RuO_2 (very popular but expensive)[238] and MnO_2 (a viable alternative to RuO_2),[239] even some conducting polymers.[240] This type of supercapacitor is more popular than EDLs because of the higher capacitance (1000s of F/g as opposed to EDLs with <100s F/g). The higher capacitance, however, does come with drawbacks; including shorter lifetime (1,000s cycles), which arises due to volume changes of the active material during charge/discharge, and slower charging rates.[231]
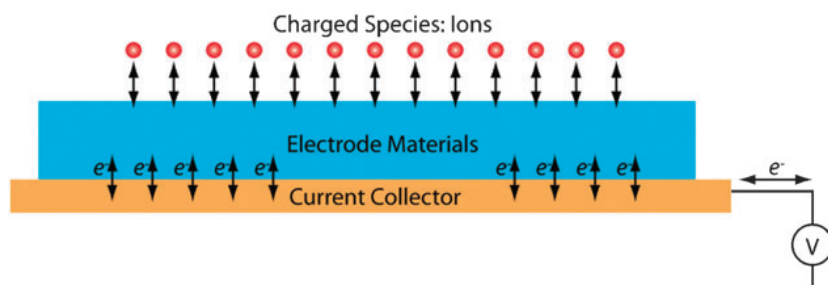
Figure A.3. Schematic of a pseudocapacitor. Retrieved from Ref. 236.

A1.2 Scientific Objectives

In both types of supercapacitors, the electrodes dictate in large part what the final capacitance will be, since in both cases, the larger the surface area of the electrode, the

better the performance will be.[234] The end-goal is to increase the capacitance as much as possible, but to the authors best knowledge, no attempt has been made at modifying a supercapacitor's ability to charge/discharge, via chemical ways. The goal of this proposal is to modify an electrode's surface with anion and cation binding groups, such that during discharge, the binding groups will prevent charges to flow rapidly, but during charge, they will increase the speed of ions due to their natural tendency to bind them. In other words, *the goal of this project is to chemically modify and electrode surface to make it charge faster and discharge more slowly*. Since the goal of this proposal is to change the kinetics of charge/discharge, an EDL design is required (given that pseudocapacitors already have defined charge/discharge rates by the type of redox reaction), and for reasons that will be explained later, the electrode material of choice is vertically grown multi-walled carbon nanotubes (MWCNT). Although the goal of this proposal is not directly intended at increasing capacitance, it is expected that if such studies were carried out, there would be a capacitance enhancement.

A1.3 Previous Work

The current supercapacitor literature is dominated by pseudocapacitors, and because of the use of metal oxides, there is a need for a highly porous, conductive and cheap substrates where the metal oxide, an insulator, can be deposited on. Graphene derivatives tend to be highly used for these purposes. Recently nitrogen-doped graphene was prepared in a one-pot reaction with Mn_3O_4 and was shown to increase nearly six-fold in capacitance over other similar Mn_3O_4 systems and retained nearly 99% of capacitance over 2000 cycles.[241] In a different example, laser-scribed

graphene/MnO_2 achieved an impressive capacitance of 1100 F/g and high energy density of 20-40 Wh/g, higher than commercially available supercapacitors.[242] With so many components to be optimized, reports on different porous materials and metal oxides are common: $Ni(OH)_2$ nanoflakes conformably coated on carbon nanofibers increased five-fold in capacitance over non-conformably coated $Ni(OH)_2$;[243] highly-functionalized activated carbons (HFAC) derived from chicken egg whites, achieved an optimized capacitance of >350 F/g at 10 A/g;[244] the more classical polyaniline(PANI)/graphene recently achieved a capacitance of 1225 F/g at 1 A/g by growing PANI vertically with the aid of a sulfonated triazine;[245] $NiCoO_4$ nanowires were deposited without the need for a binder onto self-supported electrodes, and showed excellent cyclability and high specific capacitance;[246] amorphous MnO_2 nanowires formed by electrodeposition showed three-fold increase in capacitance over crystalline MnO_2;[247] exotic oxides such as a honeycomb-structure $CoMoO_4$ on 3-D graphene achieved an astonishing 96% capacitance retention over 100,000 cycles and at discharge rates of 400 A/g.[248]

The idea of using vertically aligned carbon nanotubes (CNT) has also been explored in pseudocapacitors, especially because of the binder-free nature of the electrode. Reports on Ni nanoparticles coating vertically grown CNT increased capacitance nearly six-fold over noncoated CNTs,[249] or $NiCoO_4$ being electrodeposited onto vertically grown CNTs have shown high capacitance and relatively good cyclability, with some low power and energy density though;[250] MnO_x have also been electrodeposited on vertically grown CNT arrays and showed a capacitance of 200 F/g,

with high discharge rate of 77 A/g and excellent capacitance retention of 97% after 20,000 cycles.[251]

Reports of EDLs are much less common, with more classical porous materials dominating as substrates for electrodes. Cases of the well known CNT/polypyrrole composite, which show capacitances from the low 20s to as high as 200 F/g;[252–254] other polypyrrole/CNT composites increased cyclability to more than 1000 cycles while retaining 85% of the original capacitance.[255] Other more complex mixtures of graphene/PEDOT/CNT achieved an astounding energy density of 113 Wh/L and a very high voltage of 4 V by using an asymmetric supercapacitor consisting of graphene nanoflakes as anode and PEDOT-coated CNT as cathode.[256]

Other impressive EDL performances have been obtained with more complex materials, such as positively charged CNT bridging negatively charged graphene, which achieved a high energy density of 110 Wh/kg and high power density of 400 kW/kg;[257] "holey" graphene in a binder free electrode achieved a capacitance of almost 300 F/g and energy density of 35 Wh/kg;[258] hemp-derived carbon nanosheets achieved nearly 150 F/g capacitance, at extremely high discharge rates of 100 A/g, with retention rates of up to 92% and a decent energy density of ~30 Wh/kg;[259] vertically aligned graphene sheets achieve fast ion diffusion and rectangular CV curves at high scan speeds of up to 20 V/s.[260] Similarly as with pseudocapacitors, researchers have also studied EDLs using vertically aligned carbon nanotubes that were closely packed using the zipping effect of liquids,[261] or by growing a complex network of CNT grown on carbon nanofibers, and achieving a high energy density of almost 100 Wh/kg and an impressive 97% capacitance retention after 20,000 cycles.[262]

Overall, just about every variation of porous materials, metal oxides, binders and electrolytes have been tested, which would suggest that a common method and/or material would become the standard, but the reality could not be further from the truth. Despite the extensive research on both EDLs and pesudocapacitors, it seems that the fields are still in their exploratory phases, with the only common strategy being, regardless of the type of supercapacitor used, a high surface area material that is conductive. Nevertheless, very few studies have addressed problems such as self-discharge, or actively modified specific device characteristics.[263] It is because of these reasons that this proposal stands out among the field, not because it will achieve a particularly high capacitance (as a matter of fact, there are better materials than vertically aligned CNT to obtain high capacitance), but because it is directed at changing a specific characteristic of the device, namely the charge/discharge kinetics.

A1.4 Proposed Work

Before describing the work in detail, there are a few metrics that the reader should get acquainted with. The capacitance (C) of EDLs is calculated from the equation $C=A\varepsilon/d$, where A is the surface area of the electrode, ε is the dielectric constant of the electrolyte, and d is the thickness of the double layer. The energy output is given by the equation $E = CV^2/2$ and the power is given by $P = V^2/4R$, where V is the working voltage, and R is the equivalent series resistance (as small as possible ideally).[233] Since both energy and power are proportional to the square of voltage, the latter is usually increased by using organic solvents instead of water (water limits the

working voltage to ~1 V, organic solvents can be as high as 4 V), which increases power output at the cost of environmental friendliness.[234]

Synthesis

The proposed work requires a simple design, with the least amount of components to be optimized. Vertically aligned CNTs provide the best option for this study for a few reasons: they are grown directly onto the metal electrode, which eliminates the need for a binder (an inert material that ensures good contact between the active material and the metal collector).[262] Because they are aligned with the metal, the conductivity is almost guaranteed to be high. If the nanoubes are multi-wall, the outer walls can be chemically functionalized, while the inner tubes will retain conductivity, and last but not least, a forest of tubes will have essentially the whole length of the tube available for functionalization (sterics will play a role, but this will be discussed later), something that cannot be guaranteed by graphene or mixtures of CNTs deposited onto a substrate.

The device fabrication will start with growth of multi-wall nanotubes onto a substrate. The method will be similar as the one reported by Provencio.[264] The procedure initially used a nickel coated glass substrate, but the purposes of this proposal, the substrate will have to be a nickel-coated stainless steel one. In the process, nickel is coated using radio frequency magnetron sputtering. Next, ammonia gas is introduced for 5 in, during which time, the nickel coating is then reduced in thickness with plasma etching. Immediately after 5 min of exposure to ammonia, acetylene gas is introduced and the nanotubes grow via plasma-enhanced hot filament chemical vapor deposition (PE-HF-CVD). The reported lengths are 20 μm after 10 min

growth. A typical commercial supercapacitor has about 100-200 um thickness of active material, and although there have been reports on millimeter length nanotube growth,[265] the initial proof of principle makes growing larger tubes unnecessary. The relatively short length will have to be taken into account when calculating gravimetric and volumetric capacitance. In regards to uniformity of the nanotube growth, Figure 5.4 shows two SEM micrographs where it can be seen that growth is very homogeneous, with little variation, which can simplify further testing of built devices.
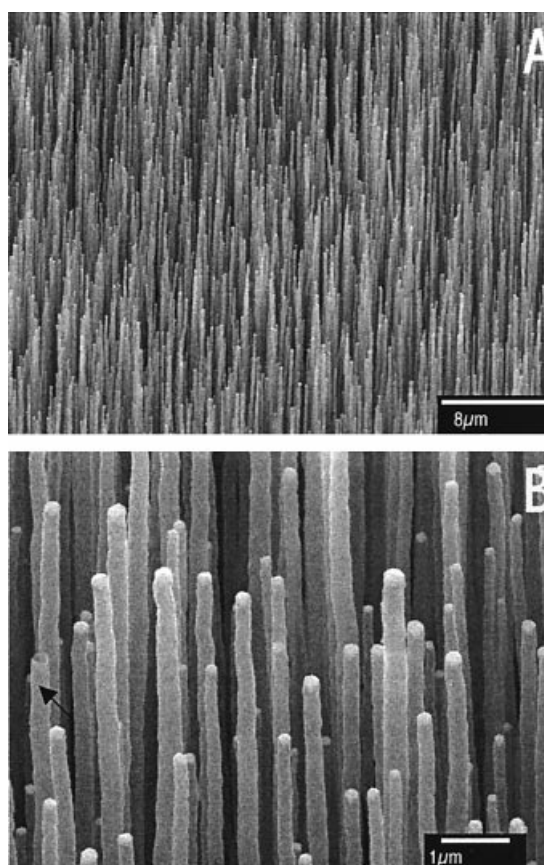
Figure A.4. MWCNT grown by PE-HF-CVD. Retrieved from Ref. 264.

The next step would be chemical functionalization of the nanotubes. Since each electrode has to have preferential binding for one type of ion (i.e. positive or negative),

then the nature of the functional groups used will necessarily have to be different. As cation binding groups, the selected hosts were crown ethers, which are well known cation hosts in the literature. Although the size of the crown ether could be varied to tune the strength of the cation binding, that avenue will not be explored in this proposal. Anion binding hosts are much more scarce, or difficult to synthesize, but a relatively simple group that does not require excessive number of steps is an amidinium ion (essentially the nitrogen analogue of a carboxylate). Scheme 5.1 shows the synthesis of both anion and cation binding units. The binding groups were selected based on the choice of the electrolyte. Since the electrolyte does not take part in the charge/discharge mechanism, it could be any salt, in any solvent, but since it needs to have ions that can be captured by chemical groups, tetramethylammonium (NMe_4OAc) acetate was chosen. Small cations like tetramethylammoniun can be captured by crown ethers, while acetate can be trapped by the amidinium ion. Acetonitrile was chosen as the solvent because it provides a higher working voltage than water, and because the power of an EDL scales with the square of the voltage.

Scheme A.1. Proposed synthesis of the cation (i-vii) and anion (viii-xii) binding groups.
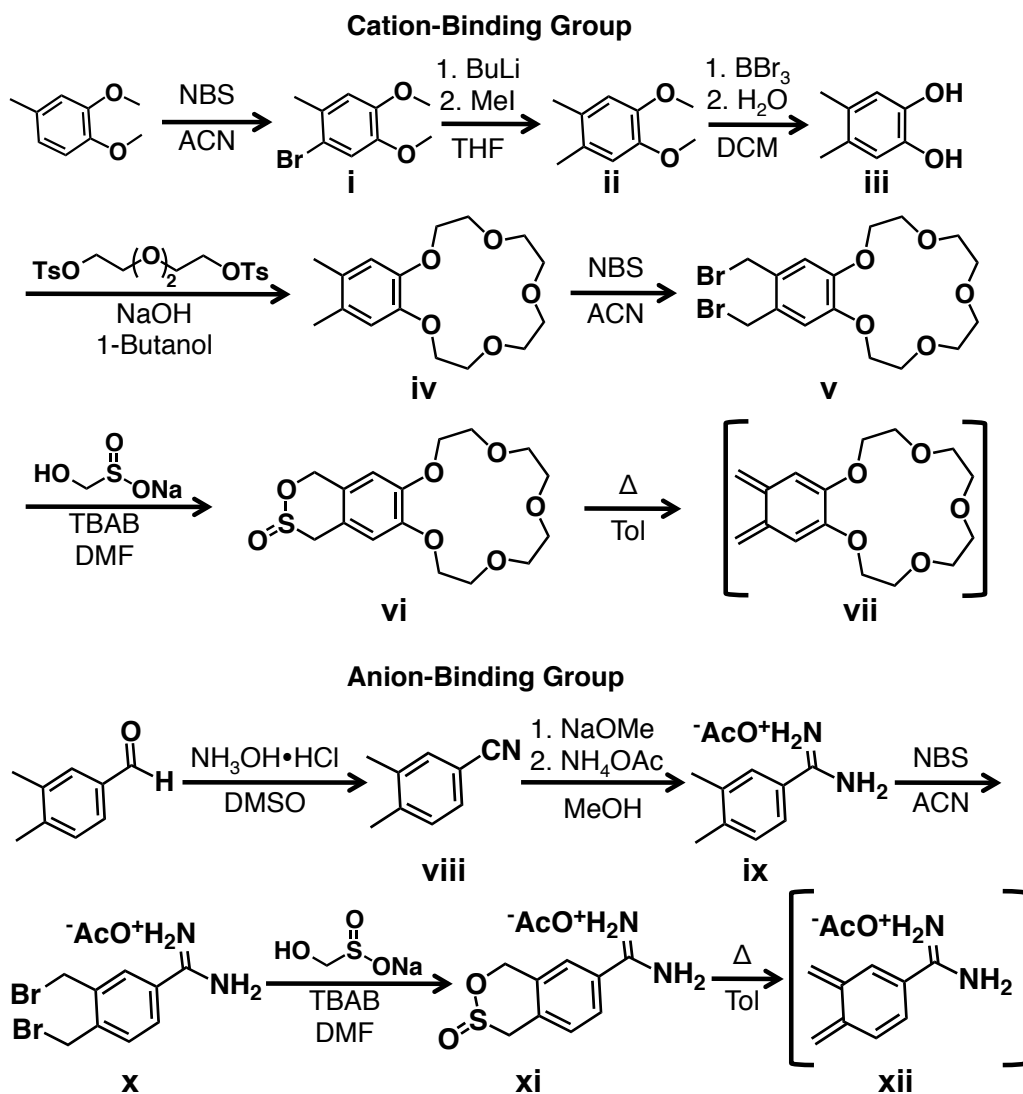
For the cation crown ether host, first, commercially available 3,4-dimethoxytoluene would be brominated with NBS in ACN;[266] the brominated product **i** would undergo lithium-bromine exchange in THF, followed by methylation with MeI to give the dimethoxyorthoxylene product **ii**; the methoxy groups would then be removed with BBr$_3$ in DCM, followed by protonation with water to give the dimethylcatechol **iii**.[267] The crown ether **iv** could then be formed according to the method developed by

Pedersen, consisting of deprotonating catechol **iii** with NaOH, then adding ditosylated teraethylene glycol, and refluxing in 1-butanol for 24 hrs.[268] The crown-ether containing xylene derivative **iv** would then be brominated with NBS once more, and the dibrominated product **v** would be reacted with sodium hydroxymethylsulfinate (rongalite) in DMF, catalyzed by TBAB, to give the sulfone **vi**.[269] The sulfone **vi** begins releasing SO_2 at around 80 °C, so intermediate **vii** cannot be isolated; since **vii** is a very reactive dienophile, it can react via a Diels-Alder reaction with the surface of the vertically grown CNT, which have a surface covered with dienes. The substrate with grown nanotubes would be submerged in a concentrated toluene solution of **vii**, then heated to reflux; the reaction has been reported to work in as little as 20 min, but refluxing in toluene overnight was required for completion (see Figure 5.5).[270]

The anion-binding group would start with commercially available 3,4-dimethylbenzaldehyde, then transform the aldehdyde into nitrile **viii** with activated DMSO. Conversion of the nitrile into the amidinium group would require reaction with NaOMe in MeOH, followed by reaction with NH_4OAc, to give the acetate salt **ix**. As with the cation binding group, bromination of the methyl groups, then reaction with rongalite would lead to the sulfone xi, which would be refluxed in toluene, or a more polar high boiling solvent like anisole for 24 hrs, with the substrate containing the CNT.

Potential synthetic problems can be encountered in the anion binding group to larger degree than the cation one. Since the amidinium group is charged, toluene will not work as a good solvent for the formation of the diene xii. Anisole was suggested as an alernative, but in extreme cases, diethylene glycol could work, and since the substrate would retain the CNTs, the excess solvent can simply be washed off. Another

potential concern is the degree of fucntionalization. Ideally, the whole outer layer fo the MWCNT would be coated, but there can be a point at which the repulsion between the groups themselves (especially in the amidinium case) would prevent further reaction. The good news is that, as before, excess reagent can be washed off, leaving the functionalized surface free of unreacted diene. In an effort to find out the maximum degree of functionalization, the ionic binding groups will each be reacted with the CNT substrate at different molar ratios, ranging from 20%-500% binding group content per mole of carbon content in the substrate. After washing and drying the substrates, the weight increase will be an indication of the degree of functionalization.

Ultimately, the performance of the supercapacitor, compared to a nonfunctionalized one will define the success of this proposal. Ideally, the surface of the CNT will be coated with the anion or cation binding group, just like Figure 5.5 depicts (Figure 5.5 only shows the cation one, but it would look similar in the anion case). As a reminder, the purpose of this proposal is to chemically functionalize the surface of vertically grown CNT with ionic binding groups, for the purpose of altering the ion kinetic exchange rate. In other words, the objective is to make an EDL to charge much faster than the discharge rate. The positive electrode would be coated with the cation binding crown ether derivative **vii** (after it has reacted), while the negative electrode will be coated with the anion binding group.
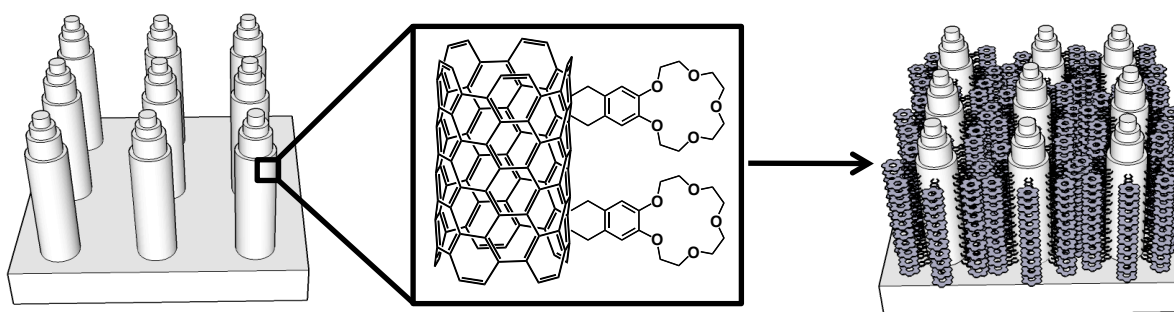
Figure A.5. Ideal functionalization of the vertically grown MWCNT (cation binding group shown for simplicity, but anion would similar).

The hypothesis behind the design is the following (for the positive electrode): it was mentioned that during charging electrons flow from the negative to positive electrode, so a positively charged surface will be more likely to accept those electrons faster to achieve charge neutralization, making charging occur faster. Conversely, during discharge, because the system is trying to move out of neutrality, the positively charged surface will resist electron migration, thus making discharge occur slower (Figure 5.6). The process would be similar in the other electrode.

Charging
Polarized surface
Fast

Discharging
Slower due
to surface
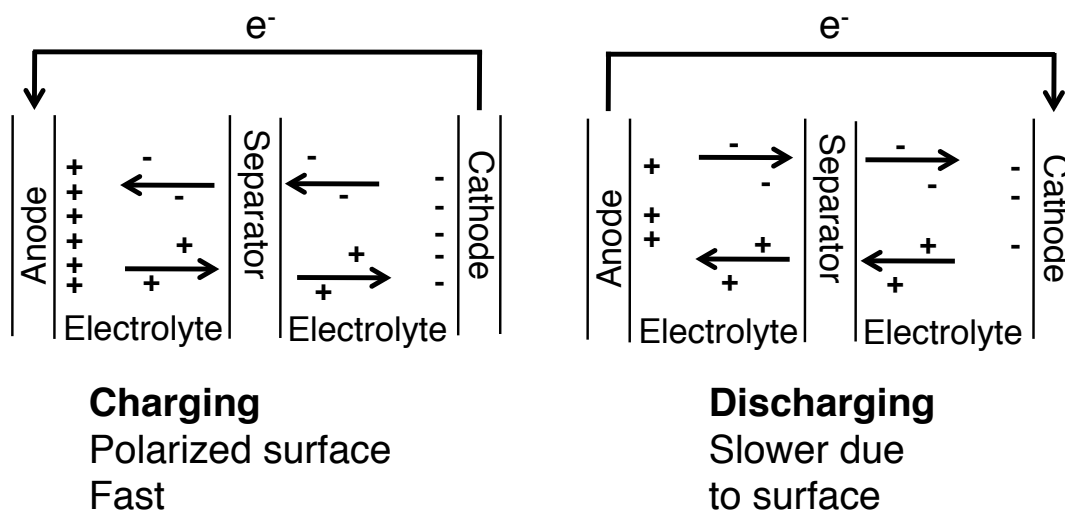
Figure A.6. Expected behavior once MWCNT are functionalized with their respective ion binding groups.

Anticipated Results

There are four main techniques used to measure the performance of a supercapacitor. A representative picture of the techniques is shown in Figure 5.7. Cyclic voltammetry measures the current response as a function of voltage; ideally, the shape of the voltammogram should be as square as possible because that would be an indication that no redox reactions are occurring (Figure 5.7a). In addition, it is common in CV to check the current response at different scan rates, for the purpose of monitoring the speed of current generation. As the voltage sweeps faster, there would be less time for the binding groups to trap ions, and unlike the example CV of Figure 5.7a, the response expected for the electrodes of this proposal should be inverse of the example (the response would follow the direction of the arrow as scan rate increases). With faster voltage, the capacitor should behave as a regular capacitor would at low scan rates, because the resistance to current flow from the binding groups would be eliminated.

Another technique analyzed would be the charge/discharge diagram; ideally, it should be as linear as possible (again, it would imply no redox reactions), and in this case the line in charging mode should be faster than the discharge mode, so instead of an isosceles triangle shape, it would be an inclined triangle shape (see bold blue line in Figure 5.7 b). The impedance plane representation (Nyquist plot) shows the EDL response as a function of frequency (Figure 5.7c). An ideal capacitor would exhibit a vertical line, but EDLs start with a 45° impedance line (called the Warburg region) as a consequence of the distributed resistance/capacitance in the pores of the electrode; at low frequencies, the line becomes almost vertical, and at higher frequencies both

resistance and capacitance decrease due to the inaccessibility of the pores, and the EDL approaches ideal behavior. The expected response is shown in the thick blue line in Figure 5.7c. Because the discharge rate would be slowed down, the EDL would behave more resistive, even at low frequencies, increasing the length of the Warburg region, then as frequency increases, it would assume a more idealistic capacitive behavior, so the line would increase slope gradually (the arrow indicates the expected response).

A different way of analyzing the performance of an EDL based on frequency would be a capacitance vs. frequency (Bode) plot. Since at low frequencies the EDL is expected to be more resistive, the Bode plot in Figure 5.7d would still be S-shaped, but it would retain capacitance better at low frequencies, and then possibly drop a bit more drastically than a non-functionalized EDL would, similar to the thick blue in the figure (again, the arrow shows the expected response). Lastly, since there would be no redox reactions, the expected capacitance dependency on cycle number would be very similar to that show in Figures 5.7 d and e (ideally a flat line over 100,000 cycles).
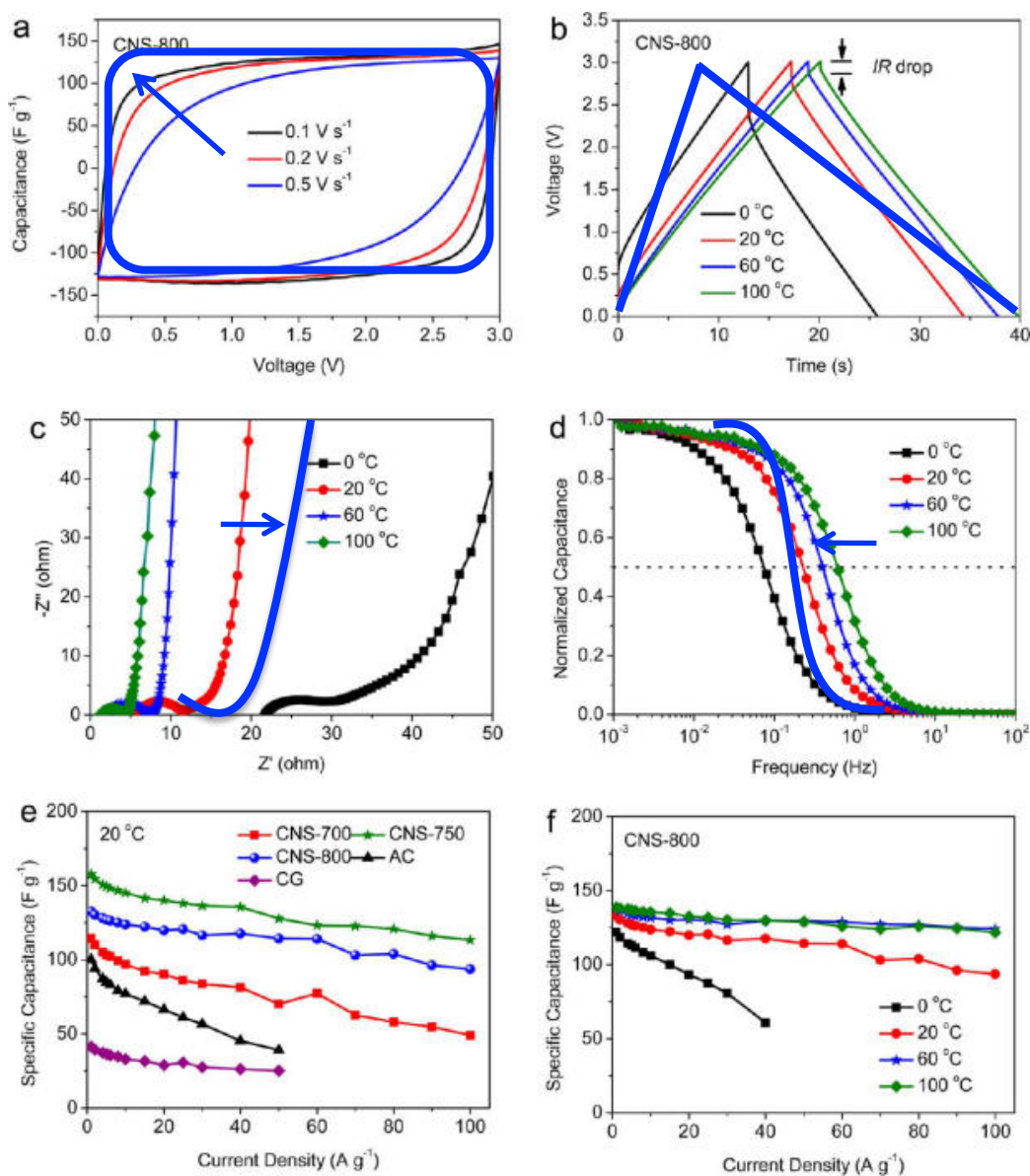
Figure A.7. Expected resuls in a) CV; b) charge/discharge rates; c) impedance plot; d) capacitance-frequency plot and capacitance dependence (e-f) plots. Main figure retrieved from ref. 259.

The anticipated pitfalls vary in terms of the severity of the problem encountered. One possible scenario would be that the binding groups work, but the end performance is opposite of what was intended, i.e. the EDL discharges faster than it charges; in that case, the polarity of the ion binding groups will be reversed, i.e., crown ethers would functionalize the negative electrode and amidinium the positive one. After that, the

same tests would be performed and check if the desired behavior is obtained. The other scenario is that even after changing the polarity, the EDL still discharges considerably faster than it charges. At this point, there would need to be a more systematic approach to fixing the problem, and so two controls in which both electrodes are coated with the same polarity would have to be run, then analyzed independently by all the mentioned techniques, then together in a device, and maybe the answer to the problem might be found there. One of the concerns of using two different binding groups is the strength of binding; in this case it is possible to find that because of the difference in binding strength of the binding groups, the effectiveness of charging does not allow discharge to occur, potentially, or it could be the opposite, where amidinium binds too strongly and prevents effective charging. If such a case were encountered, the only viable alternative would be to optimize the functionalization density so that the effect of the difference in binding groups is dimished, or eliminated. Due to synthetic limitations, finding two groups of approximately the same binding affinity might be too complicated, so the design should ideally remain the same, but optimization of functionalization density would consume considerable amounts of material, so it should be used as a last reso

A1.5 Summary and Conclusions

The objective of this proposal is aimed at altering the kinetics of ion exchange in EDLs, for the purpose of making charging rates much faster than discharge rates, effects. Achieving such objective is thought to be possible through chemical functionalization of the surface of vertically grown MWNT. Crown-ether based cation binding groups would be used in the positive electrode, while amidinium-based anion

binding groups would be used for the negative electrode. This idea has never been proposed before and the expected behavior was extrapolated from nonfunctionalized CNTs. The potential pitfalls include finding out the behavior is opposite of what was intended, in which case the polarity of the binding groups would be reversed, but from then on, the potential solution to the problem becomes more complicated. Given that the underlying nature of the proposal is its viability, changing the identity for the binding groups should be left as a last resource.

Curriculum Vitae

Leonel Barreda

2145 Sheridan Rd. Evanston, IL 60208   847-467-4928   leonelbarreda@gmail.com

Education

Northwestern University, Department of Chemistry   2010-Present
Ph.D. Candidate in Materials Chemistry, GPA: 3.33
Dissertation: Manipulation of Intermolecular Interactions for Active Layer Morphology
Optimization in Organic Photovoltaics
Advisor: Prof. Samuel I. Stupp

University of Texas at El Paso (UTEP), Department of Chemistry   May 2010
B.S. Chemistry (Physic/mathematics minor), GPA: 3.80
Thesis: Functional Self-Organization of Novel DNA Hybrid Materials
Advisor: Prof. Juan C. Noveron

Research Experience:

Northwestern University.   Sep 2010 – Present
- Supramolecular Polymers for Active Layer Organization in Photovoltaics
  Designed, synthesized and characterized several dozen organic donor libraries of
      thiophene-, benzodithiophene- and diketopyrrolopyrrole-based dyes for
      applications in organic photovoltaics, dye-sensitized and perovskite solar cells.
  Applied multi-step synthetic pathways to give rise to a novel family of
      diketopyrrolopyrrole-containing hydrogen-bonded molecules with improved
      power conversion efficiency, and developed a method for tuning molecular
      assembly in solution and on films.
  Collaborated with material scientists to optimize the electronic properties and
      performance of several hundred intermediates for photovoltaic devices.
  Incorporated device engineering requirements into molecular designs by fine-tuning
      properties such as absorption and aggregation in solution and film via synthetic
      modifications.
- Organic Charge-Transfer Complexes & Surfactant-Mediated Electrodeposition of
  Metal Oxides
  Designed and synthesized three small libraries of diimide- and naphthalene-based
      molecules for charge-transfer complexes, as well as two families of pyrene- and
      naphthalene-based surfactants for electrodeposition of cobalt oxide films.

University of Texas at El Paso.   2008 – 2010
- Functional Self-Organization of Novel DNA Hybrid Materials

Successfully polymerized several aniline derivatives in water, using DNA as a template.

Characterized DNA-polyaniline derivatives with dynamic light scattering (DLS), FTIR and AFM.

Developed a system to trap heavy metals (chromium specifically) from water by using DNA-polystyrene organo gel derivatives.

Created a DNA sensor material using complementarity of single stranded DNA in functionalized single-walled carbon nanotube-DNA hybrid materials.

Proficiencies and Skills

Synthetic Chemistry
- Air-free and moisture-free reactions (palladium-catalyzed couplings, lithiations, reductions, acylations, hydrogenation, etc)
- Solution and solid phase peptide synthesis
- Elimination, substitution, protection, alkylation and addition reactions
- Optimization of dye and surfactant properties, such as solubility (aqueous and/or organic), color, fluorescence and aggregation in solution and film

Analytical Chemistry
- Proficient in analysis by NMR, FTIR, UV-Vis, fluorescence spectroscopies, and mass spectrometry methods, including MALDI-MS and ESI-MS
- Proficient in determination of HOMO-LUMO levels via cyclic voltammetry (CV) and in topographic thin film analysis with atomic force microscopy (AFM)
- Proficient in material isolation and purification by extraction and chromatographic methods (regular phase silica gel and size-exclusion)

Software
- Familiar in the use of specialized chemical softwares (Gaussview, Hyperchem, ChemDraw, iNMR and MestReNova) and design softwares such as SketchUp, Cinema 4D and Adobe Illustrator.
- Proficient in MS Word, Excel and Powerpoint.

Languages
Professional proficiency in Spanish.

Publications and Presentations

Barreda, L.; Aytun, T.; Stupp, S.I. Supramolecular Organic Frameworks for High Efficiency Small-Molecule Organic Photovoltaics. **2016**. In preparation.

Aytun, T.; **Barreda, L.**; Santos, P.J.; Stupp, S.I. Ternary Donor Small Molecules with Additive-Like Side Chains for Improved Performance in Photovoltaics. **2016**. In Preparation.   [Co-first author]

Aytun, T.; **Barreda, L**.; Ruiz-Carretero, A.; Lehrman, J.A.; Stupp, S.I. Improving Solar Cell Efficiency through Hydrogen Bonding: A Method for Tuning Active Layer Morphology. *Chem. Mater*. **2015**, 27, 1201−1209.　　　[Co-first author]

Conference Presentations:

Barreda, L.; Aytun, T, Narayanan, A.; Fairfiel, D.J.; Stupp, S.I. Design and Synthesis of Molecules for Energy Applications. Industrial Associates Meeting, Northwestern University. 2016, Evanston IL.

Barreda, L.; Aytun, T.; Ruiz-Carretero, A.; Lehrman, J.; Stupp, S.I. Supramolecular Polymers for Active Layer Organization in Photovoltaics. Dow BEST Symposium 2015, Midland, MI

Barreda, L.; Aytun, T.; Ruiz-Carretero, A.; Lehrman, J.; Stupp, S.I. Supramolecular Polymers for Active Layer Organization in Photovoltaics. 249th ACS National Meeting, Denver, CO. 2015, ORGN 241

Barreda, L.; Porta, B.M.; Noveron, J.C. DNA-Templated Polymerization of Styrene Derivatives in Water: New Nanomaterial Composites. 237th ACS National Meeting, Salt Lake City, UT, 2009, POLY-266.

Honors and Awards

Recipient of The Graduate School (TGS) and Phi Lambda Upsilon (PLU) Travel Grants
　　　　　March 2015
Magna Cum Laude UTEP Graduate. May 2010
Recipient of the Maximizing Access for Research Careers (MARC) Undergraduate Fellowship. Jan 2009-Aug 2010

Teaching and Outreach

Northwestern University　　　　　　　　　　　　　　　　　　　　2014-2016
　Mentored two undergraduate students in organic chemistry techniques for organic photovoltaic and charge transfer complex, resulting in the synthesis of approximately fifty intermediates that were successfully tested in collaboration with materials scientists.

Phi Lambda Upsilon (PLU) Science in the Classroom (SITC)　　　　　2011-2015
　Led a group of five graduate students and performed science experiments to children in 3rd and 4th grade at Hayt Elementary School once a month to foster science careers in young students.

Department of Chemistry, Northwestern University　　　　　　　　2010-2011
　Participated as a TA in Chem 210 courses, assisting a group of twenty undergraduates perform chemical reactions and evaluated their synthetic and analytical chemistry performance.

American Chemical Society (ACS), UTEP Chapter   Summer 2009
  Helped perform chemical demonstrations for children in elementary school in Cd.
  Juarez, Mexico.